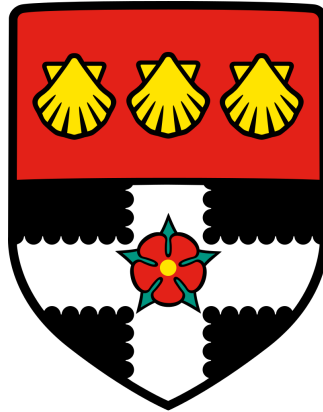


UNIVERSITY OF READING

Department of Meteorology



**The Relationship Between the  
Circumglobal Teleconnection, the  
Indian Monsoon and European  
Summer Weather**

**JONATHAN DAVID BEVERLEY**

*A thesis submitted for the degree of Doctor of Philosophy*

August 2019

---

---

# Declaration

I confirm that this is my own work and the use of all material from other sources has been properly and fully acknowledged.

Jonathan Beverley

---

---

# Abstract

European summer weather extremes can have wide-reaching and severe societal impacts, therefore the ability to forecast seasonal anomalies several weeks or months in advance would be extremely beneficial. This thesis investigates the relationship between the circumglobal teleconnection (CGT), the Indian summer monsoon (ISM) and European summer weather.

It is shown that the representation of the CGT in the ECMWF seasonal forecast model is too weak. The model has errors in the basic state, including a northward displacement of the jet stream, and these may be important in the representation of the CGT. Results from relaxation experiments, in which the model is corrected to reanalysis in specific regions, suggest that northwest Europe is more important in forcing the CGT and in the downstream development of errors in the CGT pattern than west-central Asia and the ISM, although the link between ISM precipitation and the extratropical circulation is weak in all experiments.

Thermal forcing experiments in the ECMWF model suggest that the ISM does force an extratropical, CGT-like response over east Asia, the North Pacific and North America, with upper tropospheric anticyclonic anomalies in these regions associated with increased monsoon heating. However, the response over Europe occurs largely through westward-propagating Rossby waves, as opposed to the eastward-propagating waves associated with the CGT. The frequency of blocking over Europe is also shown to be related to variations in ISM heating, with a larger number of blocked days when ISM heating is reduced, which may have implications for European circulation predictability. However, it remains unclear whether this occurs as a result of perturbations to the jet via the North Pacific, or through the westward-propagating response. This westward-propagating response, which is also seen in barotropic model experiments, was found to be crucial in the downstream reinforcement of the wave train between Asia and North America.

---

---

# Acknowledgements

I received a great deal of help and support throughout my PhD for which I am extremely grateful. Firstly, I'd like to thank my supervisors, Steve Woolnough, Laura Baker, Stephanie Johnson and Antje Weisheimer, for their help and support throughout the project. I have learnt an incredible amount over the last three and a half years and this is in no small part due to their encouragement, enthusiasm and expertise. I'd also like to thank Andy Turner, Nigel Arnell and Sean Milton for their feedback during monitoring committees and the viva, which helped to improve the thesis a great deal.

Elsewhere, I'm also grateful to Chris O'Reilly for providing me with the barotropic model code and the edited branch which allowed me to perform the ECMWF thermal forcing experiments, both of which greatly aided the analysis in the thesis, and also for providing assistance with the use of both of these when I needed it. In addition, Paul Dando at ECMWF provided excellent support, both when setting up the experiments, and getting them going again if they failed!

There are too many people to name individually, but my thanks must go to all those who made the Meteorology Department such a fantastic place to work and socialise, whether this was through performing in the panto, playing football or cricket, or simply going to the pub, I could not have completed this PhD without you. Special thanks also go to my 1U09 officemates, particularly Bethan, Jacob, Josh and Mark, for providing some memorable moments over the years and plenty of welcome (and a few not-so-welcome) distractions which helped to keep me sane.

Finally, I am particularly grateful to my family, especially my parents, whose love, support and encouragement enabled me to get to this position in the first place. I could not have done this without you.

# Contents

<b>Declaration</b>	<b>i</b>
<b>Abstract</b>	<b>ii</b>
<b>Acknowledgements</b>	<b>iii</b>
<b>Contents</b>	<b>iv</b>
<b>List of Acronyms</b>	<b>vii</b>
<b>1 Introduction</b>	<b>1</b>
1.1 Introduction and motivation . . . . .	1
1.2 Thesis aims and structure . . . . .	5
<b>2 Scientific background</b>	<b>7</b>
2.1 Factors affecting European weather . . . . .	7
2.1.1 Local drivers . . . . .	7
2.1.2 Remote drivers . . . . .	10
2.2 European seasonal forecasting . . . . .	14
2.3 Indian monsoon variability . . . . .	17
2.3.1 Interannual variability . . . . .	17
2.3.2 Intraseasonal variability . . . . .	19
2.3.3 Indian monsoon seasonal forecast skill . . . . .	20
2.4 Teleconnections associated with the Indian monsoon . . . . .	21
2.4.1 Indian summer monsoon–Europe teleconnections . . . . .	23
<b>3 Data, models and methods</b>	<b>32</b>
3.1 ECMWF Reanalysis - Interim . . . . .	32
3.2 Observational datasets . . . . .	33
3.2.1 Global Precipitation Climatology Project . . . . .	33
3.3 Models . . . . .	34
3.3.1 ECMWF Integrated Forecasting System and seasonal forecasting . . . . .	34
3.3.2 Integrated Forecasting System relaxation technique . . . . .	35
3.3.3 Thermal forcing technique . . . . .	37
3.3.4 Linear barotropic model . . . . .	38
3.3.5 Multiple sampling . . . . .	39
3.4 Fourier filtering . . . . .	40
<b>4 The representation of the circumglobal teleconnection in the ECMWF seasonal forecast model</b>	<b>41</b>
4.1 Introduction . . . . .	41
4.2 Diagnosing model performance . . . . .	42

4.2.1	Forecast skill . . . . .	42
4.2.2	Model representation of the circumglobal teleconnection . . . . .	45
4.3	Understanding errors in the model teleconnection . . . . .	50
4.3.1	Errors in the D&W region . . . . .	50
4.3.2	Rossby wave source . . . . .	51
4.4	Summary and conclusions . . . . .	57
<b>5</b>	<b>Investigating the circumglobal teleconnection mechanism using relaxation experiments</b>	<b>59</b>
5.1	Introduction . . . . .	59
5.2	Experimental design . . . . .	60
5.3	Experimental analysis . . . . .	62
5.3.1	New control experiment . . . . .	62
5.3.2	West-central Asia relaxation . . . . .	65
5.3.3	Northwest Europe relaxation . . . . .	72
5.3.4	Indian monsoon relaxation . . . . .	76
5.3.5	Comparison of relaxation experiments . . . . .	79
5.4	Barotropic model experiments . . . . .	85
5.4.1	Motivation . . . . .	85
5.4.2	Experimental design . . . . .	86
5.4.3	Experimental analysis . . . . .	88
5.5	Summary and conclusions . . . . .	91
<b>6</b>	<b>Using thermal forcing experiments to explore the role of the Indian monsoon in driving the extratropical circulation</b>	<b>94</b>
6.1	Introduction . . . . .	94
6.2	Thermal forcing experiments . . . . .	95
6.2.1	Experimental design . . . . .	95
6.2.2	Experimental analysis . . . . .	99
6.3	Barotropic model experiments . . . . .	112
6.4	Summary and conclusions . . . . .	121
<b>7</b>	<b>Discussion and conclusions</b>	<b>125</b>
7.1	Overview . . . . .	125
7.2	Discussion and conclusions . . . . .	126
7.2.1	How well is the circumglobal teleconnection represented in a state-of-the-art seasonal forecast model? . . . . .	126
7.2.2	What is the role of the Indian summer monsoon in driving the circumglobal teleconnection? . . . . .	128
7.2.3	How does the Indian summer monsoon influence circulation variability over Europe? . . . . .	132

7.3	Summary . . . . .	133
7.4	Future work . . . . .	135
7.4.1	What is the source of the weak representation of the circumglobal teleconnection in the model? . . . . .	136
7.4.2	Is the signal between the Indian summer monsoon and northwest Europe seen in the model also present in observations, and if so can it be used as a source of predictability for the European summer? . . . . .	137
7.4.3	How do other seasonal forecast models perform at representing the circumglobal teleconnection? . . . . .	137
	<b>References</b>	<b>139</b>

# List of Acronyms

Acronym	Definition
AIR	All-India Rainfall
CGT	Circumglobal teleconnection
DJF	December, January, February
D&W	Ding and Wang region
EASIA	East Asia region
ECMWF	European Centre for Medium-Range Weather Forecasts
ENSO	El Niño Southern Oscillation
EOF	Empirical Orthogonal Function
GPCP	Global Precipitation Climatology Project
IOD	Indian Ocean Dipole
ISM	Indian summer monsoon
JJA	June, July, August
MJO	Madden-Julian Oscillation
NAM	North America region
NAO	North Atlantic Oscillation
NCEP	National Centers for Environmental Prediction
NPAC	North Pacific region
NWEUR	Northwest Europe region
RWS	Rossby wave source
SNAO	Summer North Atlantic Oscillation
SRP	Silk Road Pattern
SST	Sea surface temperature

---

## Chapter 1:

# Introduction

## 1.1 Introduction and motivation

Variations in summer climate across Europe can have wide reaching and severe effects on both society and industry. In recent years, a number of extreme weather events have occurred in the summer in Europe which have highlighted the vulnerability of society to seasonal climate extremes. Possibly the most notable and widespread was the 2003 European heatwave, which was the hottest for at least 500 years in some parts of Europe (Luterbacher et al., 2004), with the highest temperatures located over central and southern Europe (Figure 1.1). Estimates of heat-related deaths range from 35,000–70,000, with some estimates exceeding these figures, most of which occurred during July and August (Robine et al., 2008). There were also widespread crop failures and loss of livestock across Europe, which were estimated to have cost European farming €13.1 billion. As recently as 2018, much of northern and western Europe experienced a prolonged heatwave that led to severe wildfires in many regions, while the UK experienced its joint-warmest summer on record (Met Office, 2018).

In contrast, there have also been a number of severe summer flooding events in recent years, such as those in 2007 and 2012 in the UK (Figure 1.2). In both of these years, frequent areas of low pressure associated with a southerly jet location resulted in exceptionally wet summers. The UK as a whole experienced its wettest June–July period on record in 2007, a record which was subsequently broken in 2012. In both years, thousands of homes were flooded and insured losses ran into the hundreds of millions of

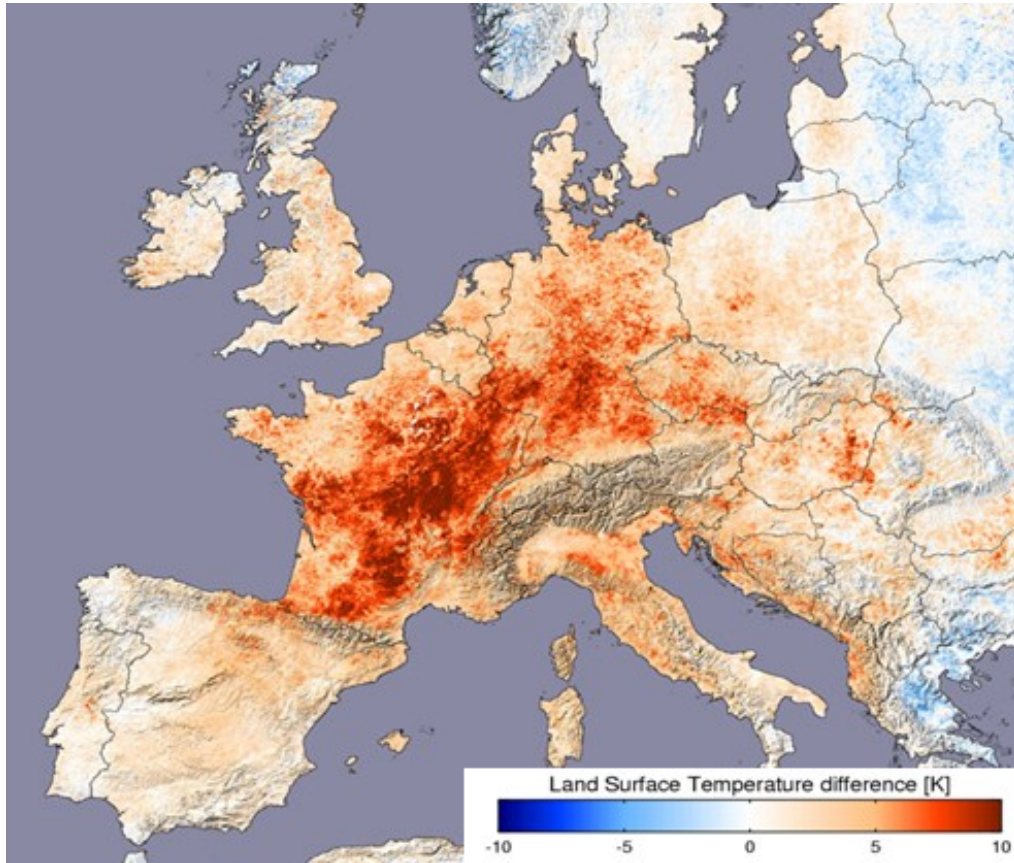


**Figure 1.1:** August 2003 temperature relative to 2000, 2001, 2002 and 2004 average (NASA Terra satellite).

pounds, although losses in 2012 were less than those seen in 2007 due to the improvements made to flood defences in the wake of the 2007 floods (Pitt, 2008; Hughes and Gambrill, 2012).



**Figure 1.2:** Flooding in the UK in recent summers: (a) in 2007 at Walham power substation, Gloucester and (b) in 2012 at Tewkesbury.

Extreme weather events such as these have emphasised the need for more accurate long-range forecasts for the European summer. In the event of either a heatwave or a flood, availability of skillful forecasts several weeks or months in advance would allow governments and businesses to plan ahead to mitigate potential impacts. This could include stockpiling water resources in the increased likelihood of a drought, or strengthening flood defences given an increased chance of excess rainfall.

A seasonal forecast attempts to provide useful information about the expected climate several weeks to months ahead. Reliable seasonal forecasts, on timescales of greater than two weeks to around one year, have only recently become possible thanks to increases in computer power and an improved understanding of the physical processes that operate on a seasonal timescale. Predictability of meteorological variables on an extended timescale relies largely on the existence of slow variations in soil moisture, sea ice and snow cover and sea surface temperature (SST) (Charney and Shukla, 1981). The slowly varying nature of SSTs in the equatorial Pacific associated with El Niño Southern Oscillation (ENSO) make it the largest known source of year-to-year climate variability. Aside from ENSO, SST anomalies in the Atlantic and Indian Oceans are also causes of seasonal climate variability.

However, despite recent advances in the understanding of global seasonal-scale drivers, seasonal forecasts still lack skill in some regions at certain times of the year, and one of these is the European summer. Figure 1.3, taken from Mishra et al. (2019), is an example of this, and shows seasonal forecast skill for surface temperature for Europe in four different coupled seasonal forecast models for summer compared to winter. While some parts of Europe, particularly southern Europe, have significant positive skill in some models, none have significant skill for northern and western Europe in summer. The current state of seasonal forecasting for the European summer is explained in more detail in Chapter 2.

The potential benefits of better, more accurate long-range forecasts for the European summer are clear. As outlined above, advance warning of an increased likelihood of flood or drought several weeks or months in advance would allow the necessary preparations and precautions to be made. One potential source of predictability on a seasonal timescale is via teleconnection mechanisms. A possible source of extratropical teleconnections in the northern hemisphere summer is the Indian summer monsoon (ISM) and this thesis focusses on one potential teleconnection mechanism in particular which may link the ISM

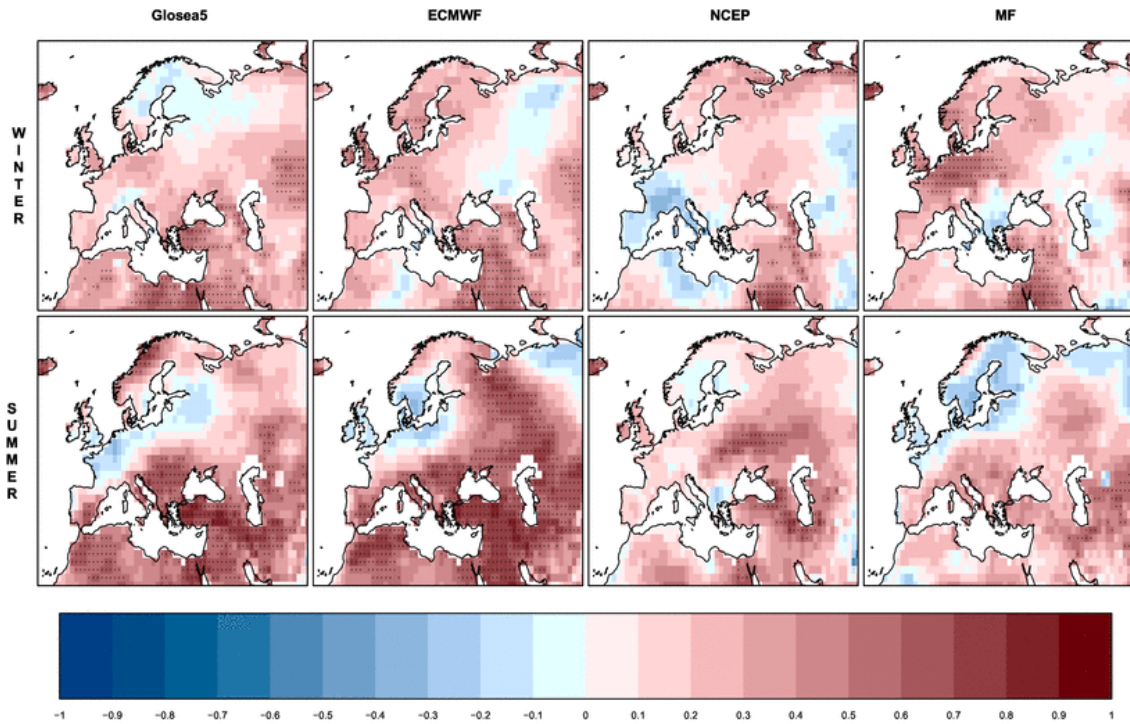


**Figure 1.3:** Anomaly correlation coefficient (ACC) between the predicted ensemble mean of each individual coupled seasonal forecast model and the observed seasonal winter (DJF; top row) and summer (JJA; bottom row) surface temperature obtained from ERA-Interim over the European region ( $20^{\circ}\text{W}$ – $70^{\circ}\text{E}$  and  $25^{\circ}\text{N}$ – $75^{\circ}\text{N}$ ) for the period 1992–2012. The individual seasonal forecast models are GloSea5, ECMWF, National Centers for Environmental Prediction (NCEP) and MeteoFrance (MF) (from left to right). Forecasts are initialised in November for DJF and in May for JJA. Areas covered in red are indicative of positive correlation, while areas covered in blue indicate negative correlation. Dots in each grid point indicate significant positive correlation at 5% significance level using one-sided Student t-test and controlling for false discovery rate. From Mishra et al. (2019).

to Europe - the circumglobal teleconnection (CGT, Ding and Wang, 2005).

The CGT is a hemispheric wave train that can influence seasonal temperature and precipitation anomalies in many parts of the northern hemisphere. Figure 1.4 shows the correlation between a 200 hPa geopotential height index centred in west-central Asia (box) and 200 hPa geopotential height elsewhere, for August. The location of the main positive centres of action of the CGT are over east Asia, the North Pacific, North America and northwest Europe, while there are negative centres over eastern Europe and the western and eastern North Pacific. The variations in the strength of the CGT were hypothesised by Ding and Wang (2005) to be at least partly driven by variations in ISM precipitation, and so the potential of the ISM as a source of subseasonal to seasonal predictability for Europe is investigated in this thesis. Further details about the CGT mechanism can be found in Chapter 2.

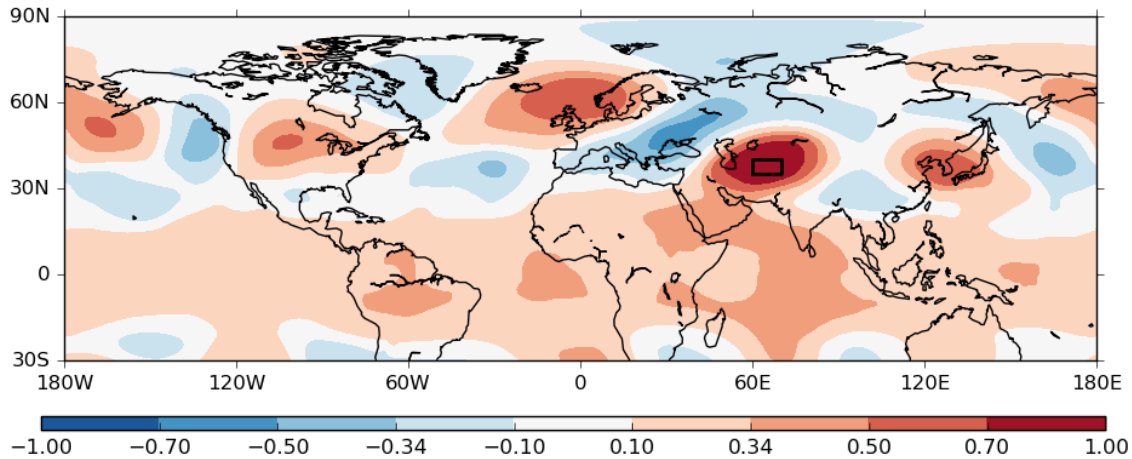


**Figure 1.4:** Correlation between ERA-Interim 200 hPa geopotential height at the base point (box, 35°–40°N, 60°–70°E) and 200 hPa geopotential height elsewhere in August. This is the CGT pattern as defined by Ding and Wang (2005). Further details can be found in Chapters 2 and 4.

## 1.2 Thesis aims and structure

Summer extremes of both temperature and precipitation in Europe are of great importance to society, and both positive and negative anomalies can have large impacts over wide regions. This thesis therefore aims to investigate the relationship between European summer seasonal forecast skill and the representation of the CGT in a seasonal forecast model, and the possible link between these and ISM precipitation. The following research questions are addressed:

1. How well is the CGT represented in a state-of-the-art seasonal forecast model?
2. What is the role of the Indian summer monsoon in driving the CGT?
3. How does the Indian summer monsoon influence circulation variability over Europe?

The rest of the thesis is structured as follows. **Chapter 2** contains an overview of the scientific background for the thesis, and a description of the relevant literature. This includes an overview of drivers of European summer weather and the causes of variability of the ISM, as well as current seasonal forecast skill for the European summer and the ISM. Also included are descriptions of possible teleconnection mechanisms associated with the ISM, including the CGT.

In **Chapter 3**, the data, including observational and reanalysis datasets, are described, along with details of the models used. Also included in Chapter 3 is a description of the relaxation technique which is implemented in Chapter 5, and the thermal forcing technique used in experiments in Chapter 6.

In **Chapter 4**, the overall skill of the model is examined, the performance of the ECMWF model at representing the CGT is analysed, and causes for errors in its representation investigated. The work in this chapter answers research question 1 given above, and has been published in a peer-reviewed journal (Beverley et al., 2019).

In **Chapter 5**, a set of relaxation experiments are described in which the circulation in several regions thought to be important for the CGT is relaxed towards ERA-Interim. These were carried out to further explore the teleconnection mechanism and its links to extratropical summer seasonal forecast skill, and were motivated by research questions 2 and 3 above. These experiments motivated the use of a barotropic model, which is used to investigate the impact of biases in the model basic state and forcing on the propagation of Rossby waves related to the CGT.

**Chapter 6** contains work motivated by results from Chapters 4 and 5. Based on findings from the barotropic model experiments at the end of Chapter 5, further experiments in the ECMWF model were carried out. In these experiments, a constant thermal forcing, both positive and negative, is applied over India to examine the impact of increased or decreased forcing from the ISM on the strength of the CGT in the model and on the circulation over Europe. This also relates to research questions 2 and 3.

Finally, in **Chapter 7**, the results and conclusions of this thesis are presented. This includes addressing the questions posed above, followed by a discussion of possible directions for future work.

## Chapter 2:

# Scientific background

This chapter contains a review of literature and the scientific background that is relevant for the subsequent chapters of this thesis. The first section includes an overview of the range of large-scale circulation patterns and drivers, both local and remote, that affect the European climate, followed by details of the current state of European summer seasonal forecast skill. An overview of the different causes of Indian summer monsoon (ISM) interannual and intraseasonal variability is then given, along with details of ISM seasonal forecast skill. Teleconnections associated with the ISM are then described, with particular emphasis on those which have a potential impact on European summer weather.

## 2.1 Factors affecting European weather

### 2.1.1 Local drivers

Although weaker in summer than in winter, the Atlantic jet and the associated storm track are still the dominant circulation systems affecting the European summer climate. The midlatitude jet stream owes its existence to the equator-to-pole temperature gradient which arises due to differences in solar heating between equatorial and midlatitude regions. There are two main processes which govern the location of the jet stream. The first is the poleward transport of momentum associated with the upper branch of the Hadley circulation. Air rises near the equator and conservation of angular momentum leads to an eastward acceleration as it moves polewards, leading to the formation of the subtropical

jet stream at upper levels. The second process involves the transient eddies that are prevalent in the troposphere. These lead to the transport of vorticity and heat which also has the net effect of accelerating the westerly wind, in particular at lower levels. These jet streams are referred to as eddy-driven jets, and tend to occur through the depth of the troposphere. In winter, there is separation between the subtropical jet and eddy-driven jet, with the subtropical jet near North Africa and the eddy-driven jet further north, but in summer there is no clear separation (Woollings, 2010).

Associated with the jet stream is the North Atlantic storm track. The European climate is strongly influenced by midlatitude storms which track across the North Atlantic from the eastern coast of North America. The path along which these storms preferentially appear and propagate is termed the storm track. As with the jet stream, the storm track arises due to the meridional gradient in temperature between equatorial regions and the midlatitudes. This means that the troposphere is baroclinically unstable and cyclones and anticyclones grow on this instability to convert available potential energy to eddy kinetic energy (Charney, 1947; Eady, 1949; Simmons and Hoskins, 1978).

Closely linked to the position of the jet stream and storm track is the North Atlantic Oscillation (NAO, Walker, 1924b) and its summer equivalent, termed the Summer North Atlantic Oscillation (SNAO, Folland et al., 2009). The NAO and SNAO represent the leading mode of surface pressure variability in the North Atlantic region in the winter and summer, respectively. The NAO is typically defined as a measure of the anticorrelation between surface pressure or geopotential over Iceland and the Azores, whereas the SNAO has a more northerly location and smaller spatial scale, with the southern node over northwest Europe and a smaller-scale Arctic node (Hurrell et al., 2003). The positive phase of the SNAO has been shown to be associated with warm and dry conditions over northwest Europe, including the United Kingdom and much of Scandinavia (Folland et al., 2009). This is the opposite of the pattern seen in winter, when a positive NAO Index is associated with a more northerly jet stream location and wetter and stormier conditions across northern Europe (Woollings et al., 2010). The summer storm track has been shown to be characterised by meridional shifts between two distinct paths. When it has a more southerly location, this is associated with enhanced precipitation over northwestern Europe and decreased precipitation over southern Europe (Dong et al., 2013b). These shifts are closely related to the phase of the SNAO. This was the case in the summer of 2012, when a negative phase of the SNAO led to the UK experiencing its wettest summer

since 1912, while there were droughts and wildfires in Spain (Dong et al., 2013a).

A further influence on European weather is blocking events. The term ‘blocking’ is generally used to refer to a weather pattern where the prevailing westerly winds and midlatitude storms are blocked by a persistent anticyclonic anomaly. Due to their broad spatial scale and persistence, blocking areas of high pressure can affect the circulation patterns and therefore weather conditions over a large region for several weeks (Rex, 1950; Tyrlis and Hoskins, 2008). Europe is one of several regions in the northern hemisphere which experience blocking events frequently and they can lead to extreme weather events in both winter and summer. In winter, blocks are associated with extended spells of cold, dry weather, such as the winter of 2009/2010, which was also associated with a record negative NAO Index (Osborn, 2011). In summer, blocking events have been shown to be associated with droughts and heatwaves (Della-Marta et al., 2007; Schaller et al., 2018; Sousa et al., 2018), such as during the central European heatwave of 2003 (Black et al., 2004; García-Herrera et al., 2010). A number of different theories have been proposed for the initiation of blocking events. One of these is that blocking events in the Euro-Atlantic region can be triggered by tropical convection, such as in the Caribbean (Hoskins and Sardeshmukh, 1987; Douville et al., 2011) or tropical Atlantic (Cassou et al., 2005), and mechanisms such as this, by which weather in the tropics can affect the weather and climate in Europe, are discussed in more detail in Section 2.1.2.

A number of studies have found links between northern European summer weather and North Atlantic sea surface temperatures (SSTs) in the preceding winter or spring. Colman (1997), and subsequently Colman and Davey (1999), found that July–August surface temperatures over much of northwest Europe are predictable using a statistical linear regression based on the January–February North Atlantic SST, with observed correlations ranging from 0.4–0.7. Sutton and Hodson (2005) investigated the link between low frequency variations of European summer weather and the North Atlantic and found that multidecadal variability of summertime climate in both North America and western Europe are closely linked to the Atlantic Multidecadal Oscillation (AMO), a result which was later confirmed by Ghosh et al. (2017). Ossó et al. (2018) found that July–August precipitation over the British Isles can be predicted using a statistical model based on the March–April North Atlantic SST anomaly. They showed that this skill comes from a lagged relationship between a particular pattern of east Atlantic atmospheric circulation, which has a strong influence on rainfall in the British Isles, and a North Atlantic SST

index, with a statistically significant model correlation skill of 0.56 compared to observations. This provides the potential for improving on the current poor skill of seasonal predictions of precipitation in the European summer.

### 2.1.2 Remote drivers

The word “teleconnection” is often used to describe the link between low frequency variability of circulation patterns, temperatures and precipitation in remote locations on Earth (Bjerknes, 1969). Teleconnections act to restore atmospheric energy budget imbalances caused by meridional differences in solar heating, SST anomalies, such as those associated with El Niño Southern Oscillation (ENSO, e.g. Philander, 1983; Trenberth, 1997), and internal variability associated with midlatitude storms. One of the primary drivers of tropical–extratropical teleconnections is Rossby waves associated with tropical convection. Rossby waves are large-scale waves that occur as a result of the latitudinal variation of the Coriolis parameter (Rossby, 1939). Stationary Rossby waves such as those described in Hoskins and Karoly (1981) are key components of teleconnection pathways, and Schubert et al. (2011) showed that they account for more than 60% of the monthly mean surface temperature variability in many regions of the extratropical northern hemisphere. The dispersion relationship that describes the propagation of Rossby waves on a background zonal flow  $U$  is:

$$\omega = Uk_x - (\beta - U_{yy}) k_x / (k_x^2 + k_y^2), \quad (2.1)$$

where  $\omega$  is the wave’s frequency,  $\beta$  is the northward gradient of the vertical component of planetary vorticity,  $(\beta - U_{yy})$  represents the poleward gradient of absolute vorticity and the wavenumber  $k \equiv (k_x, k_y)$ . This means that the phase speed is always westward with respect to the zonal wind  $U$ , and waves with the longest wavelength propagate westward most rapidly.

Following Sardeshmukh and Hoskins (1988) and James (1995), the equation governing the forcing of Rossby waves can be derived from the barotropic vorticity equation for a single level in the atmosphere:

$$\frac{\partial \zeta}{\partial t} + \mathbf{v} \cdot \nabla \zeta = -\zeta D, \quad (2.2)$$

where  $\zeta$  is the absolute vorticity,  $\mathbf{v}$  is the wind field and  $D$  is the horizontal divergence  $\partial u/\partial x + \partial v/\partial y$ . The velocity field  $\mathbf{v}$  can be decomposed into  $\mathbf{v} = \mathbf{v}_\psi + \mathbf{v}_\chi$  where  $\mathbf{v}_\psi$  is the rotational component and  $\mathbf{v}_\chi$  is the divergent component of the wind field. From this, Equation 2.2 can be written as:

$$\frac{\partial \zeta}{\partial t} + \mathbf{v}_\psi \cdot \nabla \zeta = -\zeta D - \mathbf{v}_\chi \cdot \nabla \zeta. \quad (2.3)$$

Equation 2.3 represents the partitioning between the Rossby wave propagation terms on the left hand side, which involve just the rotational part of the wind field, and the forcing terms on the right hand side, which involve the divergent part of the wind. The forcing terms can therefore be grouped into one term, the Rossby wave source (RWS):

$$RWS = -\zeta D - \mathbf{v}_\chi \cdot \nabla \zeta. \quad (2.4)$$

Therefore, the interaction of the basic state vorticity gradient with upper level divergence, such as that associated with convective precipitation, can act as a source of Rossby waves, and the wave activity associated with this provides a potential source of predictability on subseasonal to seasonal timescales. The schematic shown in Figure 2.1, taken from James (1995), shows how Rossby waves can be excited by a tropical heating source, even though  $\zeta$  is usually small in the vicinity of the heating. The divergent flow is largest around the edge of the heating region, away from the region where  $D$  is large. Closer to the subtropics the gradients of  $\zeta$  become large, so the RWS (labelled  $S$  in the schematic) can be large in the subtropics, remote from the region of maximum heating. In the northern hemisphere summer (JJA), the main areas of RWS can be found over the Mediterranean and west-central Asia, associated with divergence related to the ISM, the eastern Pacific, close to North America, and the eastern North Atlantic (Hoskins et al., 1989; Shimizu and de Albuquerque Cavalcanti, 2011).

ENSO is one of the most significant drivers of global teleconnections, and the variations of SSTs in the Pacific Ocean associated with it can affect weather patterns as far

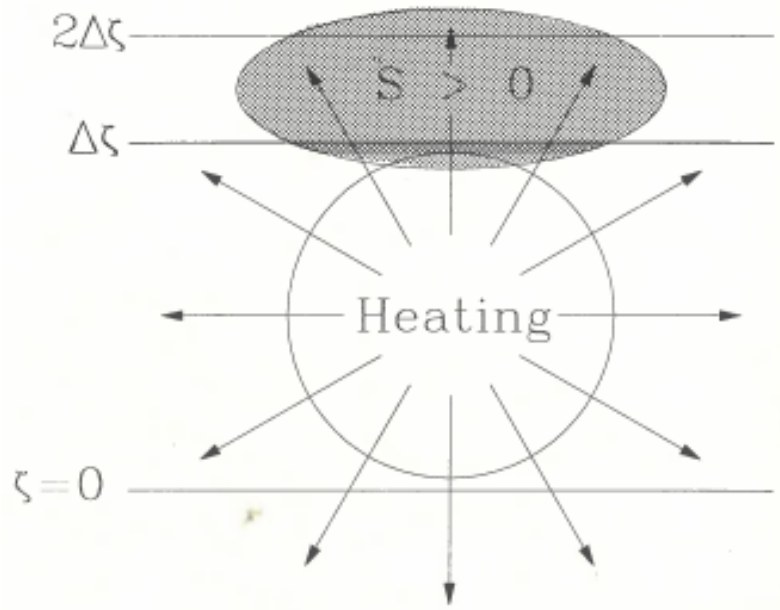


**Figure 2.1:** Schematic illustration of the forcing of a train of Rossby waves by a maximum of tropical heating. The hatched region indicates the region where the Rossby wave source function is large. From James (1995).

afield as Africa and North America. During an El Niño event the Walker circulation weakens or reverses, causing the warm pool, which in normal conditions is situated in the West Pacific and Maritime Continent, to spread eastwards along the equator. This results in a deepening of the thermocline in the East Pacific, associated with reduced cold upwelling in this region. During a La Niña event the opposite occurs, with increased cold upwelling in the East Pacific resulting in cooler SSTs in the Central and East Pacific. Precipitation in the equatorial Pacific tends to occur in the location of the warmest SSTs or steepest SST gradients, so the variations of SSTs associated with the different phases of ENSO can affect the location from which Rossby waves are excited. This in turn can result in differing impacts in those regions known to be affected by ENSO, such as parts of North and South America, Africa, Asia and Australia (Ropelewski and Halpert, 1987).

The effects of ENSO on European climate are much less well understood, and the main impacts occur during mid- to late-winter. Walker (1923, 1924a) and Walker and Bliss (1932) were the first to identify a link between the Southern Oscillation Index (SOI) and the NAO and European climate in the winter. They found that an El Niño event (negative SOI) corresponds to negative rainfall anomalies in Scandinavia and positive rainfall anomalies over western Europe between approximately 35°N and 50°N, consistent with a negative phase of the NAO. Later studies, such as that of van Loon and Madden

(1981), also show similar findings indicating a significant relationship between ENSO and winter sea level pressure and temperature in the North Atlantic/European sector, although exact details of the impacts have varied in different periods of the 20<sup>th</sup> century (Gouirand and Moron, 2003). Broadly speaking, the European signal in late winter is similar to the negative phase of the NAO for El Niño events and the positive phase for La Niña (Brönnimann, 2007). The positive NAO-like phase is pronounced for La Niña events (Pozo-Vázquez et al., 2001), and can also be associated with a weakening of the North Atlantic jet stream (Cassou and Terray, 2001).

The ENSO–Europe signal in the summer is generally much weaker, with no clear signal in the temperature and sea level pressure fields. This is due to differences in the background state, such as the more northerly location of the jet stream and the weaker amplitude of ENSO during the boreal summer. However, significant relationships have been found between ENSO and precipitation in some parts of Europe. Muñoz-Díaz and Rodrigo (2005) showed that in summer La Niña events lead to drought across southwest Spain, whereas an opposite signal is seen over parts of France (Mariotti et al., 2002). The phase of the SNAO can also be affected by ENSO, with La Niña conditions associated with a negative SNAO phase, although this relationship is weak and the effect in El Niño conditions is not significant (Folland et al., 2009).

Another important driver of tropical–extratropical teleconnections is the Madden-Julian Oscillation (MJO, Madden and Julian, 1971, 1972). The MJO consists of large-scale patterns of atmospheric circulation and convection which propagate slowly eastwards at around  $5 \text{ m s}^{-1}$ , with each cycle lasting approximately 30–60 days. It is known to influence the variability of precipitation in many regions of the tropics, including the monsoon regions of Asia and Australia, parts of North and South America and also in Africa (Jones et al., 2004; Donald et al., 2006; Lorenz and Hartmann, 2006). Given its wide-ranging impacts on tropical precipitation, the MJO can subsequently affect the weather in extratropical regions through the excitation and modulation of Rossby wave trains. Cassou (2008) found a link between the MJO and the NAO in winter, whereby the probability of a positive phase of the NAO is significantly increased around 10 days after phase 3 of the MJO, when convection is located over the Indian Ocean, and significantly decreased around 10 days after phase 6, when convection is situated over the equatorial West Pacific, and vice versa. There is no known link between the MJO and European summer weather, however the MJO is known to be a major driver of monsoon active/break peri-

ods (Annamalai and Slingo, 2001) through its summer manifestation, the boreal summer intraseasonal oscillation (BSISO). Through affecting monsoon precipitation variability, the MJO could therefore have an impact on European summer weather.

## **2.2 European seasonal forecasting**

It is difficult to predict European summer weather and climate on forecast lead times of longer than a few days. Recent research has led to improvements in European winter seasonal forecasts (e.g. Scaife et al., 2011; Stockdale et al., 2015; Dunstone et al., 2016), however there has been less of a focus on the summer season and so seasonal forecasts often show little skill (Mishra et al., 2019). As described in Section 2.1, there are a large number of drivers of European summer weather, both local, such as the SNAO and blocking, and remote, via teleconnections, such as those from ENSO. This makes seasonal forecasting for Europe particularly challenging as there are a large number of different factors to consider.

There are large differences in European forecast skill between summer and winter. One possible reason for this is that the drivers of European weather vary between summer and winter. There are also many differences in skill between different models. Figure 2.2, taken from Mishra et al. (2019), shows the forecast skill for surface temperature for four different coupled seasonal forecast models, for both winter (DJF) and summer (JJA). The four models are the Met Office Global Seasonal forecasting system version 5 (GloSea5), ECMWF System 4, National Centers for Environmental Prediction (NCEP) System 2 and MeteoFrance System 5. Of note is that all of the four models have limited skill for northwest Europe in the summer, with the GloSea5 and ECMWF models showing negative correlations over the British Isles and southern parts of Scandinavia. The skill for southern Europe and the Mediterranean varies more widely between the models in summer, with GloSea5 and ECMWF exhibiting significant skill in these regions, whereas the skill in the NCEP and MeteoFrance models is generally not significant. Comparing summer to winter in each model, it can be seen that generally there is more skill in southern Europe in summer than in winter, but across northern and western parts of Europe the skill tends to be better in winter.

For precipitation (Figure 2.3) there is almost no skill anywhere in Europe for any

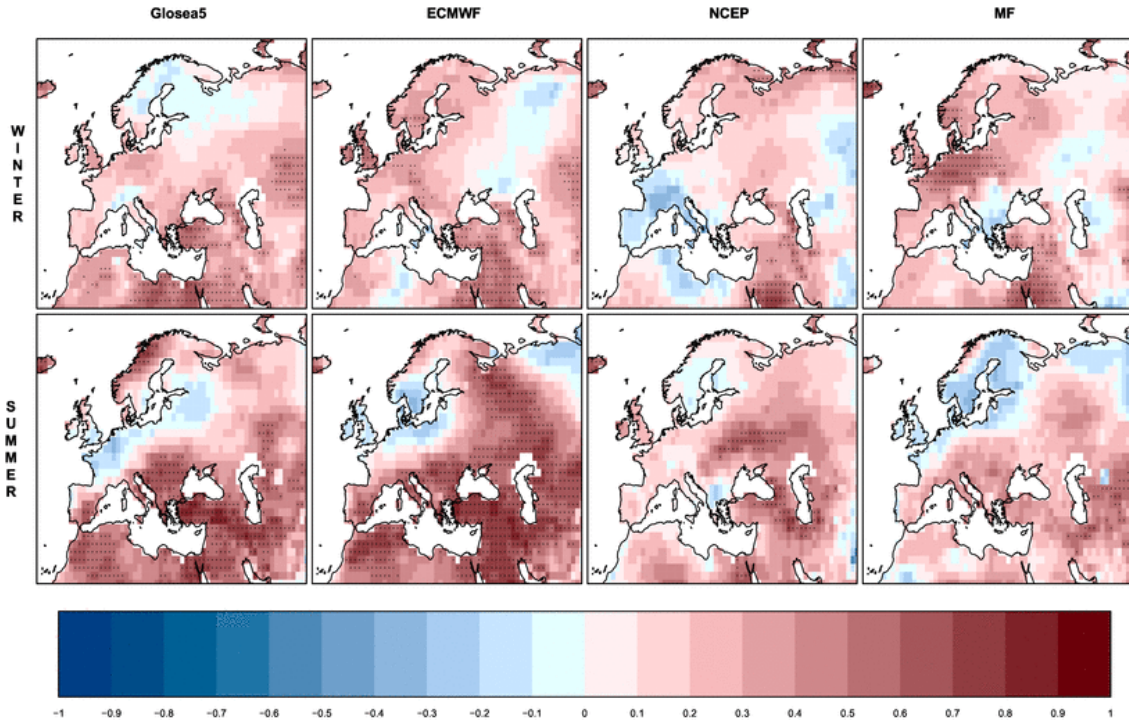


**Figure 2.2:** Anomaly correlation coefficient (ACC) between the predicted ensemble mean of each individual coupled seasonal forecast model and the observed seasonal winter (DJF; top row) and summer (JJA; bottom row) surface temperature obtained from ERA-Interim over the European region (20°W–70°E and 25°N–75°N) for the period 1992–2012. The individual seasonal forecast models are GloSea5, ECMWF, National Centers for Environmental Prediction (NCEP) and MeteoFrance (MF) (from left to right). Forecasts are initialised in November for DJF and in May for JJA. Areas covered in red are indicative of positive correlation, while areas covered in blue indicate negative correlation. Dots in each grid point indicate significant positive correlation at 5% significance level using one-sided Student t-test and controlling for false discovery rate. From Mishra et al. (2019).

model, summer or winter, with the exception of the Iberian Peninsular for GloSea5 and ECMWF in summer, and parts of far-eastern Europe, mostly in winter. However, Dunstone et al. (2018) found that skillful precipitation predictions are possible using a seasonal forecast model. Using the Met Office Decadal Prediction System (DePreSys3, Dunstone et al., 2016), which is initialised with 40 ensemble members on 1<sup>st</sup> November and 1<sup>st</sup> May, they found that significant skill is achieved for summer (JJA) rainfall for a northern European domain over a 58 year hindcast period, with a correlation of 0.47. However, due to the weak amplitude of the forced model signal, to achieve this skill a very large ensemble is required, in this case 80 members. The primary source of skill in this case is from convective rainfall, which in turn comes from skillful predictions of low-frequency variations in North Atlantic SSTs, which determine moisture availability.

A new version of the ECMWF seasonal forecast model, SEAS5, was recently made

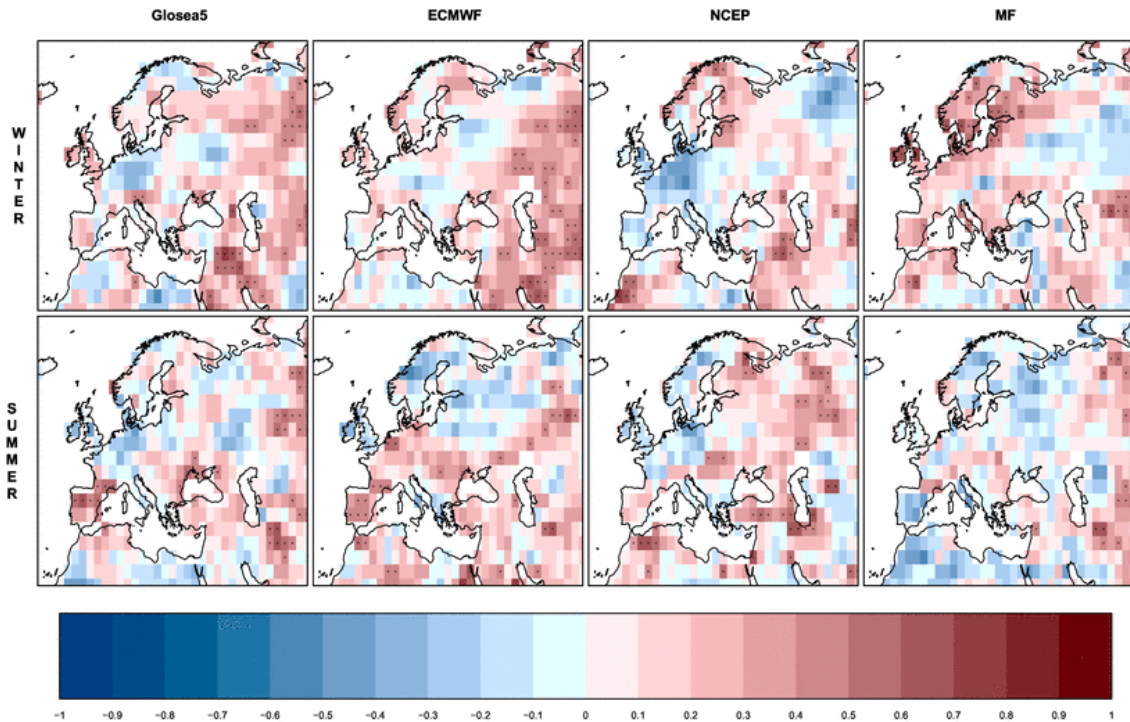


**Figure 2.3:** Same as Figure 2.2 but for precipitation, with reference data from GPCP. From Mishra et al. (2019).

operational, replacing System 4. While this version of the model does improve the simulation of many aspects of the climate system, such as ENSO, other aspects show poorer skill compared to System 4. In particular, the northern hemisphere jet stream biases are larger than those in System 4, which may inhibit the skill of representing teleconnections in the model. There are also increased biases in 500 hPa geopotential height, particularly over Europe, which affects the circulation skill in this region and may also be related to the increased jet stream biases (Johnson et al., 2019).

One teleconnection between the ISM and southern Europe is the monsoon-desert mechanism (Rodwell and Hoskins, 1996), whereby monsoon heating can enhance descent over the Mediterranean through a Rossby wave response (explained in further detail in Section 2.4.1.1). Cherchi et al. (2014) examined the representation of this mechanism in the Coupled Model Intercomparison Project 5 (CMIP5, Taylor et al., 2012) models and found that the descent region over the eastern Mediterranean is well located and of realistic intensity. They also showed that diabatic heating over the Bay of Bengal and Arabian Sea results in the largest descent, and that the models tend to underestimate the heating at upper levels while overestimating it at lower levels, which results in a weaker response overall with weaker descent over the eastern Mediterranean. Seasonal forecast

models have been shown to exhibit biases in precipitation (heating) in parts of the Bay of Bengal and Arabian Sea (see Section 2.3.3), which will therefore affect their ability to accurately represent the monsoon-desert mechanism.

## **2.3 Indian monsoon variability**

The heating associated with the ISM is able to affect the circulation patterns in many regions of the northern hemisphere, possibly including Europe. Therefore, the ISM offers a potential source of predictability for extratropical summer weather on subseasonal to seasonal timescales.

At a basic level, the ISM is driven by the temperature contrast that develops between the land in South Asia and oceanic regions further south in late spring, which induces cross-equatorial surface flow. The elevated heating of the Himalayas and Tibetan Plateau also results in a strong vertical temperature gradient, which acts to enhance the monsoon circulation over India (Chou, 2003). When the upper tropospheric temperature gradient reverses so that air in the subtropics is warmer than air near the equator, upper air easterly winds develop and a strong off-equatorial meridional circulation develops, with upper air easterlies and surface westerlies which transport moisture from the Indian Ocean across the Indian subcontinent.

The ISM exhibits a large amount of variability on both interannual and intraseasonal timescales, and if this variability is predictable then this may provide an indirect source of predictability for European summer weather. In this section, the main drivers of ISM interannual and intraseasonal variability are described.

### **2.3.1 Interannual variability**

Interannual variability of the ISM is strongly correlated with El Niño Southern Oscillation (ENSO, e.g. Shukla and Paolino, 1983; Ropelewski and Halpert, 1987). An El Niño event warms the sea surface temperatures (SSTs) in the equatorial eastern Pacific Ocean, causing convection associated with the Walker cell to shift eastwards, and the location of the warmest SST anomalies determines which regions are more likely to experience suppressed or enhanced precipitation. Generally, an El Niño event tends to lead to

suppressed monsoon precipitation, whereas a La Niña event has the opposite effect (Ju and Slingo, 1995). Kumar et al. (2006), among others, showed that central Pacific warm events are more likely to strongly suppress ISM precipitation than eastern warm events, and that the most severe droughts have all occurred during El Niño years.

Another driver of ISM interannual variability is the Indian Ocean Dipole (IOD). The IOD is an atmosphere-ocean coupled mode of SST variability in the Indian Ocean, similar in many ways to ENSO. A positive IOD is associated with cooler than average SSTs in the eastern equatorial Indian Ocean, caused by anomalous easterlies which increase upwelling, and warmer than average SSTs in the western Indian Ocean. This change in the SST gradient between the eastern and western Indian Ocean reinforces the easterly wind anomalies. Ashok et al. (2001) showed that a positive IOD event causes anomalous low-level convergence in the western equatorial Indian Ocean, and divergence in the eastern equatorial Indian Ocean, resulting in an overall strengthening of the monsoon circulation and an increase in monsoon rainfall over India.

The IOD and ENSO have differing regional impacts on ISM rainfall. Rainfall anomalies associated with the IOD tend to be confined to the monsoon trough region over India, whereas ENSO affects rainfall anomalies over much of the Indian subcontinent (Figure 2.4, from Ashok and Saji, 2007). This is due to the different mechanisms by which they affect ISM rainfall: a positive IOD event causes an overall strengthening of the monsoon circulation, whereas an El Niño event results in anomalous subsidence over India, which acts to suppress convection over a wider region. However, both indices are significantly correlated with All-India Rainfall (AIR).

The relationship between the IOD and ENSO, particularly concerning the dependence or independence of the IOD and ENSO, is not fully understood (Annamalai et al., 2003; Xie et al., 2009). Ashok et al. (2003) suggest that the IOD is able to operate independently of ENSO, with strong positive IOD events such as those in 1961, 1967 and 1994 occurring when there was no El Niño event. They also found that the variance of the IOD Index which is explained by variations of the Niño3 Index is small, although the two indices are correlated. However, Allan et al. (2001) dispute this, claiming that if the varying lag correlations between the IOD and ENSO indices are taken into account, the independence of the IOD from ENSO disappears. It has also been suggested that different types of El Niño event have different levels of coupling with the IOD, with eastern Pacific El Niño events having a stronger correlation with the IOD than central Pacific El Niño events, due

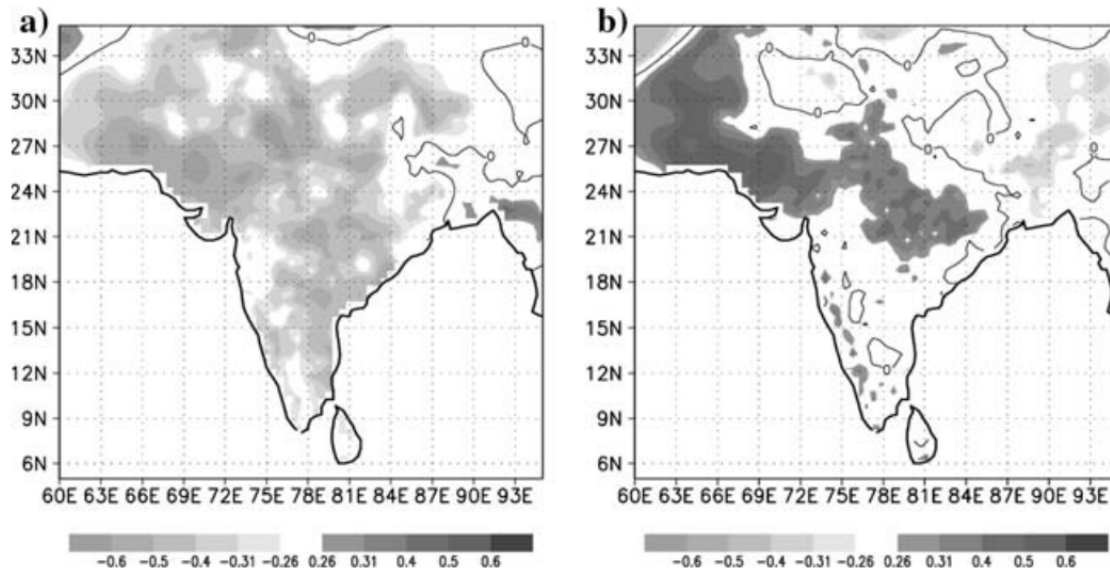


**Figure 2.4:** JJAS partial correlations between anomalies of rainfall and (a) NINO3 SST anomaly and (b) IOD mode index. From Ashok and Saji (2007).

to the lack of accompanying anomalous easterlies over the eastern Indian Ocean during the latter type of event (Zhang et al., 2015).

The IOD can also alter the effect of ENSO on ISM rainfall. Ashok et al. (2004) showed that a positive IOD event significantly reduces the impact of an El Niño event on ISM rainfall, whereas a negative IOD event lessens the impact of a La Niña. They suggest that this is due to the formation of an anomalous Walker cell over the IOD region in years when IOD and ENSO events occur together, which results in an intensification of the cross-equatorial Hadley circulation and an increase in ISM rainfall.

### 2.3.2 Intraseasonal variability

The boreal summer intraseasonal oscillation (BSISO) is one of the main sources of intraseasonal variability of the ISM. It is the summer manifestation of the Madden-Julian Oscillation (MJO, Madden and Julian, 1971) and operates on a roughly monthly timescale. It exhibits complex propagation characteristics which include eastward equatorial propagation, northward propagation over the northern Indian Ocean and western Pacific (Hsu et al., 2004) and southward propagation into the southern hemisphere. During active phases of the monthly (30–60 days) mode, convection is enhanced over India, the Bay of Bengal, Maritime Continent and equatorial West Pacific. This mode is strongest

during the onset phase of the ISM and can also excite Rossby waves which propagate into the extratropics and affect the extratropical circulation (Annamalai and Slingo, 2001).

There is also a second mode of intraseasonal variability, which consists of westward propagation into the Indian monsoon region from the western Pacific on a shorter timescale of approximately two weeks (10–20 days) associated with westward propagating Rossby waves. This mode is more active during the established phase of the ISM (July–August). Compared to the 30–60 day mode, the 10–20 day mode is more regional, with its influence mostly related to the local Hadley circulation in the monsoon domain. The westward and northward events modulate monsoon precipitation and are a major driver of monsoon active/break periods, with  $2/3$  of the subseasonal variability explained by the 30–60 day mode and  $1/4$  explained by the 10–20 day mode (Annamalai and Slingo, 2001).

### **2.3.3 Indian monsoon seasonal forecast skill**

Accurate forecasting of both the seasonal total rainfall and intraseasonal variability of the monsoon represents a considerable challenge. Although the ISM has a number of potential sources of predictability, such as ENSO, the IOD and snow cover over Asia, the skill for monsoon rainfall is modest in seasonal prediction systems. The ENSEMBLES multi-model seasonal prediction system (Weisheimer et al., 2009), which consists of six global coupled atmosphere-ocean climate models, including models from the UK Met Office and ECMWF, has a multi-model ensemble correlation coefficient of 0.45 for precipitation over India compared to observations (Rajeevan et al., 2012). While this represents an improvement compared to the equivalent value from the earlier DEMETER multi-model ensemble (0.28), systematic precipitation biases are still present. These are partly due to excessive forcing of the atmosphere over the equatorial Indian Ocean through an overestimation of the air-sea coupling in the Indian Ocean.

Kim et al. (2012) examined the representation of the Asian summer monsoon in the ECMWF System 4 and NCEP CFS version 2 seasonal prediction systems. They found that for the seasonal (JJA) ensemble mean precipitation, neither model has significant positive correlation skill over India, although the interannual variability of the overall Asian monsoon circulation pattern is well captured by these models. They also accurately represent the ENSO–ISM teleconnection, albeit with a stronger than observed relationship. Johnson et al. (2016) evaluated the performance of the Met Office GloSea5-GC2

coupled ensemble forecast system at representing ISM rainfall and found that, similar to ECMWF System 4 and NCEP CFS, the skill for the seasonally averaged precipitation was modest (correlation of 0.41) whereas the skill for predicting the large-scale circulation was much higher. They also showed that the link between ENSO and ISM rainfall is well represented in the model, but the link between ISM rainfall and the IOD is too weak.

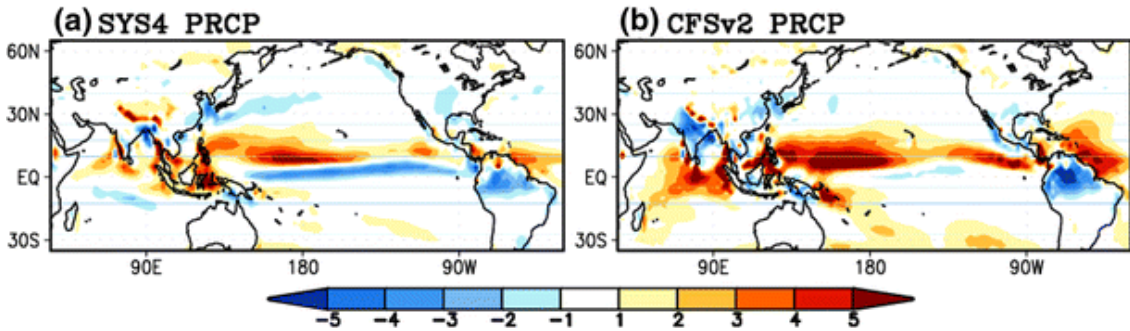


**Figure 2.5:** Climatological summer mean (JJA) bias (model-observation) of precipitation ( $\text{mm day}^{-1}$ ) for (a) ECMWF System 4 and (b) CFSv2. From Kim et al. (2012).

As well as displaying limited skill, seasonal forecast models also exhibit biases in their simulation of the ISM. GloSea5-GC2 has a systematic dry bias over India, with an AIR deficit of  $0.72 \text{ mm day}^{-1}$ , which is largely due to a late onset of the monsoon in the model (Johnson et al., 2016). These biases are similar to those in found in climate models, such as the CMIP5 models, which also have a weaker than observed relationship between ENSO and the ISM (Sperber et al., 2013). The ECMWF System 4 has a smaller overall ISM rainfall bias, but still has excess precipitation over the Western Ghats, whereas the NCEP CFSv2 has a dry bias across much of the Indian subcontinent and a wet bias over the equatorial Indian Ocean (Figure 2.5, from Kim et al., 2012).

## 2.4 Teleconnections associated with the Indian monsoon

As described earlier, the convective heat source over the Bay of Bengal and the ISM region and its associated upper tropospheric divergence can serve as a Rossby wave source, and there are a range of different teleconnection mechanisms that are associated with the monsoon diabatic heating. A number of studies have identified a significant positive correlation between Indian monsoon precipitation and precipitation in northern China on an interannual timescale (e.g. Kripalani and Kulkarni, 1997, 2001; Zhang et al., 1999). Wei et al. (2014) linked this mechanism to the position of the South Asian High (SAH), with

increased Indian monsoon precipitation resulting in a westward shift of the position of the SAH. This in turn affects precipitation over China, with less precipitation over eastern-central China and more over north and south China. Kripalani and Kulkarni (2001) also found that rainfall over southern Japan is anticorrelated with ISM precipitation.

A number of studies have found that strong ISM precipitation is associated with two areas of anticyclonic anomalies over the Eurasian continent: one over west-central Asia and one over east Asia, near Japan (e.g. Wang et al., 2001; Wu and Wang, 2002). They suggested that the east Asian anticyclonic anomaly accounts for the increased rainfall over northern China and decreased rainfall over Japan seen in earlier studies (e.g. Kripalani and Kulkarni, 1997, 2001; Zhang et al., 1999). Wu and Wang (2002) hypothesised that the west-central Asia anomalous anticyclone is modulated by ISM rainfall as a result of a Rossby-type response to off-equatorial heating (Gill, 1980). This anomalous anticyclone then perturbs the upper level flow and the subsequent downstream propagation results in the formation of the anomalous anticyclone over east Asia. These anticyclones are also part of a wave train linking Asia and North America (Wang et al., 2001). Using empirical orthogonal function (EOF) analysis, Lau and Weng (2002) found that interannual variations of precipitation in North America are linked to a wave train that originates in Asia. Lau et al. (2004) named this teleconnection the “Tokyo–Chicago Express”.

Joseph and Srinivasan (1999) also found that during the early monsoon season (May) the west-central Asia and east Asia anticyclones are related to the heat source over the Bay of Bengal, which can generate large amplitude stationary Rossby waves. The phase of these Rossby waves was shown to differ by around 20° longitude between above- and below-normal ISM years. Lu et al. (2002) also identified a teleconnection pattern that connects Europe with east Asia and found links with the ISM. This mechanism was also examined by Enomoto et al. (2003). They hypothesised that the propagation of stationary Rossby waves in the upper atmosphere along the Asian jet leads to the formation of the equivalent-barotropic ridge, and that the regions of descent over the Mediterranean and Aral Seas act as two major wave sources. They called this teleconnection the “Silk Road Pattern” (SRP).

Wang et al. (2017) examined the interdecadal variations of the SRP, which explain around 50% of its total variance, and found that the interdecadal SRP has two components: one which resembles the interannual SRP which consists of a wave train along the Asian jet, and another weaker component over northern Eurasia, resulting in a greater

overall meridional extent. Stephan et al. (2019) also looked at the decadal variability of the SRP and identified a positive feedback loop between the SRP and vertical motion over India and the Mediterranean, whereby more coherent monsoon precipitation leads to increased descent over the Mediterranean region, via the Rodwell and Hoskins (1996) monsoon-desert mechanism (described in Section 2.4.1.1). This subsequently induces anomalous ascent over India following wave propagation along the subtropical westerly jet in a positive feedback loop. They also found that decadal variability of the SRP is linked to variability of precipitation over northwest India, southwest India and an area over the Bay of Bengal, which alters the background state and affects intraseasonal variability of the SRP.

All of the studies described above focussed largely on teleconnection patterns which occur over the Eurasian continent or between Asia, the North Pacific and North America. Branstator (2002) had previously shown that a circumglobal teleconnection is present in the northern hemisphere winter which is trapped in the westerly jet stream. The study by Ding and Wang (2005) (described in more detail in Section 2.4.1.2), however, was the first to show that a circumglobal teleconnection (CGT) also exists across the whole of the northern hemisphere in the summer months, and that the ISM–East Asian summer monsoon teleconnection, the Tokyo–Chicago Express and the Silk Road Pattern can be viewed as local manifestations of the CGT (Chen and Huang, 2012; Kosaka et al., 2012; Hong and Lu, 2016).

### **2.4.1 Indian summer monsoon–Europe teleconnections**

The ISM is able to perturb the northern hemisphere jet location, and so can affect the circulation well away from India. This means that the ISM may also affect the circulation and weather patterns over Europe. Here, the two main mechanisms that have been proposed as linking the ISM to European summer weather are outlined.

#### **2.4.1.1 Monsoon-desert mechanism**

It was shown in the idealised heating simulations of Gill (1980) that a region of weak descent is seen to the west of areas of imposed equatorial and off-equatorial heating. Following on from this work, using an idealised model, Rodwell and Hoskins (1996)

imposed an off-equatorial heating in the ISM region, mimicking the monsoon onset, and showed that upper tropospheric divergence associated with diabatic heating in the ISM region does indeed induce a Rossby wave pattern to its west. This can be seen in Figure 2.6, taken from Rodwell and Hoskins (1996), which shows the perturbation surface pressure at days 3, 7 and 11 after the off-equatorial heating is applied. The signature of the westward-propagating Rossby wave can be clearly seen by day 11, by which point the surface pressure anomalies have extended across the Mediterranean and North Africa. Embedded with this Rossby wave pattern is a warm thermal structure that, when interacting with air on the southern edge of the midlatitude westerly jet stream, leads to increased descent over the Mediterranean and eastern Sahara desert. Rodwell and Hoskins (1996) also suggested that this forced descent may lead to clear air, which in turn can result in a local diabatic enhancement of the descent as a result of increased radiative cooling under clear skies. This descent acts to reduce the precipitation in the regions over which it occurs, and may explain why precipitation in the Mediterranean and eastern Sahara is at its lowest during the summer, despite zonal-mean subtropical descent associated with the Hadley circulation being virtually zero at this time. Through this mechanism, remote changes in monsoon strength, both on an interannual and interdecadal timescale, can alter the climate of the Mediterranean and eastern Sahara. Rodwell and Hoskins (2001)

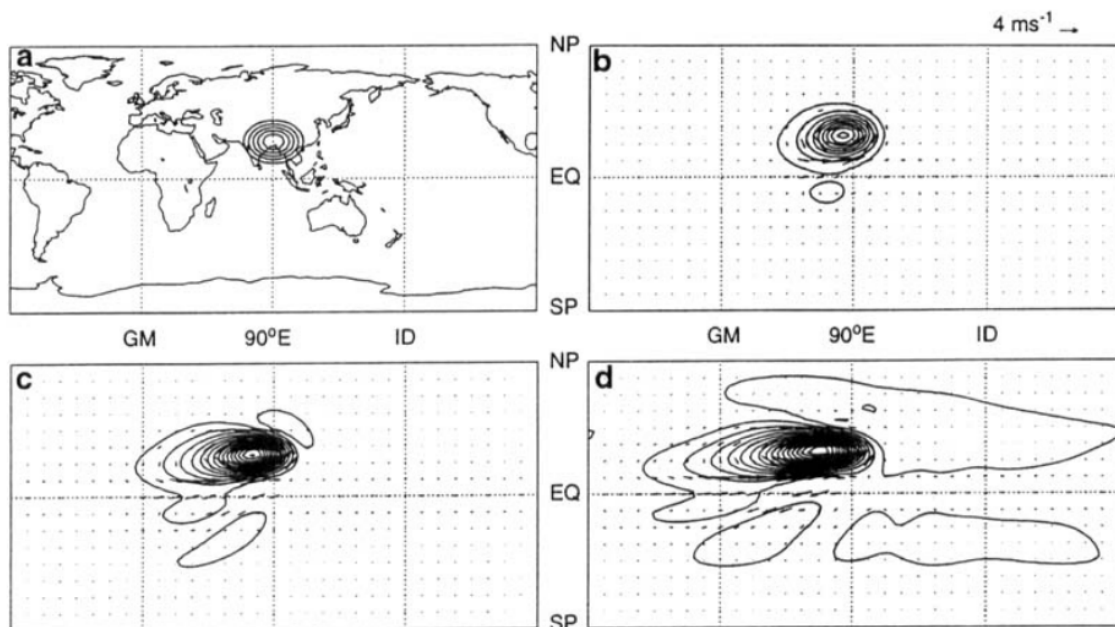


**Figure 2.6:** (a) Column-mean diabatic heating centred at 90°E, 25°N. The contour interval is  $50 \text{ W m}^{-2}$  with no zero contour shown. (b), (c) and (d) show the corresponding perturbation surface pressure and 887 hPa horizontal winds for an integration linearised about a resting basic-state at (b) day 3, (c) day 7 and (d) day 11. The contour interval is 1 hPa. From Rodwell and Hoskins (1996).

showed that similar mechanisms exist for other monsoon systems around the world, such as those in North and South America, which induce the Mediterranean-type climates of California and Chile.

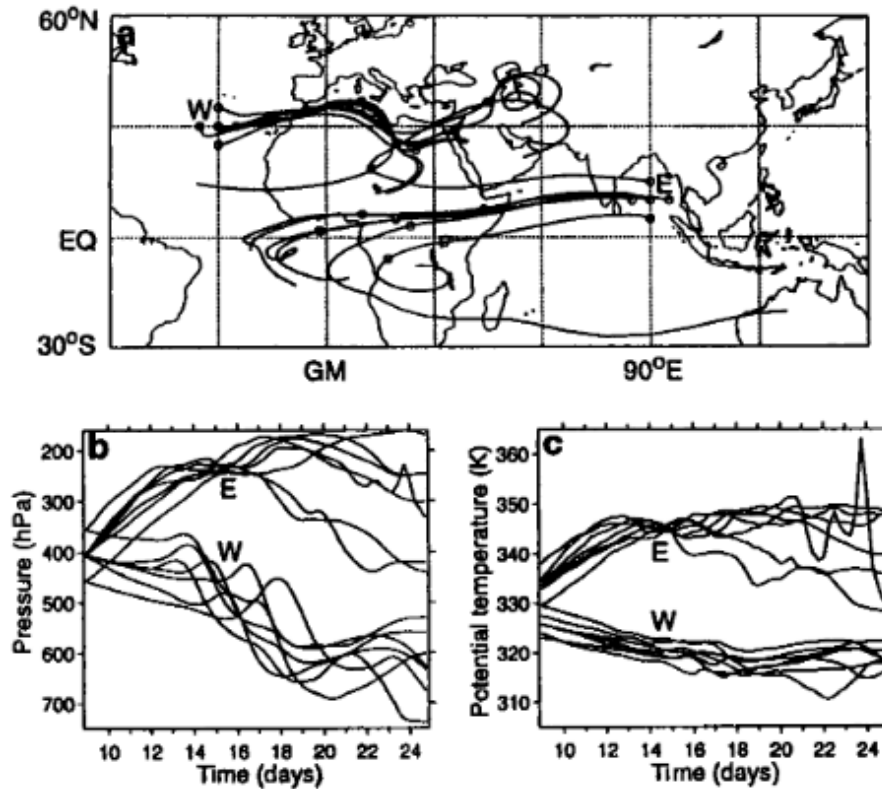


**Figure 2.7:** Trajectories for two clusters of seven particles released at day 9 advected in three-dimensional space until day 25. Initially, one cluster (termed ‘W’) is centred on the southern flank of the midlatitude westerlies around at 30°W, 30°N, and the other (termed ‘E’) is centred in the tropical easterly flow around 90°E, 10°N. In each cluster, six particles are initially displaced by  $\pm 5^\circ$  of longitude,  $\pm 5^\circ$  of latitude. (a) Horizontal projections of the trajectories - small circles indicate the positions of the particles at days 9 and 17; (b) pressure at each position of each particle; (c) potential temperature at each position of each particle. From Rodwell and Hoskins (1996).

Rodwell and Hoskins (1996) also showed that this mechanism is not a simple overturning circulation or Walker cell. Figure 2.7a shows the horizontal projection of some trajectories initiated at around 400 hPa at day 9. The descending air, seen in Figure 2.7b, can be seen to be mainly of midlatitude origin, travelling from the North Atlantic from around the southern flank of the midlatitude westerlies, across the Mediterranean and North Africa.

Tyrlis et al. (2013) found evidence for this proposed mechanism in observations, where they observed sharp slopes in the isentropes associated with the warm thermal structure linked to the Rossby wave activity. The slopes in the isentropes further amplify

subsidence as the northern and western edges of the warm structure are exposed to the midlatitude westerlies. They also argued that successive ‘pulses’ of Rossby wave activity are released from the monsoon onset until the peak monsoon activity is reached in July, which explains why regions of subsidence advance with the progression of the monsoon season.

#### **2.4.1.2 Circumglobal teleconnection**

The term “circumglobal teleconnection” (CGT) was first coined by Branstator (2002) who, focussing on the northern hemisphere winter (DJF), identified a circumglobal wavenumber-5 teleconnection that exists trapped in the waveguide (the westerly jet). However, the summertime CGT was first documented by Ding and Wang (2005). Based on the pattern of standard deviation of JJAS 200 hPa geopotential height shown in Figure 2.8a (from Ding and Wang, 2005), they defined a geopotential height index centred in west-central Asia ( $35^{\circ}$ – $40^{\circ}$ N,  $60^{\circ}$ – $70^{\circ}$ E, hereafter the D&W Index). This region was chosen as it is the location of the upstream anomalous anticyclone which forms part of the ISM–East Asian summer monsoon teleconnection described in Section 2.4 (Wang et al., 2001; Wu and Wang, 2002). Given the importance of the ISM in driving the northern hemisphere summer circulation, they constructed a one-point correlation of northern hemisphere JJAS geopotential height with reference to this index (Figure 2.8b). From this, they identified a wavenumber-5 structure (Figure 2.8c) where the pressure variations over the northeast Atlantic, east Asia, North Pacific and North America are all nearly in phase with the variations over west-central Asia. Using empirical orthogonal function (EOF) analysis, they showed that the leading mode of low frequency (interannual) variability of the northern hemisphere summer features a zonally oriented band of above-normal height around  $50^{\circ}$ N which extends from east Asia across the North Pacific. They also showed that the CGT represents the second EOF and that this EOF mode is significantly correlated with precipitation over northwest India.

Ding and Wang (2005) also examined the effect of the CGT on precipitation and temperature anomalies in individual summer months. Figure 2.9 (also from Ding and Wang, 2005) is the panel for August, when the most significant anomalies are seen over Europe. In this month a positive phase of the CGT corresponds to positive geopotential height anomalies over northwest Europe, east Asia, the North Pacific and North

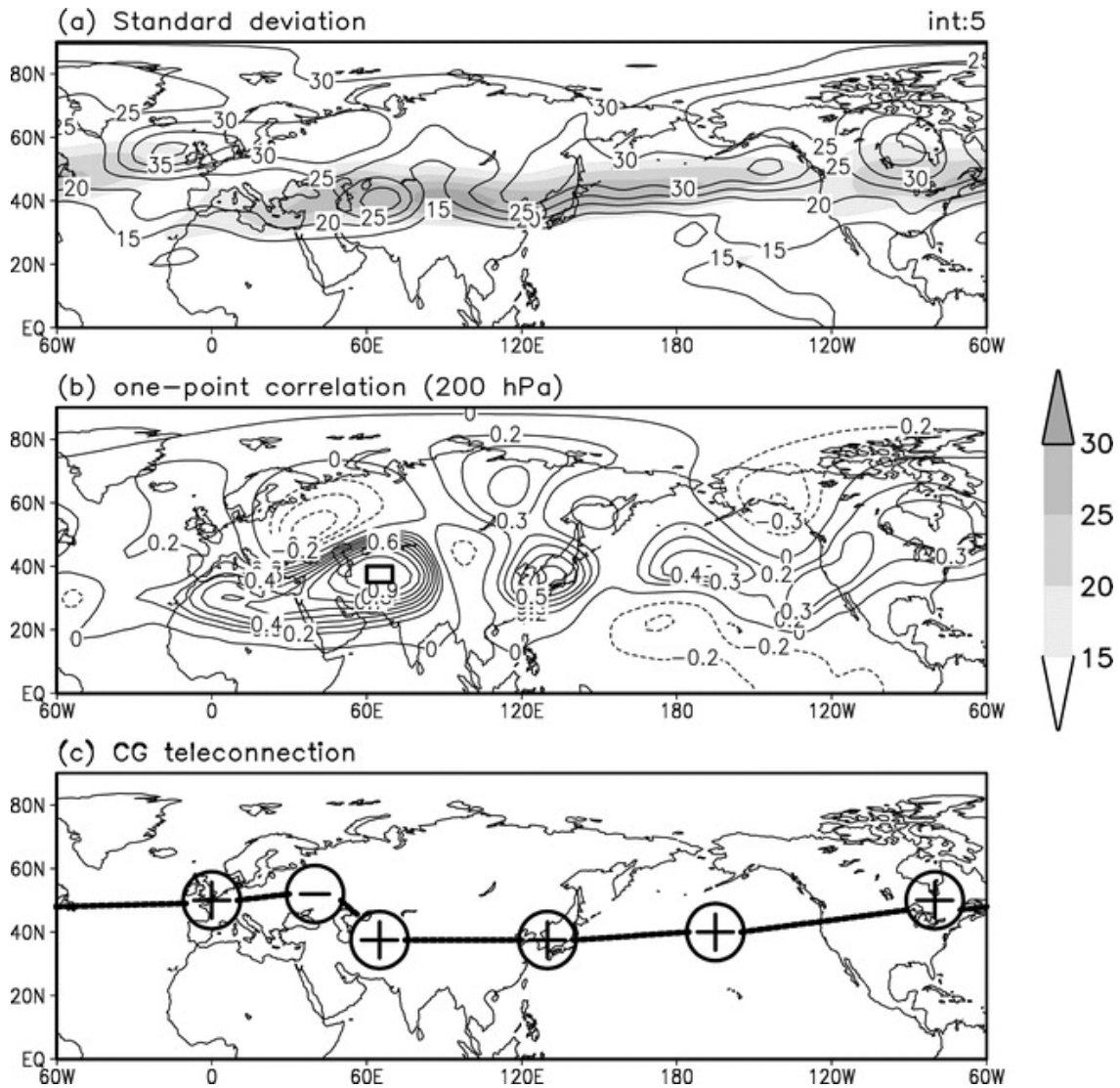


**Figure 2.8:** (a) Standard deviation of summer (JJAS) 200 hPa geopotential height (contour) and climatological 200 hPa jet stream (zonal wind) with magnitude greater than  $15 \text{ m s}^{-1}$  (shading) for the period of 1948–2003, for the NCEP–NCAR reanalysis dataset (Kalnay et al., 1996). (b) One-point correlation map between the base-point (box) and JJAS 200 hPa geopotential height for 1948–2003. (c) Schematic illustrating six main centres of action of the CGT. From Ding and Wang (2005).

America. There are significant negative precipitation anomalies over much of northwest Europe, while there are positive anomalies over eastern parts of Europe. Also of note is that the positive geopotential height anomalies over west-central Asia are concurrent with increased precipitation over northern and western parts of India, in agreement with previous studies suggesting that the anticyclone in this region forms as a result of a Gill-type response to off-equatorial heating (Gill, 1980; Rodwell and Hoskins, 1996; Wu and Wang, 2002; Enomoto et al., 2003).

The CGT is also associated with significant temperature anomalies over Europe.

These are most obvious in August, with positive anomalies over much of northwest Europe in largely the same region as the negative precipitation anomalies. There are also positive temperature anomalies associated with the positive geopotential height anomalies over west-central Asia, east Asia and North America.

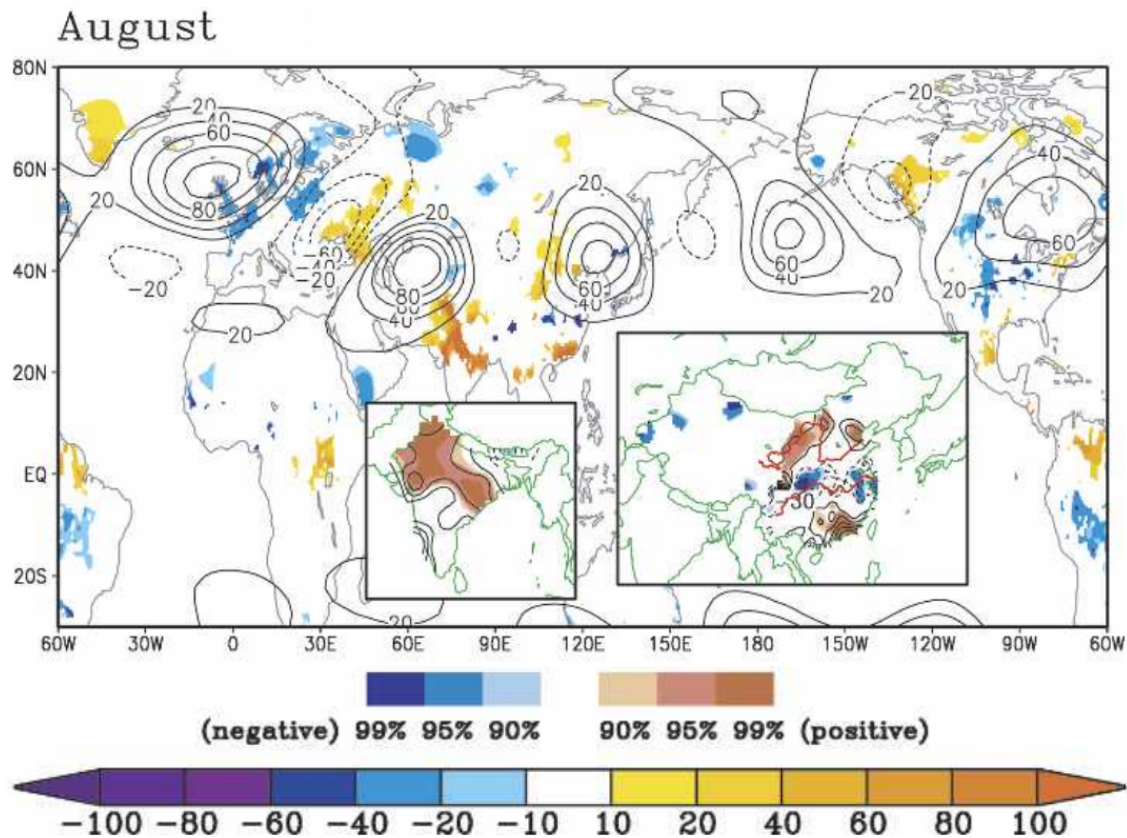


**Figure 2.9:** Composite difference of global precipitation (Delaware precipitation dataset (Willmott and Matsuura, 2001), background map) and station precipitation (small maps, inset) between positive and negative CGT years for August. Differences ( $\text{mm month}^{-1}$ ) above 90% statistical significance level are shown by shading on the global map. The corresponding CGT geopotential height anomalies are shown as contours. For India and China station data, red shading denotes regions of difference at 90%, 95%, and 99% confidence levels with a positive value, and blue shading denotes regions of difference at 90%, 95%, and 99% confidence levels with a negative value. Contour intervals are  $30 \text{ mm month}^{-1}$  (... , -60, -30, 30, 60, ...). From Ding and Wang (2005).

Ding and Wang (2005) also explored the relationship between the CGT and ENSO. They removed 12 El Niño and 12 La Niña years from the dataset and recalculated the global CGT correlations, shown in Figure 2.10a. They found that during non-ENSO years the structure of the correlations of geopotential height and precipitation still appear CGT-like. They also did the same for monsoon precipitation by removing the 12 highest and lowest AIR years and the correlation pattern nearly completely vanishes (Figure 2.10b). EOF-2 calculated for non-ENSO years (Figure 2.10c) is also very similar to the equivalent

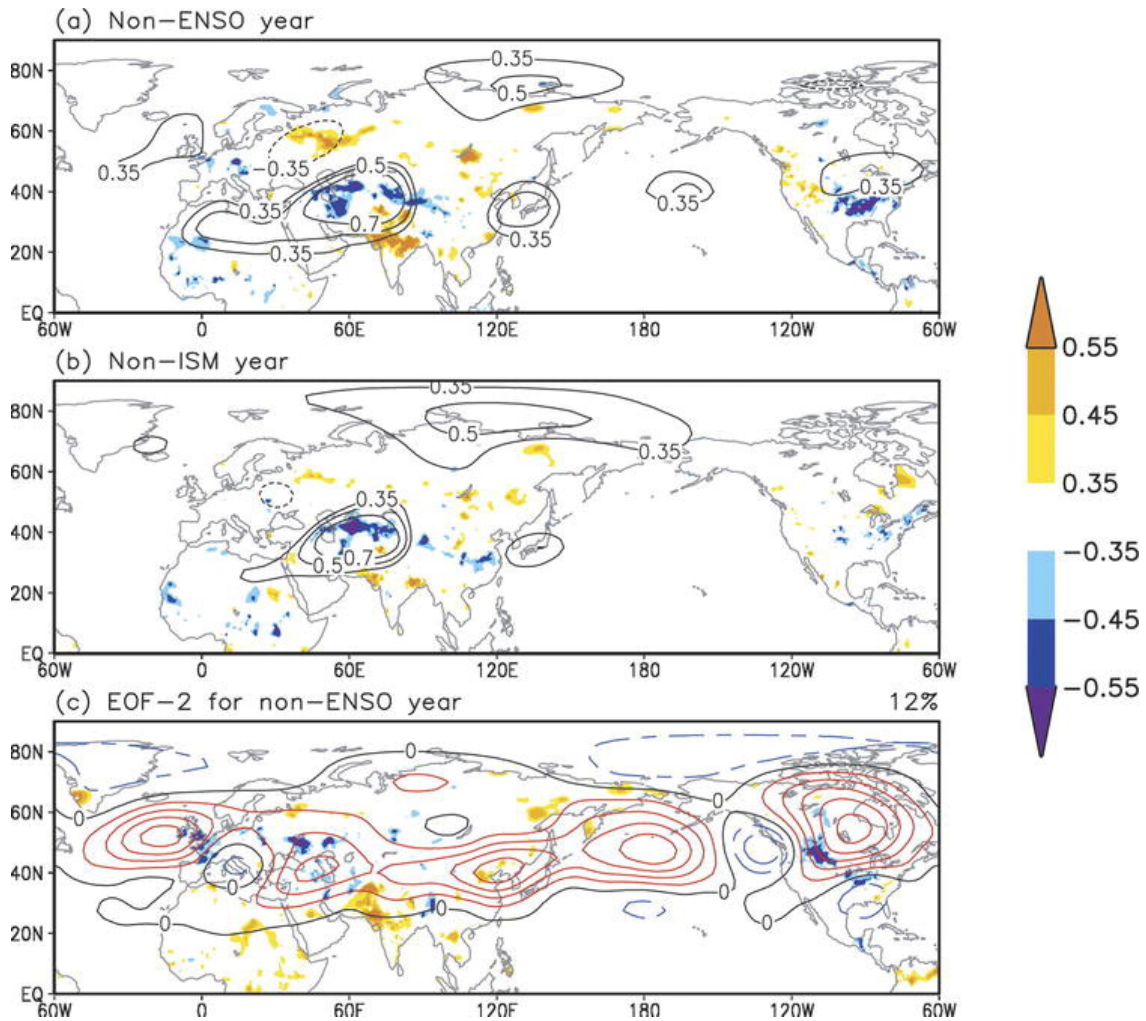


**Figure 2.10:** One-point correlation map between the JJAS CGT Index and 200 hPa geopotential height (from the NCEP–NCAR reanalysis dataset, contour) and global precipitation (Delaware precipitation dataset, shading) for (a) non-ENSO years (32 years) and (b) non-ISM years (32 years). The contours and shading denote significant correlations above 95% confidence level ( $\pm 0.35$ ). (c) EOF-2 of JJAS geopotential height anomalies at 200 hPa for non-ENSO years. EOF-2 associated with the CGT explains 12% of the total variance. The significant (above 95% confidence level) correlation coefficient between time series of EOF-2 and precipitation data is shown as shading. From Ding and Wang (2005).

calculated for all years (not shown) and this gives strong evidence that the CGT operates independently of ENSO. However, the CGT is significantly correlated with the Niño-3 Index, so they hypothesised that the ISM can act as a “conductor” that connects ENSO and the extratropical northern hemisphere circulation.

Two potential mechanisms for the generation and maintenance of the CGT were proposed by Ding and Wang (2005). In the first scenario, enhanced ISM precipitation generates an anomalous anticyclone in west-central Asia, which then excites successive

downstream cells which propagate along the westerly jet which acts as a waveguide. In the second scenario, the North Atlantic jet exit region excites Rossby waves which propagate across Europe to west-central Asia. This generates the anomalous west-central Asian high which enhances the convection over northwest India and which subsequently reinforces the downstream propagation of the wave train.

In a subsequent study, they suggested that the second scenario is the more likely, and that convection over northwest India is initially triggered by the west-central Asian high, associated with the Rossby waves which propagate from Europe to Asia (Ding and Wang, 2007). This convection and associated diabatic heating in turn excites a Rossby wave response, which reinforces the west-central Asian high, and this then enhances downstream circulation anomalies through the propagation of these waves along the waveguide (Liu and Wang, 2013). They also showed that the midlatitude wave train from Europe–Asia influences the occurrence of active and break conditions over northern India. Chen and Huang (2012) explored the excitation mechanisms of the SRP (which can be viewed as the Eurasian part of the CGT), as well as the relationship between the SRP and the CGT, and found that the CGT can be considered as the interannual component of the SRP. They also showed that heating anomalies over the northern Indian Ocean are largely responsible for forcing the CGT pattern. However, Yasui and Watanabe (2010) suggested that the heating anomalies most responsible for forcing the CGT are situated over the eastern Mediterranean, in a similar location to the region of descent identified by Enomoto et al. (2003) as being a major wave source and driver of the SRP.

It has also been shown that the CGT varies on an interdecadal timescale. Wang et al. (2012) found that since 1979 the major centres of action of the CGT have weakened, with a large change over the North Atlantic and Europe. They attributed this to a weakening of the coupling between ISM precipitation and the midlatitude circulation as a result of reduced ISM precipitation variability, which in turn is due to a change of ENSO properties. They also attribute the changes over the North Atlantic and Europe to a southward shift of the jet stream.

The CGT has been shown to be a source of climate variability and predictability in the northern hemisphere summer on intraseasonal (Ding and Wang, 2007), seasonal (Ding and Wang, 2005; Lee et al., 2011) and interannual timescales. Ding et al. (2011) linked interannual changes in the CGT pattern to ENSO variability by showing that the leading maximum covariance analysis mode, which resembles the CGT pattern, is associated

with the developing phase of ENSO and appears preferentially in summers before an El Niño event. They suggested that this link is primarily through the modulation of ISM precipitation by ENSO.

The CGT has also been linked to individual seasonal extreme events. Blackburn et al. (2008) found that in the summer of 2007, when the UK experienced large-scale flooding, the streamfunction anomalies from June to July were similar to the July CGT pattern. Ha et al. (2012) also linked cool conditions which were experienced across northern central Asia, east Asia and central North America during the summer of 2009 to a strong negative CGT pattern, which itself was associated with low ISM precipitation and a developing El Niño event.

Extreme precipitation events over northwest India and Pakistan have also been linked to large-scale northern hemisphere wave activity. Lau and Kim (2012) linked the 2010 Pakistan floods, which caused the worst flooding in 100 years, to a large-scale atmospheric Rossby wave train stretching from western Russia to northwest China. This was also accompanied by anomalously strong southeasterly flow, which transported moisture from the Bay of Bengal (Houze Jr et al., 2011). The wave train was also associated with a record heatwave and prolonged drought over western Russia, which led to severe wildfires affecting over 5000 km<sup>2</sup>.

The teleconnections from the ISM to Europe described in Section 2.4.1 provide a potential source of predictability for European summer weather. Therefore, accurate representation of these mechanisms in state-of-the-art seasonal forecast models is likely to be crucial for the improvement of European summer seasonal predictions. In this thesis, the representation of the CGT in a seasonal forecast model is examined, and the link between errors in its representation and European summer seasonal forecast skill is investigated. The role of the ISM in influencing the northern hemisphere circulation more generally is also investigated.

## Chapter 3:

# Data, models and methods

The questions outlined in Chapter 1 require the analysis of data from observations, reanalysis and models. In this chapter, the datasets and techniques used to address these questions are outlined. The reanalysis dataset used is described in Section 3.1, and the observational dataset in Section 3.2. Details about the two models used in the thesis - the ECMWF seasonal forecast model and a barotropic vorticity model - are given in Section 3.3. Also in this section are a description of the relaxation technique used (Section 3.3.2) and the method used for applying a thermal forcing in the ECMWF model (Section 3.3.3). Finally, an overview of the multiple sampling technique used is given, before information about the filtering of data.

### 3.1 ECMWF Reanalysis - Interim

Reanalysis datasets provide a best estimate of the historical state of the atmosphere based on the assimilation of meteorological observations. A single data assimilation system is used throughout the length of the time period analysed, which allows for the creation of a homogeneous dataset with a range of meteorological variables on a global grid (Trenberth et al., 2008). As new technologies become available or as observing networks begin or cease the collection of data, the range of observations assimilated into the reanalysis dataset can change. Changes to the location and quantity of observations over time is a common cause of inhomogeneity in reanalysis products, although these issues are more common in longer datasets which span either side of the introduction of satellite

data in around 1980 (Sterl, 2004).

In this thesis, the ECMWF Reanalysis Interim (ERA-Interim, Dee et al., 2011) dataset is used for observational analysis, to evaluate model performance, and also for initialisation of the seasonal forecast model. ERA-Interim is produced at T255 resolution ( $\sim 80$  km,  $0.7^\circ$  in latitude and longitude) with 60 vertical levels, from the surface up to 0.1 hPa. Data is available from 1979 to the present, but for the purpose of this thesis data from 1981–2014 is used. We look at winds, pressure and geopotential height as they are well constrained by observations so are a good representation of the state of the atmosphere, particularly for large-scale features. For variables such as these, observations are assimilated using a 4D-VAR data assimilation scheme with cycles every 12 hours at 0000 UTC and 1200 UTC. For each cycle, observations are combined with information from a forecast model in order to estimate the evolution of the global atmosphere. ERA-Interim precipitation is a forecast model product, with no observational information going into producing it other than the way that the precipitation is constrained by the circulation. As a result, ERA-Interim precipitation has known biases when compared to observational datasets, particularly in tropical regions where it tends to underestimate extreme precipitation events (Sun et al., 2018), so precipitation data is taken from the GPCP dataset described below.

## **3.2 Observational datasets**

### **3.2.1 Global Precipitation Climatology Project**

The Global Precipitation Climatology Project dataset (GPCP, Adler et al., 2003) is a merged analysis that incorporates surface rain gauge observations and satellite data from both low-Earth orbit (microwave) and geostationary (infrared) satellites. The low-Earth orbiting satellite data has higher accuracy, so is used to calibrate the more frequent geostationary infrared data. This combined satellite-based data is then adjusted based on the rain gauge data.

The GPCP data used in this thesis is monthly analysis at  $2.5^\circ$  by  $2.5^\circ$  resolution, from 1981–2014. GPCP data is used in preference to ERA-Interim precipitation data due to the known biases in ERA-Interim data, in tropical regions in particular. The heavy

weighting towards gauge-based data, where available, means that GPCP data typically has a good level of accuracy, particularly when compared to ERA-Interim (Sun et al., 2018; Kim et al., 2019).

## **3.3 Models**

### **3.3.1 ECMWF Integrated Forecasting System and seasonal forecasting**

The work in this thesis uses seasonal hindcasts (or reforecasts). A hindcast set is essentially a number of forecasts initialised using initial conditions from past dates, all run using the same model version. As hindcasts can be run for a large number of different start dates, this means that model performance can be evaluated without needing to wait for verifying observations, as in the case of a forecast.

The numerical model used for the hindcasts is the European Centre for Medium-Range Weather Forecasts (ECMWF) Integrated Forecasting System (IFS), coupled to the Nucleus for European Modelling of the Ocean model (NEMO). The IFS is being continually developed and updated, so for the purpose of this thesis a single model cycle is used, Cycle 41r1 (Cy41r1). This atmospheric model version is a more recent one than in the former operational model, System 4 (Molteni et al., 2011), which uses Cycle 36r4, but older than the current seasonal forecasting system, SEAS5. Cycle 41r1 was introduced around four and a half years after Cycle 36r4 and includes updates to the cloud scheme, which improve the modelling of cloud cover and precipitation, particularly for heavy rainfall events, as well as changes to the data assimilation system. Improvements were also made to the convection scheme, including modification of convective entrainment and detrainment, and better representation of frozen precipitation (Bauer and Andersson, 2011; ECMWF, 2015; Haiden et al., 2015; Richardson and Bauer, 2015).

Cy41r1 became operational on 12<sup>th</sup> May 2015. The horizontal spectral resolution of the atmospheric model (T255) is the same as System 4 and corresponds to a grid length of approximately 80 km, while the ocean model has a resolution of approximately 1 degree with 42 vertical levels (Weisheimer et al., 2017). In this thesis, two different vertical resolutions of the atmosphere are used. In Chapter 4, the model is run with 91 vertical levels, whereas in Chapters 5 and 6 60 levels are used. The hindcasts were performed

using the ECMWF ERA-Interim and Ocean Reanalyses (ORAS4, Balmaseda et al., 2013) for initialisation of the atmosphere and ocean, respectively. Seasonal hindcasts over four months (123 days) were initialised on 1<sup>st</sup> May for the period 1981–2014, therefore covering the boreal summer season of June–August (JJA) and much of the ISM season, and the majority of the analysis presented here uses monthly mean values for May–August from these hindcast runs. In Chapters 4 and 5 the model was run with 25 ensemble members, whereas the experiments in Chapter 6 used five members.

### 3.3.2 Integrated Forecasting System relaxation technique

In Chapter 5, relaxation experiments in the ECMWF model are performed in order to further understand the CGT mechanism and errors associated with its representation in the model. Relaxation of the atmosphere in a model is a well-established technique for analysing model performance and deficiencies. The technique (also known as nudging) involves relaxing model fields towards a reference state (usually reanalysis) throughout the length of a forecast in a pre-defined region. By relaxing the tropics, Ferranti et al. (1990) used this technique to show the level of extratropical dependence on poorly represented tropical variability, and Klinker (1990) showed that global mean errors are dependent on those in certain parts of the tropics in particular. Relaxation experiments have also been used to diagnose the role of tropical forecast errors on extended-range extratropical northern hemisphere skill (Jung et al., 2010a) as well as to investigate the origin of atmospheric circulation anomalies in the northern hemisphere in specific extreme seasons (Jung et al., 2010b; Douville et al., 2011; Watson et al., 2016).

The relaxation of variable  $X$  is carried out through the addition of an extra term,  $X_{\text{relax}}$ , to the ECMWF model:

$$\frac{\partial X}{\partial t} = S + X_{\text{relax}}, \quad (3.1)$$

where  $S$  represents the source terms used to produce the forecast, which include advection and sources and sinks due to physical parametrisations in the model, and where  $X_{\text{relax}}$  is of the form:

$$X_{\text{relax}} = -\frac{X_{\text{old}} - X_{\text{ref}}}{\tau}, \quad (3.2)$$

where  $X_{\text{old}}$  is the model variable being relaxed,  $X_{\text{ref}}$  is the reference state towards which the model is drawn (in this case ERA-Interim) and  $\tau$  is the relaxation timescale. So we have:

$$X_{\text{relax}} = X_{\text{new}} - X_{\text{old}} = -\left(\frac{X_{\text{old}} - X_{\text{ref}}}{\tau}\right) \Delta t, \quad (3.3)$$

where  $\Delta t$  is the model time step. Letting  $\lambda = \Delta t/\tau$ , Equation 3.3 can be written as:

$$X_{\text{new}} = X_{\text{old}} - X_{\text{old}}\lambda + X_{\text{ref}}\lambda, \quad (3.4)$$

$$= (1 - \lambda) \left( X_{\text{old}} + X_{\text{ref}} \frac{\lambda}{(1 - \lambda)} \right). \quad (3.5)$$

This can be written as:

$$X_{\text{new}} = \frac{X_{\text{old}} + \alpha X_{\text{ref}}}{(1 + \alpha)}, \quad (3.6)$$

where

$$\alpha = \frac{\lambda}{(1 - \lambda)}, \quad (3.7)$$

$$= \frac{\Delta t}{(\tau - \Delta t)}. \quad (3.8)$$

The relaxation timescale  $\tau = 2.75$  hours and  $\Delta t = 0.75$  hours, so  $\alpha = 0.375 = 0.5\Delta t$ . The relaxation is applied every time step, with  $X_{\text{ref}}$  updated by linear interpolation between the 6-hourly data from ERA-Interim.

In order to avoid adverse effects at the boundaries of the relaxation region,  $X_{\text{relax}}$  is multiplied by a weighting function  $\gamma(\phi, \lambda)$ , which governs the transition from relaxed to non-relaxed regions. Here  $\phi$  is the latitude and  $\lambda$  the longitude of the relaxation region boundaries. For the experiments in Chapter 5,

$$\gamma(\phi, \lambda) = f(\phi, \phi_1, \phi_2) f(\lambda, \lambda_1, \lambda_2), \quad (3.9)$$

where

$$f(\beta, \beta_1, \beta_2) = \left( \frac{1}{1 + e^{\delta(\beta - \beta_1)}} \right) \left( 1 - \frac{1}{1 + e^{\delta(\beta - \beta_2)}} \right), \quad (3.10)$$

with  $\delta$  equal to  $-0.5 \text{ rad}^{-1}$ .  $\phi_1$  &  $\phi_2$ , and  $\lambda_1$  &  $\lambda_2$  are parameters which determine the northern and southern, and western and eastern edges of the relaxation region, respectively. The size of the relaxation region determines the overall width of the relaxation tapering band, although  $\gamma$  is always 0.5 at the midpoints of the relaxation boundaries and 0.01 about  $10^\circ$  outside of the boundaries. An example one component of the tapering function (either latitudinal or longitudinal) is shown in Figure 3.1.  $\beta_1$  and  $\beta_2$  are the defined boundaries of the relaxation region, and the value of  $\beta_{\max}$  depends on the size of the relaxation region. The example shown in Figure 3.1 is for a difference of  $20^\circ$  between  $\beta_1$  and  $\beta_2$ , and this gives a value of  $\gamma_{\max}$  of 0.99.

### 3.3.3 Thermal forcing technique

In Chapter 6, we perform thermal forcing experiments in the ECMWF model in which we impose a heating through the addition of an extra temperature term,  $\mathcal{H}$ , at each model time step, so that:

$$\frac{\partial T}{\partial t} = S + \mathcal{H}, \quad (3.11)$$

where  $S$  is the original model forecast.  $\mathcal{H}$  is defined as:

$$\mathcal{H} = f(\phi, \phi_1, \phi_2) f(\lambda, \lambda_1, \lambda_2) f(z, z_1, z_2), \quad (3.12)$$

where  $f(\phi, \phi_1, \phi_2)$  and  $f(\lambda, \lambda_1, \lambda_2)$  have the same definition as in Section 3.3.2. Here,  $f(z, z_1, z_2)$  defines the vertical profile of the heating, and has the following form:

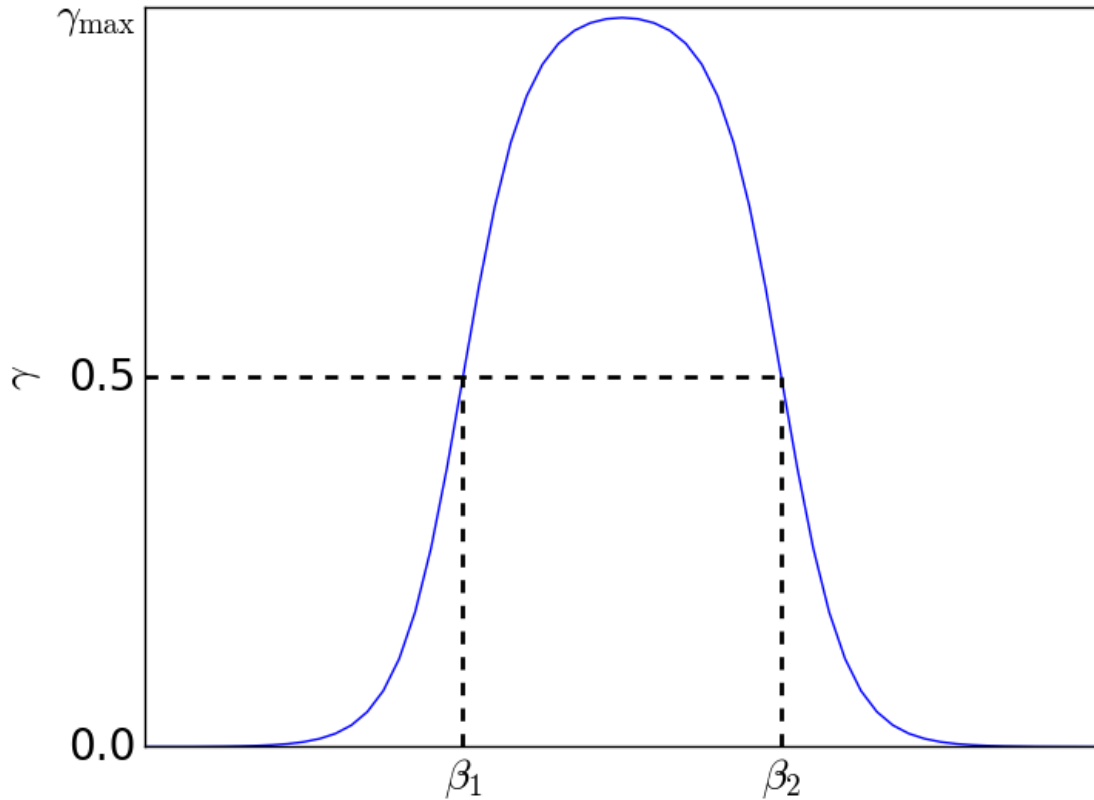


**Figure 3.1:** An example of one component of the weighting function,  $\gamma$ , used to taper the transition from relaxed to non-relaxed regions.  $\beta_1$  and  $\beta_2$  are the relaxation region boundaries and the value of  $\gamma_{\max}$  depends on the size of the relaxation region used.

$$f(z, z_1, z_2) = \left( \frac{1}{1 + e^{-(Z - Z_{\min})}} \right) \left( \frac{1}{1 + e^{-0.5(Z_{\max} - Z)}} \right) \quad (3.13)$$

where  $Z$  is the level number and  $Z_{\min}$  and  $Z_{\max}$  are the lower and upper bounds, at which the heating rate is half of the peak value. An example of the vertical profile used for the thermal forcing experiments can be seen in Chapter 6 (Figure 6.3).

### 3.3.4 Linear barotropic model

In Chapters 5 and 6, an idealised model is employed to explore ECMWF model errors. The barotropic model used integrates the barotropic vorticity equation on a sphere, following Hoskins and Ambrizzi (1993):

$$\left( \frac{\partial}{\partial t} + u_{\psi} \cdot \nabla \right) \zeta = F - \lambda \zeta - \mu \nabla^4 \zeta, \quad (3.14)$$

where  $u_\psi$  is the rotational velocity field,  $\zeta$  is the absolute vorticity,  $\xi$  is the relative vorticity,  $F = \bar{F} + F'$  is a constant forcing,  $\lambda$  is a linear damping with a timescale of 10 days and  $\mu = 2.4 \times 10^{16} \text{ m}^4 \text{ s}^{-1}$  is a diffusion coefficient. Here,  $\bar{F}$  is chosen to keep the model stationary in the absence of any forcing so that it exactly maintains the basic state:

$$\bar{F} = u_\psi \cdot \nabla \zeta + \lambda \xi + \mu \nabla^4 \xi. \quad (3.15)$$

The equation is solved using spectral harmonics with triangular truncation at wavenumber 42 (T42). The model is initialised from the basic state and integrated forward for 50 days.

Two different types of anomalous forcing,  $F'$ , are used. In Chapter 5, this is chosen to be the regression of the Rossby wave source (RWS, described in Chapter 2.1.2) against the geopotential height in a region which is an important component of the CGT wave train, applied only in this region. In Chapter 6, barotropic model experiments using a RWS forcing applied over India are performed. In both cases, the anomalous forcings are scaled to be small so that the response can be interpreted as linear. Further details about each set of experiments can be found in the relevant chapters.

### 3.3.5 Multiple sampling

The ECMWF forecast system provides us with multiple realisations in the form of 25 ensemble members. When analysing model output, a common technique is to use the ensemble mean. However, using the ensemble mean reduces the noise and the contribution of the forced variability is increased relative to the total variability. Therefore, to ensure that we do not mistake noise in the observations for forced variability, we need to compare individual ensemble members from the hindcast dataset to the observations. To do this, we follow the method of Johnson et al. (2016) and construct many time series of monthly averaged variables by randomly selecting an ensemble member from each year and repeating this until we have 2000 sets of time series, of 34 years each. We are then able to compare the single realisation of the observed system to multiple realisations of the simulated system.

## **3.4 Fourier filtering**

Throughout this thesis, following Ding and Wang (2005), to focus on year-to-year variability and to account for differences in trends in the model and observations, monthly mean data has been filtered to remove the long term trend and decadal variations with a period of longer than 8.5 years using Fourier harmonic analysis. This was achieved by performing a discrete real Fourier Transform of the input data, setting the second, third and fourth Fourier cosine coefficients to zero, then computing the inverse of the real Fourier transform.

## Chapter 4:

# The representation of the circumglobal teleconnection in the ECMWF seasonal forecast model

*This chapter is adapted from work published in Climate Dynamics:*

Beverley, J. D., S. J. Woolnough, L. H. Baker, S. J. Johnson, and A. Weisheimer, 2019: The northern hemisphere circumglobal teleconnection in a seasonal forecast model and its relationship to European summer forecast skill. *Clim. Dyn.*, **52**, 3759–3771.

## 4.1 Introduction

The CGT represents one of the leading modes of summertime climate variability in the northern hemisphere extratropics. As described in Chapter 2, variations associated with the CGT pattern can influence temperature and precipitation anomalies across the northern hemisphere. Therefore, accurate representation of the CGT in seasonal forecasting systems may be an important source of skill for summer forecasts. In order to analyse the relative importance of the CGT as a source of predictability for the European summer, it must first be determined how well the ECMWF model (described in Chapter 3.3.1) represents the mechanism. Therefore, in this chapter, the ability of the model to

represent the CGT pattern is examined. This work was carried out to address research question 1 in Chapter 1, in order to understand how the model performs at representing the CGT mechanism and what the relationship is between its representation and seasonal forecast skill for Europe.

First, the overall skill of the model and its performance at representing the CGT is analysed in Section 4.2. In Section 4.3, possible causes of errors in the model’s representation of the CGT are examined. The conclusions and summary of this chapter are in Section 4.4.

## 4.2 Diagnosing model performance

### 4.2.1 Forecast skill

As a first order measure of model forecast skill we examine the 25 member ensemble mean skill compared to ERA-Interim for 200 hPa geopotential height in the northern hemisphere (Figure 4.1). For the first month of the forecast the model has good skill across the northern hemisphere, with positive correlations everywhere. However, in June, July and August the skill is much reduced, with large areas of negative correlation (no skill) developing over many regions, including much of Europe. When comparing the observed August CGT pattern in Chapter 1 to the August skill map in Figure 4.1, it can be seen that the areas of reduced extratropical skill are closely aligned with the location of the centres of action of the CGT. Therefore, in order to analyse whether the reduced 200 hPa geopotential height skill, in particular over Europe, arises as a result of a poor representation of the CGT, the overall representation of the CGT in the model is now examined in detail.

**Table 4.1:** CGT 200 hPa geopotential height indices

Index	Abbreviation	Domain
Ding and Wang	D&W	60°–70°E, 35°–40°N
Northwest Europe	NWEUR	15°W–10°E, 50°–70°N
East Asia	EASIA	110°–140°E, 30°–50°N
North Pacific	NPAC	180°–150°W, 40°–60°N
North America	NAM	120°–90°W, 40°–60°N

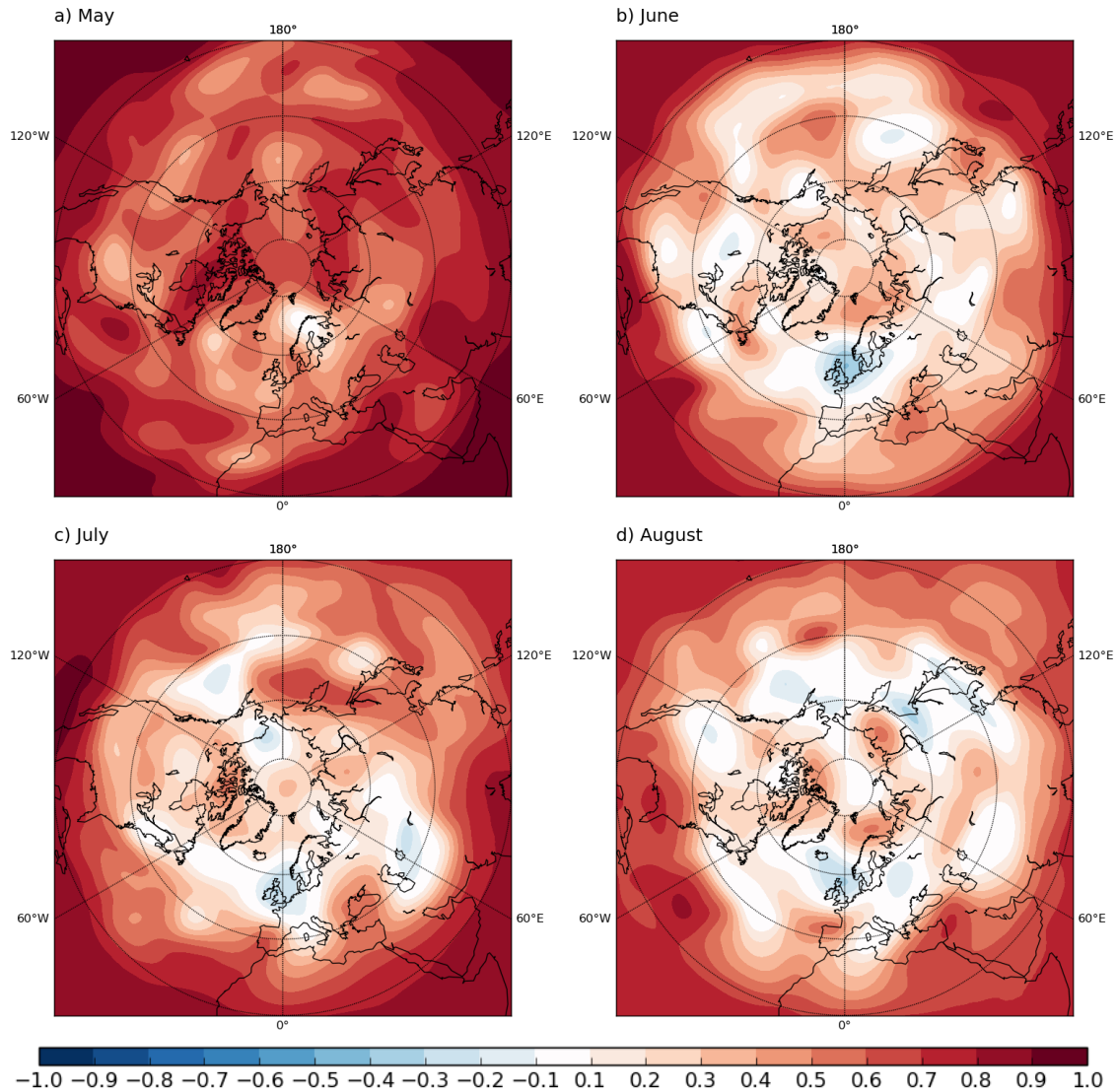


**Figure 4.1:** Model skill for 200 hPa geopotential height as defined as the correlation between ERA-Interim and the 25 member ensemble mean for (a) May, (b) June, (c) July and (d) August.

Figure 4.2 shows the observed CGT pattern as defined in Ding and Wang (2005) as the correlation between the D&W Index and 200 hPa geopotential height elsewhere, using ERA-Interim data (1981–2014 to align with the model forecast period) for May–August. Of the four months, May has the weakest CGT pattern, with little evidence of a wave train outside of Asia and so we will not focus on May from hereon. However, there is more evidence of a circumglobal wave train in June–August. In June, the correlation pattern is dominated by a region of positive correlation to the west of the D&W region, extending across the Sahara and parts of the Mediterranean. This is related to the monsoon-desert mechanism proposed by Rodwell and Hoskins (1996) (described in Chapter 2.4.1.1), where there is a westward retreat of the west-central Asian high following the onset of the monsoon at the beginning of June. There are also areas of significant positive correlation

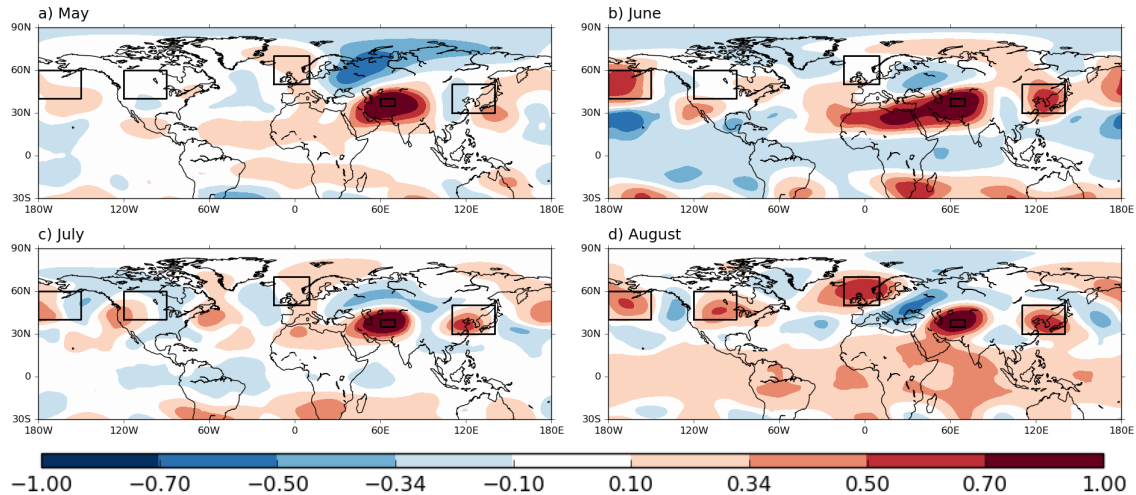


**Figure 4.2:** One-point correlation between 200 hPa geopotential at the base point (D&W region, 35°–40°N, 60°–70°E) and 200 hPa geopotential elsewhere in the ERA-Interim (1981–2014) reanalysis dataset, for (a) May, (b) June, (c) July and (d) August. Correlation values of  $\pm 0.34$  are significant at the 5% level. The boxes indicate the regions defined as the “centres of action” of the CGT.

located in east Asia and the North Pacific, although there is little signal over North America and western Europe. In July a wave train is visible at around 45°N which has a wavenumber-6 structure. In August the CGT pattern becomes stronger due to the enhanced Asian jet (Enomoto et al., 2003), and the locations of the correlation centres shifts slightly compared to July, associated with a change to a wavenumber-5 structure. As August has the strongest CGT pattern, we define several geopotential height indices based on the correlation pattern in this month. These are overlaid as boxes on Figure 4.2, and are also listed in Table 4.1, and we refer to them as “centres of action” of the CGT.

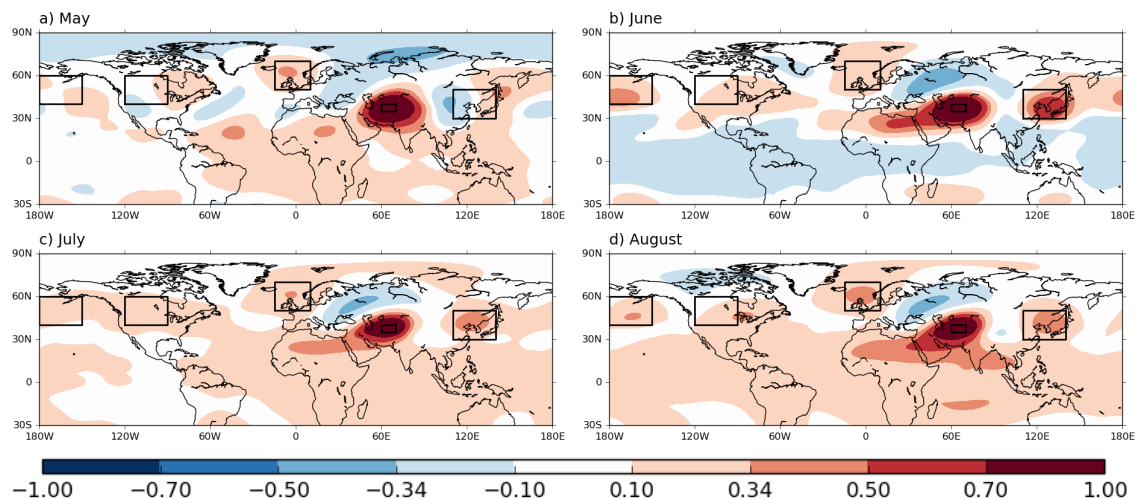
In August there are particularly strong correlations between the northwest Europe (NWEUR), Ding and Wang (D&W), East Asia (EASIA) and North Pacific (NPAC) regions. There are weaker correlations between the NPAC and North America (NAM) and NAM and NWEUR regions, which perhaps suggests that the NAM region is less instrumental in the CGT, and an observed correlation of 0.46 in August (when the CGT is strongest) between the NPAC and NWEUR regions supports this.

The observed CGT pattern has a slightly different phase in July, and to a lesser extent in June, compared to August. This means that the boxes used for the indices, which are defined based on the August pattern, are not all aligned with the centres of positive correlation in June and July. This may partly account for some of the differences

in observed and model correlations between different regions seen later in this chapter.

#### 4.2.2 Model representation of the circumglobal teleconnection

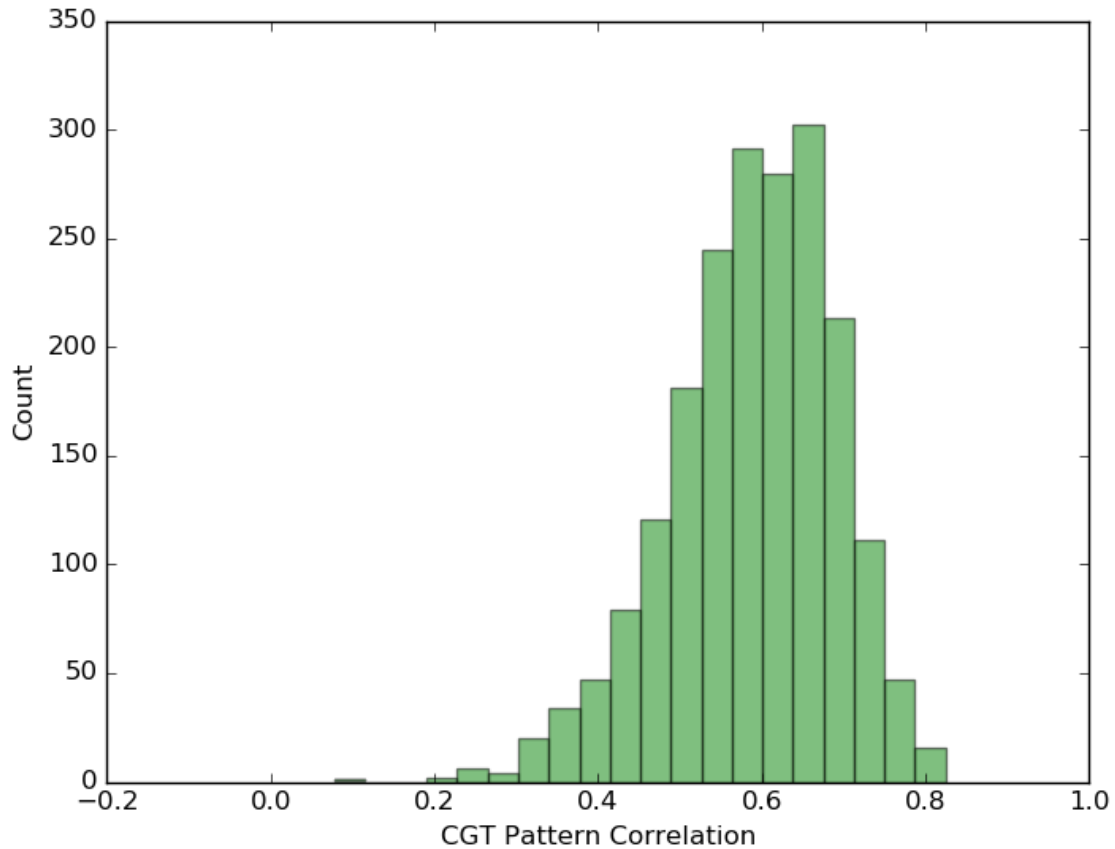
We now examine the representation of the CGT in the model. One-point correlations with the D&W Index are shown in Figure 4.3. In order to get an idea of the mean model response, but without using the ensemble mean (which will over-emphasise the forced response), these correlations were calculated for each of the 25 ensemble members, and the average of these 25 correlations maps was taken. In June, the model accurately captures the effect of the Rodwell and Hoskins mechanism, visible in the westward lobe of positive correlations extending from the D&W region, albeit with slightly less of a westward extension and slightly weaker magnitude than is observed, and the northern hemisphere pattern correlation is high at 0.81. The centre of action over east Asia is also very accurately simulated, in both location and magnitude, and this seems to be one area in which the model does well in all months. By July the model has developed a weak positive correlation across much of the northern hemisphere and the tropics and this contributes towards a reduced pattern correlation (0.60). Although the pattern correlation increases slightly in August (0.70), the correlations at the centres of action are still much too weak. The negative correlations, particularly in August, are virtually non-existent, probably in part as a result of the developing hemisphere-wide positive correlation.



**Figure 4.3:** Same as Figure 4.2, but for the average of 25 ensemble member correlations for the model hindcasts, for (a) May, (b) June, (c) July and (d) August

To get an idea of the spread in the model of the representation of the CGT, the pattern correlations of the CGT correlation maps for August compared to ERA-Interim

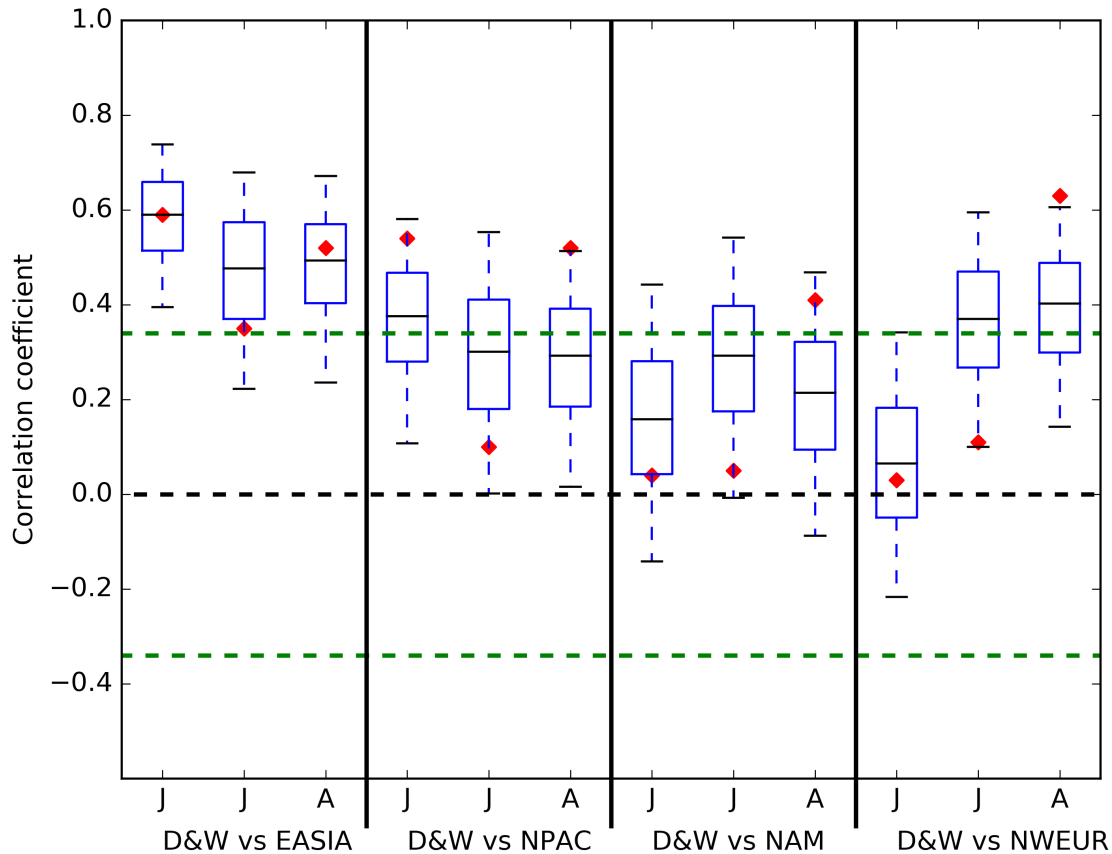
(Figure 4.2d) were calculated. To enable a more robust statistical analysis, these were calculated for 2000 time series created using the method described in Chapter 3.3.5. Figure 4.4 is a histogram of the distribution of the CGT pattern correlations for August, calculated for all longitudes between 30°–70°N. The pattern correlation values range from around 0.2–0.8 with a median of 0.60, indicating that the model does have some skill at representing the CGT. However, much of this skill comes from the ability of the model to represent the NWEUR–D&W–EASIA portion of the wave train. When analysing the pattern correlation for the eastern and western hemispheres separately, there is a clear difference in the median values. For the western hemisphere (180°W to the Greenwich Meridian) the median pattern correlation is 0.41, but for the eastern hemisphere (the Greenwich Meridian to 180°E, which encompasses much of the NWEUR–D&W–EASIA part of the wave train) it is much higher, at 0.70.



**Figure 4.4:** Histogram of the pattern correlations between model control experiment and ERA-Interim CGT correlations for August, calculated using 2000 time series created from the 25 ensemble members. The pattern correlations were calculated for all longitudes between 30°–70°N and the median value is 0.60.

We now look in more detail at the relationships between the CGT centres of action in the model, and how they differ from observations. The correlation analysis that follows

also uses the multiple time series as described in Chapter 3.3.5. This analysis allows us to determine whether the model correlation is consistent with observations. If it is not, then either the model is good and the observed pattern has a very low probability of occurrence, or the model is unable to capture the observed teleconnection pattern.



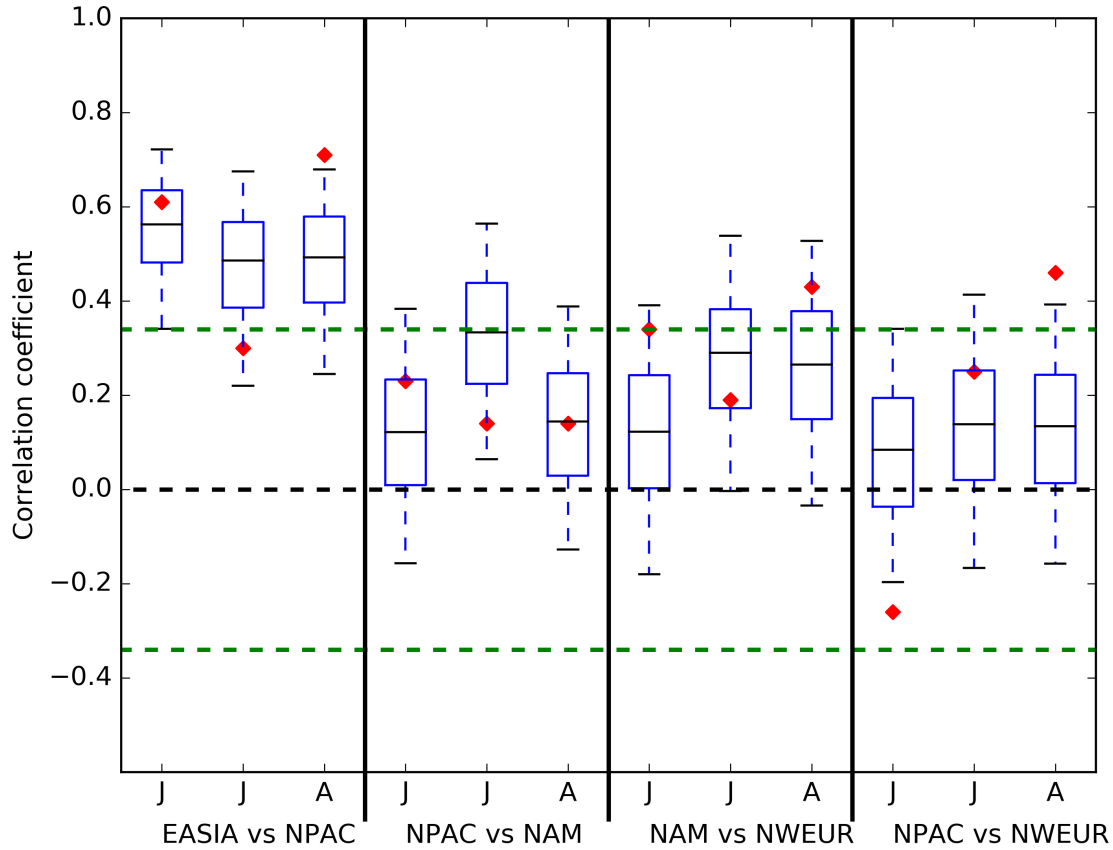
**Figure 4.5:** Distribution of correlation coefficients for the D&W Index correlated against the other centres of action of the CGT, calculated using the multiple samples. The box plots represent the upper and lower quartiles, and the whiskers extend to the 5<sup>th</sup> and 95<sup>th</sup> percentiles. The black horizontal line represents the median value and the red diamond the observed correlation coefficient from ERA-Interim. 5% significance levels ( $\pm 0.34$ ) are indicated by the green dashed lines.

Figure 4.5 shows the distributions of the correlation values between the D&W Index and the other centres of action of the CGT, which are listed in Table 4.1 and shown as boxes on Figures 4.2 and 4.3, for both the model and ERA-Interim for June, July and August. As may be expected given the correlations in Figure 4.3, the correlation with the D&W Index decreases further downstream from this region. The representation by the model of the relationship between the D&W Index and the EASIA region is generally very good, with the observed correlation falling between the 20<sup>th</sup> and 80<sup>th</sup> percentiles in all three months, and the model captures the observed significant correlations in June, July and August. Wu et al. (2016) suggested a link between East Asian Summer Mon-

soon precipitation and the CGT, via the Pacific–Japan (PJ) pattern (Nitta, 1987). Our analysis suggests that while the PJ pattern has a weak but significant positive correlation with the EASIA region in July (0.40), the correlation with the D&W region is negative ( $-0.33$ ), suggesting that the relationship between the PJ pattern and the EASIA region is independent of the CGT.

The model is not as good at capturing the relationship between the D&W Index and the other centres of action. The performance in August is the worst, with the observed correlation between the D&W Index and the NPAC, NAM and NWEUR regions all falling in the 90<sup>th</sup> percentile or above, meaning that the model underestimates the link between these regions in August. This corroborates what is shown in Figure 4.3, that the modelled CGT correlations are much too weak in August. In general, the model tends to overestimate the strength of the correlations in July, and underestimates them in August. This is potentially related to the difference in the observed CGT wave train in July compared to August. In July, the CGT has a wavenumber-6 structure, with the NPAC and NAM centres of action displaced westwards relative to August, when there is a wavenumber-5 structure. This means that in July there are both positive and negative contributions from the correlations in these centres of action, and so the observed July correlations are reduced compared to August. As the correlations in the model in July and August are of similar magnitude, this suggests that the model does not capture the difference in the CGT wavenumber between these months and has a wavenumber-5 structure in both. The observed CGT is strongest in August and is related to significant temperature and precipitation anomalies in Europe in this month, so the inability of the model to capture the strength of the relationship between the D&W Index and these centres of action may impact on forecast skill for these variables.

Figure 4.6 shows the distribution of model correlations between each CGT centre of action and its neighbouring centres of action. It was shown in Figure 4.5 that the model representation of the relationship between the D&W region and EASIA region is good. However, the model is less able to capture the relationships between subsequent downstream centres of action. The relationship between the EASIA and NPAC regions is good in June, but in July the model overestimates the magnitude of the correlation between these regions. As previously mentioned, this is in part due to the slightly different spatial structure of the observed CGT correlations in July, with the NPAC centre of action shifted westwards towards the date line, and an area of negative correlations in its place.



**Figure 4.6:** Same as Figure 4.5, but for each centre of action of the CGT against the neighbouring centre of action.

In August there is an observed correlation of 0.71 between these regions, but this falls in the 98<sup>th</sup> percentile of the distribution with an ensemble median correlation of around 0.50. As the model underestimates the strength of the relationship between these regions in August, this limits the ability of the model to represent the August CGT accurately and will also affect the subsequent downstream representation of the CGT from the NPAC region eastwards.

The observed correlations between the NPAC and NAM regions are not significant in all months. The model captures this with a reasonable degree of success, with the observations lying between the 10<sup>th</sup> and 90<sup>th</sup> percentiles in all months, although the model does overestimate the magnitude of the correlation in July. The observed correlations between the NAM and NWEUR regions are significant in June and August (0.34 and 0.43 respectively). For both months the observations lie within the spread of the model distribution, although the median of the model correlations is lower than observed in both cases.

There is an observed correlation of 0.46 between the NPAC and NWEUR regions in August. The model underestimates the strength of this correlation by a large margin, and this is consistent with correlations between other regions, where the correlations tend to be underestimated by the model in August associated with a weaker than observed CGT.

### **4.3 Understanding errors in the model teleconnection**

Several possible causes of the errors in the model representation of the CGT are now examined, and the possible role that each has in causing errors in the teleconnection is determined. These include errors in the forcing of the wave train, and also errors in the basic state which could affect the wave propagation in the model, as the propagation of Rossby waves is an important part of the CGT mechanism.

#### **4.3.1 Errors in the D&W region**

We first look at the variance of the D&W Index in the model compared to observations, noting that if the model variability in that region is small, the variance associated with that in other centres of action may be reduced. If the variance is weak, it is an indication that the region is not being forced as it should be. If the variance is strong, this suggests that it is the model teleconnection mechanism that is wrong.

Figure 4.7 shows the distribution of the variance of the D&W Index in the model and observations. The variance of the D&W Index is greatest in June, and the model reflects this, with the observations lying well within the interquartile range of the model distribution. However, in July and August the model underestimates the variance in this region, most notably in July when the observed variance falls well outside of the model distribution. In August the observed variance does lie within the model distribution but falls in the 92<sup>nd</sup> percentile. The underestimation of the variance in this region by the model suggests that even if the teleconnection pathway is correctly represented in the model, it will still underestimate the strength of the teleconnection.

To identify a possible cause of the low variance in the model D&W Index in July and August we examine the relationship between geopotential height in this region and precipitation in the North Indian Summer Monsoon region (NISM), a region first defined in

Ding and Wang (2007). We know from observations that there is a significant correlation between precipitation in this region and the D&W Index (correlations of 0.51, 0.61, 0.56 for June, July and August respectively), partly as a result of the effect of the west-central Asian high in triggering precipitation across northern parts of India (Ding and Wang, 2007), and partly as a result of the subsequent reinforcement of the west-central Asian high as a result of a Gill-type response to the diabatic heating associated with this precipitation (Gill, 1980; Ding and Wang, 2005). Therefore if the model does not represent the relationship between these regions well, this may affect its ability to correctly simulate the CGT.

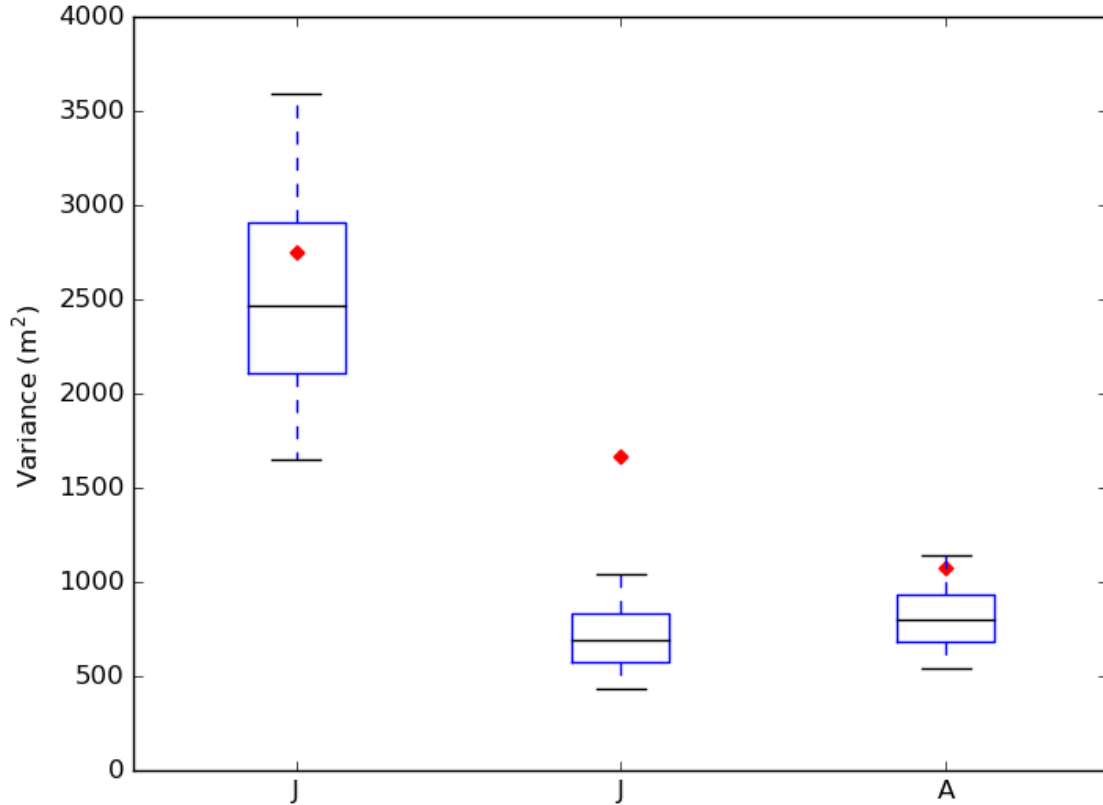
Figure 4.8a shows the observed and model correlations between the D&W Index and NISM precipitation. During July and August, when the variance in the D&W Index is reduced, the model underestimates the correlation between NISM precipitation and the D&W Index (Figure 4.8a) and also underestimates the variance in NISM precipitation during these months (Figure 4.8b). This suggests that the poor variance of the D&W Index in July and August and the poor representation of NISM precipitation in the model may be linked.

It was shown in Ding et al. (2011) that the CGT pattern is favoured in summers preceding the peak phases of ENSO. Correlating the difference in the Niño3.4 Index in the preceding winter (DJF) and the subsequent winter against individual centres of action results in negative but not significant correlations. The equivalent model correlations are also not significant but are generally less negative than the observations (not shown). Therefore while the CGT itself may be correlated with ENSO, there is no obvious link between ENSO and the individual centres of action. This may be because there are a number of other drivers for each of the centres of action individually which may mask the influence of ENSO.

### **4.3.2 Rossby wave source**

The CGT mechanism relies on the generation and propagation of Rossby waves. The Rossby wave source (RWS) describes the forcing of Rossby waves by the divergent flow; further details about the RWS term can be found in Chapter 2.1.2. Here, the RWS is calculated using the  $u$  and  $v$  components of the wind at 200 hPa. Given the likely interaction between Rossby waves generated by the ISM and the CGT, we compare the

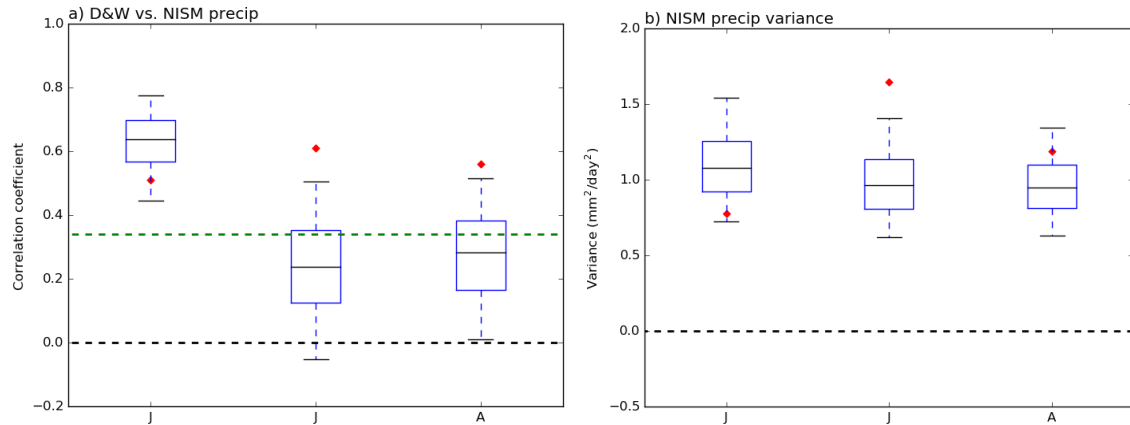
RWS in the model to ERA-Interim to help understand the role of any errors in RWS in the representation of the CGT in the model. We first focus on the D&W region, given its key role as a centre of action of the CGT, and the fact that there is a significant correlation between the D&W Index and RWS located near the D&W region in July and August ( $-0.50$  and  $-0.42$  respectively).



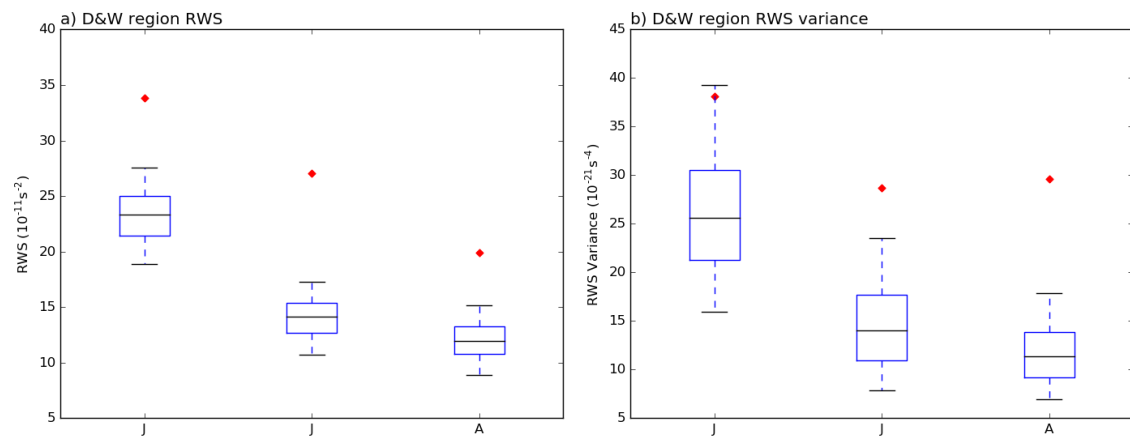
**Figure 4.7:** Distribution of variances of the D&W Index, calculated using the multiple samples. The box plots represent the upper and lower quartiles, and the whiskers extend to the 5<sup>th</sup> and 95<sup>th</sup> percentiles. The black horizontal line represents the median value and the red diamond the observed variance from ERA-Interim.

Figure 4.9a shows the RWS averaged over the D&W region in the model and observations. It is clear that the model RWS in this region is too low in all months, with the observations lying well outside the model distribution. The variance of the RWS in this region is also too low (Figure 4.9b) in the model in both July and August, and to a slightly lesser extent in June. If the strength and variance of the forcing in this region are not accurately represented then Rossby waves that are excited may be weaker than observed and this will affect their propagation characteristics and as such will result in errors in the modelled CGT.

To gain an understanding of the reasons for the differences seen in Figure 4.9 we examine the mean RWS across a wider region. All of the panels in Figure 4.10 are



**Figure 4.8:** Same as Figure 4.7, but for (a) the correlation coefficient between the D&W Index and NISM precipitation and (b) the variance of NISM precipitation. The green dashed line on (a) represents the 5% significance level.



**Figure 4.9:** (a) Rossby wave source (RWS) in the model (box plots) and observations (red diamond) and (b) variance in the RWS in the model and observations. In both panels the box plots represent the upper and lower quartiles, and the whiskers extend to the 5<sup>th</sup> and 95<sup>th</sup> percentiles. The black horizontal line represents the median value and the red diamond the observed value from ERA-Interim.

for August only, as this month has the strongest CGT wave train and the patterns are representative of those seen in June and July (not shown). Figures 4.10a and 4.10b show the mean August RWS term, calculated using Equation 2.4, in ERA-Interim and the model ensemble mean respectively in the coloured contours, and the 200 hPa zonal wind in the black contours. The first thing we note is that the centre of positive RWS located at approximately 40°N, 60°E, which, along with the source over the Mediterranean, is a major wave source (Enomoto et al., 2003), is broader and is located further to the north in the model than in ERA-Interim. This appears to be associated with a northward displacement of the model jet stream by several degrees when compared to ERA-Interim, and also explains the lower than observed RWS in the D&W region in the model shown in Figure 4.9a. This displacement in both RWS and jet location is also present in both

June and July (not shown).

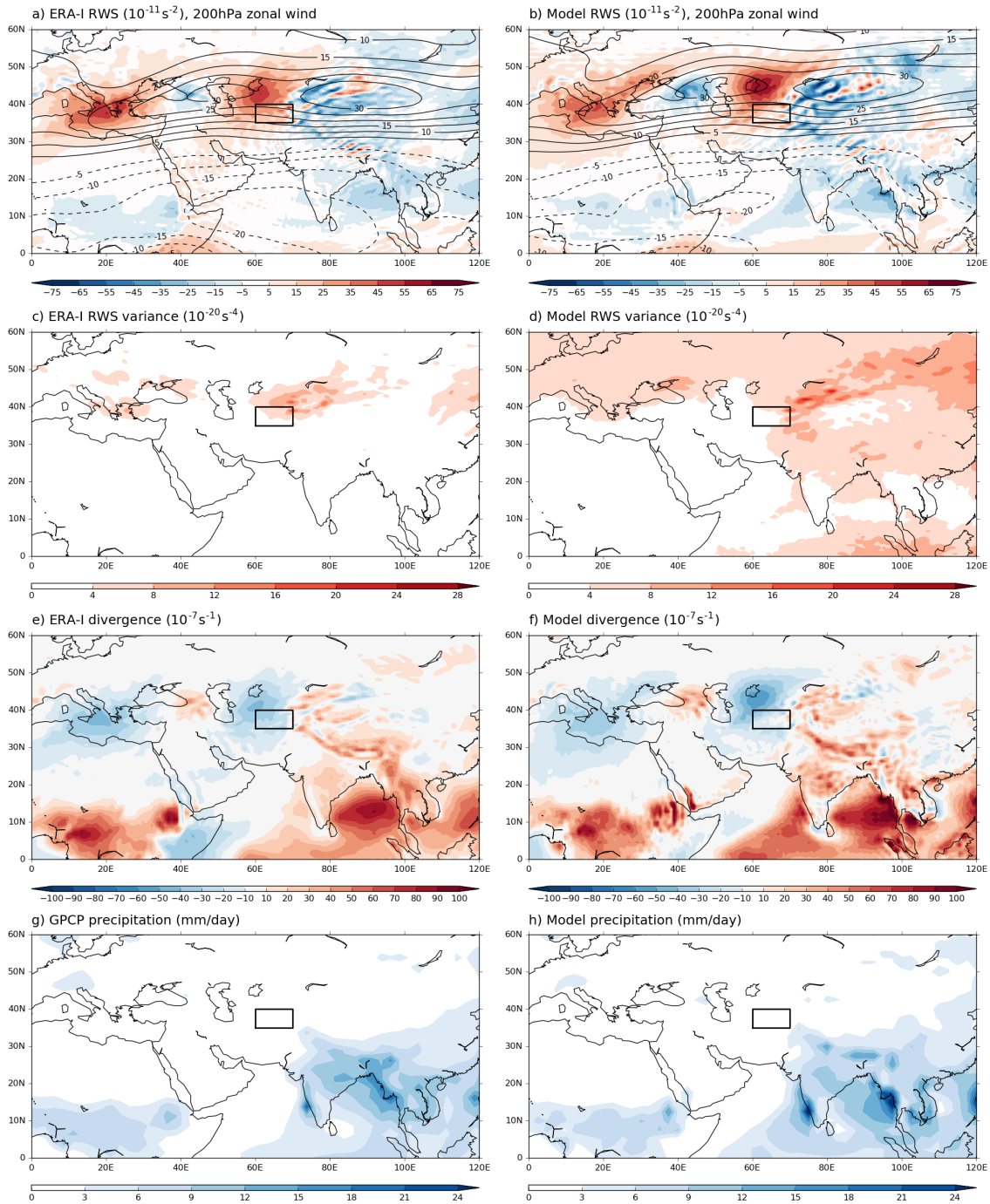


**Figure 4.10:** (a) ERA-Interim and (b) model ensemble mean RWS term (filled contours) and 200 hPa zonal wind (black contours). (c) ERA-Interim and (d) model variance of the RWS term. The model variance is for all members concatenated together. (e) ERA-Interim and (f) model ensemble mean divergence. (g) GPCP and (h) model ensemble mean precipitation. All panels are for August, and the D&W region is marked as a box.

Figure 4.9b shows that the variance of the RWS in the D&W region is lower in the model than in observations, however we see from Figures 4.10c and 4.10d that this is generally not the case over a wider region. Indeed, in most parts of the region of interest

the variance of the RWS in ERA-Interim (Figure 4.10c) is lower than in the model (Figure 4.10d). This is because the amplitude of the RWS in the model is generally larger, therefore horizontal gradients in the RWS are larger. This means that horizontal displacements in the centres of maxima and minima from year-to-year give greater variance. The northward position of the jet stream in the model may also account for the generally larger variance in RWS between 50°N and 60°N, due to the increased vorticity gradient here.

The mean divergence field is shown in Figures 4.10e (ERA-Interim) and 4.10f (model). The centre of negative divergence (convergence) located at approximately 40°N, 60°E (in the same location as the centre of large RWS in Figure 4.10a) is both larger in magnitude and located further to the north in the model than in ERA-Interim. This centre of convergence was shown to be localised in this region by the presence of the Zagros mountain chain (Rodwell and Hoskins, 1996). Where the jet is located may determine where the divergence and convergence is, but we know, by comparing to the RWS computed from the rotational flow of ERA-Interim with the model divergent flow, that errors in the RWS primarily come from errors in the divergent flow (not shown). The errors in divergence are largest over both the Arabian Sea and the Bay of Bengal. Here, the divergence is much greater in the model than in ERA-Interim, associated with too much precipitation in the model in these regions (Figures 4.10g and 4.10h). Conversely, precipitation over the Indian subcontinent is lower in the model than in observations, and the variance of NISM precipitation is also too low (Figure 4.8). These differences in the distribution and variance of monsoon precipitation may affect the link between the monsoon and the extratropical circulation, and thus the forcing of the CGT, in the model. The RWS term is also dominated by the divergence component, and therefore the convergence in the model (which is both too strong and located in the wrong place) is likely to be an important factor in the errors in RWS in the model. These errors in the RWS may impact on European summer forecast skill through errors in the CGT, so more accurate representation of the link between monsoon heating and the extratropical circulation may be important for improving European summer forecasts. This will be investigated further in Chapters 5 and 6.

We also note that the jet biases over the Mediterranean are much smaller than over west-central Asia, and the location of the centre of convergence in the model in this region closer resembles ERA-Interim. Where there are larger wind biases over west-central Asia

there is a greater displacement of the centre of convergence, and this strengthens the argument that the jet location is an important factor in these errors.

The propagation of Rossby waves generated in this region relies on the jet stream, which acts as a waveguide. As seen in Figures 4.10a and 4.10b, the model jet stream is located too far to the north over Asia. It can be seen from Figure 4.11 that there is a clear northward bias in the position of the jet over much of the northern hemisphere, particularly in June, July and August. This is shown by the positive biases to the north and negative biases to the south of the observed jet stream. The wind biases are smallest early on in the simulation, when the maximum biases are around  $4 \text{ m s}^{-1}$ . However, these biases quickly become larger, reaching a maximum of around  $8 \text{ m s}^{-1}$  in June. The magnitude of the maximum biases then remains approximately constant for the remainder of the hindcast period. The largest wind biases are seen in the RWS region over Asia which means that Rossby waves forced in this region will have different wave propagation characteristics to reality - they may propagate at the incorrect speed, in the wrong direction or may not propagate at all. The combination of the errors in RWS along with the model jet biases may be crucial in the poor representation of the CGT in the model, and this provides a motivation for the experiments which are shown in Chapter 5.

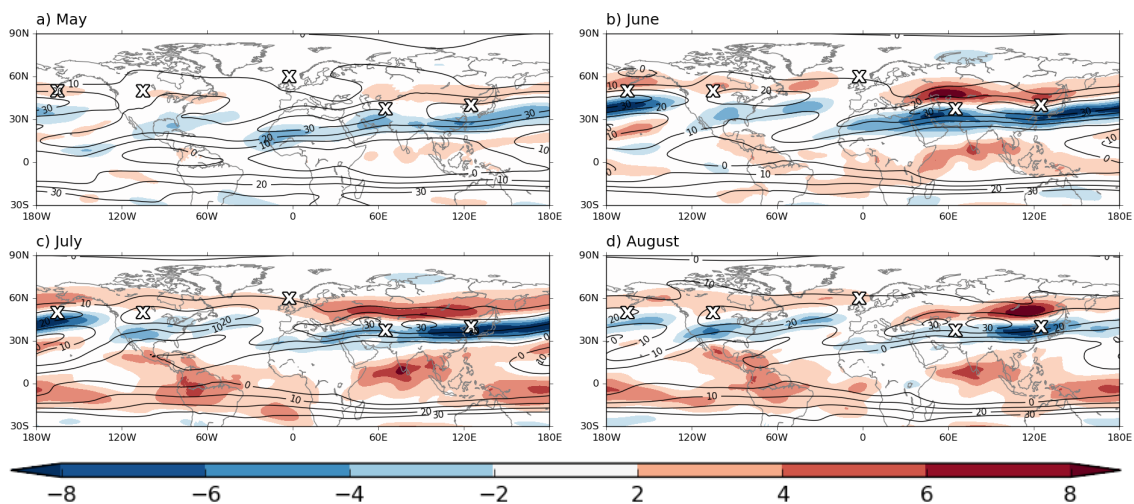


**Figure 4.11:** Model 200 hPa zonal wind bias (filled contours,  $\text{m s}^{-1}$ ), defined as the model ensemble mean minus ERA-Interim zonal wind, and ERA-I 200 hPa zonal wind (black contours) for (a) May, (b) June, (c) July and (d) August. To show the position of the observed jet, only the 0, 10, 20 and  $30 \text{ m s}^{-1}$  isotachs have been plotted. For orientation, the location of the centres of action of the CGT are marked with white crosses.

## 4.4 Summary and conclusions

In this chapter analysis of the ability of the ECMWF seasonal forecast model, as described in Section 3.3.1, to represent the CGT has been presented. The model representation of the CGT was found to be too weak, particularly in July and August, when the observed correlations associated with the CGT wave train are at their strongest and the link between the CGT and European weather and climate is large. It was also found that the model underestimates the strength of the correlation between many of the centres of action of the CGT. The model performance in August was found to be particularly poor, with the observed correlation between the D&W Index and the NPAC, NAM and NWEUR regions lying in the upper end of the distribution of model correlations (Figure 4.5). The model is able to capture the relationship between the D&W and EASIA regions in all months, but further downstream from this region correlations are much weaker than observed (Figure 4.6). In general, the model tends to underestimate the strength of the correlations in August. We have looked at the relationship between the Rossby wave source and the monsoon heating but we have not looked at the relationship between the CGT pattern and tropical precipitation in other regions, such as the tropical Atlantic (Lu et al., 2002), Central America or West Africa (Hall et al., 2013), and this may merit further investigation as a cause of the lack of skill for the CGT.

We identified several errors in aspects of the model's simulation which may be important for the generation and maintenance of the CGT, including:

1. **Weak variability in the D&W region:** We found that the model accurately captures the strength of interannual variability in this region in June, but performs much worse in July and August. This means that, assuming the other drivers of variability in remote regions remain the same, the D&W Index will explain less of the variance.
2. **Poor representation of the link between the D&W Index and NISM precipitation:** Weak variability in the D&W Index may be related to a weak correlation with NISM precipitation and weak variability of NISM precipitation during July and August. The similarity between the location of the observations in the box plots in Figures 4.7 and 4.8 suggests that poor representation by the model of the relationship between these regions in July and August is an important factor

in explaining the low model variance in the D&W Index in these months. Ding and Wang (2007) hypothesised that NISM precipitation is modulated by the propagation of the wave train between Europe and west-central Asia, before reinforcing the west-central Asian high and the subsequent downstream propagation of the wave train. Therefore, the weak link between these two regions may be important in the weak representation of the CGT.

3. **Errors in the RWS:** There are errors in the RWS in and around the D&W region. In particular, the main centre of RWS is stronger and is displaced northwards and eastwards in June, July and August. This error is largely related to errors in the divergence, and is likely to be associated with greater than observed precipitation over the Bay of Bengal and Arabian Sea.
4. **Errors in the jet location:** There is a northward displacement of the jet around the D&W region in June, July and August, which may be partially responsible for the displacement of the centres of convergence and RWS. There is also a displacement of the jet in much of the northern hemisphere, and this error, along with errors in the forcing of Rossby waves, may be a key factor in the poor representation of the CGT in the model, and as such may be an important contributor to the poor forecast skill over Europe. This hypothesis will be tested in the next two chapters.

It seems likely that the pattern of reduced skill in Figure 4.1, with negative correlations located at the centres of action of the CGT, including over Europe, is related to the poor representation of the CGT wave train in the model, either as a result of a poor representation of the monsoon heating and its associated Rossby wave response, or biases in the jet location. This also raises the question that if the model's representation of the CGT was improved, would that lead to an improvement in forecast skill for the European summer? This motivates sensitivity experiments in which the circulation is relaxed to observations in several regions that are potentially important parts of the CGT in order to explore the impact on forecast skill for European summer weather and on the representation of the CGT in the model. These experiments will also allow us to learn more about the CGT mechanism, in particular relating to the possible forcing mechanisms. Analysis of these experiments can be found in the next chapter.

## Chapter 5:

# Investigating the circumglobal teleconnection mechanism using relaxation experiments

## 5.1 Introduction

In the previous chapter, several errors in the model representation of the CGT were identified. These include weak variability in the D&W region, a weak link between the D&W Index and ISM precipitation, errors in the RWS associated with ISM precipitation and a northward shift of the jet across much of the northern hemisphere. In order to understand the evolution and potential causes of these errors, as well as to further improve knowledge of the CGT mechanism, a set of experiments was performed in which the circulation in regions thought to be important for the CGT was relaxed towards ERA-Interim. In this chapter, details of these experiments are presented. Firstly, an overview of the design of the experiments, including the motivation for the relaxation regions used, is given in Section 5.2. The analysis of these experiments is presented in Section 5.3, and this motivated experiments using the barotropic model described in Chapter 3.3.4. The motivation and design of these barotropic model experiments is given in Section 5.4, followed by analysis of these experiments. A discussion of the results and the main conclusions is given in Section 5.5.

## 5.2 Experimental design

In this chapter, analysis of three relaxation experiments is presented. These were designed to explore different aspects of the CGT mechanism and how the model represents these. In the relaxation experiments, the temperature, winds and humidity-based variables, such as specific humidity, specific cloud liquid water content and cloud cover, are relaxed towards ERA-Interim in a specific region, as described in Chapter 3.3.2. As the model is being relaxed in specific areas, through analysing where the skill is improved away from the relaxation region, the regions which are connected in the model can be determined.

One of the main motivations for the relaxation regions used was the pattern of reduced geopotential height skill shown in Chapter 4 (Figure 4.1). There are two main features to note from this figure. The first is that an area of reduced skill develops over west-central Asia by July, in the approximate location of the D&W region. This region is used as the base point for the CGT correlations, so weak forcing from this region may be one reason why the model representation of the CGT is too weak. The second is that an area of reduced skill (negative correlations) develops over northwest Europe in June and persists through July and August. This area of reduced skill develops before the reduction in skill is observed over west-central Asia and east Asia.

Another motivation from Chapter 4 is the weak model variability in the D&W region and the weak link between the D&W Index and monsoon precipitation. If the CGT is forced or maintained by the ISM via the D&W region, then this weak forcing may be important in explaining the weak representation of the CGT in the model. These results raised the following questions:

1. What is the role of the D&W region in forcing the CGT pattern, and what is its relationship with errors in the extratropical northern hemisphere?

**Table 5.1:** Relaxation regions

Experiment name	Region	Domain
DW_RELAX	Ding and Wang	35°–45°N, 55°–75°E
NWEUR_RELAX	Northwest Europe	45°–65°N, 25°W–5°E
ISM_RELAX	Indian monsoon	0°–30°N, 60°–100°E

2. How important is the northwest Europe/northeast Atlantic region in the development of errors over Asia, and in the forcing of the CGT?
3. How do errors in the monsoon circulation affect the representation of the CGT and model skill in the extratropics?

In order to answer these questions, three relaxation experiments were carried out. In the first, the circulation was relaxed towards ERA-Interim near the D&W region to determine whether errors in the CGT pattern arise from model errors over west-central Asia. The region chosen is centred slightly to the north of the D&W region, in order to minimise the impact of the relaxation on the ISM circulation. In the second experiment, a slightly larger region over northwest Europe was relaxed, to investigate whether the model errors over west-central Asia and subsequently east Asia arise as a result of the propagation of errors from northwest Europe. The third experiment relaxed most of the ISM region, to investigate the impact of correcting the monsoon circulation on the representation of the CGT and on skill in the midlatitudes.

The boundaries of the relaxation regions used in these experiments are shown in Table 5.1. To avoid adverse effects close to the relaxation boundaries, the transition from relaxed to non-relaxed regions is smoothed through using a relaxation coefficient,  $\gamma$ . Following e.g. Jung et al. (2008), the tapering is carried out over bands of latitude and longitude. The size of the relaxation region determines the width of these tapering bands, and the boundaries given in Table 5.1 refer to the centre of the band, where  $\gamma=0.5$ . For all experiments,  $\gamma$  is 0.01 about  $10^\circ$  outside of the boundaries. Therefore, the area that is being fully relaxed i.e. where  $\gamma = 1$  is smaller than the defined region. The horizontal tapering functions (masks,  $\gamma$ ) are shown in Figures 5.1, 5.2 and 5.3. As the region used in the first experiment is relatively small, the maximum value of  $\gamma$  is 0.84. In the second and third experiments, the relaxation regions are larger, so the maximum value of  $\gamma$  is 0.99. The relaxation technique is explained in more detail in Chapter 3.3.2.

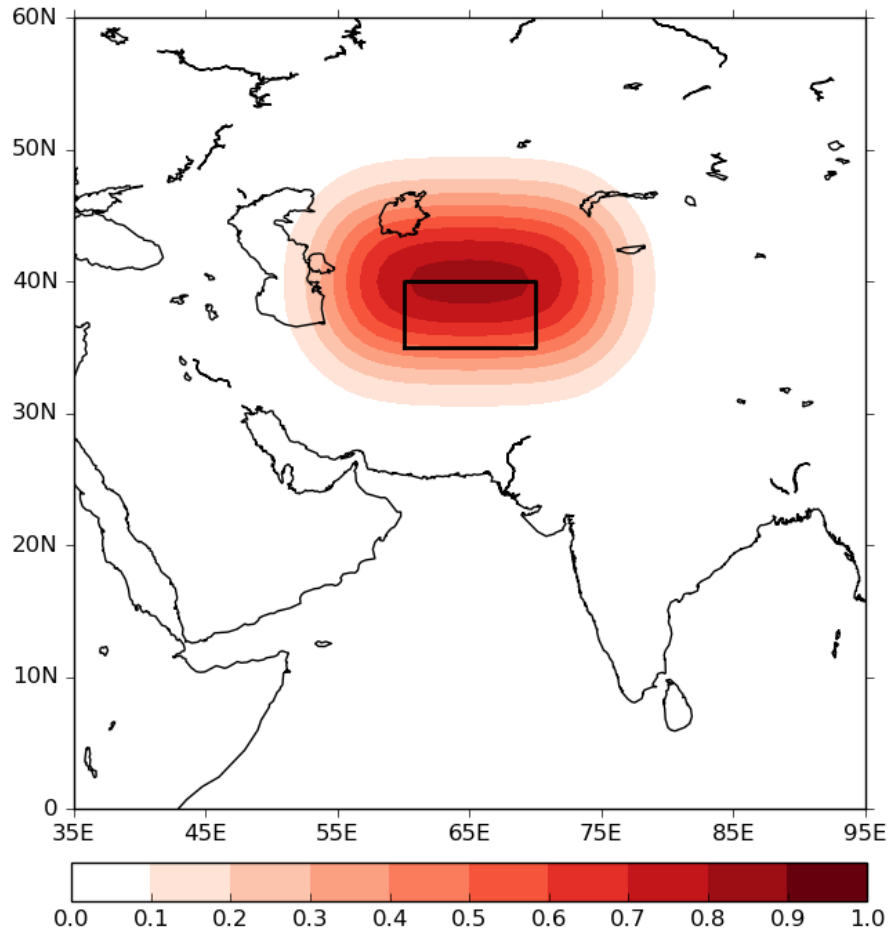


**Figure 5.1:** Horizontal relaxation coefficient ( $\gamma$ ) used in the first relaxation experiment (DW\_RELAX). For orientation, the D&W region is shown as a box.

## 5.3 Experimental analysis

### 5.3.1 New control experiment

Relaxation in the IFS requires there to be the same number of levels in the reference dataset as in the model run, in order to enable the relaxation to take place on all levels. The control experiment presented in Chapter 4 was run with 91 levels, whereas ERA-Interim has 60 levels. Therefore, to allow a fair comparison to be made between the control run and the relaxation experiments, a new control experiment was run with 60 vertical levels, and it is this control run that is used for the comparisons within this chapter. To demonstrate that changing the vertical resolution of the model has not altered the model skill or representation of the CGT very much, and also for comparison with results from the relaxation experiments, three figures from the new control experiment are shown. The

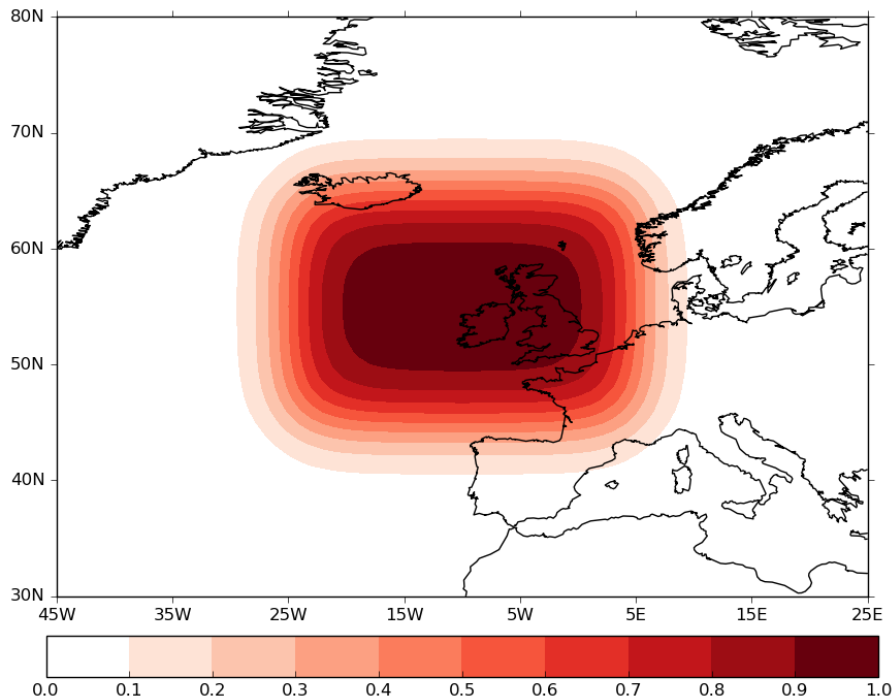


**Figure 5.2:** Horizontal relaxation coefficient ( $\gamma$ ) used in the second relaxation experiment (NWEUR\_RELAX).

first is the skill of 200 hPa geopotential height (Figure 5.4) and the pattern of reduced skill in all months is very similar to that for the control run used in Chapter 4 (Figure 4.1).

The second figure is of the zonal wind biases. As seen in Chapter 4, the model has a jet stream that is shifted northwards, a bias which develops soon after the forecast is initialised and persists throughout the four month forecast. From Figure 5.5 it can be seen that the jet biases in the new control experiment are also similar to those seen in Chapter 4.

The CGT pattern is strongest in August, so our analysis of the CGT focusses on August. Examples of members from the 25 original members which have a good and bad representation of the CGT are shown in Figure 5.6 to give an indication of what a CGT pattern with a high and low pattern correlation looks like. The member with a pattern correlation of 0.75 (Figure 5.6b) has a very accurate representation of the centres of action over northwest Europe and east Asia, and the centres over the North Pacific and North America are well located, albeit with correlations that are weaker than observed. The member with a pattern correlation of 0.41 (Figure 5.6c) has a much poorer representation. In this member, there is much less evidence of a circumglobal wave train, although the

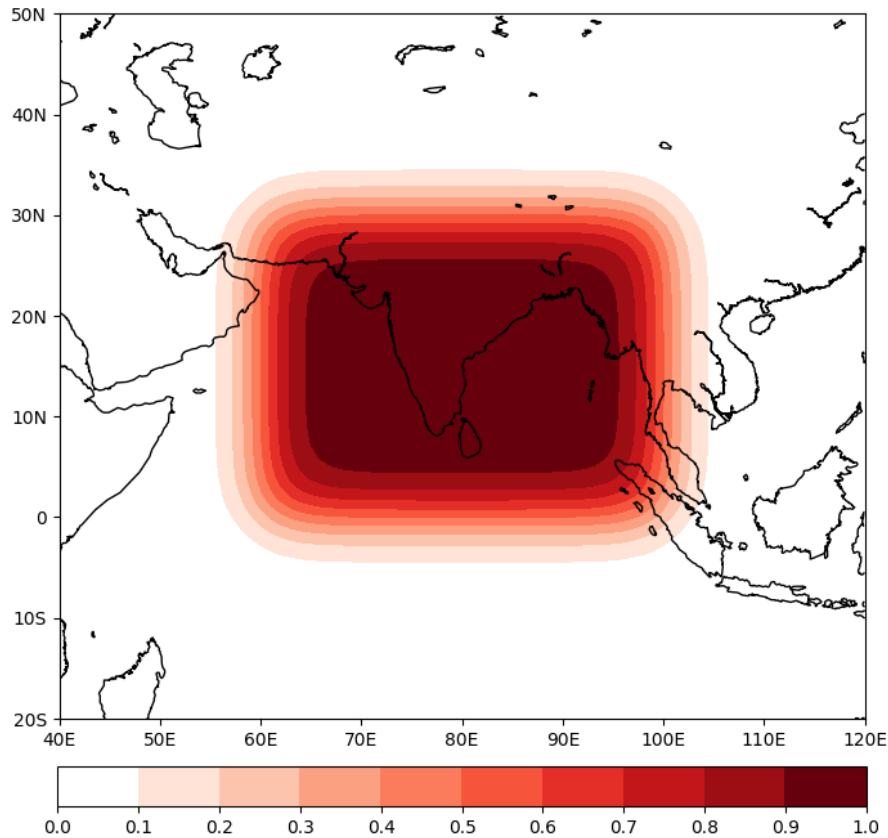


**Figure 5.3:** Horizontal relaxation coefficient ( $\gamma$ ) used in the third relaxation experiment (ISM\_RELAX).

correlations over northwest Europe and east Asia have the correct sign. There is also a much stronger tropics-wide positive response, which is more similar to observations than the higher pattern correlation member, although it is stronger than in observations. These two examples represent the two tails of the distribution in Figure 5.7, so the majority of members will have a CGT pattern that lies somewhere between these two extremes.

Figure 5.7 is a histogram of ensemble member pattern correlations of the CGT correlation maps calculated between  $30^{\circ}$ – $70^{\circ}$ N compared to ERA-Interim, in the new control experiment. As with the histogram in Chapter 4, these were calculated for 2000 time series created using the method described in Section 3.3.5. Again, there is very little difference compared to the distribution for the higher vertical resolution control, with the median values almost exactly the same. The pattern correlation values range from around 0.2–0.8 with a median of 0.59, indicating that the model does have some skill at representing the CGT. By comparing the distribution of the pattern correlation values from the control and relaxation experiments, the effect of the relaxations on the representation of the CGT can be analysed.

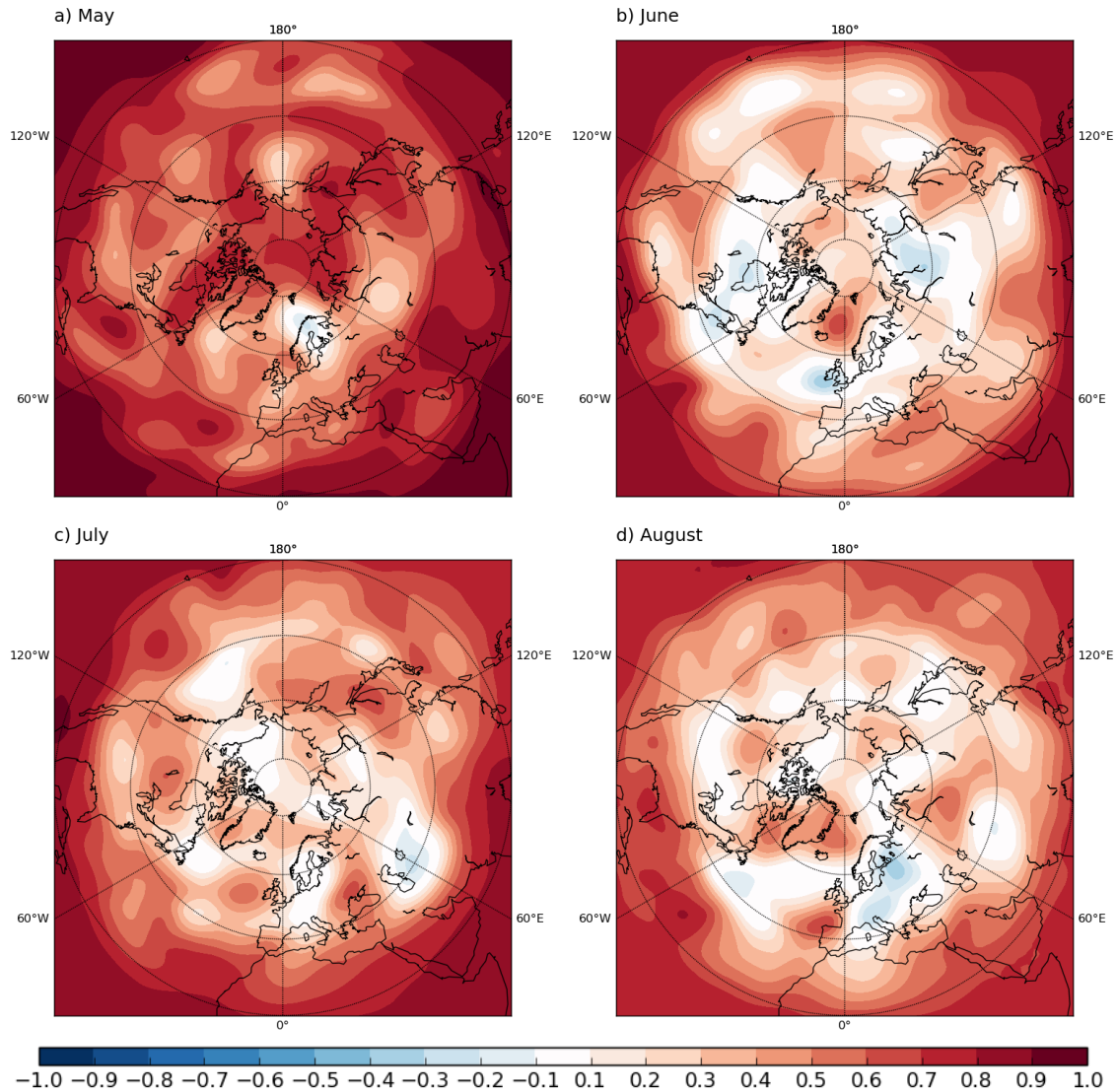


**Figure 5.4:** Skill for 200 hPa geopotential height in the new control experiment, as defined as the correlation between ERA-Interim and the 25 member ensemble mean for (a) May, (b) June, (c) July and (d) August.

### 5.3.2 West-central Asia relaxation

From Figure 5.4 it can be seen that errors in 200 hPa geopotential height develop in the control run in much of the northern hemisphere, including over west-central Asia, in the D&W region. To investigate whether model errors in the CGT pattern arise as a result of the development of errors in this region, in “DW\_RELAX”, the temperature, winds and humidity-based variables were relaxed in a region centred approximately over the D&W region (Figure 5.1), using the method described in Chapter 3.3.2. It was hypothesised by Ding and Wang (2005), and subsequently Ding and Wang (2007), that the D&W region is important for either forcing or maintaining the CGT, so analysis of this experiment will determine whether correcting the circulation in this area results in an improved model

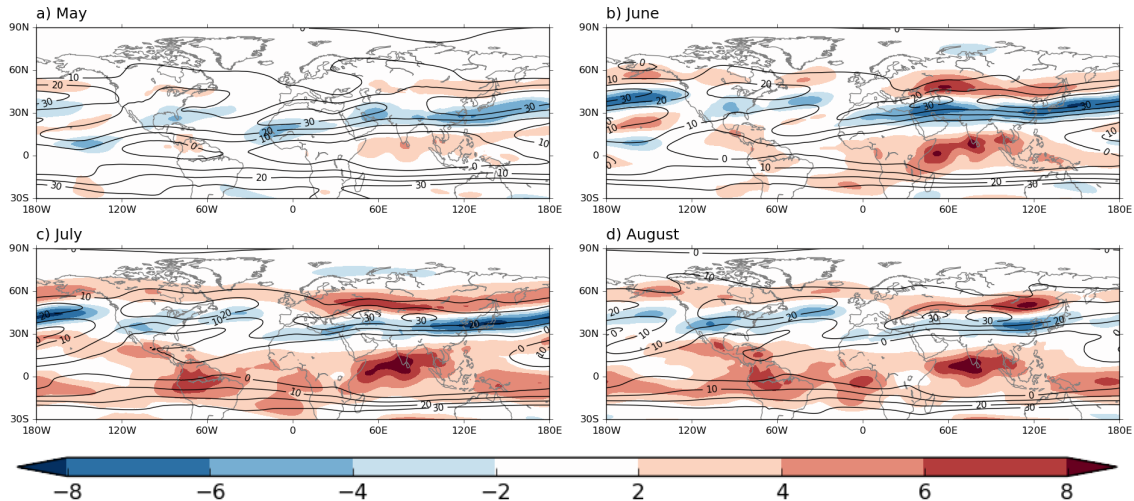
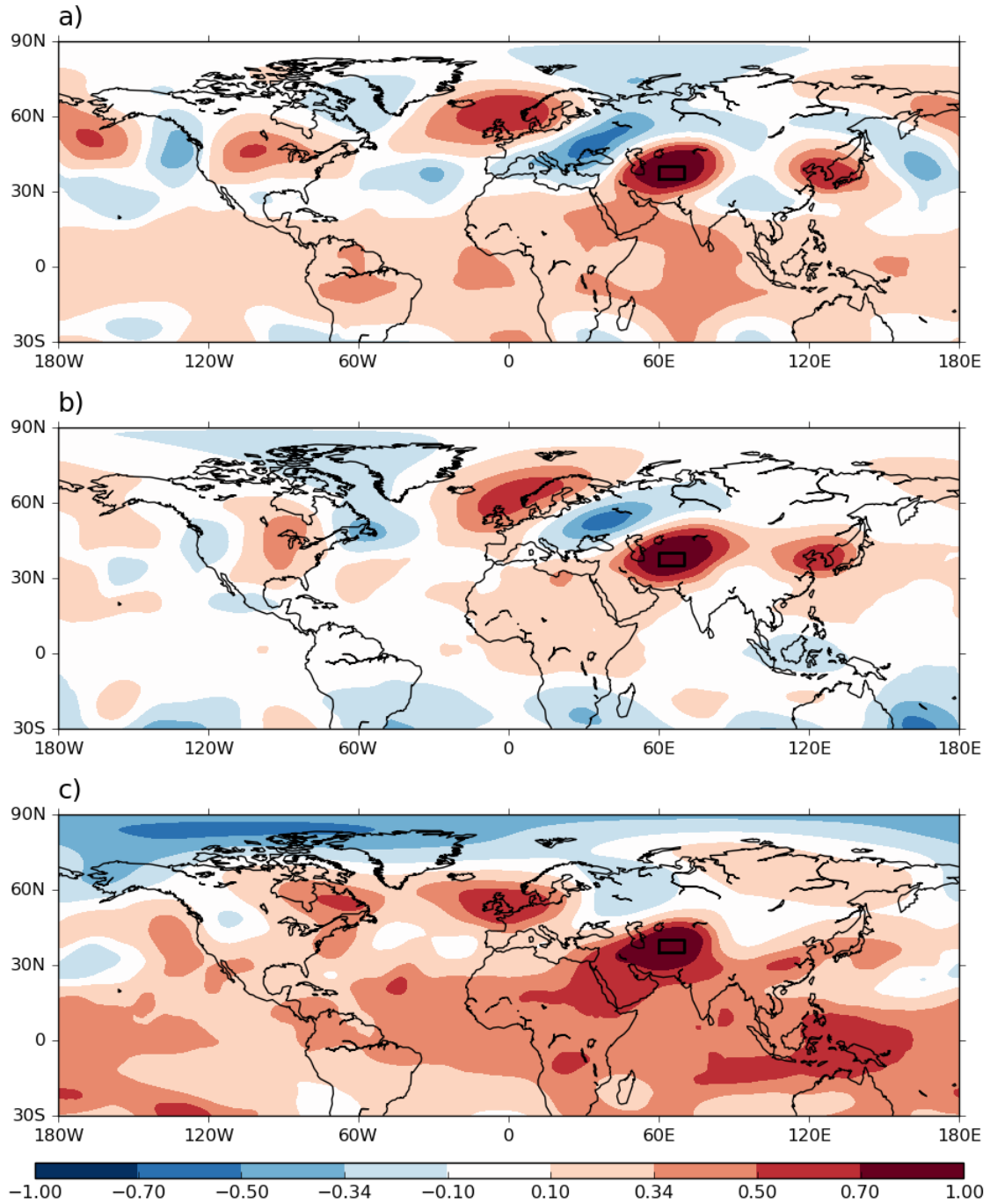


**Figure 5.5:** Control experiment 200 hPa zonal wind bias (filled contours,  $\text{m s}^{-1}$ ), defined as the model ensemble mean minus ERA-Interim zonal wind, and ERA-Interim 200 hPa zonal wind (black contours) for (a) May, (b) June, (c) July and (d) August. To show the position of the observed jet, only the 0, 10, 20 and  $30 \text{ m s}^{-1}$  isotachs have been plotted.

representation of the CGT.

Figure 5.8 shows the difference in ensemble mean 200 hPa geopotential height skill (defined as the correlation between the model ensemble mean and ERA-Interim) between the new control experiment and DW\_RELAX. This is defined such that a positive value indicates that the skill in the relaxation experiment is higher than in the control, and vice versa. As expected, there are large improvements in skill in and around the relaxation region. Away from this region, improvements are largely confined to central and east Asia, downstream of the relaxation region. There is very little change in skill over the centres of action in the North Pacific, North America or Europe. Indeed, in June and July in particular, there is actually a large reduction in skill in some parts of Europe. This implies that the poor forecast skill over Europe is not directly related to errors in the D&W region. The upstream reduction in skill may be a result of waves propagating into this region being out of phase compared to observations, and when forced towards ERA-Interim by the relaxation get partially reflected.

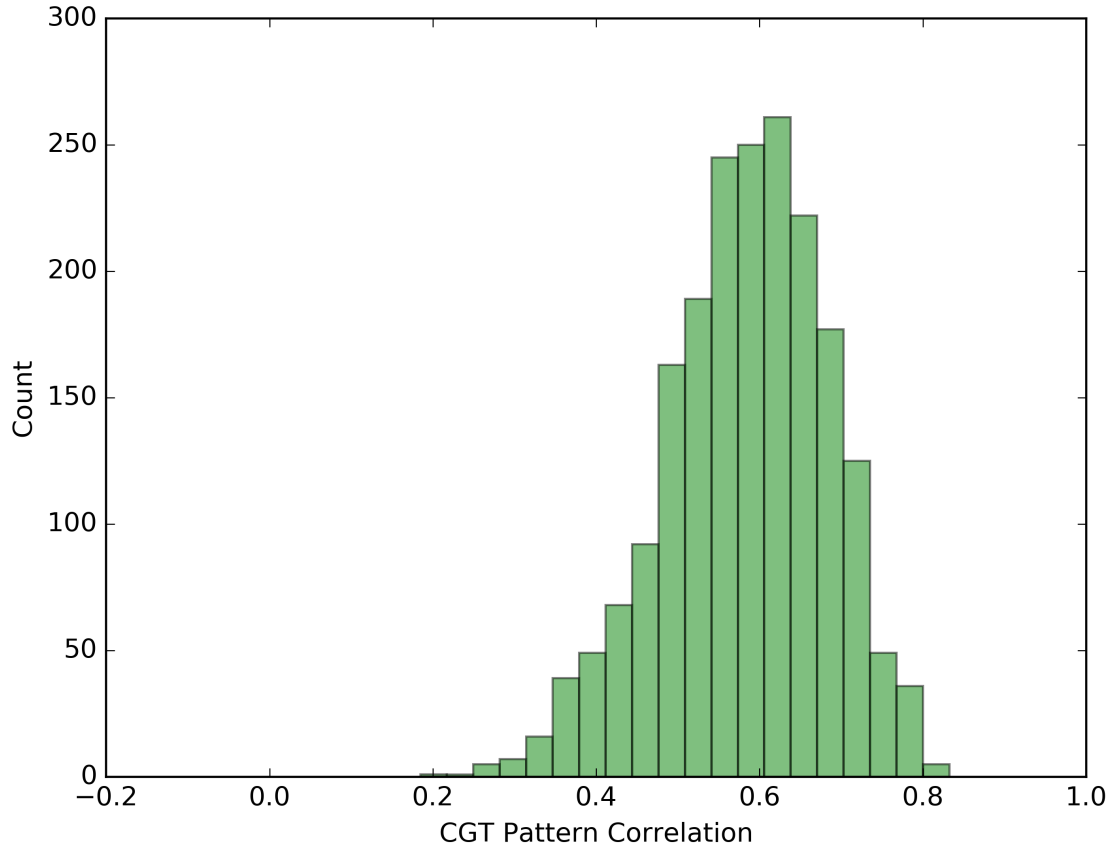
As a result of the relaxation, the ensemble spread in the relaxation region is reduced to close to zero as each ensemble member is being relaxed to the same ERA-Interim reference dataset. The influence of this change on other regions of the hemisphere can be used to help determine what teleconnections may be present in the model; if there is a strong link between the relaxation region and a remote region then the ensemble spread in the remote region may also be expected to reduce, even if the model skill in that area



**Figure 5.6:** (a) August CGT pattern from ERA-Interim. (b) and (c) Members from the control experiment with a 30°–70°N CGT pattern correlation of (b) 0.75 and (c) 0.41. The base point for the correlations (the D&W region, 35°–40°N, 60°–70°E) is shown as a box. Correlation values of  $\pm 0.34$  are significant at the 5% level.

is not improved in the relaxation experiment.

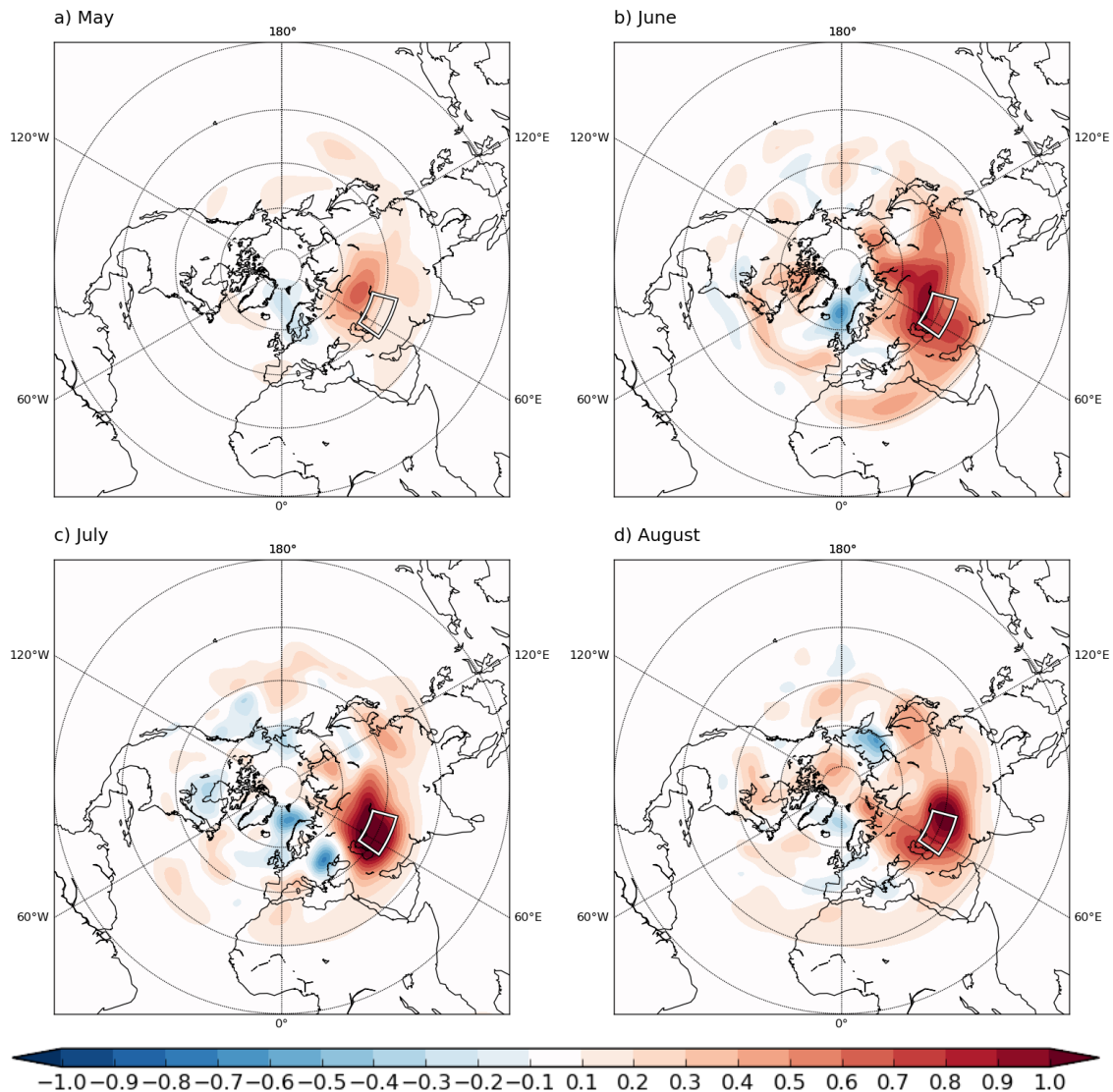
Figure 5.9 shows the ratio of the monthly standard deviation of the 25 ensemble members in DW\_RELAX compared to the control. This has been calculated for 200 hPa geopotential height for each year, then averaged over all years. Areas with a value of



**Figure 5.7:** Histogram of the pattern correlations between the model control experiment and ERA-Interim CGT correlations for August, calculated using 2000 time series created from the 25 ensemble members. The pattern correlations were calculated for all longitudes between 30°–70°N and the median value is 0.59.

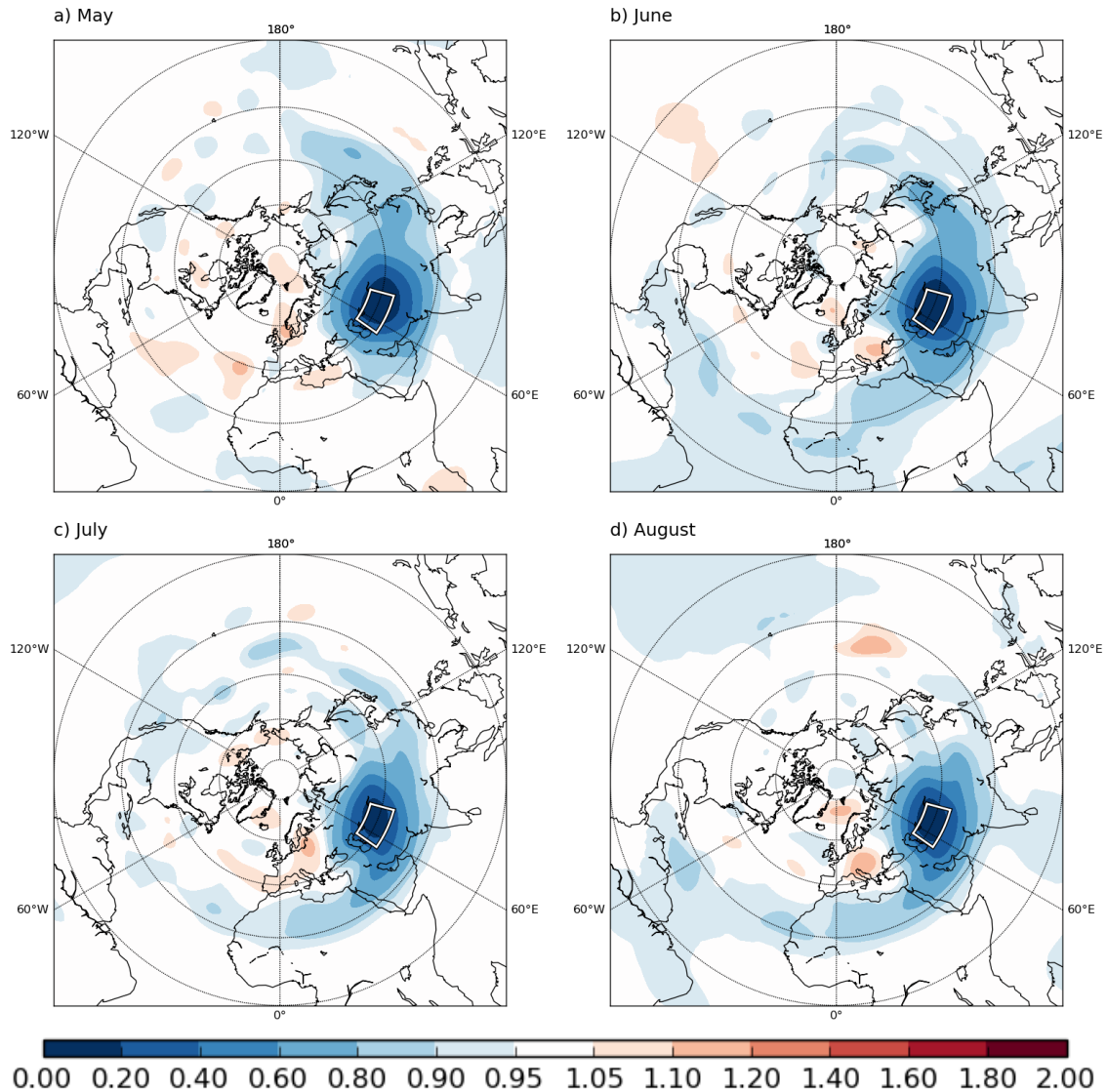
less than one (blue) are where the ensemble spread has been reduced with respect to the control experiment, and vice versa. There has been a reduction in the ensemble spread in some regions away from the relaxation region, but these are mainly confined to central and east Asia and some parts of the North Pacific. In general, the areas of reduced ensemble spread coincide with areas where the 200 hPa geopotential height skill was improved. The general lack of reduction in ensemble spread away from the relaxation region (particularly in August, when the CGT is strongest) implies that either west-central Asia is not a forcing region for other parts of the northern hemisphere, or that the model is unable to reproduce any observed teleconnections from this region, for example as a result of jet stream biases.

Figure 5.10 shows the range of the pattern correlations between the CGT pattern in ERA-Interim and DW\_RELAX, plotted as the blue bars, calculated in the same way as for the control experiment. When compared to the equivalent histogram for the control



**Figure 5.8:** DW\_RELAX 200 hPa geopotential height correlation skill minus control 200 hPa geopotential height skill for (a) May (b) June (c) July and (d) August. A positive value indicates that the skill is increased in the relaxation experiment compared to the control. The box indicates the relaxation region used.

experiment (green bars), it can be seen that relaxing in west-central Asia has actually resulted in a worsening of the representation of the CGT in the model. The range of pattern correlations in DW\_RELAX is around  $-0.1$ – $0.7$ , with a much lower median value of  $0.35$ . Given that in this experiment the D&W Index has been corrected to ERA-Interim, this may suggest that this region is not actually forcing the CGT pattern. This is consistent with the findings of Ding and Wang (2007), who hypothesised that variations in Indian summer monsoon (ISM) precipitation reinforce the west-central Asian high and re-energise the further propagation of the wave train but do not force it directly. However, while the D&W region may not be a sufficient driver of the CGT on its own, it is still a necessary component of it and errors in this region do have a negative impact on skill



**Figure 5.9:** Ratio of standard deviation of 200 hPa geopotential height in the 25 ensemble members in DW\_RELAX compared to the control for (a) May (b) June (c) July and (d) August. A value of less than 1 indicates that the ensemble spread in the experiment is reduced compared to the control, and vice versa. The box indicates the relaxation region used.

downstream.

Another explanation may relate to the lower than observed variance in the model D&W region seen in Chapter 4, Figure 4.7. One impact of relaxing in west-central Asia will have been to increase the variance in the D&W region so that it more closely matches observations. If the model teleconnection pathway is wrong then this may mean that in this experiment a stronger version of the incorrect pattern is being forced, which could explain the reduction in pattern correlation. If the errors in the CGT pattern arise because of errors in the Rossby wave propagation rather than in the wave generation, then relaxing

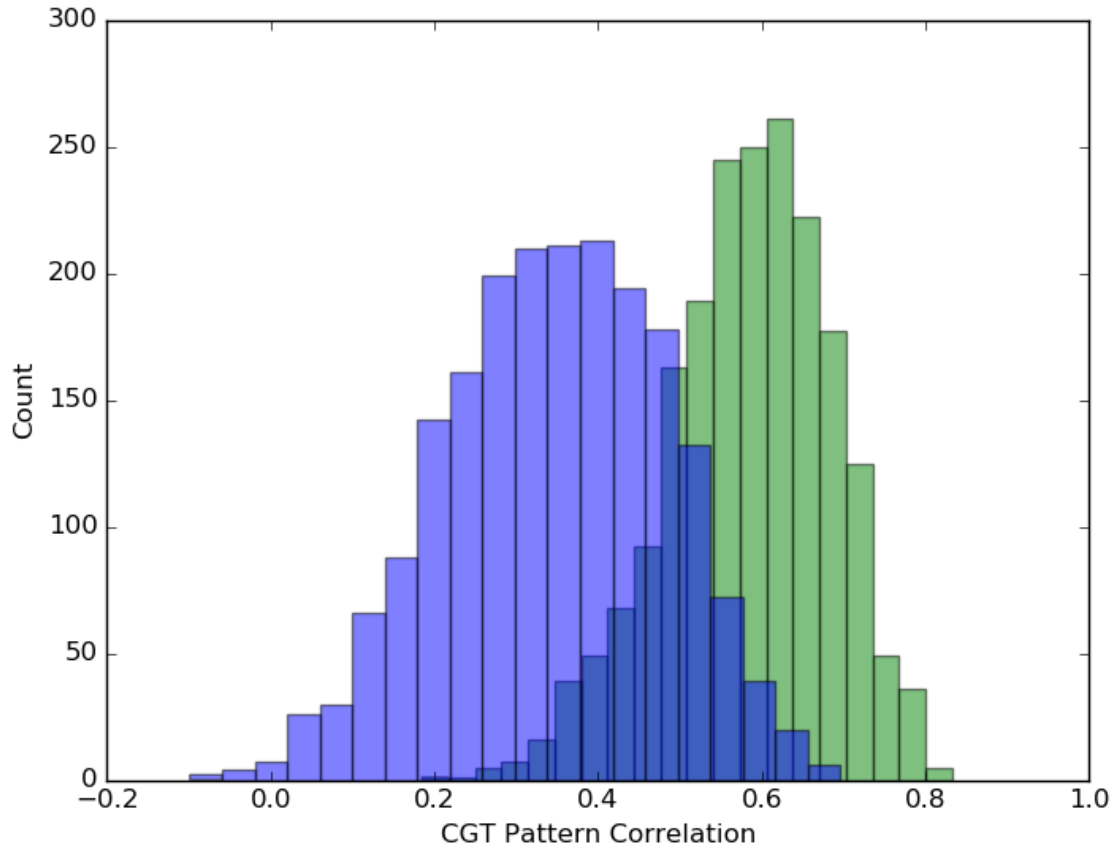


**Figure 5.10:** Histograms of the pattern correlations for the control (green) and DW\_RELAX (blue) against the ERA-Interim CGT correlations for August, calculated using 2000 time series created from the 25 ensemble members. The pattern correlations were calculated for all longitudes between  $30^{\circ}$ – $70^{\circ}$ N. The median value for the control is 0.59 and for DW\_RELAX is 0.35.

in west-central Asia may not be expected to improve the model CGT pattern if the wave propagation away from this region is still incorrect.

One possible reason for errors in the wave propagation can be seen in Figure 5.11, which shows the zonal wind bias in DW\_RELAX. While the relaxation has reduced the jet bias in the immediate area around the relaxation region, elsewhere in the hemisphere the biases remain very similar to in the control experiment. This means that there are still likely to be errors in Rossby wave propagation, which may explain the lack of improvement in model skill away from the relaxation region and the poor representation of the CGT in this experiment.

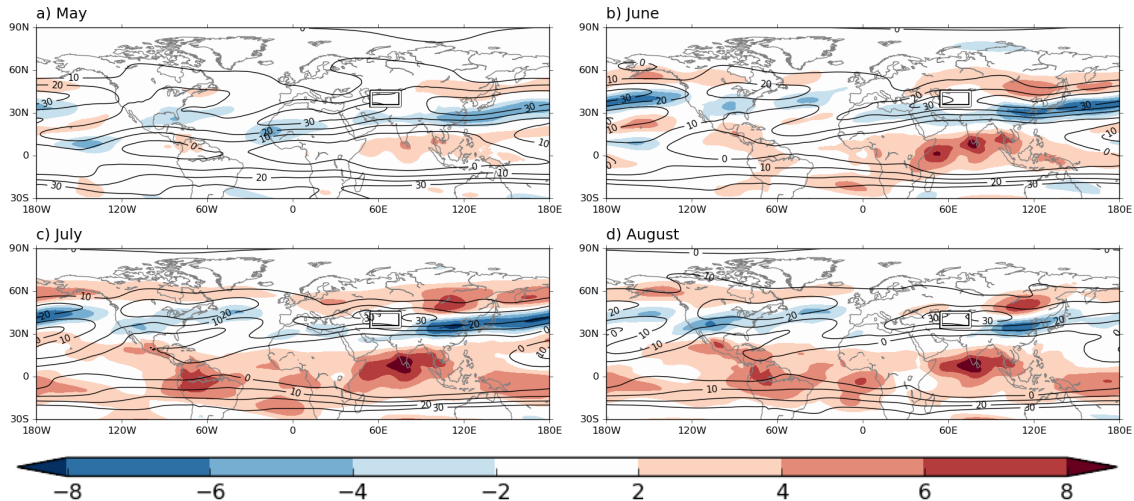
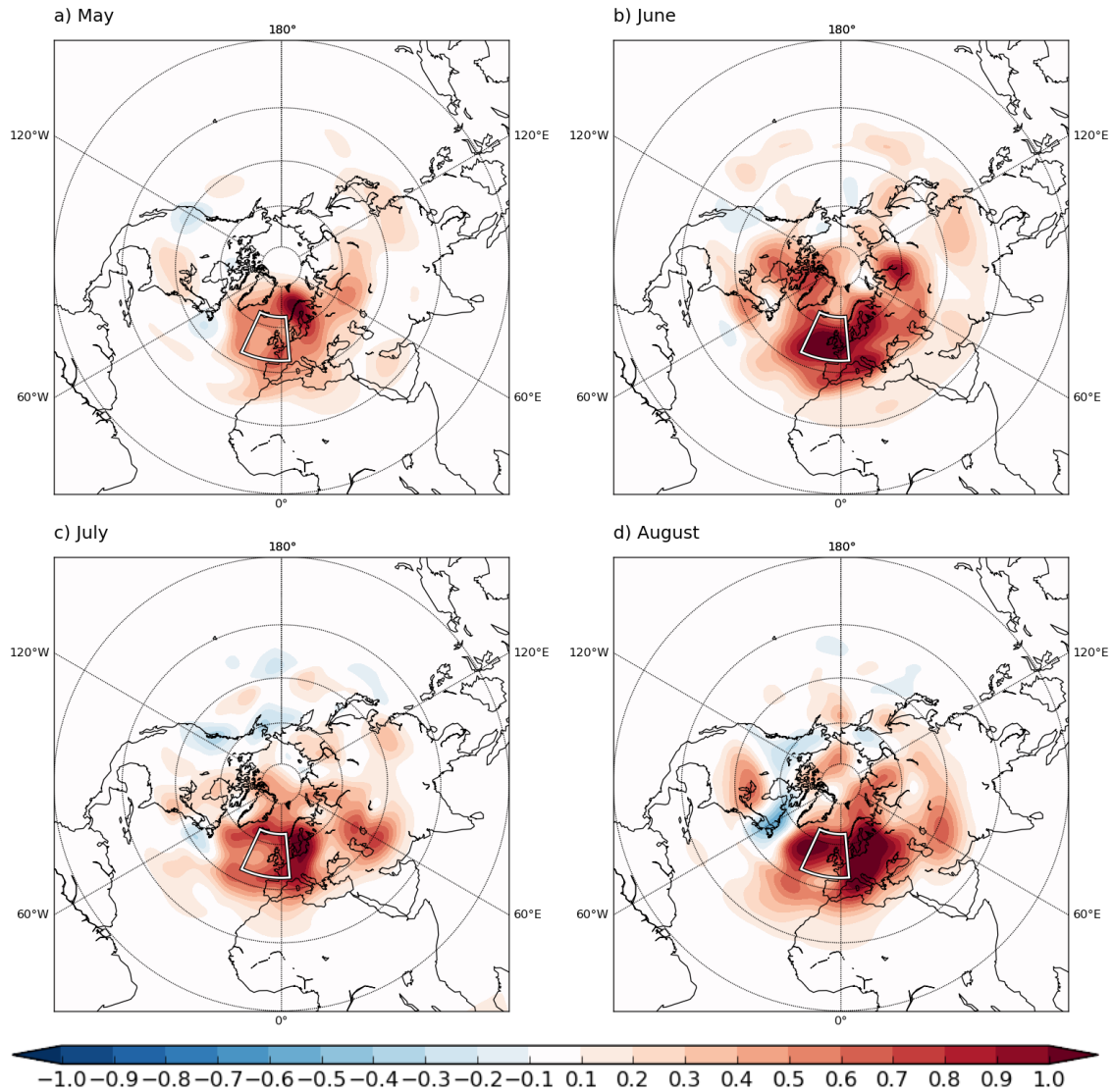


**Figure 5.11:** DW\_RELAX 200 hPa zonal wind bias (filled contours,  $\text{m s}^{-1}$ ), defined as the model ensemble mean minus ERA-Interim zonal wind, and ERA-Interim 200 hPa zonal wind (black contours) for (a) May, (b) June, (c) July and (d) August. To show the position of the observed jet, only the 0, 10, 20 and 30  $\text{m s}^{-1}$  isotachs have been plotted. The box indicates the relaxation region used.

### 5.3.3 Northwest Europe relaxation

Ding and Wang (2005, 2007) hypothesised that the midlatitude wave train originates in the jet exit region over northwest Europe and subsequently propagates across Europe to west-central Asia. In addition, it can be seen in Figure 5.4 that areas of poor skill (negative correlation) appear over northwest Europe in June, before they appear over west-central Asia. Therefore, to determine whether the errors seen over the D&W region arise as a result of errors propagating from northwest Europe, a second experiment (hereafter “NWEUR\_RELAX”) was carried out where a region in northwest Europe (Figure 5.2) was relaxed.

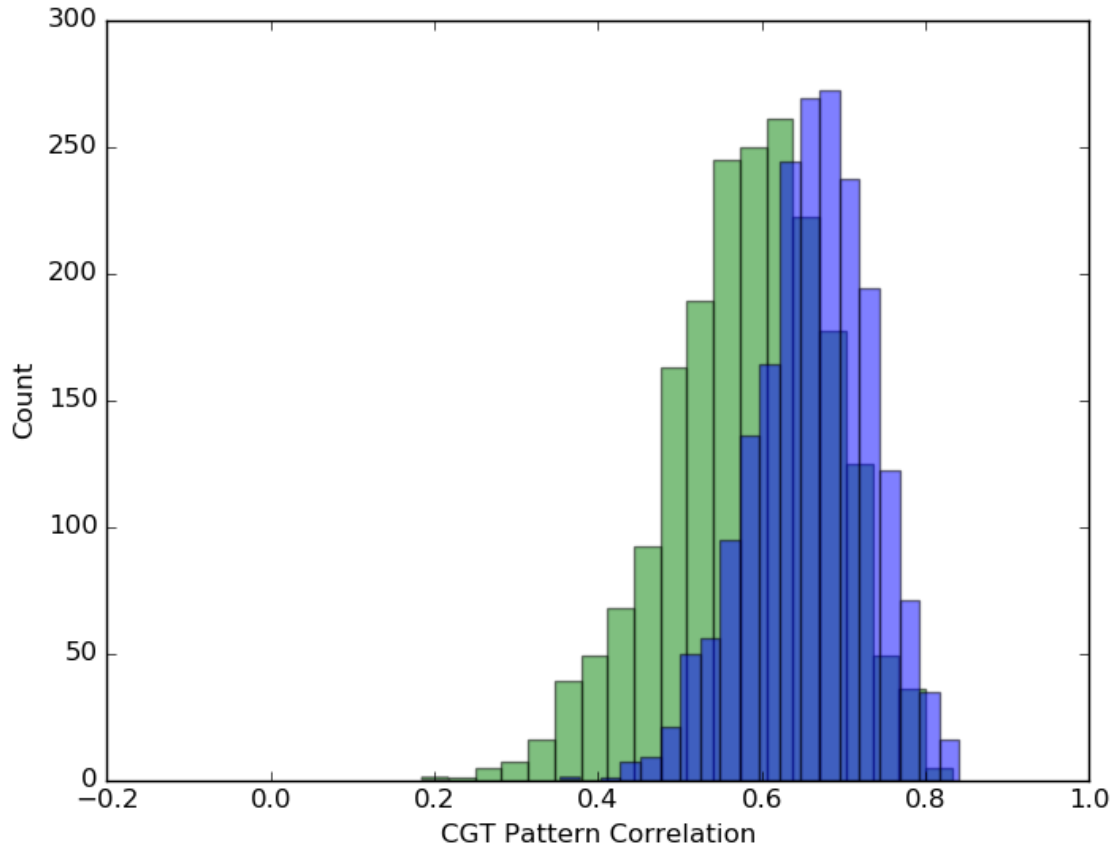
Figure 5.12 shows the difference in ensemble mean 200 hPa geopotential height skill between the new control experiment and NWEUR\_RELAX. As before, this is defined such that a positive value indicates that the skill in the model experiment is higher than in the control, and vice versa. When compared to Figure 5.8, it can be seen that relaxing over northwest Europe results in a more widespread hemispheric improvement in skill than in DW\_RELAX. In NWEUR\_RELAX, improvements in skill are made across much of Eurasia. In particular, the skill in west-central Asia (in the D&W region) is improved, implying that errors from northwest Europe propagate to this region. However, similar to DW\_RELAX, this relaxation has caused a reduction in skill upstream of the relaxation region. In general, the relaxation in NWEUR\_RELAX appears to have resulted in a larger



**Figure 5.12:** NWEUR\_RELAX 200 hPa geopotential height correlation skill minus control 200 hPa geopotential height skill for (a) May (b) June (c) July and (d) August. A positive value indicates that the skill is increased in the relaxation experiment compared to the control. The box indicates the relaxation region used.

improvement in skill across the northern hemisphere than in DW\_RELAX, implying that northwest Europe is a more important region for the generation of errors in the ECMWF model than west-central Asia.

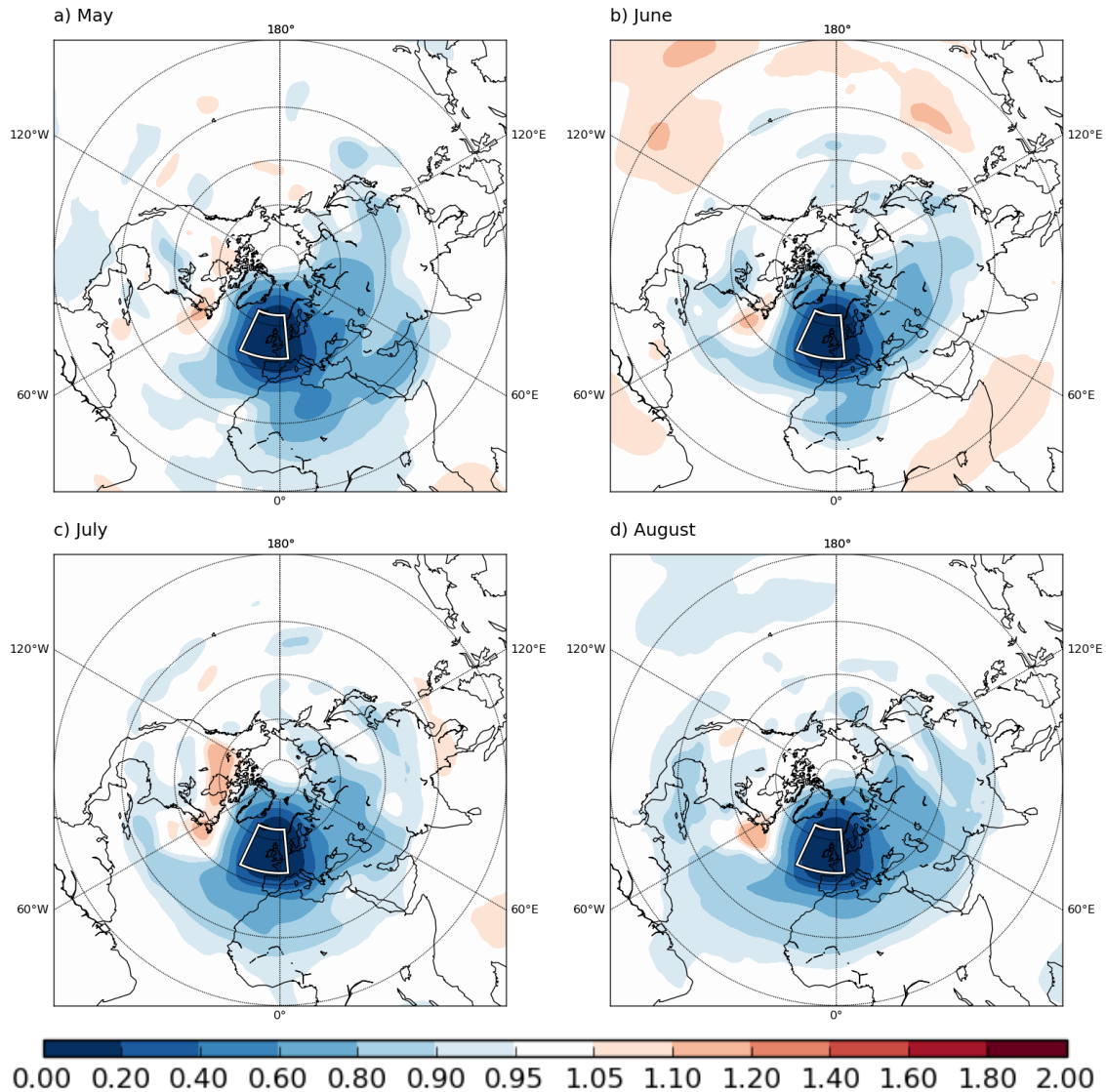
The range of the pattern correlations between the CGT pattern in ERA-Interim and NWEUR\_RELAX is shown in Figure 5.13 as blue bars. Contrary to DW\_RELAX, relaxing over northwest Europe results in an improvement of the representation of the CGT in the model compared to the control, with a median pattern correlation of 0.67. The distribution is also much narrower than in the control (green bars) and DW\_RELAX, indicating that more members have a good pattern correlation, and the range of pattern



**Figure 5.13:** Histograms of the pattern correlations for the control (green) and NWEUR\_RELAX (blue) against the ERA-Interim CGT correlations for August, calculated using 2000 time series created from the 25 ensemble members. The pattern correlations were calculated for all longitudes between  $30^{\circ}$ – $70^{\circ}$ N. The median value for the control is 0.59 and for NWEUR\_RELAX is 0.67.

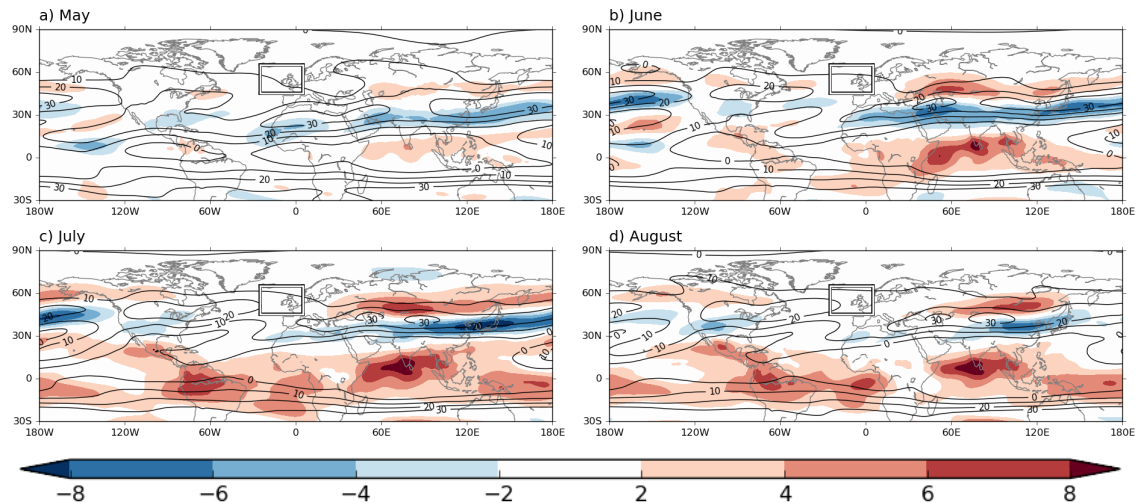
correlations is around 0.35–0.85. The improvements seen in this experiment are largely due to an improvement of the representation of the wave train between northwest Europe and east Asia. Most members in NWEUR\_RELAX have a wave train that closely resembles that seen in ERA-Interim. Histograms of the pattern correlation for both the eastern and western hemispheres separately have also been produced (not shown), and the median value for the eastern hemisphere (0.77) is much greater than that for the western hemisphere (0.46), indicating that the improvement in the CGT in this experiment arises largely from improvements in the eastern hemisphere. This suggests that northwest Europe is more likely to be forcing west-central Asia, rather than the other way round. This wave train was also identified in the composite analysis in Ding and Wang (2007), where a Rossby wave is seen propagating from northwest Europe from eight days before a maximum in the west-central Asian high.

Figure 5.14 is equivalent to Figure 5.9 but for NWEUR\_RELAX. Here, the relax-



**Figure 5.14:** Ratio of standard deviation of 200 hPa geopotential height in the 25 ensemble members in NWEUR\_RELAX compared to the control for (a) May (b) June (c) July and (d) August. A value of less than 1 indicates that the ensemble spread in the experiment is reduced compared to the control, and vice versa. The box indicates the relaxation region used.

ation has resulted in a reduction of the ensemble spread in more parts of the northern hemisphere than in DW\_RELAX. This may in part be due to the relaxation region being slightly larger in NWEUR\_RELAX than in DW\_RELAX, but there are also reductions in spread further downstream from the relaxation region than in Figure 5.9. Focussing on August, these include in several centres of action of the CGT: the spread is reduced in the D&W region and also to a certain extent in the EASIA, NPAC and NAM regions. This further suggests that northwest Europe is more of a driver of northern hemisphere variability than west-central Asia.



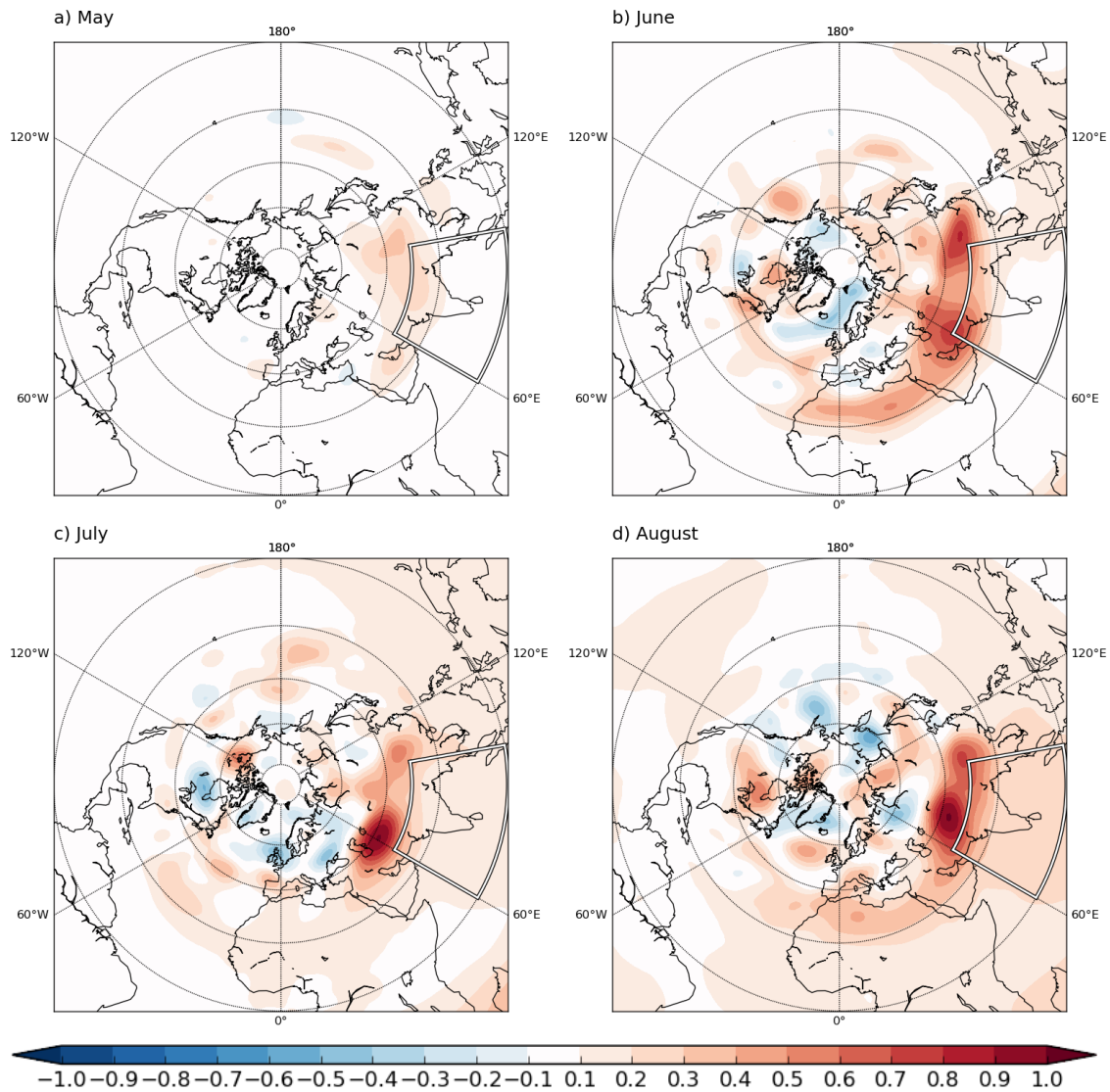
**Figure 5.15:** NWEUR\_RELAX 200 hPa zonal wind bias (filled contours,  $\text{m s}^{-1}$ ), defined as the model ensemble mean minus ERA-Interim zonal wind, and ERA-Interim 200 hPa zonal wind (black contours) for (a) May, (b) June, (c) July and (d) August. To show the position of the observed jet, only the 0, 10, 20 and  $30 \text{ m s}^{-1}$  isotachs have been plotted. The box indicates the relaxation region used.

Figure 5.15 shows the zonal wind bias in NWEUR\_RELAX compared to ERA-Interim. As in DW\_RELAX, jet biases remain throughout much of the northern hemisphere. In August, the Asian jet bias is similar to that in DW\_RELAX, but the biases over the North Pacific and North America (and the North Atlantic, near the relaxation region) have reduced. This may partially explain the greater improvement in model skill seen in these regions compared to DW\_RELAX. Overall, relaxing over northwest Europe has resulted in a reduction in the jet biases compared to the control experiment, particularly in August when the only significant bias is over central and east Asia. This ties in with the improved representation of the CGT that is seen in Figure 5.13, where there is a median pattern correlation of 0.67 of the CGT in NWEUR\_RELAX compared to ERA-Interim.

### 5.3.4 Indian monsoon relaxation

To investigate the impact of errors in the model representation of the ISM on the simulation of the CGT and on extratropical skill, the third relaxation experiment (“ISM\_RELAX”) relaxed in the ISM region to correct the monsoon circulation (Figure 5.3). It was shown in the previous chapter that the link between ISM precipitation and the D&W region is too weak in the model. Therefore, this experiment was designed to try and correct this link in the model. Relaxing in this region also avoids the issues relating to

errors introduced upstream of the relaxation region seen in the previous two experiments as it lies to the south of the midlatitude jet.



**Figure 5.16:** ISM\_RELAX 200 hPa geopotential height correlation skill minus control 200 hPa geopotential height skill for (a) May (b) June (c) July and (d) August. A positive value indicates that the skill is increased in the relaxation experiment compared to the control. The box indicates the relaxation region used.

As for the previous two experiments, Figure 5.16 shows the difference in ensemble mean 200 hPa geopotential height correlation skill between the control experiment and ISM\_RELAX. The changes in the relaxation region in this experiment are smaller compared to the previous relaxation experiments. This is because the overall skill for 200 hPa geopotential height in the tropics tends to be much better than for the extratropics (Figure 5.4), although there are errors in the monsoon circulation in this region in the control (Figure 5.5). Compared to DW\_RELAX and NWEUR\_RELAX, the extratropical improvements in skill are generally more modest. There are some large increases in skill to

the north of the relaxation region, including in the D&W region where there was poor skill in the control experiment. Away from the relaxation region, the patterns of skill change vary from month-to-month. In June, there are some increases in skill over parts of the North Pacific and North America, although these are generally fairly small. The skill over Europe is largely unchanged, apart from some slight reductions in skill, and this is also the case in July, when the reductions in European skill are slightly larger. However, in August, when the observed CGT wave train is strongest, the changes in skill over Europe are almost completely positive, which may suggest that the ISM is a potential source of skill in this month.

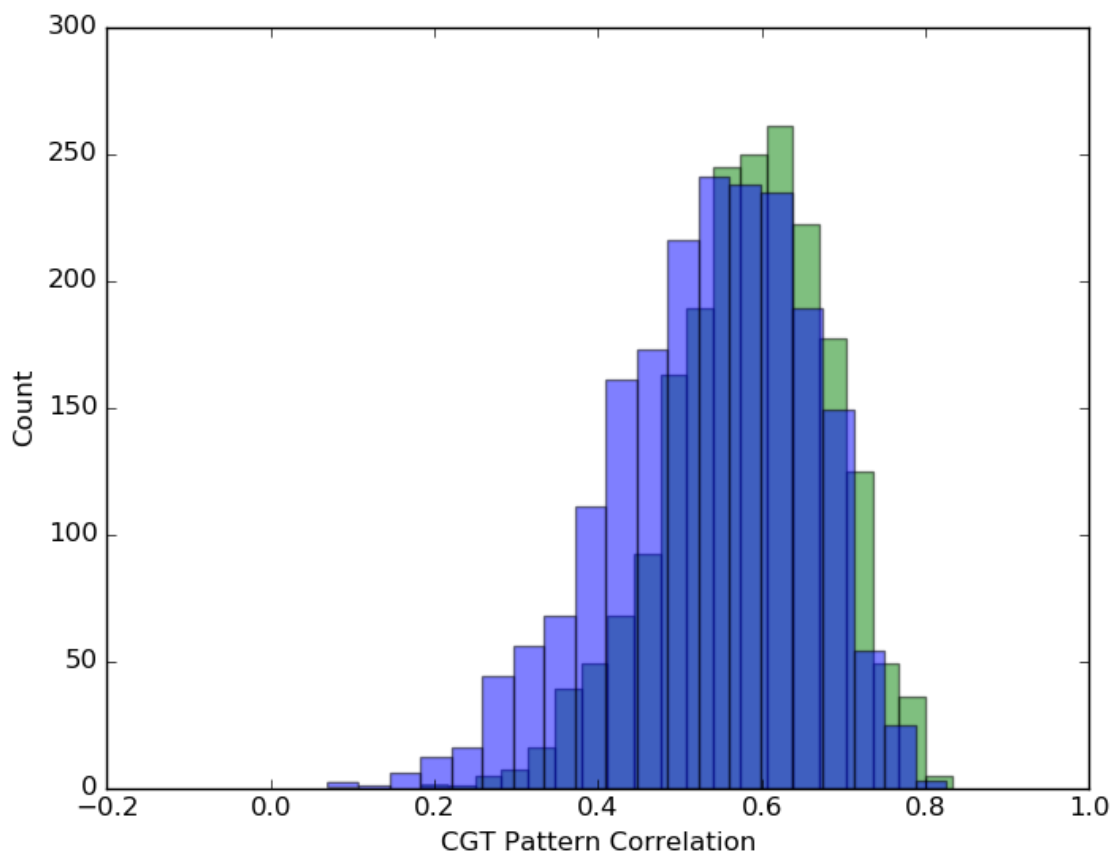


**Figure 5.17:** Histograms of the pattern correlations for the control (green) and ISM\_RELAX (blue) against the ERA-Interim CGT correlations for August, calculated using 2000 time series created from the 25 ensemble members. The pattern correlations were calculated for all longitudes between  $30^{\circ}$ – $70^{\circ}$ N. The median value for the control is 0.59 and for ISM\_RELAX is 0.55.

However, from Figure 5.17, which shows the range of pattern correlations in ISM\_RELAX (blue bars), it can be seen that the representation of the CGT in this experiment is very similar to the control (green bars). The two distributions are very alike, with similar median values (0.55 for ISM\_RELAX and 0.59 for the control), sug-

gesting that the simulation of the CGT has not been improved by correcting the monsoon circulation. This suggests that either the ISM is not a driver of the CGT, or that the pathway that connects the ISM to the CGT has not been improved by the relaxation.

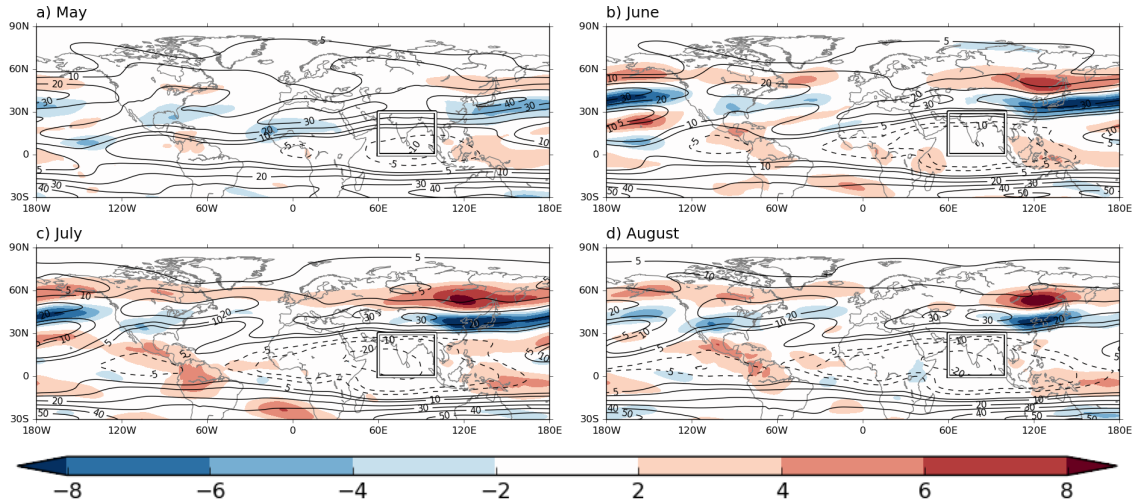


**Figure 5.18:** ISM\_RELAX 200 hPa zonal wind bias (filled contours,  $\text{m s}^{-1}$ ), defined as the model ensemble mean minus ERA-Interim zonal wind, and ERA-Interim 200 hPa zonal wind (black contours) for (a) May, (b) June, (c) July and (d) August. To show the position of the observed jet, only the 0, 10, 20 and 30  $\text{m s}^{-1}$  isotachs have been plotted. The box indicates the relaxation region used.

From Figure 5.18 it can also be seen that the northward shift of the jet stream in the model that was also present in the other experiments is also still prevalent in ISM\_RELAX. The zonal wind biases away from the relaxation region are still largely unchanged compared to the control, which is likely to restrict any improvements in the representation of the CGT in this experiment due to the different Rossby wave propagation characteristics in the model compared to observations.

### 5.3.5 Comparison of relaxation experiments

Having examined each relaxation experiment individually, we now compare them. Figure 5.19 shows the range of the ensemble correlations of the D&W Index against the other centres of action of the CGT, for each relaxation experiment and for the control for August. These correlations were calculated using the 2000 time series created from the 25 ensemble members. The relationship between the D&W and EASIA regions is actually well captured in the control experiment, with the distribution centred almost exactly at the observed correlation value. NWEUR\_RELAX has a similar distribution to the control, but with a slightly smaller ensemble spread. However, relaxing in the ISM

region has had a large negative impact, with a large reduction in the model correlations in this experiment and almost all of the ensemble members with a correlation that is not significant. DW\_RELAX also has a poorer representation than the control, with almost all ensemble members with a correlation that is weaker than is observed.

The relationship between the D&W Index and the NPAC region is poorly represented in the control and all of the relaxation experiments. Almost all members of all experiments have a weaker correlation than in ERA-Interim, and the majority have a correlation that is not significant. The model struggles to represent the NPAC region of the CGT generally, with few members of either the control or the relaxation experiments locating a centre of action in this region. This may be because the jet biases between the EASIA and NPAC regions are among the largest in the northern hemisphere, thus wave propagation between these regions is likely to differ to observations.

The correlation between the D&W Index and NAM region is represented slightly better with respect to observations in the control and NWEUR\_RELAX. Similar to the D&W vs. NPAC correlations, DW\_RELAX and ISM\_RELAX have a poorer representation. As with the NPAC region, the model tends to have more variability in the location and strength of the correlation in the NAM region, and this may be partly due to the NAM region being furthest away from the D&W region. There is therefore more scope for variability in wave propagation from the D&W region, leading to greater spatial differences in the location of the NAM region and a reduced strength of correlation overall.

The correlations for which there is the largest difference between the different relaxation experiments is between the D&W and NWEUR regions. In ERA-Interim there is a strong correlation between these regions (0.63) and this is reasonably well captured in the control experiment, with almost all members with a significant positive correlation, albeit weaker than in ERA-Interim. Relaxing over northwest Europe (NWEUR\_RELAX) results in a very good relationship between these regions, with a small spread and a median ensemble correlation that is almost exactly as in ERA-Interim. This improved relationship is due to a good representation of the wave train between northwest Europe and west-central Asia, with most members capturing this wave train with a high level of accuracy. DW\_RELAX, however, has a very poor representation of these correlations, with the distribution centred around zero. This may be because, when relaxing in west-central Asia, this introduces upstream errors as waves that propagate into this region are forced towards ERA-Interim by the relaxation on a relatively small spatial scale.

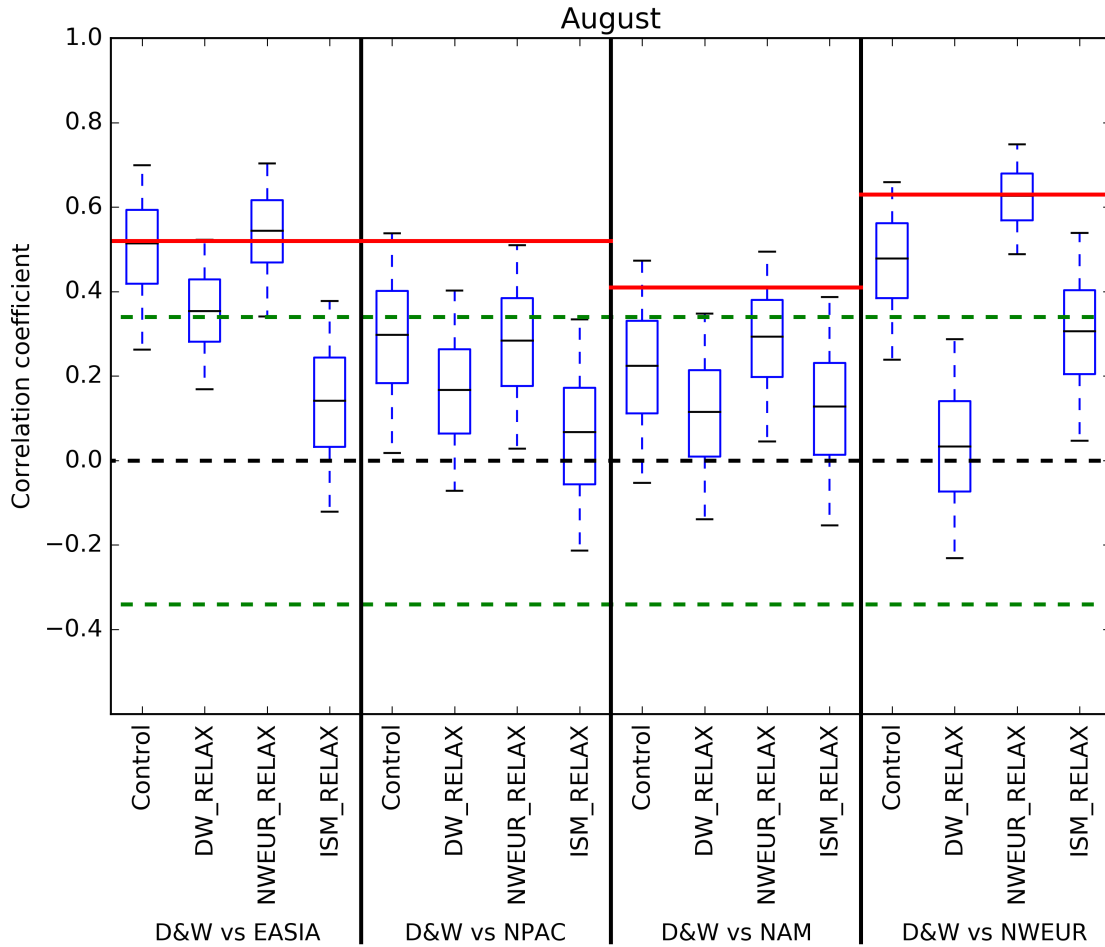


**Figure 5.19:** A comparison of the correlations between the D&W Index and the other centres of action of the CGT for the control and the three relaxation experiments for August, calculated using the 2000 samples. The box plots represent the upper and lower quartiles, and the whiskers extend to the 5<sup>th</sup> and 95<sup>th</sup> percentiles. The black horizontal line represents the median value and the red horizontal lines the observed correlation coefficient from ERA-Interim. 5% significance levels ( $\pm 0.34$ ) are indicated by the green dashed lines.

ISM\_RELAX also has a poor representation of this relationship, with all members with a correlation weaker than is observed, although the correlations are slightly better than for DW\_RELAX.

A common theme between the relaxation experiments for the correlations between the D&W Index and all other centres of action is that DW\_RELAX is poorer than NWEUR\_RELAX and the control. This is perhaps unexpected, given that in DW\_RELAX the D&W Index is the same (or nearly the same) as in ERA-Interim. What this may imply is that the D&W region, while being an important centre of action of the CGT, is not the driver of it, and the improvements to the representation of the CGT seen in

NWEUR\_RELAX suggest that northwest Europe is much more influential. ISM\_RELAX is also poorer than NWEUR\_RELAX and the control for all regions, and given that in this experiment the monsoon circulation has been corrected, this suggests that the either ISM is not a driver of the CGT or that biases in the jet location mean that the RWS is not correctly represented. A further possibility is that a different driver of the CGT, one that is separated from the ISM, is not accurately represented.

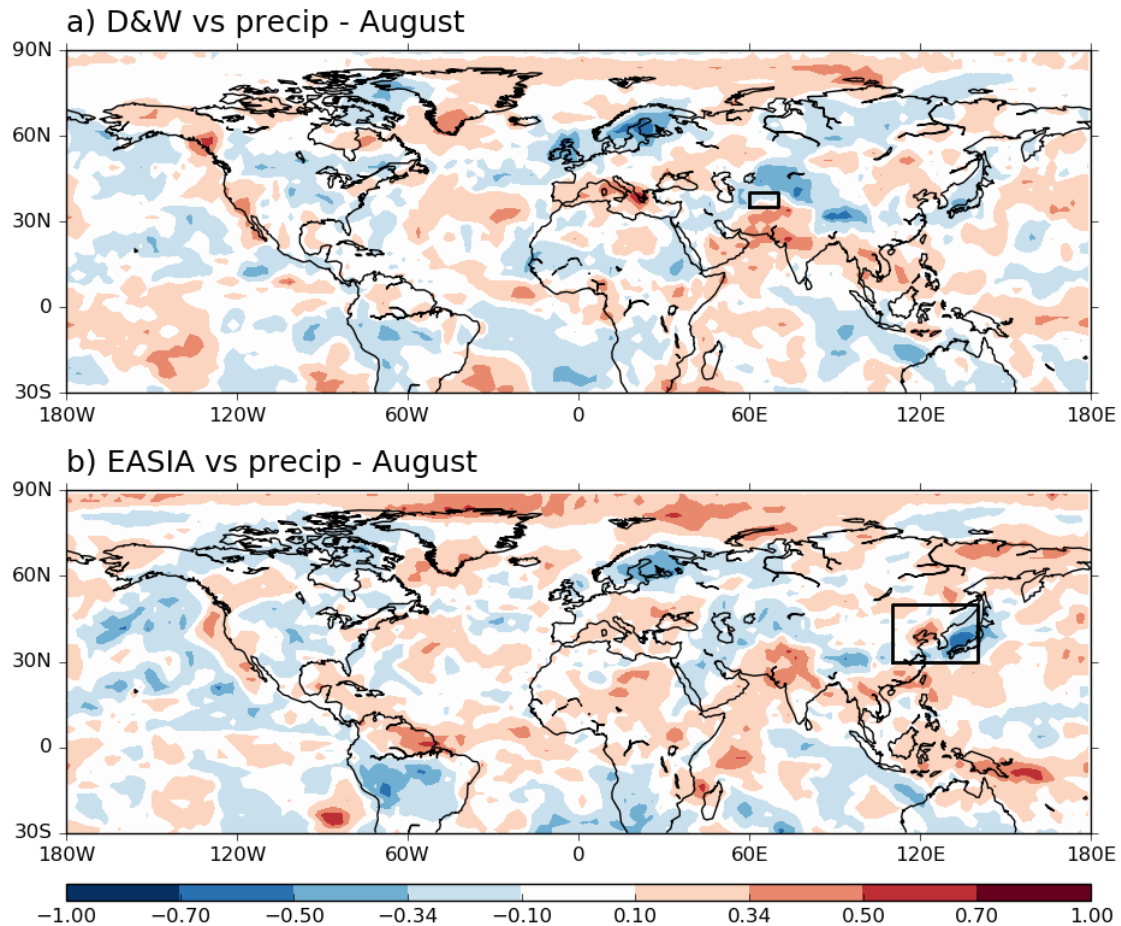


**Figure 5.20:** Correlation between ERA-Interim (a) D&W Index and (b) EASIA Index and GPCP precipitation elsewhere for August. The base points for the correlations are indicated by boxes. Correlation values of  $\pm 0.34$  are significant at the 5% level.

It is perhaps surprising that the correlation between the D&W Index and EASIA region in DW\_RELAX is further from ERA-Interim than in the control and NWEUR\_RELAX, given that the skill of 200 hPa geopotential height in EASIA in DW\_RELAX is increased. A possible explanation for this is that there is an external driver that is forcing both the D&W Index and EASIA independently. By performing the relaxation, the link between the D&W Index and the independent driver is broken, so the correlation in individual members is reduced. However, the mean response in EASIA

to the external driver is still present, hence the improved skill in EASIA but reduced correlation with the D&W Index, as less of the variance of the EASIA region is being explained by the D&W Index.

To identify regions of precipitation which are correlated with both the D&W and EASIA indices, Figure 5.20 shows the correlation between these two indices and GPCP precipitation for August. The main region that stands out as being positively correlated with both indices is across northern parts of India. Therefore, it is possible that the reduction in the correlation between the D&W Index and EASIA in DW\_RELAX compared to the control is due to a weakening of the link between the D&W Index and monsoon precipitation.

To explore this idea further, Figure 5.21 shows the correlation between an Indian summer monsoon heating index (ISMH), defined as the precipitation averaged between 20°–27.5°N, 70°–85°E, and the D&W and EASIA regions. This region was chosen as precipitation here is closely associated with variations of the D&W Index and there is a significant correlation (0.52) between the D&W Index and ISMH in observations, and it is also approximately in the location of positive correlations in Figure 5.20. As hypothesised, the correlations between ISMH and the D&W Index in DW\_RELAX are weaker than in both the control and NWEUR\_RELAX, suggesting that the link between these two regions has been partially broken by relaxing in the D&W region. However, the link between ISMH and the EASIA Index, also shown on Figure 5.21, is improved in DW\_RELAX compared to the control and NWEUR\_RELAX. This means that ISMH is still driving the variations in the EASIA Index in DW\_RELAX, and the relationship is actually closer to the observed relationship, which results in an improvement in geopotential height skill in EASIA in this experiment. However, as the D&W Index explains less of the variance in EASIA, the correlation between the two regions is reduced in DW\_RELAX.

Another thing to note from Figure 5.21 is that the model has a poor representation of the link between the D&W Index and ISMH, with the majority of control members with correlations that are not significant. As explained above, DW\_RELAX has a poorer representation of this correlation, with the upper 95<sup>th</sup> percentile not significant. NWEUR\_RELAX has correlations which are closer to the observed value than the control, but they are still weaker than observations and the majority are still not significant. Another thing to note is that the correction of the monsoon circulation in ISM\_RELAX has not resulted in an improvement in the relationship between ISM precipitation and

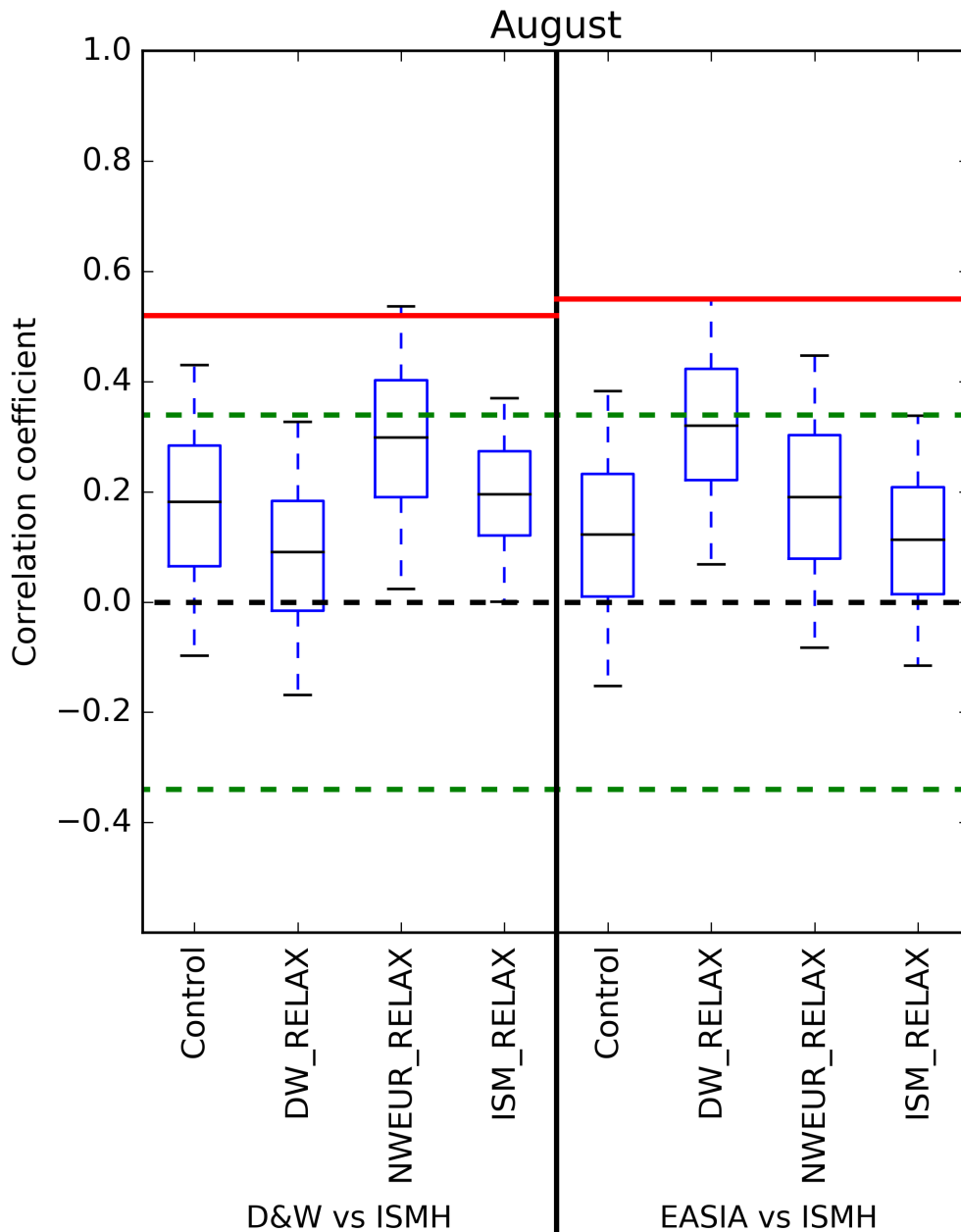


**Figure 5.21:** A comparison of the correlations between the Indian summer monsoon heating (ISMH) and D&W and EASIA regions for the control and the three relaxation experiments for August, calculated using the 2000 samples. The box plots represent the upper and lower quartiles, and the whiskers extend to the 5<sup>th</sup> and 95<sup>th</sup> percentiles. The black horizontal line represents the median value and the red horizontal lines the observed correlation coefficient from ERA-Interim. 5% significance levels ( $\pm 0.34$ ) are indicated by the green dashed lines.

the D&W Index, and although NWEUR\_RELAX has the best representation of the link between monsoon precipitation and the D&W Index, it is still much weaker than observed and this is potentially limiting the skill of the model in simulating the CGT. This provides a motivation for further model experiments, results from which can be found in Chapter

6.

## 5.4 Barotropic model experiments

Analysis of the relaxation experiments in the previous section demonstrated that northwest Europe plays a greater role in influencing model errors in the northern hemisphere. Relaxing in this region also resulted in an improvement in the simulation of the CGT compared to the control, possibly due to a reduction in the jet biases in this experiment. The relaxation experiments also raised the question: Why does forcing in the D&W region not lead to a signal over northwest Europe? It is possible that the CGT could simply be a result of sampling noise in the observations; if the model cannot reproduce it, this could be because the model is wrong, or because the teleconnection to Europe does not really exist. In order to investigate these questions, a number of experiments using a barotropic model were carried out to explore the role of differences in the background state and strength of forcing in the D&W region, results from which are presented in this section.

### 5.4.1 Motivation

It has been hypothesised that heating associated with ISM precipitation plays an important role in the maintenance of the CGT through its influence on the D&W region. It is hypothesised that this interaction occurs as a result of a Rossby-type response to off-equatorial heating associated with the ISM, which modulates the strength of the west-central Asian high (Wu and Wang, 2002). However, as shown in Figure 5.21 in the previous section, the link between monsoon precipitation and the west-central Asia anti-cyclone is not well represented in either the control or the relaxation experiments, with the strength of the correlation between these two regions underestimated in almost all members. Therefore, in order to explore whether the weak representation of the CGT in the ECMWF model is due to a lack of reinforcement of the wave train over Asia, a number of experiments using a barotropic model were carried out.

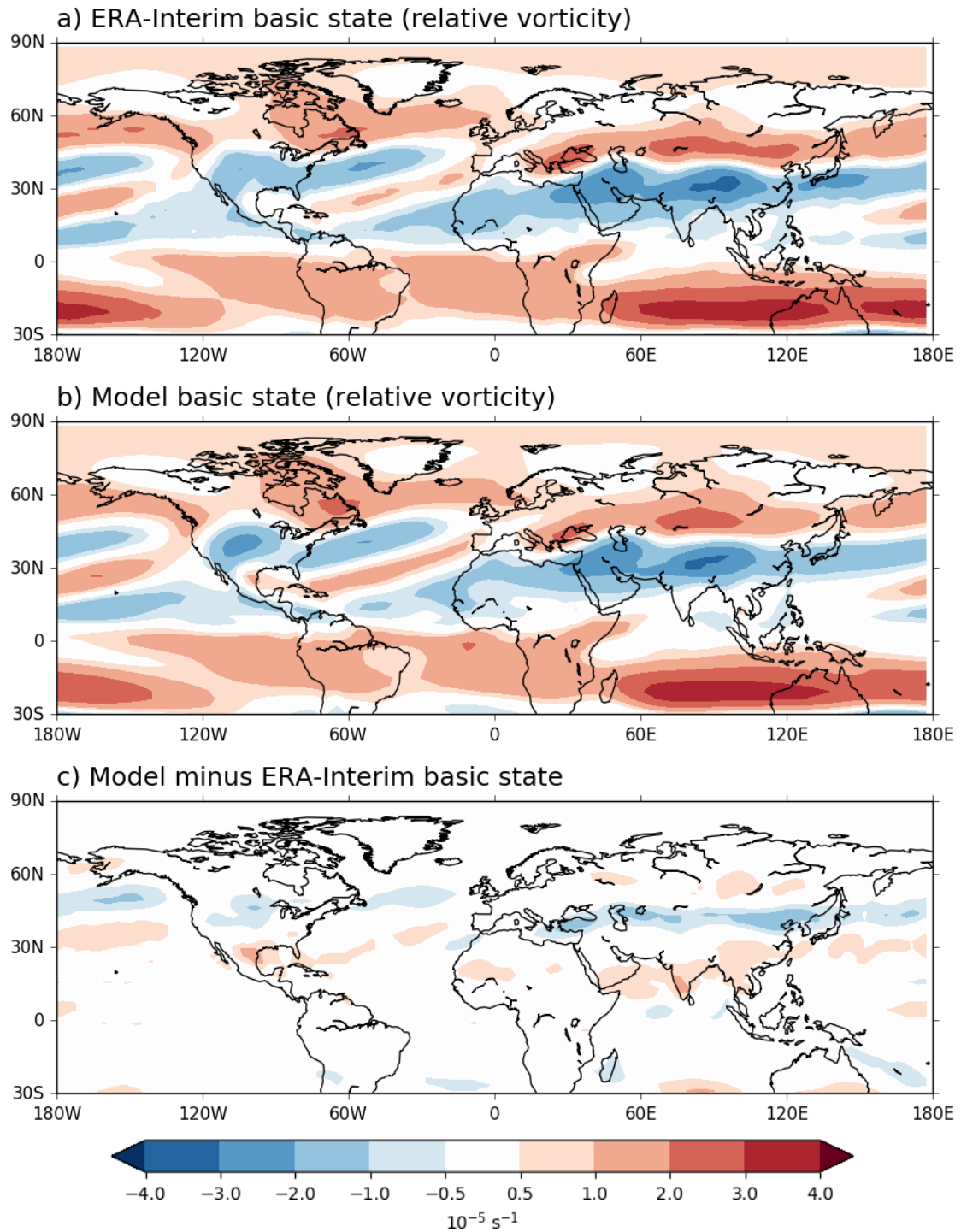


**Figure 5.22:** 200 hPa relative vorticity used as the background state for the barotropic model experiments for (a) ERA-Interim (b) the ECMWF model ensemble mean and (c) the difference between them (ECMWF model minus ERA-Interim).

### 5.4.2 Experimental design

In these experiments, the barotropic model (described in Chapter 3.3.4) was run with two different basic states: one from ERA-Interim and one from the ECMWF model

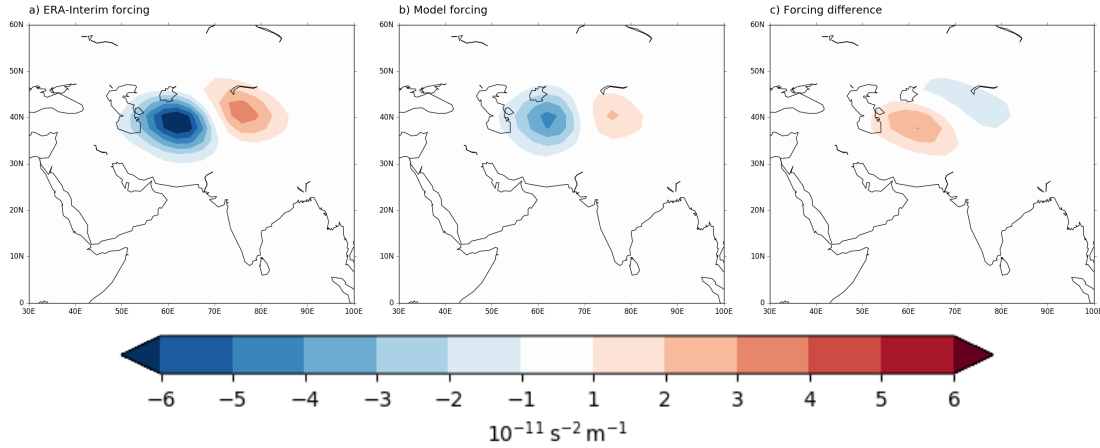


**Figure 5.23:** Forcings used in BT\_DW\_BEFE, BT\_DW\_BMFE, BT\_DW\_BEFM and BT\_DW\_BMFM. This is the regression of the RWS against the D&W Index, per standard deviation of the D&W Index, for (a) ERA-Interim (BT\_DW\_BEFE and BT\_DW\_BMFE) (b) the ECMWF model (BT\_DW\_BEFM and BT\_DW\_BMFM) and (c) the difference between them (ECMWF model minus ERA-Interim).

control experiment used in the previous section. The basic state was taken to be the climatological summer (JJA) relative vorticity field at 200 hPa. The ERA-Interim and ECMWF model background states, and the difference between them, can be seen in Figure 5.22. The upper troposphere was chosen because this is where divergent outflow from tropical heating is strongest and the jet streams along which Rossby waves propagate are not present lower in the atmosphere. The barotropic model is initialised from the basic state and integrated forwards for 50 days. The phase of the response becomes quasi-stationary after around 14 days, but the magnitude of anomalies continues to increase until around Day 35, so the response shown is the average of days 40–50.

The forcing used in these barotropic model experiments is the RWS regressed against the JJA D&W Index, per standard deviation of the D&W Index, for both ERA-Interim and the ECMWF model control experiment. For the ECMWF model basic state and regression, the ensemble mean was used, but experiments run using a single ensemble member also showed very similar results. A Gaussian weighting function is applied to the regression fields so that the barotropic model is only forced in an area near the D&W region. This Gaussian function has latitudinal width of  $\sigma = 10^\circ$  and longitudinal width of  $\sigma = 20^\circ$ , centred at  $40^\circ\text{N}$ ,  $60^\circ\text{E}$ . The two different forcings used, and the difference between them, can be seen in Figure 5.23. The use of two different basic states and two different forcings allows four different experiments to be performed - these are ERA-Interim basic state and forcing (“BT\_DW\_BEFE”), ECMWF model basic state and ERA-

Interim forcing (“BT\_DW\_BMFE”), ERA-Interim basic state and ECMWF model forcing (“BT\_DW\_BEFM”) and ECMWF model basic state and forcing (“BT\_DW\_BMFM”). These four experiments can be compared to examine the effect of changing the basic state but keeping the same forcing, and changing the forcing but keeping the same basic state.

**Table 5.2:** Combination of forcing and basic state used in the barotropic model experiments

		Basic state	
		ERA-Interim	Model
Forcing	ERA-Interim	BT_DW_BEFE	BT_DW_BMFE
	Model	BT_DW_BEFM	BT_DW_BMFM

### 5.4.3 Experimental analysis

The upper two panels in Figure 5.24 show the effect of running the barotropic model with the same forcing (the regression of the D&W Index against the RWS from ERA-Interim) but with different basic states and are the 200 hPa streamfunction anomalies averaged over Days 40–50. It can be seen that forcing in the D&W region does result in a response that bears a close resemblance to the CGT pattern, with centres of positive streamfunction anomaly over west-central Asia, east Asia, North America and northwest Europe, although the North Pacific centre is shifted slightly compared to the observed CGT pattern. It can also be seen that, while there are some amplitude differences between these two experiments, the location of the positive and negative anomalies are very similar. This suggests that when using different basic states, the wave propagation is similar, which implies that errors in the basic state alone are not responsible for the differences between the observed and ECMWF model CGT pattern. However, errors in the basic state could also lead to errors in the RWS, which could mask the influence of errors in the basic state on wave propagation.

Results from two further experiments are shown in the lower two panels in Figure 5.24. In these experiments, the regression forcing is from the ECMWF model ensemble mean. As in BT\_DW\_BEFE and BT\_DW\_BMFE, there is only a slight difference in the

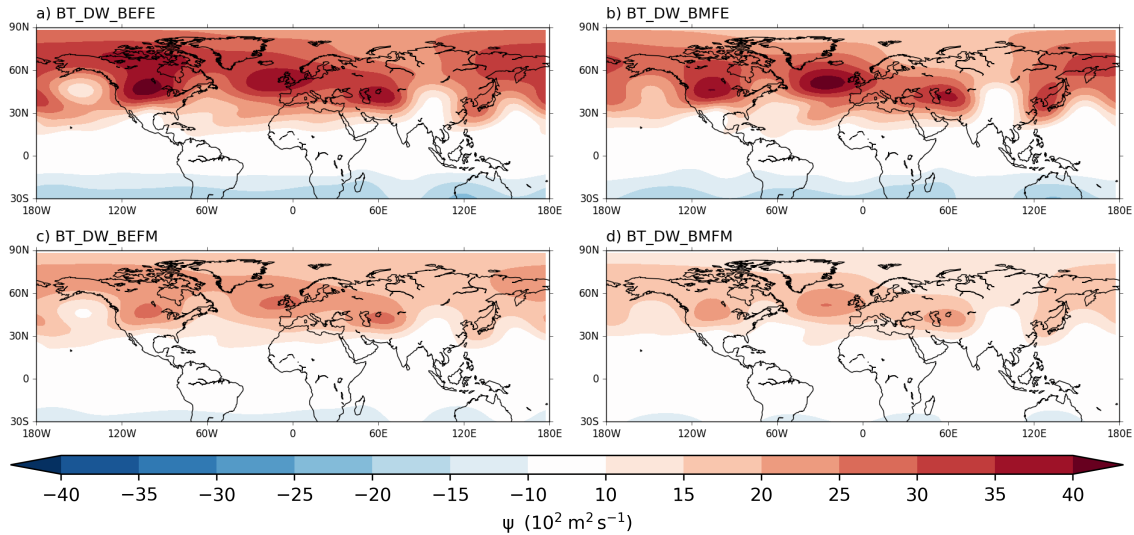


**Figure 5.24:** 200 hPa streamfunction anomaly averaged over days 40–50 in the four barotropic model experiments listed in Table 5.2: (a) BT\_DW\_BEFE (ERA-Interim basic state and forcing) (b) BT\_DW\_BMFE (ECMWF model basic state and ERA-Interim forcing) (c) BT\_DW\_BEFM (ERA-Interim basic state and ECMWF model forcing) (d) BT\_DW\_BMFM (ECMWF model basic state and forcing).

magnitude of the streamfunction anomalies between the two experiments, with no noticeable phase or wavenumber difference. However, when comparing BT\_DW\_BEFE & BT\_DW\_BEFM (Figures 5.24a and 5.24c) and BT\_DW\_BMFE & BT\_DW\_BMFM (Figures 5.24b and 5.24d), which have the same basic state but different forcings, a noticeable difference in the magnitude of the anomalies can be seen, although there is still no appreciable difference in either wavenumber or phase of the response. The forcing from ERA-Interim has greater magnitude than the ECMWF model forcing (Figure 5.23), so this suggests that a stronger response occurs when there is a stronger forcing. These results suggest that differences between the ECMWF model and observed CGT patterns can't be explained by errors in the basic state, but might be explained by differences in the strength of the forcing.

To demonstrate how the anomalies in these experiments develop over time, Figure 5.25 shows the evolution of the streamfunction anomalies in BT\_DW\_BEFE every day from Days 1–10, then every other day up to Day 18. There are both eastward- and westward-propagating components, with the positive anomalies over east Asia and the North Pacific associated with the eastward-propagating waves, while the response over Europe develops via the westward-propagating signal. Where these waves meet over North America there is another area of positive anomalies, although it is unclear whether these anomalies occur as a result of the eastward- or westward-propagating waves.

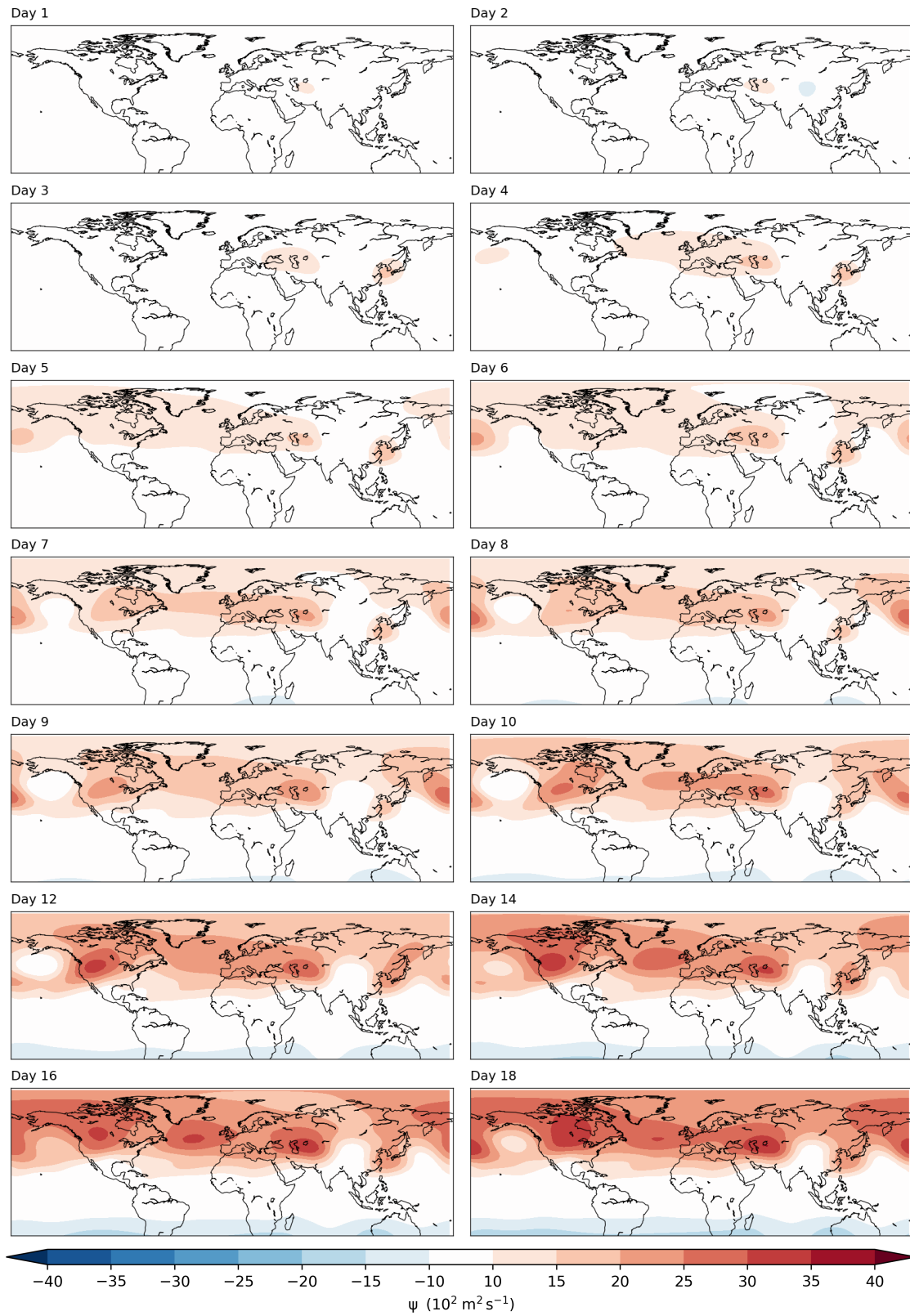


**Figure 5.25:** Evolution of the 200 hPa streamfunction anomalies in BT\_DW\_BEFE (ERA-Interim basic state and forcing) for Days 1–10, then Days 12, 14, 16 and 18.

The results from these experiments motivate the work in the next chapter, which explores whether the weaker than observed representation of the CGT in the ECMWF model is as a result of a weak forcing, through carrying out further experiments in the IFS in which an idealised thermal forcing is applied.

## 5.5 Summary and conclusions

In this chapter, analysis of three relaxation experiments was presented. These experiments were designed to explore different aspects of the CGT and the relationship between hemispheric errors in 200 hPa geopotential height and a weak representation of the CGT in the ECMWF model. It was shown in Chapter 4 (Figure 4.1), and in Figure 5.4, that errors in 200 hPa geopotential height develop in several of the centres of action of the CGT, including in the D&W region, which is used as the base point for the calculation of the CGT correlations. With this in mind, the first relaxation experiment (DW\_RELAX) relaxed in a region centred near the D&W region (Figure 5.1) to explore whether correcting the circulation in this region resulted in an improved representation of the CGT and what the impact was on errors elsewhere in the northern hemisphere, particularly over Europe.

In DW\_RELAX, improvements in skill away from the relaxation region were limited largely to central and east Asia. Some improvements were also seen over the North Pacific and North America, but these were smaller in magnitude. Of particular note in this experiment was that the changes seen over Europe were either neutral or negative, particularly in June and July when some regions saw a change in the correlation of  $-0.5$  or greater. This is likely to be in part due to the imbalance between forced waves leaving the relaxation region eastwards and unforced waves entering it from the west. However, this also suggests that the errors over Europe are not dependent on errors over west-central Asia.

The representation of the CGT in DW\_RELAX is poorer than in the control experiment. The median pattern correlation of the CGT in August compared to ERA-Interim between  $30^{\circ}$ – $70^{\circ}$ N is 0.35, compared to a value of 0.59 in the control. Therefore, correcting the circulation in the D&W region does not improve the representation of the CGT in the model which may suggest that the CGT is not forced from the D&W region.

However, northward jet biases that are seen in the control experiment are still present in DW\_RELAX, which may affect the propagation of Rossby waves in this experiment and thus the ability of the model to accurately represent the CGT.

It was shown in Figure 5.4 that errors in 200 hPa geopotential height skill develop over northwest Europe before west-central Asia, so NWEUR\_RELAX involved relaxing the circulation over northwest Europe (Figure 5.2) towards ERA-Interim to determine the role of these errors in the subsequent development of errors elsewhere in the northern hemisphere.

Compared to DW\_RELAX, relaxing over northwest Europe resulted in a larger area of improved skill, with most of Eurasia seeing an increase. The reduction of skill upstream of the relaxation region, as seen in DW\_RELAX, is also present in this experiment, although only in August. The distribution of CGT pattern correlations in NWEUR\_RELAX is narrower than both DW\_RELAX and the control, and the median value increased to 0.67. This is largely due to an improved representation of the Europe–Asia portion of the wave train, with most members accurately simulating this. This is illustrated in the comparison of the correlation between the D&W Index and the other centres of action of the CGT in Figure 5.19. This shows a large difference between the ensemble correlations in DW\_RELAX and NWEUR\_RELAX for the D&W Index vs. NWEUR region, with DW\_RELAX performing much more poorly than both the control and NWEUR\_RELAX. Also illustrated in Figure 5.19 is that the correlations in DW\_RELAX are further away from the ERA-Interim value than both the control and NWEUR\_RELAX for all regions. In the case of the EASIA region, it is hypothesised that the relaxation in the D&W region resulted in a weakening of the link between the D&W Index and monsoon precipitation, but an improvement in the relationship between monsoon precipitation and EASIA. This means that less of the variance of the EASIA region is explained by the D&W Index, and so the correlation between the two regions is reduced, whereas the geopotential height skill in EASIA is improved.

To investigate the impact of errors in the representation of the ISM on the CGT and on extratropical forecast skill, the third relaxation experiment relaxed the monsoon circulation towards observations. Generally, improvements in skill away from the relaxation region are small, and only in August are there any positive skill changes over Europe. The representation of the CGT in this experiment is very similar to the control, which suggests that either the ISM is not a driver of the CGT or that the link between ISM

precipitation and the CGT is not well captured. Indeed, it was found that the link between ISM precipitation and the D&W Index is poorly captured in the control and all relaxation experiments. Very few members in any of the relaxation experiments capture the significant correlation between these regions, and this may mean that the CGT wave train is not being correctly reinforced by monsoon precipitation, as hypothesised by Ding and Wang (2007), which may impact on its subsequent downstream propagation.

Results from barotropic model experiments when forcing in the D&W region show a response that is similar in appearance to the CGT, with centres of positive streamfunction anomalies located near the CGT centres of action. These experiments also suggest that differences in the basic state have less of an influence on the representation of the CGT in the ECMWF model than the strength of the forcing. Differences in the basic state have little impact on the phase and wavenumber of the response, whereas when the barotropic model is forced with a stronger forcing, the response is also stronger. The development of the response is also different to what may be expected for the CGT, with the anomalies over Europe seeming to develop through a westward mechanism. These results provide a motivation for further experiments in the IFS which are the subject of the next chapter.

## Chapter 6:

# Using thermal forcing experiments to explore the role of the Indian monsoon in driving the extratropical circulation

## 6.1 Introduction

In Chapter 5, the ECMWF model was relaxed to observations in several regions to see whether correcting the model in certain key regions improves the model representation of the CGT. This was generally not the case, and results from barotropic model experiments also shown in Chapter 5, which were run using combinations of the background state and forcing from ERA-Interim and the ECMWF model, suggested that differences in the CGT pattern are more likely to arise as a result of differences in the strength of the forcing rather than the basic state. It was also found in Chapter 4 that the ECMWF model has a weak connection between ISM rainfall and the D&W region, and this was not improved in the relaxation experiments in Chapter 5, suggesting that the D&W region is more forced by Rossby waves propagating from northwest Europe. Based on these results, a set of further experiments in the ECMWF model were carried out in which a thermal forcing was applied in the ISM region to explore the northern hemispheric response to heating associated with the ISM. These were designed to further address questions 2 and 3 posed

in Chapter 1, as well as:

- What impact does heating associated with the ISM have on the extratropical circulation?

In this chapter, results from these thermal forcing experiments are shown. The design of these experiments, including how the heating region was selected, is given in Section 6.2.1, and results of these experiments are given in Section 6.2.2. Based on these results, further experiments in the barotropic model were carried out, which are presented in Section 6.3. Finally, a discussion of the overall results and main conclusions from this chapter is given in Section 6.4.

## **6.2 Thermal forcing experiments**

### **6.2.1 Experimental design**

In order to test the response of the model to heating in the monsoon region, a set of thermal forcing experiments was carried out. We already know that the relationship between ISM heating and the D&W region in the model is too weak compared to observations, so it is worth noting that we may not expect the model CGT to respond to the applied heating in the same way as it would in the real world. Nevertheless, these experiments can still be used to provide insight into the relationship between monsoon heating and the extratropical circulation in the model.

In these experiments, a heating in the form of an extra temperature tendency is applied at each model time step. As with the experiments carried out in Chapter 5, the model is run from the beginning of May, but the heating is only applied from the 1<sup>st</sup> July onwards, until the end of the model run at the end of August. Each experiment has five ensemble members.

In order to find the most suitable region to apply the heating to, the regression of August global precipitation against the D&W Index was calculated to determine which regions of tropical precipitation (particularly in the vicinity of the ISM) are most closely associated with variations of the D&W Index. This is shown in Figure 6.1, which shows

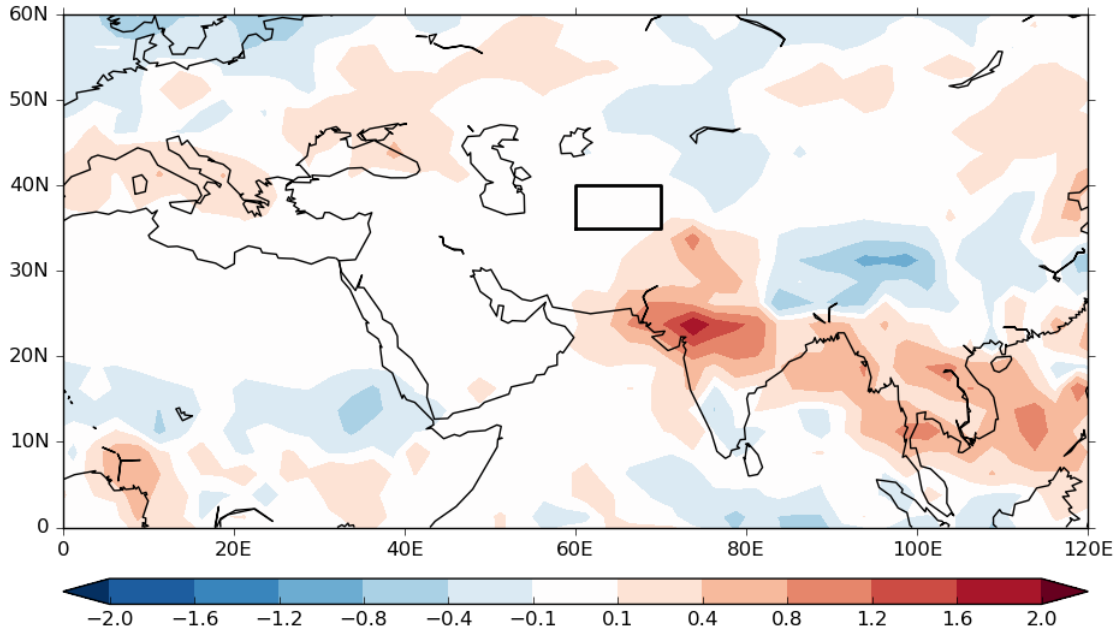


**Figure 6.1:** Regression of global precipitation ( $\text{mm day}^{-1}$ ) against the D&W Index (200 hPa geopotential height, box) for August for ERA-Interim/GPCP precipitation, per standard deviation of the D&W Index (32.9 m).

that the strongest regression is located over northwest India, indicating that precipitation in this region has a close relationship with variations of geopotential height in the D&W region. This is in agreement with other studies which have shown that ISM precipitation is associated with an anticyclonic anomaly over west-central Asia (e.g. Wang et al., 2001; Wu and Wang, 2002).

To further explore the relationship between heating in this region and the circulation

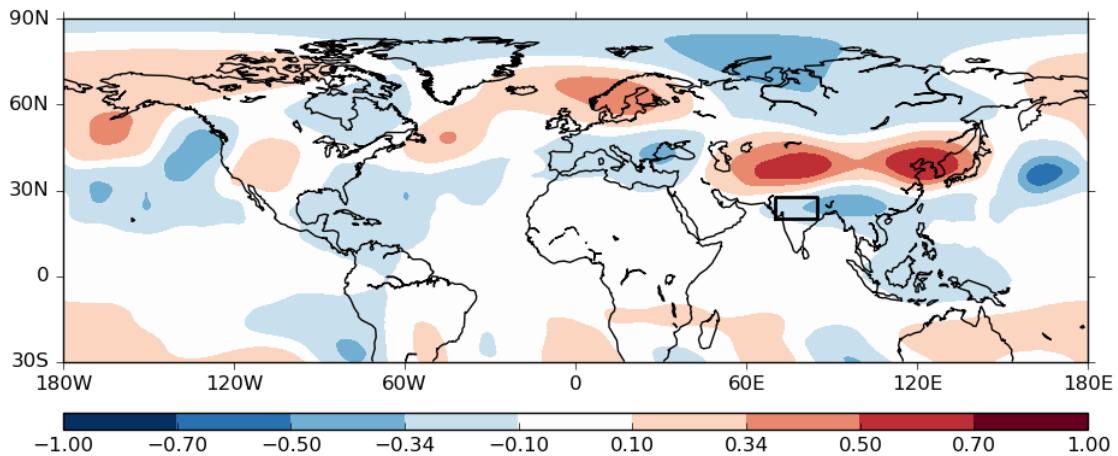


**Figure 6.2:** Correlation between GPCP precipitation in northern India ( $20^{\circ}$ – $27.5^{\circ}$ N,  $70^{\circ}$ – $85^{\circ}$ E, box) and ERA-Interim 200 hPa geopotential height elsewhere for August. Correlation values of  $\pm 0.34$  are significant at the 5% level.

elsewhere in the northern hemisphere, the correlation between precipitation in a box centred over the area of strong regression seen in Figure 6.1 ( $20^{\circ}$ – $27.5^{\circ}$ N,  $70^{\circ}$ – $85^{\circ}$ E, the same region (ISMH) as used in Figure 5.21) and 200 hPa geopotential height was calculated and is shown in Figure 6.2. The pattern of the correlations (and also the equivalent regression, not shown) looks very similar to the August CGT pattern (Figure 4.2d), which suggests that precipitation (and therefore heating) in this region is strongly related to the strength of the CGT. Therefore, this region was chosen as the location in which to apply the thermal forcing in the ECMWF model.

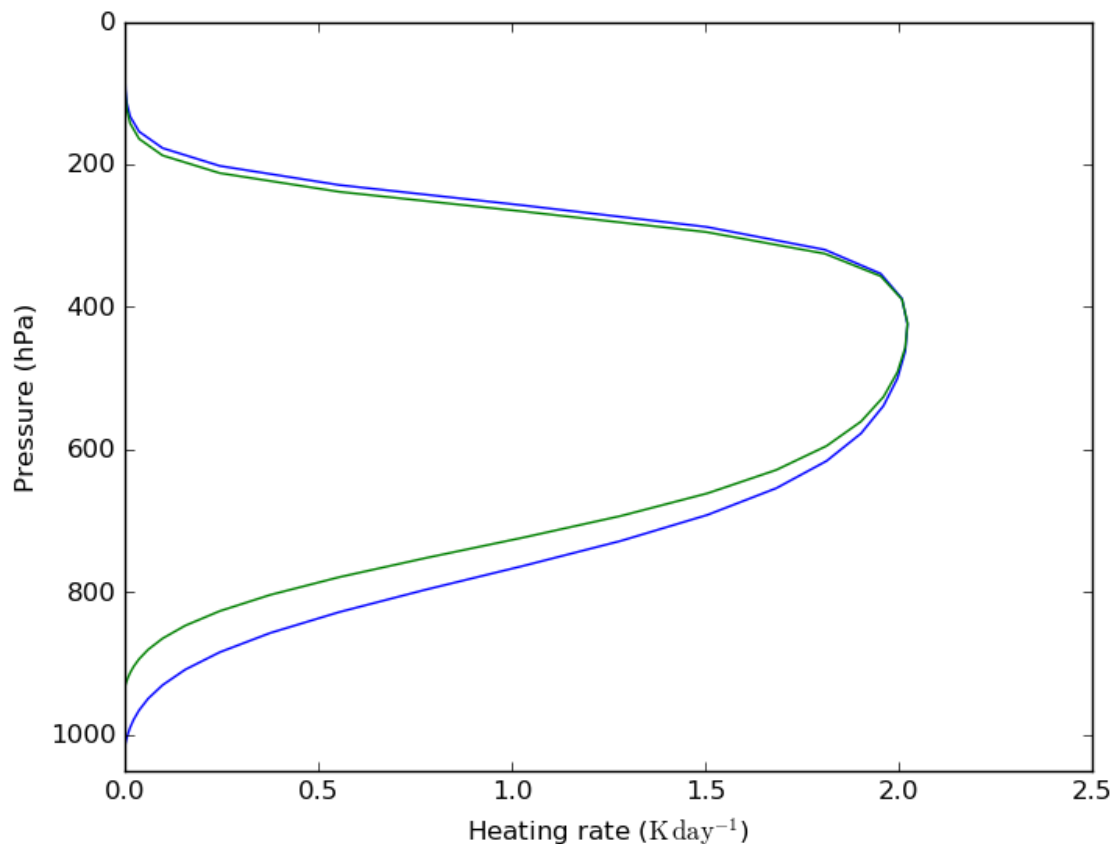


**Figure 6.3:** Vertical heating profile used in the thermal forcing experiments - for a surface pressure of 1012 hPa (blue line) and 930 hPa (green line).

In the thermal forcing experiments, the horizontal structure of the heating which is applied is given by a Gaussian function which is set to zero outside a certain region. The imposed heating has a vertical structure similar to a “typical” tropical convective heating profile, such as those shown in Figure 3 of Schumacher et al. (2004) or Figure 6 of Li et al. (2009). It increases fairly steadily to a peak at around 400 hPa, before dropping away sharply near the tropopause (Figure 6.3). The blue line on Figure 6.3 is the profile for a surface pressure of 1012 hPa, however, the surface orography means that in most of the heating region the surface pressure is less than 1012 hPa (Figure 6.4). The green line

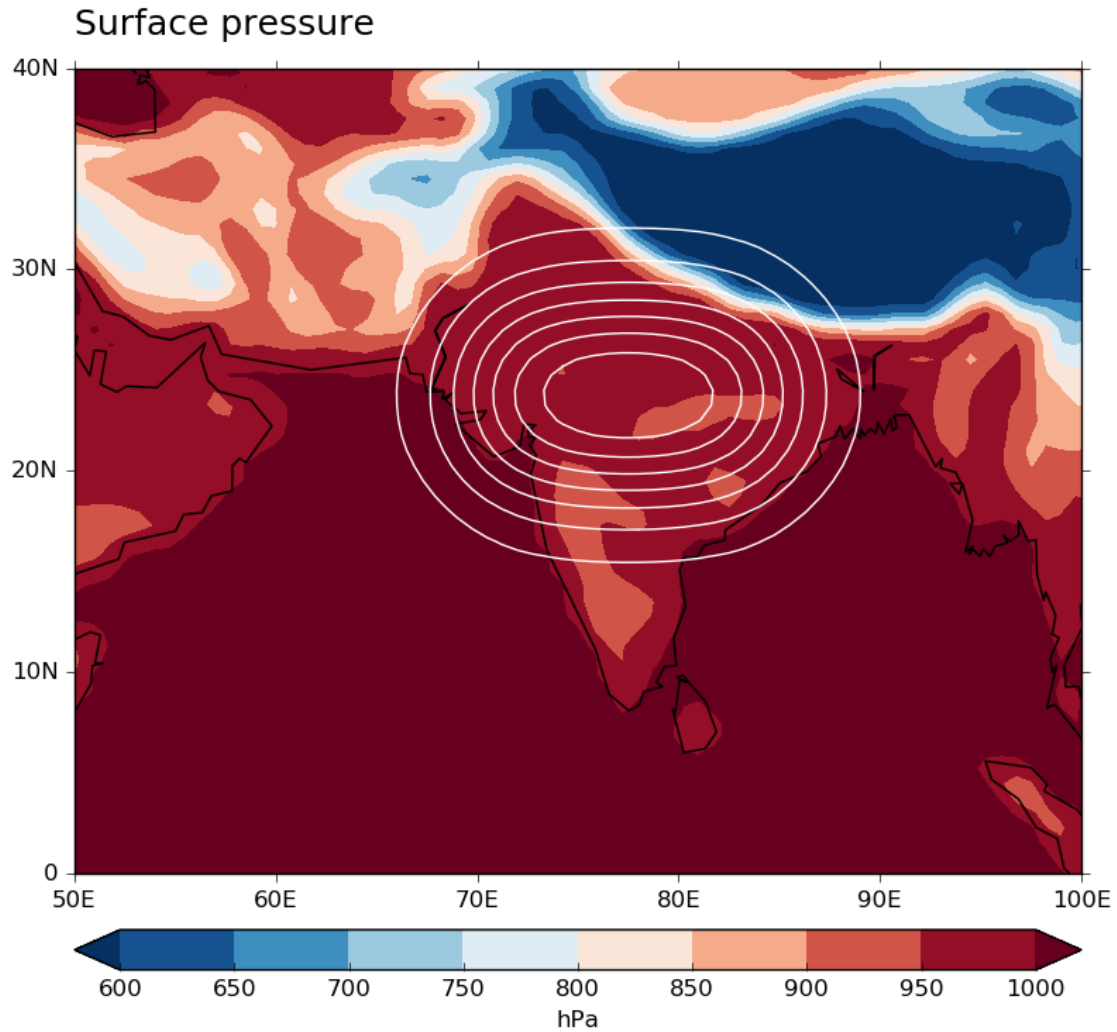


**Figure 6.4:** Surface pressure (orography) - the solid white contours indicate the location of the imposed heating, with contours every  $15 \text{ W m}^{-2}$  from  $15 \text{ W m}^{-2}$  at the edge of the heating region to  $105 \text{ W m}^{-2}$  at the centre.

on Figure 6.3 is the vertical profile calculated for a surface pressure of 930 hPa. In this case, the heating is concentrated slightly higher in the atmosphere due to the adjustment of the model levels to account for the surface orography. In most of the heating region the surface pressure is 950 hPa or greater (Figure 6.4) and it is only at the edges of the heating region where the surface pressure drops significantly below 950 hPa, so the impact of the orography on the heating profile is assumed to be small. Further details about the thermal forcing technique can be found in Chapter 3.3.3.

In these experiments we look at the impact of applying both a positive and a negative heating over the ISM region. The amount of heat added in the heating region was specified to have a peak value which is equivalent to approximately  $4 \text{ mm day}^{-1}$  of extra precipitation in the positive heating experiment, and vice versa in the negative heating

experiment. This corresponds approximately to a two standard deviation change in the D&W Index (Figure 6.1), and equates to a peak thermal forcing of  $\pm 2.02 \text{ K day}^{-1}$ .

Figure 6.5 shows the column integrated heating associated with the thermal forcing ( $Q$ ). This was calculated using:

$$Q = \frac{c_p}{g} \sum H(p) \Delta p, \quad (6.1)$$

where  $c_p$  is the specific heat capacity of dry air at constant pressure ( $1004 \text{ J kg}^{-1} \text{ K}^{-1}$ ),  $g$  is the acceleration due to gravity,  $\Delta p$  is the pressure difference between model levels and

$$H(p) = H_r \eta. \quad (6.2)$$

Here,  $H_r$  is the heating rate ( $0.08 \text{ K h}^{-1}$ ) and  $\eta$  is a function of the horizontal and vertical components of the heating profile. It can be seen that the column integrated heating which is applied in the positive thermal forcing experiment is equivalent to a peak of around  $120 \text{ W m}^{-2}$  of latent heating (Figure 6.5). However, in addition to this heating, we also have to consider increases or decreases in precipitation which arise in response to the imposed heating. The latent heating associated with precipitation (“precipitation flux equivalent”, PFE) was calculated using:

$$PFE = \rho_{\text{water}} L P, \quad (6.3)$$

where  $\rho_{\text{water}}$  is the density of water ( $1000 \text{ kg m}^{-3}$ ),  $L$  is the latent heat of evaporation for water ( $2.501 \times 10^6 \text{ J kg}^{-1}$ ) and  $P$  is the precipitation rate in  $\text{m s}^{-1}$ . The total heating in the thermal forcing experiments is therefore calculated as the sum of  $Q$  and  $PFE$ , and in the control is equal to  $PFE$ .

### 6.2.2 Experimental analysis

The effect of the thermal forcing on monsoon precipitation with respect to the control experiment is shown in Figure 6.6. In the positive heating experiment (Figures 6.6a and

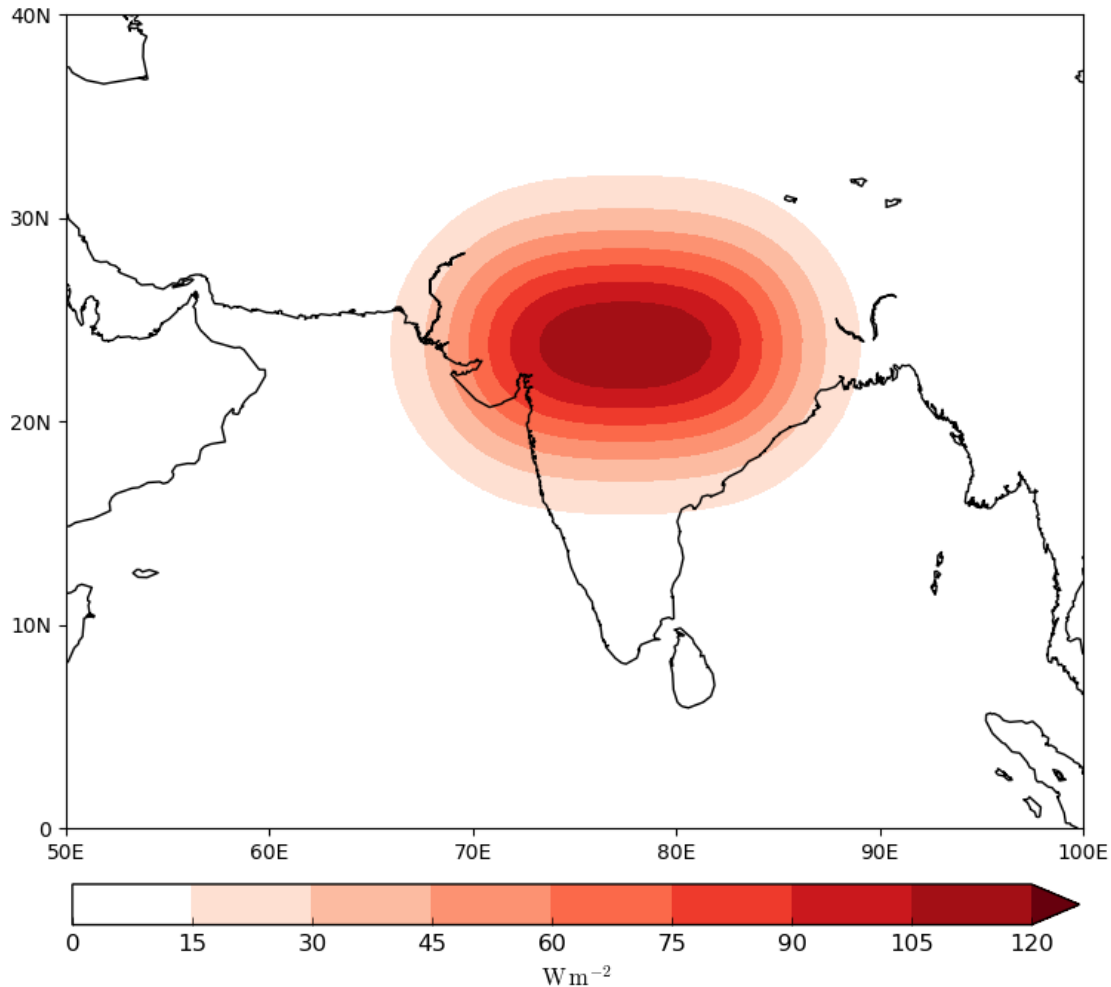


**Figure 6.5:** Column integrated heating applied in the positive heating experiment. The heating for the negative heating experiment is the same, but with the opposite sign.

6.6b) the heating has resulted in an increase in precipitation over northwest India, while there is a reduction in precipitation further south, especially over the Western Ghats. The largest reduction in precipitation in the negative heating experiment is situated slightly further east, over central northern India (Figures 6.6c and 6.6d). Also shown in Figure 6.6 are the 850 hPa winds in each of the thermal forcing experiments, and the increase in precipitation in the positive heating experiment can be seen to be associated with an extension of the monsoon circulation further north, with stronger winds in this region bringing increased moisture.

The combined effect of the imposed thermal forcing in Figure 6.5 and the precipitation changes in Figure 6.6 on the overall differences in heating in the thermal forcing experiments are shown in Figure 6.7. These were calculated using Equations 6.1 and 6.3 and are with respect to the control experiment.

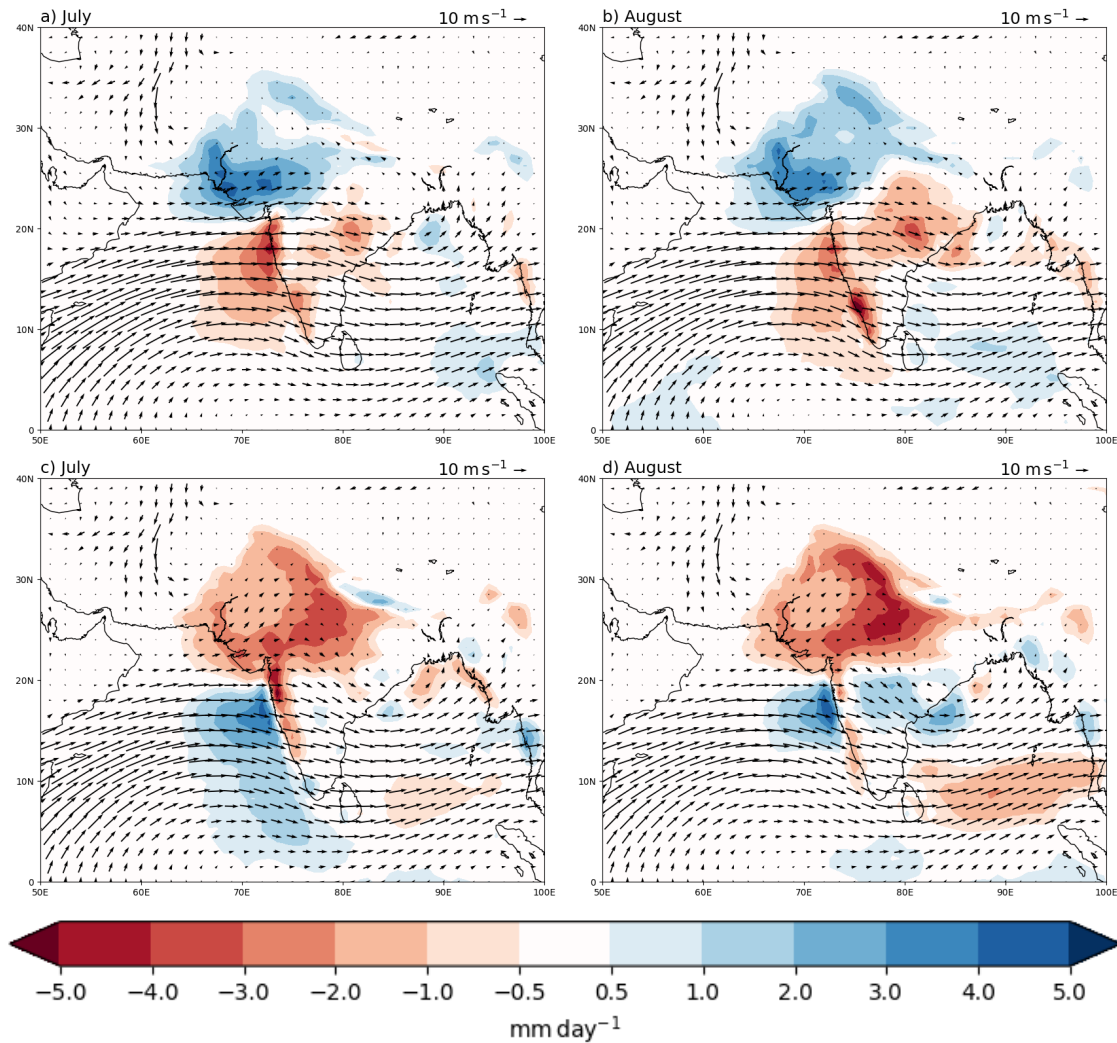


**Figure 6.6:** Ensemble mean precipitation difference ( $\text{mm day}^{-1}$ ) for the positive heating experiment minus the control for (a) July and (b) August, and for the negative heating experiment minus the control for (c) July and (d) August, averaged over all years. The wind barbs show the absolute 850 hPa wind for (a) and (b) the positive heating experiment and (c) and (d) the negative heating experiment.

From Figures 6.7a and 6.7b it can be seen that the maximum increase in heating in the positive heating experiment is centred slightly to the west of the region in which the heating was imposed. This is in the region of the largest increases in precipitation seen in Figure 6.6. This precipitation increase is in a similar location to the region of observed positive regression of precipitation against the D&W Index in Figure 6.1. The increase is also accompanied by a slight decrease in heating further south, over central parts of India and the Western Ghats, associated with the reduction in precipitation in these areas.

The heating differences seen in the negative heating experiment (Figures 6.7c and 6.7d) are slightly stronger in magnitude than for the positive heating experiment. They

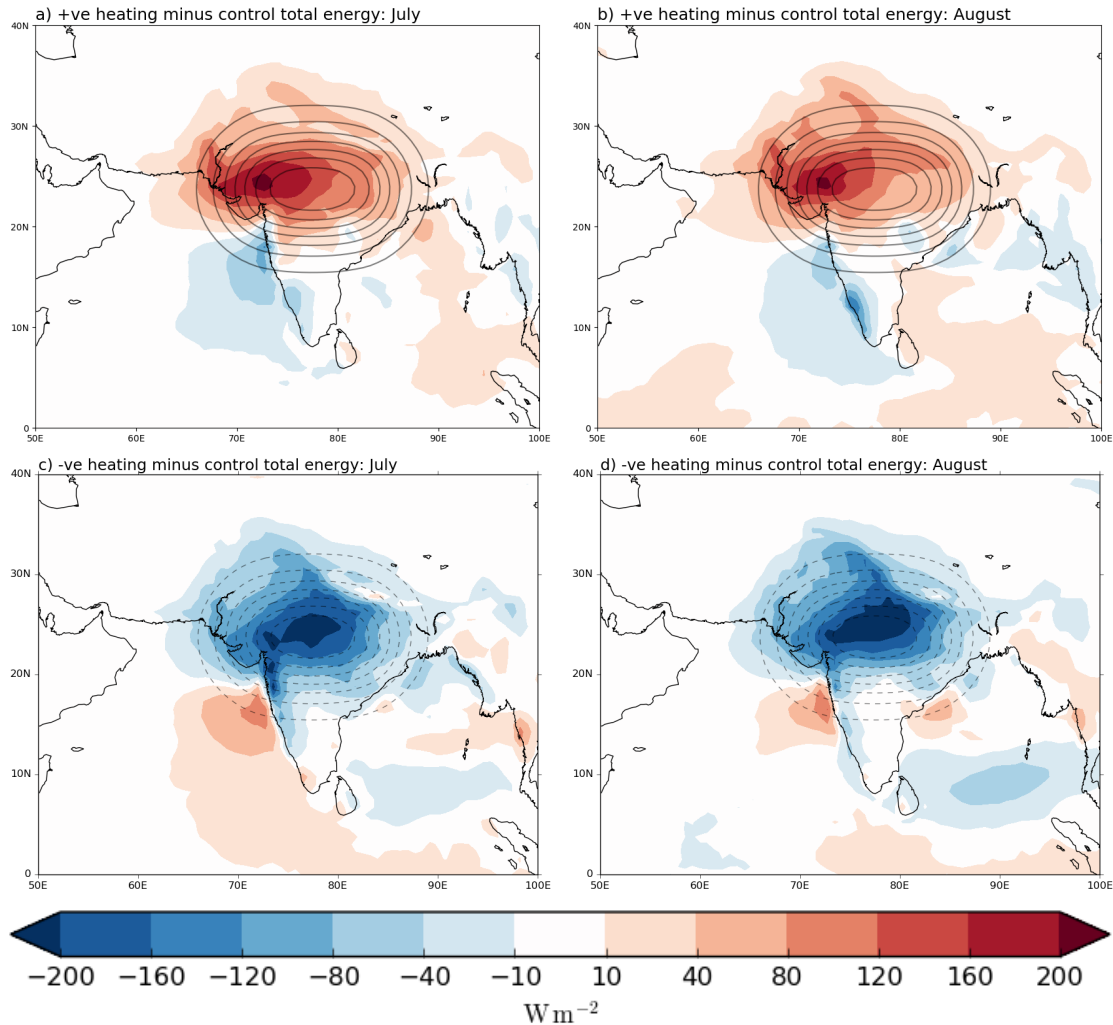


**Figure 6.7:** Ensemble mean latent heating difference ( $\text{W m}^{-2}$ ) for the positive heating experiment minus the control for (a) July and (b) August, and for the negative heating experiment minus the control for (c) July and (d) August, averaged over all years. The black contours indicate the location of the imposed heating - contours every  $15 \text{ W m}^{-2}$  from  $15 \text{ W m}^{-2}$  to  $120 \text{ W m}^{-2}$  (dashed contours for negative values).

are also positioned more towards the centre of the forcing region, associated with the reduction in precipitation over central and northern parts of India, as well as the imposed negative heating which has a peak of  $-120 \text{ W m}^{-2}$ . There is also a slight increase in heating over the Arabian Sea, to the west of India.

Figure 6.8 shows the hemisphere-wide difference in ensemble mean precipitation between the positive and negative heating experiments, and compared to the local response shown in Figure 6.6, the response across the rest of the hemisphere is small. The only noticeable changes outside the tropics are found over east Asia, consistent with a CGT response. A link between the ISM and precipitation over northern China has been found in a number of previous studies (e.g. Kripalani and Kulkarni, 1997, 2001; Yunyun and

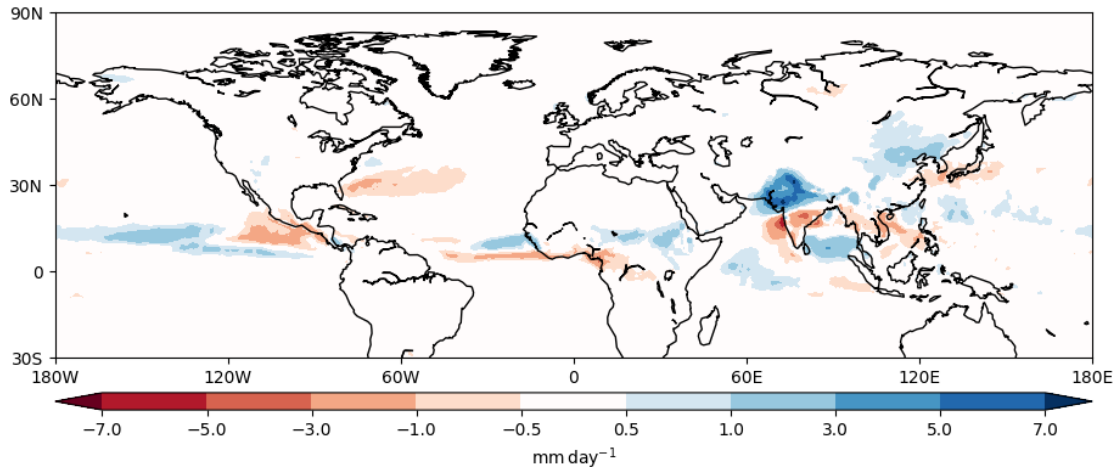


**Figure 6.8:** Ensemble mean precipitation difference ( $\text{mm day}^{-1}$ ) for the positive minus negative heating experiment for August, averaged over all years.

Yihui, 2008) and the precipitation changes over northern China seen in Figure 6.8 suggest that this link is present in the ECMWF model.

The monthly mean response of the ECMWF model to the thermal forcing can be seen in Figure 6.9. This shows the difference in ensemble mean 200 hPa geopotential height for the positive minus negative heating experiments for July and August. It can be seen that amplifying and damping the heating associated with the ISM has resulted in a hemisphere-wide response. In particular, the geopotential height in several of the centres of action of the CGT has been affected by the heating. The geopotential height in the east Asia and North Pacific regions, and also to a lesser extent the North America region, is up to 50 m higher in the positive than in the negative heating experiment, and the location of the centres of increased geopotential height bears a strong resemblance to the CGT in these regions. The differences over east Asia and the North Pacific are approximately equivalent to those associated with a two standard deviation change in the D&W Index, and the North America anomalies are equivalent to a one standard deviation change (not shown). This suggests that heating associated with the ISM is a driver of the variability in these parts of the northern hemisphere through driving a wave-like response. The response in east Asia, and to a certain extent the North Pacific, is also consistent with the regions of positive correlation of 200 hPa geopotential height against ISM precipitation shown in Figure 6.2, although there are no negative anomalies visible between these regions as in Figure 6.2 and the response in the other CGT centres of action is different.

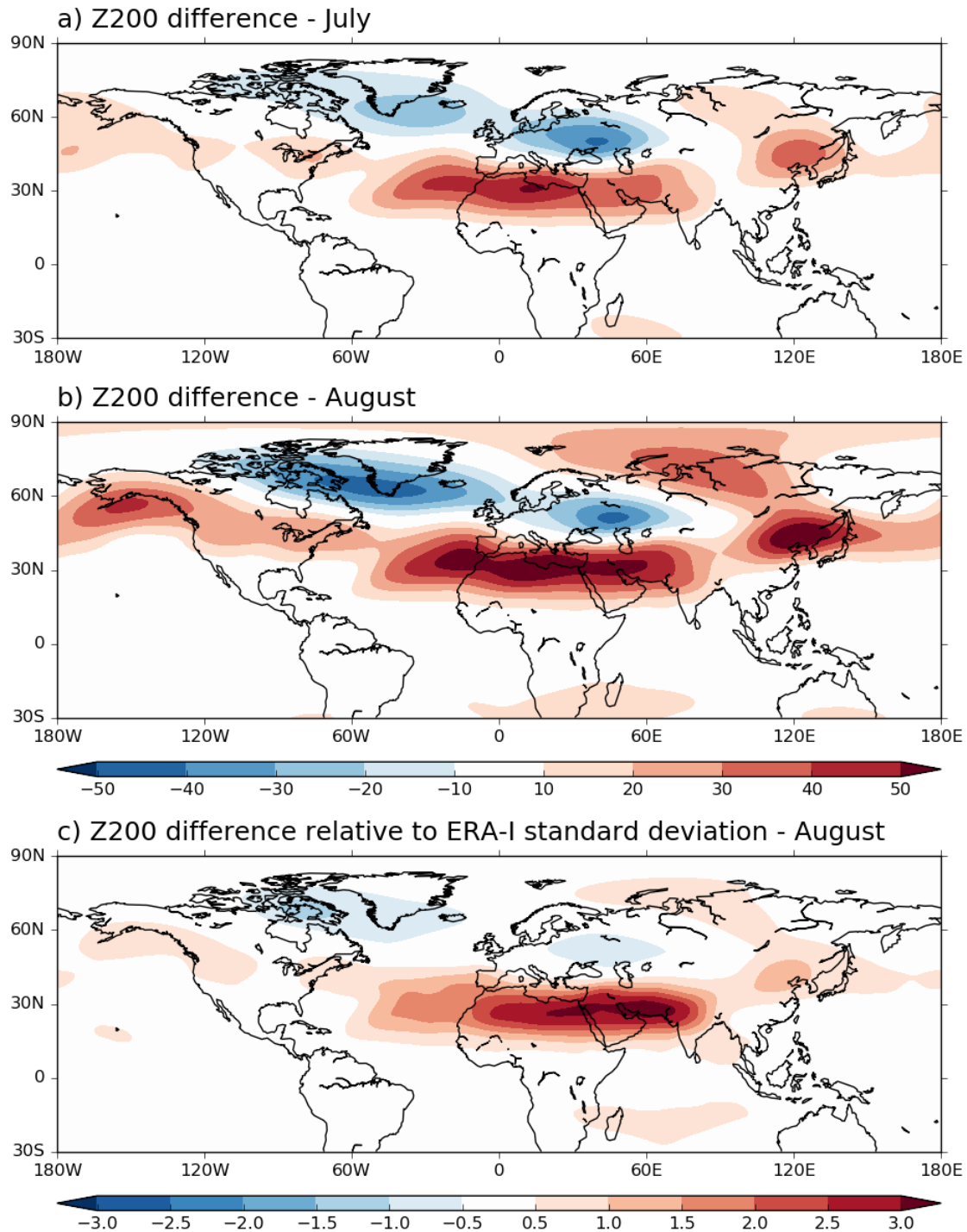


**Figure 6.9:** Ensemble mean 200 hPa geopotential height difference (m) for the positive minus negative heating experiment for (a) July and (b) August, averaged over all years. c) August 200 hPa geopotential height difference relative to ERA-Interim August standard deviation (difference divided by standard deviation).

However, the response over the North Atlantic and the NWEUR region is different to the CGT. Over central and northern Europe and the far North Atlantic, there are broadly cyclonic anomalies, which are the opposite of what would be expected in the

NWEUR region due to the CGT. There is a strong response visible over North Africa and the Mediterranean, as a result of the Rodwell and Hoskins (1996) monsoon-desert mechanism whereby heating associated with the monsoon triggers westward-propagating Rossby waves. These propagate much further west than the observed Rossby waves associated with the monsoon-desert mechanism, which do not travel much further west than 10°W. The response over North Africa and the Mediterranean is also very different to that seen in Figure 6.2. This may suggest that the precipitation in the heating region is a response to forcing from the CGT, rather than a driver of it. This is further backed up by the different response in the D&W region when compared to the CGT, with no positive anomalies located in this region.

The August difference in 200 hPa geopotential height relative to the standard deviation of ERA-Interim is shown in Figure 6.9c. The differences seen associated with the monsoon-desert mechanism are equivalent to up to 3 times the observed standard deviation, indicating that these are significant differences. The difference over east Asia is between 1 and 1.5 observed standard deviations, although the changes over the North Pacific, North America and Europe are equivalent to less than 1 standard deviation.

To examine how the response to the thermal forcing develops over time, Figure 6.10 shows the difference in 200 hPa geopotential height between the two experiments averaged over five day periods after the heating is applied. In this figure, Day 0 is the first day after the heating is turned on (1<sup>st</sup> July). In the first five days, the only anomalies that are visible occur as part of the monsoon-desert mechanism, with anticyclonic anomalies appearing in and to the west of the heating region, and a weak cyclonic anomaly to the north of this, which grows in magnitude by Days 6–10. By this point, anticyclonic anomalies have also appeared over east Asia and have begun to grow over the North Pacific as an eastward propagating Rossby wave response develops. The westward-propagating anomalies have also extended across North Africa to the North Atlantic, and by Days 16–20 these anomalies have reached their peak magnitude, from which point they remain almost constant. The east Asia anomalies also reach their peak magnitude by Days 16–20, while the North Pacific and North America nodes continue to grow until Days 21–25. From then on, the response is largely stationary over the Mediterranean, east Asia and the North Pacific, but the node over North America is a little more transient, shifting in location between west and east North America, and the response is stationary by around Day 40.

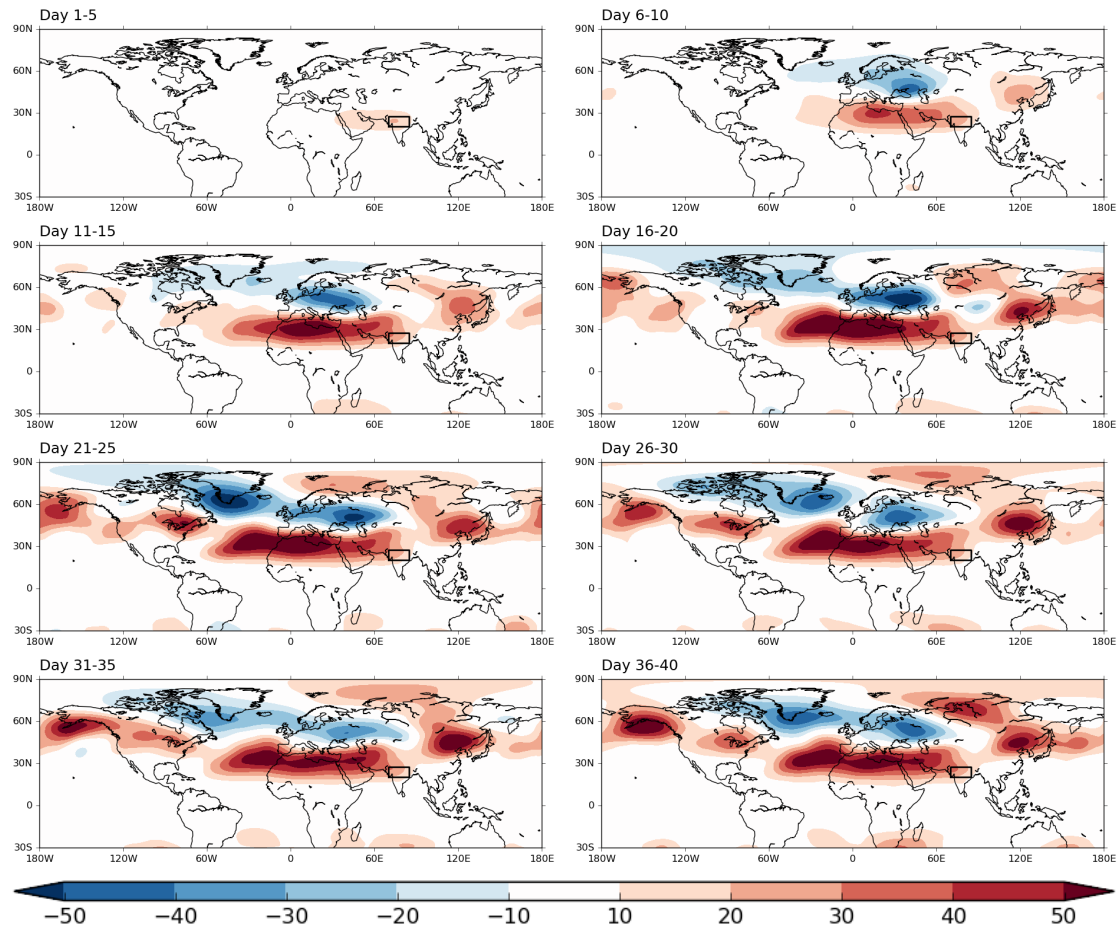


**Figure 6.10:** Difference in 200 hPa geopotential height between the positive and negative heating experiments (m), averaged over five day periods after the heating is switched on at the start of July (day 0 = 1<sup>st</sup> July). The region in which the thermal forcing is applied is shown by the box (20°–27.5°N, 70°–85°E).

The European response is set up within 10–15 days of the heating being applied, and it is clear that the main differences seen over Europe occur not as a result of the propagation of Rossby waves eastwards from the heating region, as in the case of a CGT-like response, but as a direct consequence of the westward-propagating Rossby waves associated with the monsoon-desert mechanism. Throughout the period shown in Figure 6.10 the differences in the NWEUR CGT centre of action are cyclonic, unlike the anticyclonic differences seen elsewhere in the hemisphere, and they appear to be the opposite of what would be expected for a CGT-like response.

Figure 6.11 is a Hovmöller diagram of the difference in meridional wind between the positive and negative heating experiments, averaged between 30°–60°N for a 30 day period after the heating is switched on. The propagation of Rossby waves from longitudes near the heating region (around 60°E) in an eastward direction can clearly be seen in

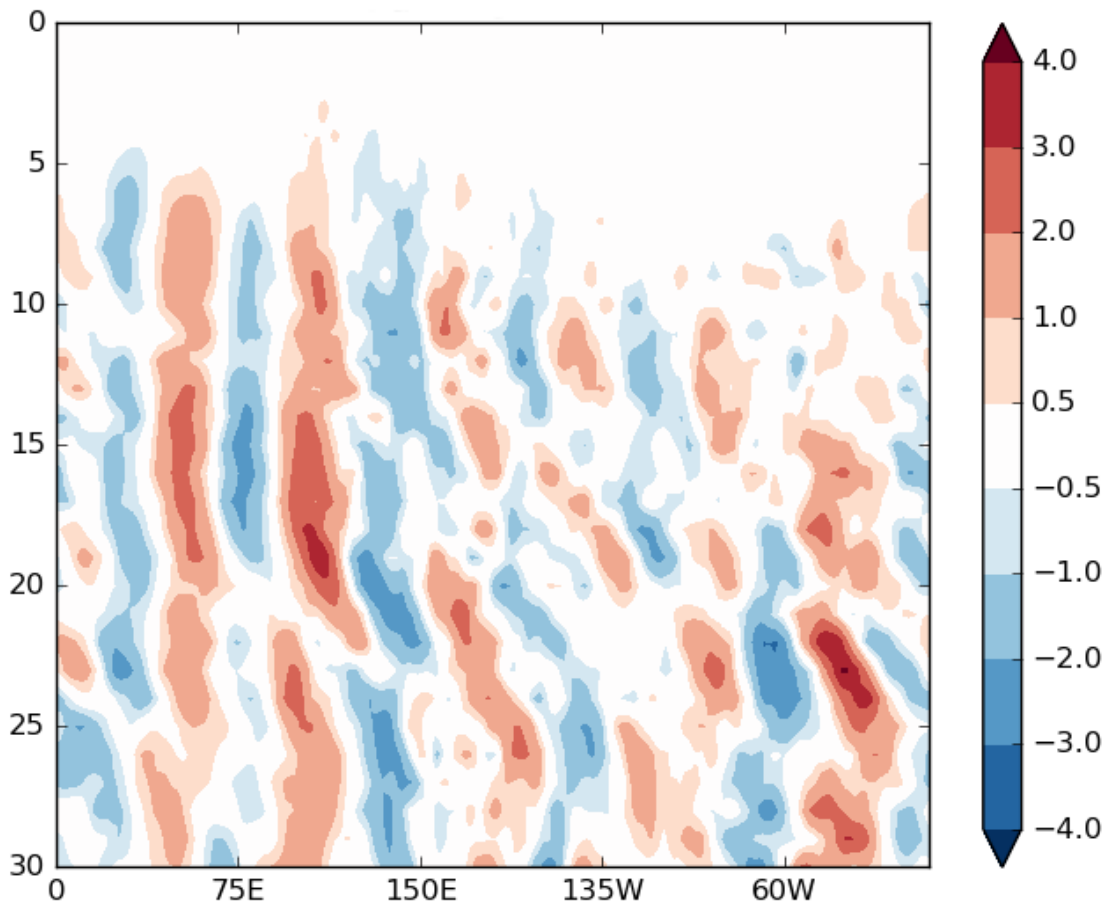


**Figure 6.11:** Hovmöller diagram of the ensemble mean 200 hPa meridional wind difference ( $\text{m s}^{-1}$ ) for the positive minus negative heating experiment, averaged over all years between  $30^{\circ}$ – $60^{\circ}$ N, for 30 days after the heating is switched on (Day 0).

the oscillation of positive to negative anomalies from around Day 5 onwards. These anomalies are more well defined closer to the heating region, before the wave begins to weaken close to the date line. The wave propagates at an approximately constant speed, until around  $70^{\circ}$ W, at which point the anomalies become indistinguishable from noise, with little evidence that the wave influences the anomalies over Europe. This agrees with Figure 6.10, and suggests that European circulation changes as a result of the thermal forcing do not occur due to the eastward propagation of Rossby waves from the ISM region. The response appears to be largely stationary, and the propagation of energy away from the forcing region can be clearly seen.

Although the response seen over Europe is not CGT-like, it is still related to heating associated with the ISM, so we now examine the impact that the thermal forcing has had on the circulation over Europe. First, we look at the impact on the frequency of

atmospheric blocking. We choose the total number of blocked days as this is a cumulative field of daily data and so eliminates the risk of the signal being masked by using monthly means. Blocking frequency is examined for all days in July and August (62 days in total) and as there are five members in these experiments this means that there is a total of 310 days in each experiment each year.

An atmospheric blocking index is defined, following Tibaldi and Molteni (1990) and Scherrer et al. (2006). This is based on the gradient of 500 hPa geopotential height. The gradients, GHGS and GHGN, which are the southern and northern boundaries for the gradient calculation, respectively, are defined as follows:

$$GHGS = \frac{Z(\phi_0) - Z(\phi_S)}{(\phi_0 - \phi_S)}, \quad GHGN = \frac{Z(\phi_N) - Z(\phi_0)}{(\phi_N - \phi_0)}. \quad (6.4)$$

These are calculated at all grid latitudes between 35°N and 75°N, with each latitude band between these used as the central latitude  $\phi_0$ . The difference between the central latitude and the northern  $\phi_N$  and southern latitudes  $\phi_S$  for which the gradient is calculated is taken to be 15°. A given grid point is defined as “blocked” if, on a specific day, the following conditions are satisfied:

$$GHGS > 0, \quad GHGN < -10 \text{ m/degree latitude}. \quad (6.5)$$

Here, the blocking index is evaluated for the grid points in the NWEUR region, and the region is defined as being “blocked” if one or more grid points in the region satisfy the criteria in Equation 6.5.

This index is calculated for all members and all years in the two thermal forcing experiments, and Figure 6.12 shows the difference in the number of blocked days between the two experiments each year. This is calculated over all five ensemble members, as using the ensemble mean smoothes the geopotential height field so that no blocking can be detected. The values in Figure 6.12 are for the difference between the totals calculated from all members.

On average, there is a larger number of blocked days in the negative than in the positive heating experiment. Of the 34 years, seven have a positive difference, three of

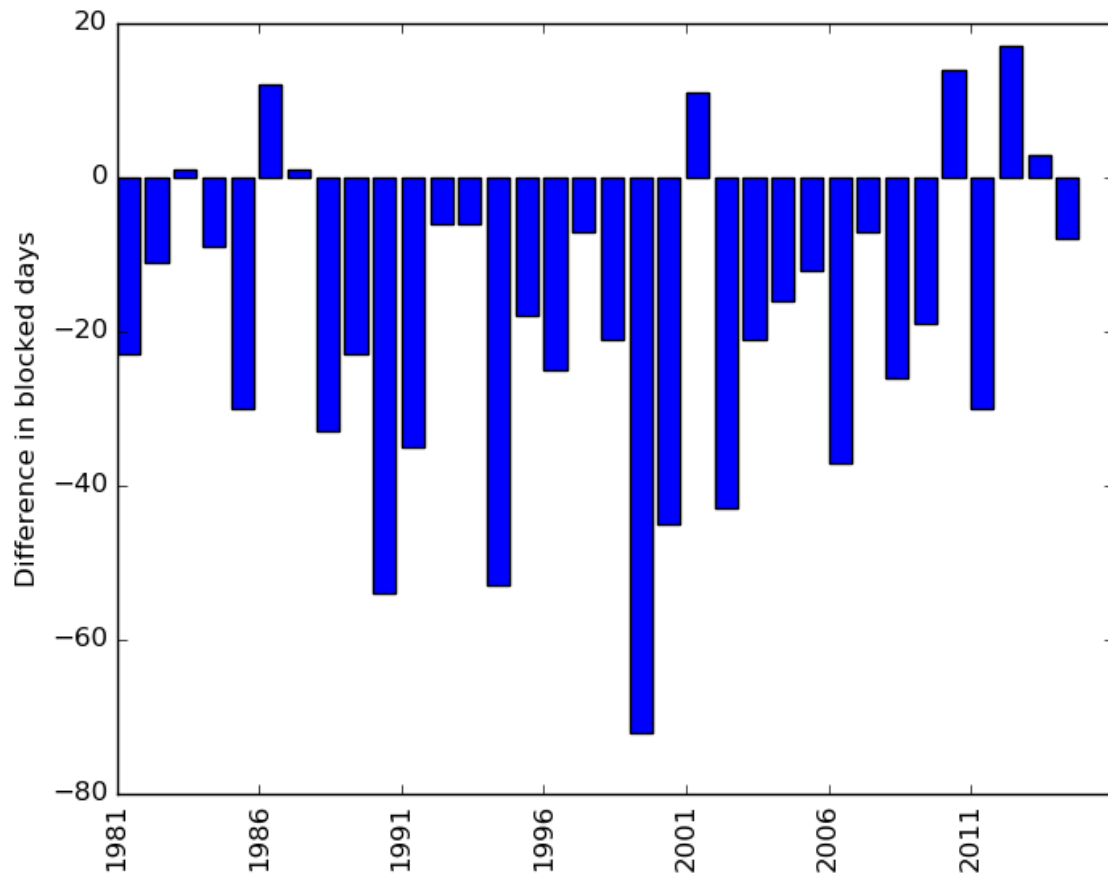


**Figure 6.12:** Difference in the total number of blocked days in the NWEUR region between the positive and negative heating experiments. The total is over all members for each year in July and August (310 days each year in total).

which are only marginally positive. The positive and negative heating experiments have an average of 102 and 121 blocked days in total, respectively, which means that there is approximately 20% more blocked days in the negative heating experiment. Therefore, the circulation over Europe has been significantly altered by the different thermal forcings, although earlier analysis suggests that this is unlikely to be as a result of a CGT-like response. This figure also gives an indication of the interannual response to the heating, with a large amount of year-to-year variability evident. When analysing the control experiment, the mean difference between the number of blocked days in two different sets of five members is close to zero, indicating that the differences seen in the thermal forcing experiments are significant.

From Figure 6.12 it can be seen that there is a large amount of interannual variability in the difference in number of blocked days between the two experiments. Therefore, to determine possible reasons for this variability in the response to the heating, we now

examine the basic state in the five years with the largest negative and largest positive differences. The years with the largest negative difference are 1990, 1994, 1999, 2000 and 2002, and the five with the largest positive difference are 1986, 2001, 2010, 2012 and 2013.

Figure 6.13a shows the ensemble mean July–August averaged difference in the control experiment 200 hPa zonal wind for the largest negative minus positive difference years. This analysis of the control experiment allows us to determine if there are any differences in the ECMWF model basic state which may contribute to the interannual variability in blocking frequency in the thermal forcing experiments which are independent of the heating. The most noticeable anomalies are located over the western North Pacific, near Japan. Here, there is a dipole structure, with positive anomalies to the north and negative anomalies to the south. This indicates a more northerly location of the jet stream in the years when there is a larger negative difference in the frequency of blocking in the thermal forcing experiments. The positive anomalies are also greater than the negative anomalies, indicating that the jet speed is also higher, as well as being in a more northerly location.

The difference in the intensity and location of the jet stream over the North Pacific may mean that the jet stream is in a different location relative to the forcing region in the two experiments. This will affect the Rossby wave propagation away from the source region in the two experiments, with different propagation characteristics in these years, and thus the influence on the downstream circulation is different, resulting in a greater difference in the occurrence of blocking over Europe. A similar dipole pattern over the North Pacific is also present when analysing the same years in the two thermal forcing experiments, in addition to a pattern over Europe which itself is a signature of the differences in blocking frequency (not shown).

The potential role of differences in sea surface temperatures (SSTs) between the two sets of five years has also been investigated. Figure 6.13b is equivalent to Figure 6.13a, but is for SST differences. The SST anomalies over the North Pacific are likely to be related to the difference in jet position between the two sets of five years seen in Figure 6.13a. There is also an area of negative differences across parts of the North Atlantic. SSTs in this region have previously been shown to be related to summertime weather across northern Europe (Ossó et al., 2018) so the negative differences seen here may be related to this mechanism. There are also negative differences in the equatorial Indian Ocean, which are similar to those associated with a positive phase of the Indian Ocean Dipole (IOD). There are no noticeable anomalies in either the tropical Pacific or tropical

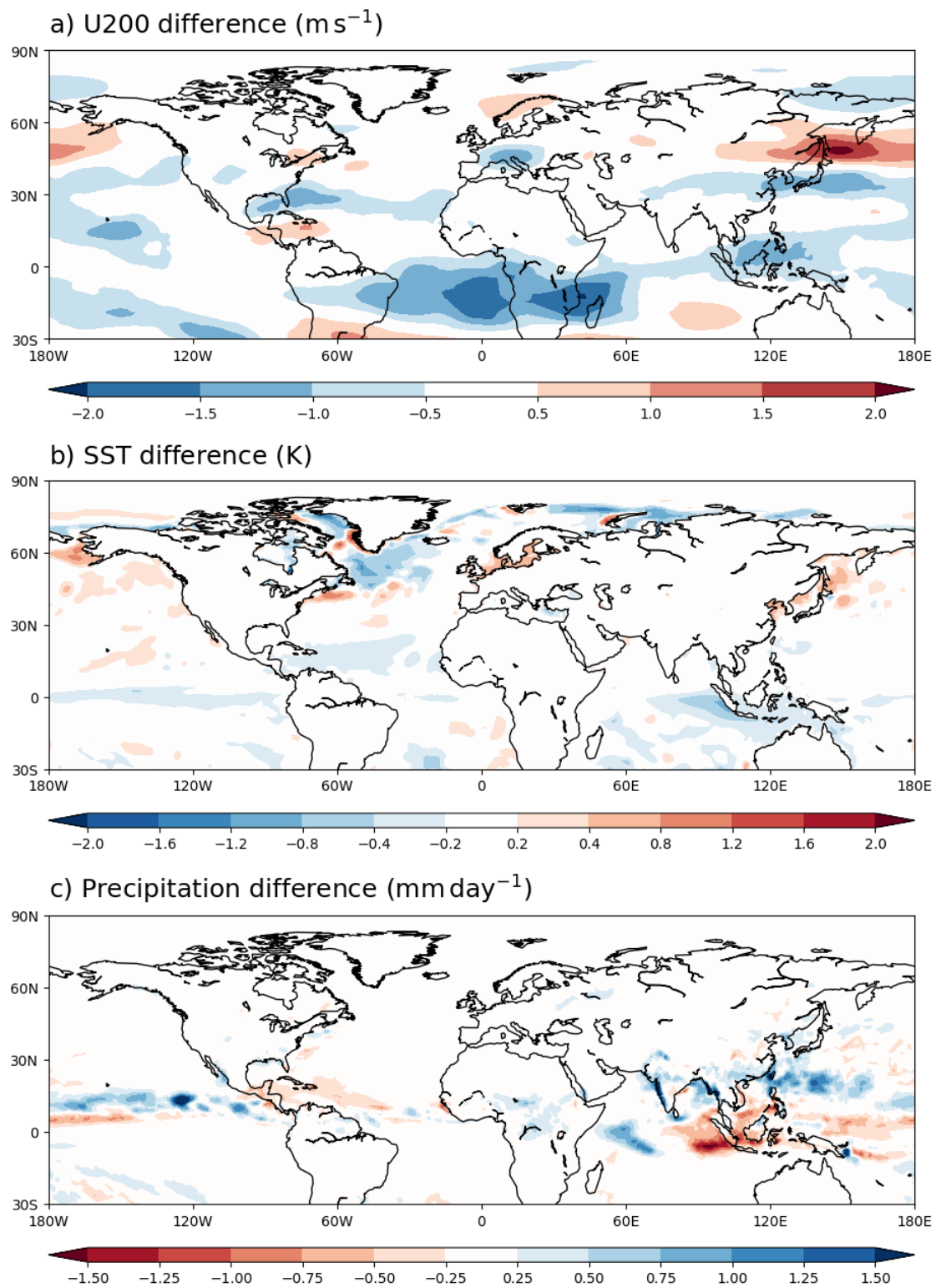


**Figure 6.13:** Difference in ensemble mean July–August average a) 200 hPa zonal wind b) sea surface temperature and c) precipitation in the control experiment between the five years when the difference in the number of blocked days in the NWEUR region is the most negative (1990, 1994, 1999, 2000 and 2002) and the five years with the largest positive difference (1986, 2001, 2010, 2012 and 2013).

Atlantic, suggesting that the differences in European blocking frequency in these years are not related to either El Niño or the Atlantic Equatorial Mode, sometimes known as Atlantic Niño (Zebiak, 1993).

Precipitation differences between the two sets of years are shown in Figure 6.13c. Again, the signal over the equatorial Indian Ocean is consistent with the positive phase of the IOD, with reduced precipitation over the eastern equatorial Indian Ocean and increased precipitation over the western equatorial Indian Ocean and over parts of India. There are also positive differences over parts of the western and equatorial Pacific, which suggests that variations in tropical precipitation may partly explain the interannual variability in the response to the heating.

### 6.3 Barotropic model experiments

To help understand the response to heating in the ISM region, we now force the barotropic model used in Chapter 5 with the RWS calculated using the anomalous divergence associated with the thermal forcing that was applied in the earlier ECMWF model experiments. In these experiments, the barotropic model is forced over India with the

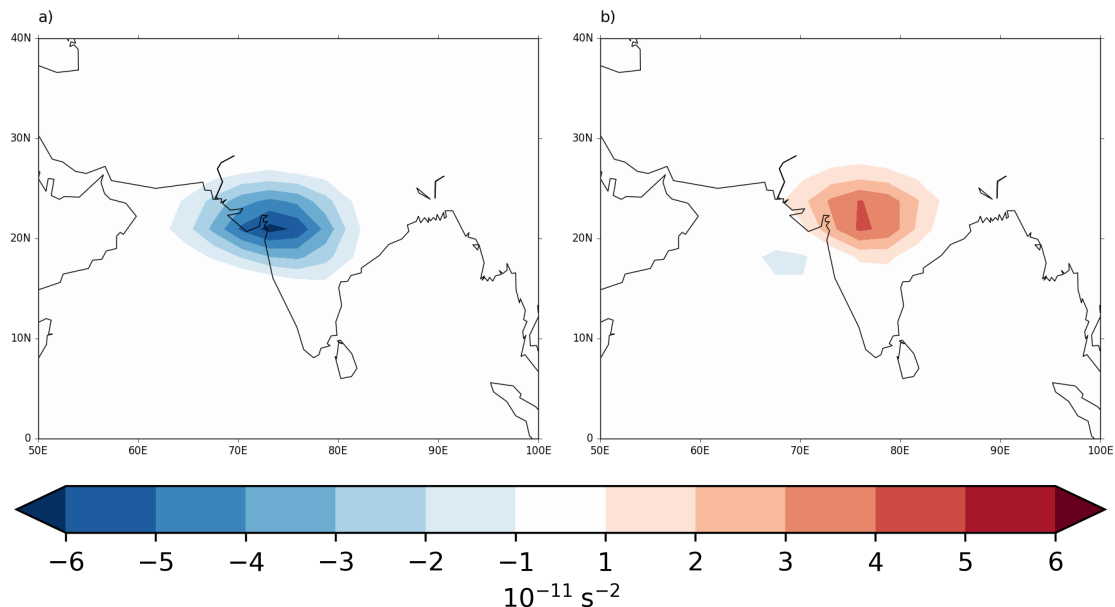


**Figure 6.14:** RWS forcing used in the barotropic model experiments calculated using the difference in divergence between a) the positive heating experiment and the control (BT\_ISMN) and b) the negative heating experiment and the control (BT\_ISMP).

RWS calculated from the difference in divergence between the positive heating experiment and the control (a negative RWS, “BT\_ISMN”) and the negative heating experiment and the control (positive RWS, “BT\_ISMP”). The vorticity is taken from the ECMWF model control experiment, and so Equation 2.4 becomes:

$$RWS = -\zeta_{\text{control}} D_{\text{exp}} - \mathbf{v}_{\chi \text{ exp}} \cdot \nabla \zeta_{\text{control}}, \quad (6.6)$$

where the terms with subscript “exp” are calculated from the divergence difference for the two thermal forcing experiments with respect to the control. The calculated RWS forcings used in these experiments are shown in Figure 6.14. The basic state used is from the ECMWF model control experiment, and is the July–August averaged 200 hPa relative vorticity field.

Figure 6.15 shows the evolution of the streamfunction anomalies in the negative RWS forcing (positive heating, BT\_ISMN) experiment each day from Day 1–10, then every other day from Day 12–18. There is a clear eastward propagation of Rossby waves from the forcing region across the North Pacific to North America. Associated with these are centres of action (positive, anticyclonic streamfunction anomalies) in east Asia and the North Pacific, although these are shifted westwards relative to the location of the centres of action of the CGT. There is also a westward-propagating signal which influences the circulation over the Mediterranean and North Africa, which is consistent with that seen in the thermal forcing experiments. The wave signal becomes less clear over North America as it interacts with the westward propagating waves, and this interaction means that there is no clear centre of action over North America. The propagation of the waves in this experiment is highly consistent with the results from the thermal forcing experiments shown earlier. The evolution of the signal over Europe in these experiments is also similar to the thermal forcing experiments, whereby the circulation anomalies in this region appear to be influenced by a westward- or northwestward-propagating signal from the forcing region, rather than from the west via a CGT-like response.

The simulations from BT\_ISMP show very similar, but opposite, results. To demonstrate this, Figure 6.16 shows the 200 hPa streamfunction anomalies from both BT\_ISMN and BT\_ISMP, averaged over Days 40–50. The location of the centres of positive/negative streamfunction anomalies are very similar, with the magnitude of the anomalies the only

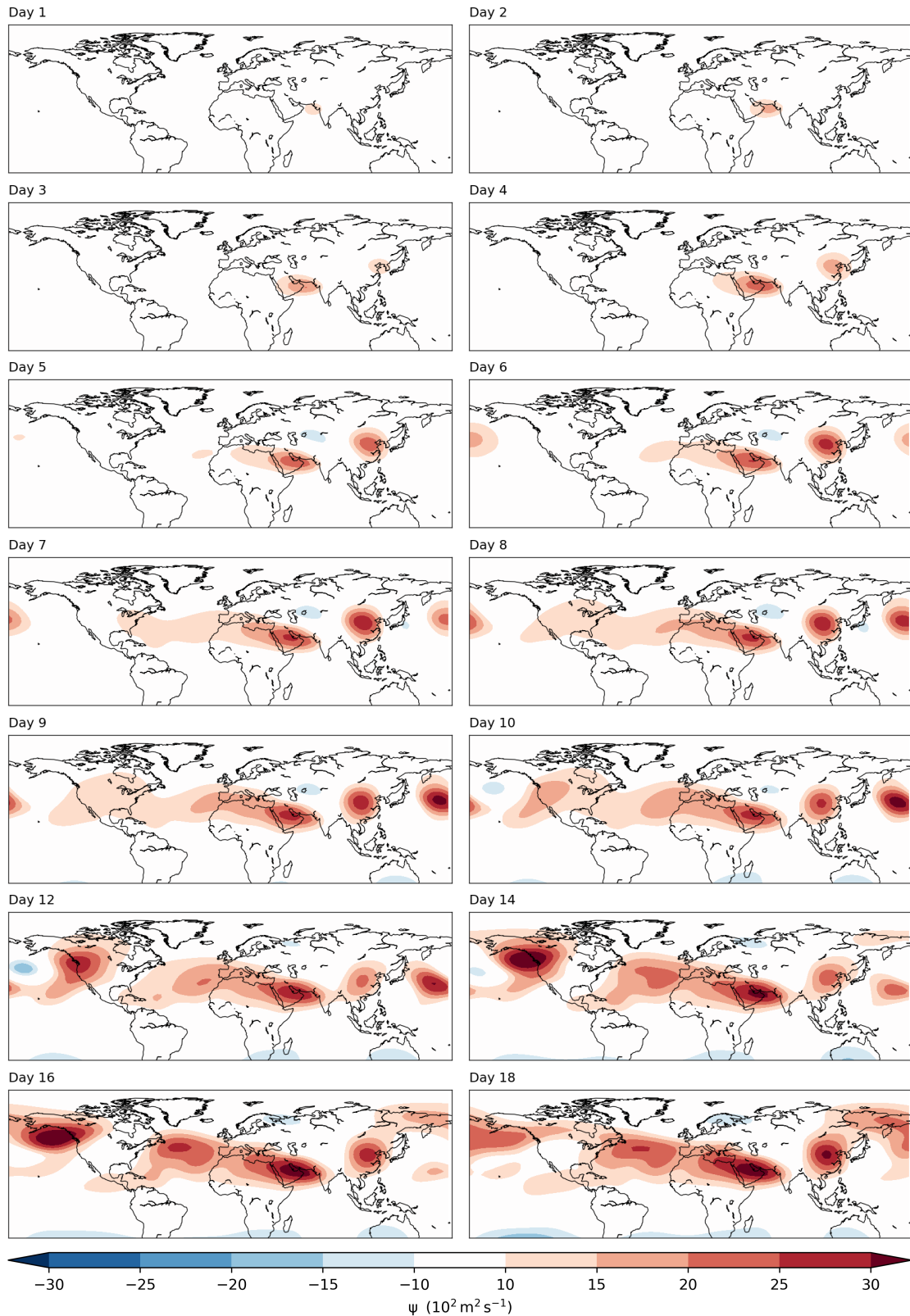


**Figure 6.15:** 200 hPa streamfunction anomaly for each day from Days 1–10, and then every other day up to Day 18, in the barotropic model experiment which is forced over India using the RWS calculated from the difference in divergence between the positive thermal forcing experiment and the control (BT\_ISMN). The forcing used is shown in Figure 6.14a.

noticeable difference between the two experiments. This difference in magnitude is due to the difference in the strength of the forcing used in each experiment. The forcing in BT\_ISMN has a magnitude of around  $-6 \times 10^{-14} \text{ s}^{-2}$  at the peak whereas the forcing in BT\_ISMP peaks at around  $4 \times 10^{-14} \text{ s}^{-2}$  (Figure 6.14).

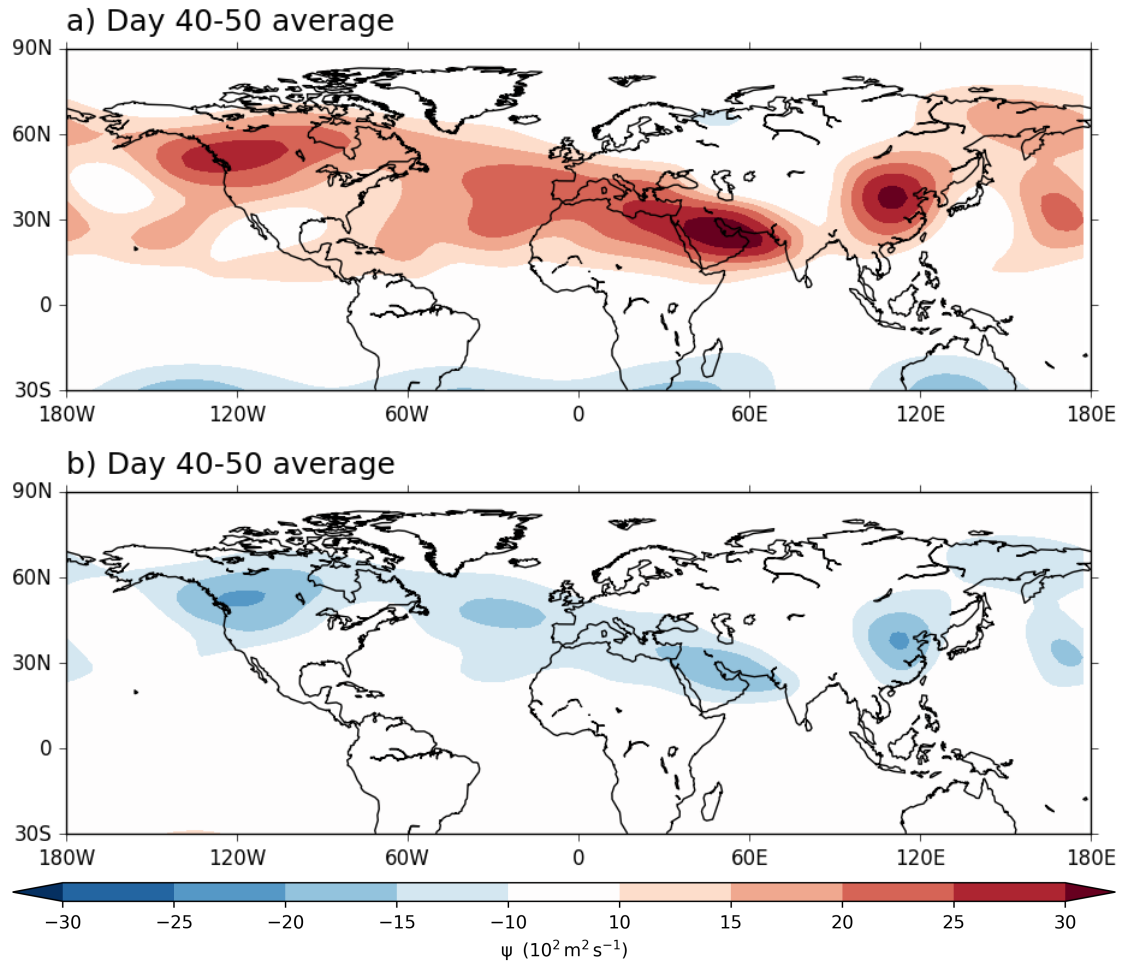


**Figure 6.16:** 200 hPa streamfunction anomaly averaged over Days 40–50 in a) BT\_ISMN and b) BT\_ISMP.

To investigate the impact of differences in the basic state on the propagation of Rossby waves associated with the ISM forcing, a further experiment was run which is equivalent to the negative RWS forcing experiment, but using ERA-Interim relative vorticity for the basic state (“BT\_ISMN\_ERA”). The evolution of the 200 hPa streamfunction anomalies every four days in these two comparable experiments is shown in Figure 6.17.

In the barotropic model experiments presented in the previous chapter, which used a Rossby wave regression forcing applied in the D&W region, changing the basic state did not have much of an impact on the phase or wavenumber of the response, with anticyclonic anomalies in all experiments in very similar locations. However, from Figure 6.17 it can

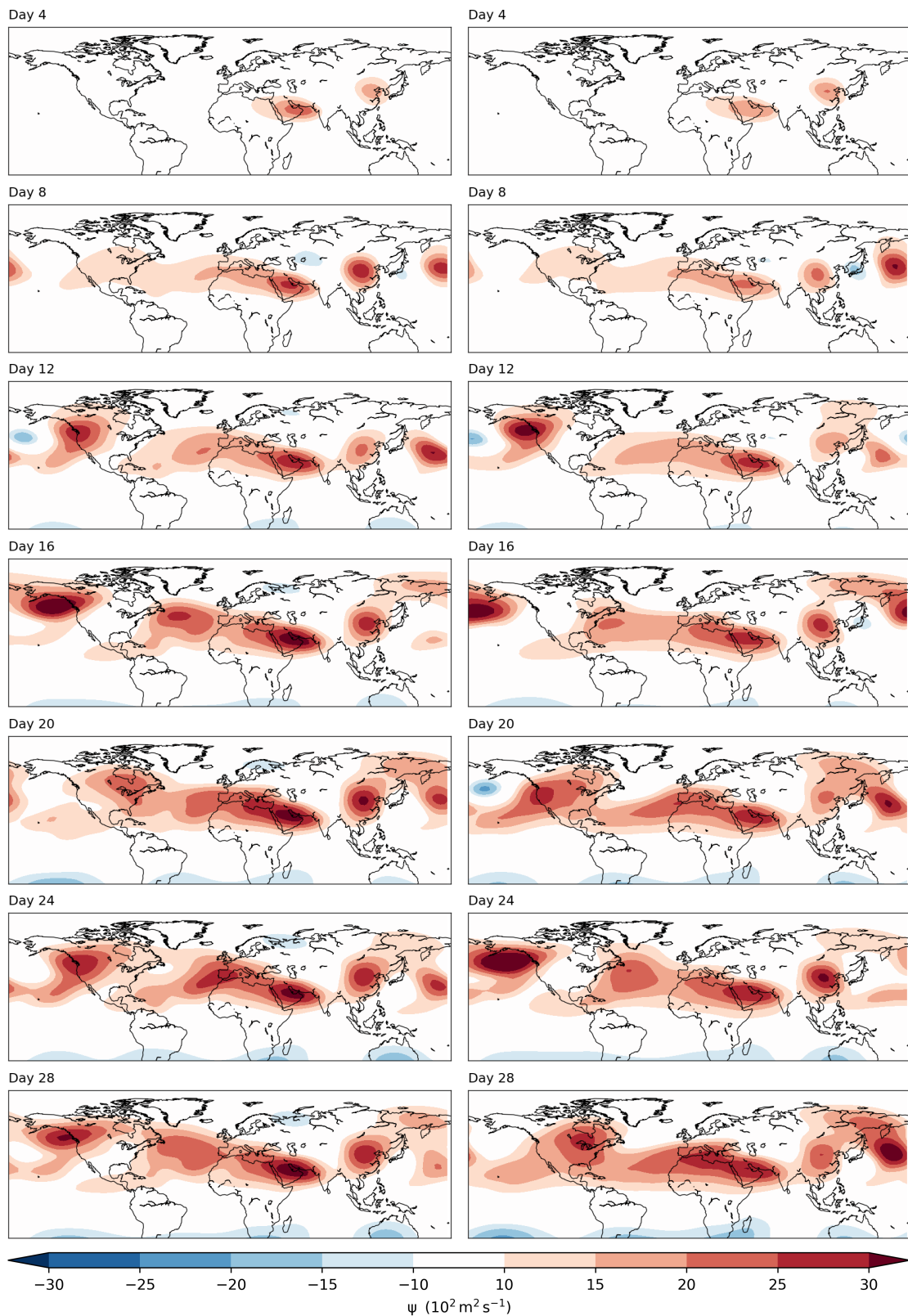


**Figure 6.17:** 200 hPa streamfunction anomaly every four days in the two negative RWS forcing experiments - using the ECMWF model control vorticity as the basic state in the left-hand column (BT\_ISMN) and ERA-Interim vorticity as the basic state in the right-hand column (BT\_ISMN\_ERA).

be seen that changing the basic state when using a RWS forcing applied over India does affect the wave propagation characteristics. Initially, up until around Day 12, the response in both experiments is very similar. However, from this point onwards the two solutions diverge. Differences first appear over the North Pacific, before propagating downstream. By Day 28, the two solutions are very different across much of the hemisphere, aside from in the immediate vicinity of the forcing region. These differences may in part be due to different wave propagation speeds in the two experiments. The waves propagate faster when using the ERA-Interim basic state, so that the pattern of anomalies at Day 20 when using the ERA-Interim basic state looks very similar to Day 24 when using the ECMWF model basic state, and likewise comparing Days 24 and 28. By the time a steady state is reached (around Day 40–50), the two responses look more similar, although there are still some differences between them, largely over North America and the North Atlantic (not shown).

To explore the development of the European response in greater detail, we now follow the method of Shaman and Tziperman (2007) and O’Reilly et al. (2018) and add sponge layers at specific longitudes which damp the nearby vorticity anomalies and prevent the zonal propagation of Rossby waves. These sponge layers, which have a Gaussian longitudinal profile, were implemented through the addition of a term on the right-hand side of the vorticity equation (Equation 3.14) of the form:

$$-r_D (\zeta - \bar{\zeta}), \quad (6.7)$$

where

$$r_D = \exp\left(-2\left(\frac{\lambda - \lambda_{\text{DAMP}}}{15}\right)^2\right). \quad (6.8)$$

Here,  $\lambda$  is the longitude and  $\lambda_{\text{DAMP}}$  is the longitude at which the damping is centred. The first of these sponge layers was added at 60°W, from pole-to-pole, and the comparison of the evolution of the vorticity anomalies in this experiment (“BT\_NAM\_DAMP”) every four days with the equivalent experiment with no damping (BT\_ISMN) is shown in Figure 6.18. It can be seen that the midlatitude response in these two experiments develops in a very similar manner, with an obvious wave train propagating eastwards from the forcing

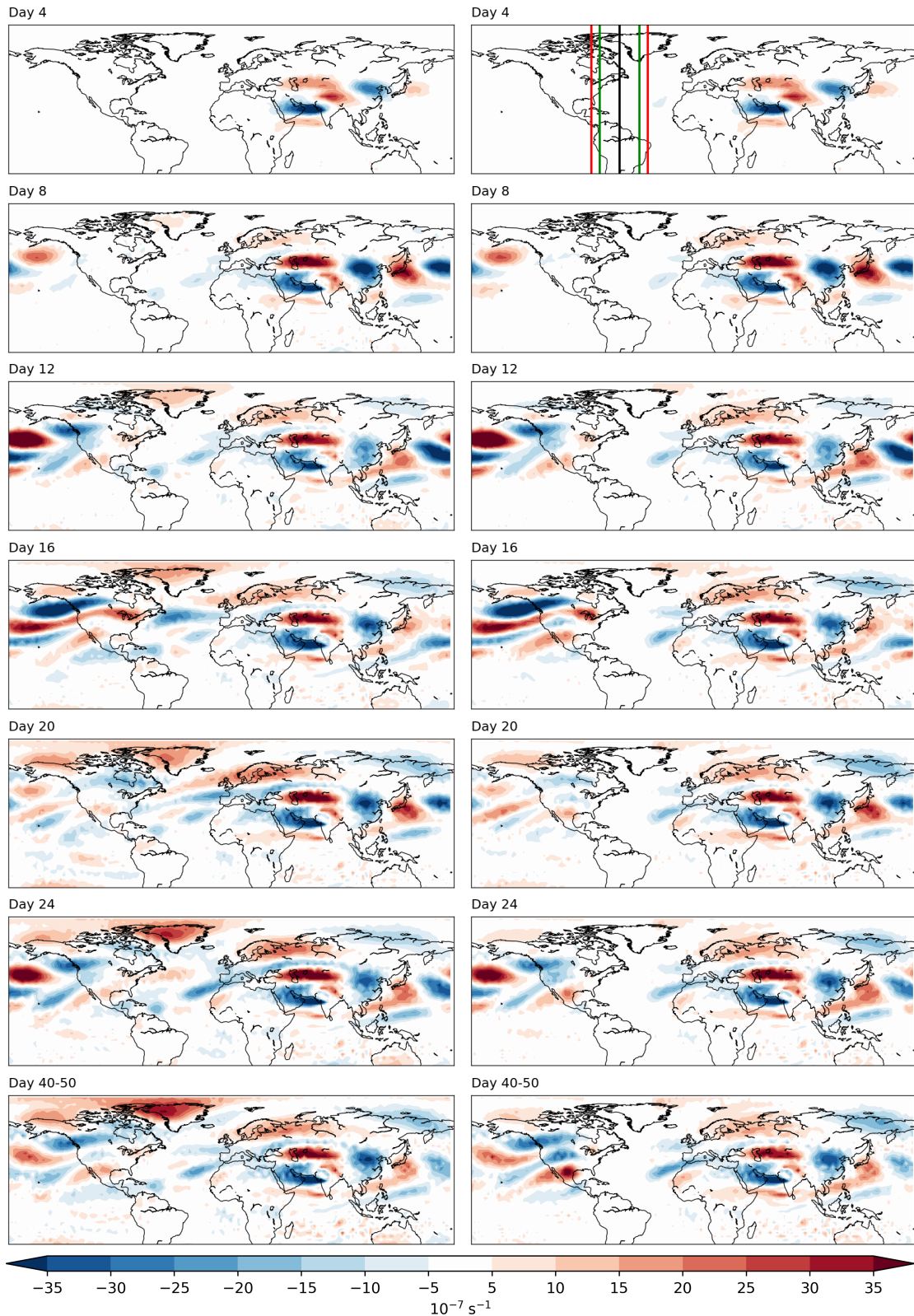


**Figure 6.18:** Left-hand column: Vorticity anomaly every four days in the same barotropic model experiment as in Figure 6.15 (BT\_ISMN), with the 40–50 day average in the bottom panel. Right-hand column: Same as the left-hand column, but with a longitudinal damping applied at 60°W (BT\_NAM\_DAMP). The vertical lines indicate the damping timescale at different longitudes: 15 minutes (black line) 2.5 hours (green lines) and 25 hours (red lines).

region. The westward propagating signals in these two experiments are also extremely similar, such that by Day 24 the anomalies over Europe are almost identical in the two experiments, providing further evidence that the response in this region to forcing from the ISM occurs via westward-propagating Rossby waves, as opposed to a circumglobal wave train. These results are similar to those of Shaman (2014), who found that the response over Europe to ENSO-related forcing in late summer (JAS) is dominated by a westward-propagating signal, and also the results from the tropical Pacific forcings of O'Reilly et al. (2018), in which a similar signal was observed.

Stephan et al. (2019) proposed a positive feedback loop between ascent over India and descent over the Mediterranean, whereby the ISM-induced Mediterranean descent (which occurs through the monsoon-desert mechanism) can subsequently induce rising motion over South Asia following the propagation of anomalies along the Asian jet, associated with the Silk Road Pattern (Lu et al., 2002; Enomoto et al., 2003). To investigate this mechanism, and its relationship to the development of downstream anomalies over North America, a further experiment was carried out, this time with the sponge layer centred at 30°E (“BT\_EUR\_DAMP”). The vorticity anomalies in this experiment, along with those from the equivalent experiment with no damping, are shown in Figure 6.19. Comparing the two experiments, the effect of preventing the westward-propagating waves can be clearly seen. Early in the simulation, until around Day 8, the eastward-propagating response is similar in both experiments. However, from this point on, the anomalies in the damped experiment are generally weaker. This can be seen clearly in the 40–50 day average, shown in the bottom panel of Figure 6.19, where the response over east Asia, the North Pacific and North America is weaker. This suggests that a response between Asia and North America, associated with the “Tokyo–Chicago Express” wave train (Lau and Weng, 2002; Lau et al., 2004), does occur when the westward-propagating waves are damped, but it is much weaker. This agrees with the hypothesis of Stephan et al. (2019), and implies that the westward-moving Rossby wave response is crucial in amplifying the subsequent eastward propagation of the wave train between Asia and North America.

We now examine the response near the forcing region in BT\_EUR\_DAMP in greater detail to further understand the reasons for the differences in the response seen in this experiment. Figure 6.20 shows the vorticity and wind anomalies in the same two experiments as in Figure 6.19 (BT\_ISMN and BT\_EUR\_DAMP), focussing this time on the forcing region in the first few days of the simulation. As in Figure 6.19, the vorticity and

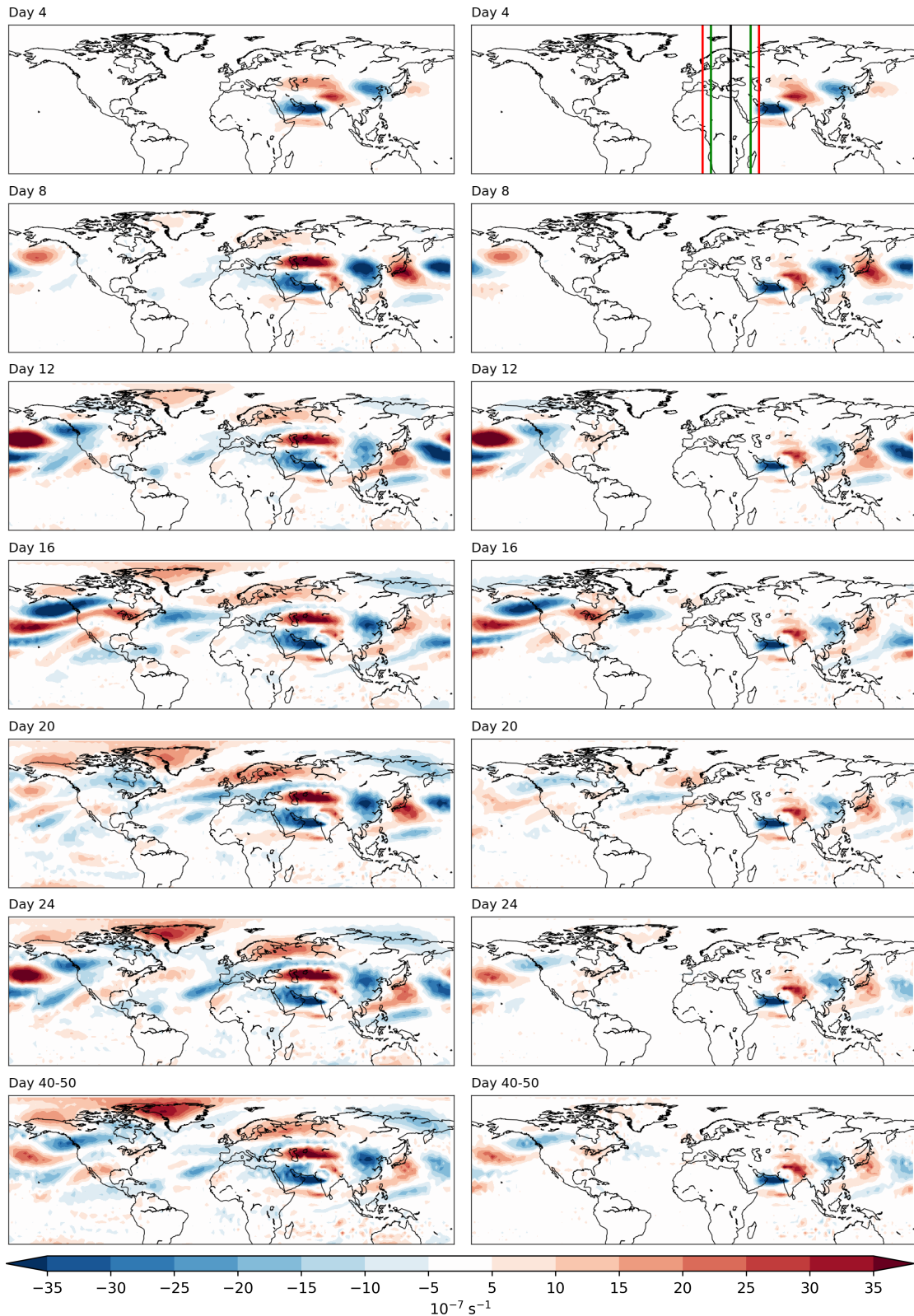


**Figure 6.19:** Left-hand column: Vorticity anomaly every four days in the same barotropic model experiment as in Figure 6.15 (BT\_ISMN), with the 40–50 day average in the bottom panel. Right-hand column: Same as the left-hand column, but with a longitudinal damping applied at 30°E (BT\_EUR\_DAMP). The vertical lines indicate the damping timescale at different longitudes: 15 minutes (black line) 2.5 hours (green lines) and 25 hours (red lines).

wind anomalies early in the simulation are very similar in the two experiments, with little difference between them at hour 42. However, from this point on, the anomalies in the two experiments begin to differ. In BT\_ISMN (left-hand column of Figure 6.20) a strong westward-propagating negative vorticity anomaly is able to develop, and this extends across the northern Arabian Sea and the Middle East by hour 138. In BT\_EUR\_DAMP, these anomalies are prevented from extending much beyond the eastern parts of the Middle East. As a consequence of this, there is a much greater southerly component to the anomalous wind over the Middle East in the damped experiment and these southerly wind anomalies will advect low vorticity air to higher latitudes. This prevents the development of the area of positive vorticity anomalies near the Caspian Sea that can be seen in the experiment with no damping, which are hypothesised to be important in the subsequent downstream reinforcement of the wave train through the propagation of these anomalies along the Asian jet stream. When no damping is applied, the negative vorticity anomalies associated with the westward-moving response effectively cut off the anomalous southerlies, allowing the positive vorticity anomalies to develop to the north.

## 6.4 Summary and conclusions

Results from barotropic model experiments presented in Chapter 5 suggested that the strength of the forcing associated with the monsoon may be important in explaining the weak representation of the CGT in the model. These results motivated thermal forcing experiments in the ECMWF model, to examine the impact of changing the heating associated with ISM precipitation on the extratropical circulation. Two experiments were carried out, consisting of both a positive and negative heating which was imposed over India from the start of July.

The response of the ECMWF model to the thermal forcing shows a similar structure to the CGT over east Asia, the North Pacific and North America, with the positive heating resulting in the development of anticyclonic anomalies in these regions, and vice versa for the negative heating experiment. On a daily timescale, it was found that these anomalies develop as a result of eastward-propagating Rossby waves, with the response over east Asia developing in the first 10 days, and over the North Pacific and North America by around Day 20. A strong Rodwell and Hoskins (1996) monsoon-desert mechanism response is also set up within the first 15 days, and this extends across North Africa and

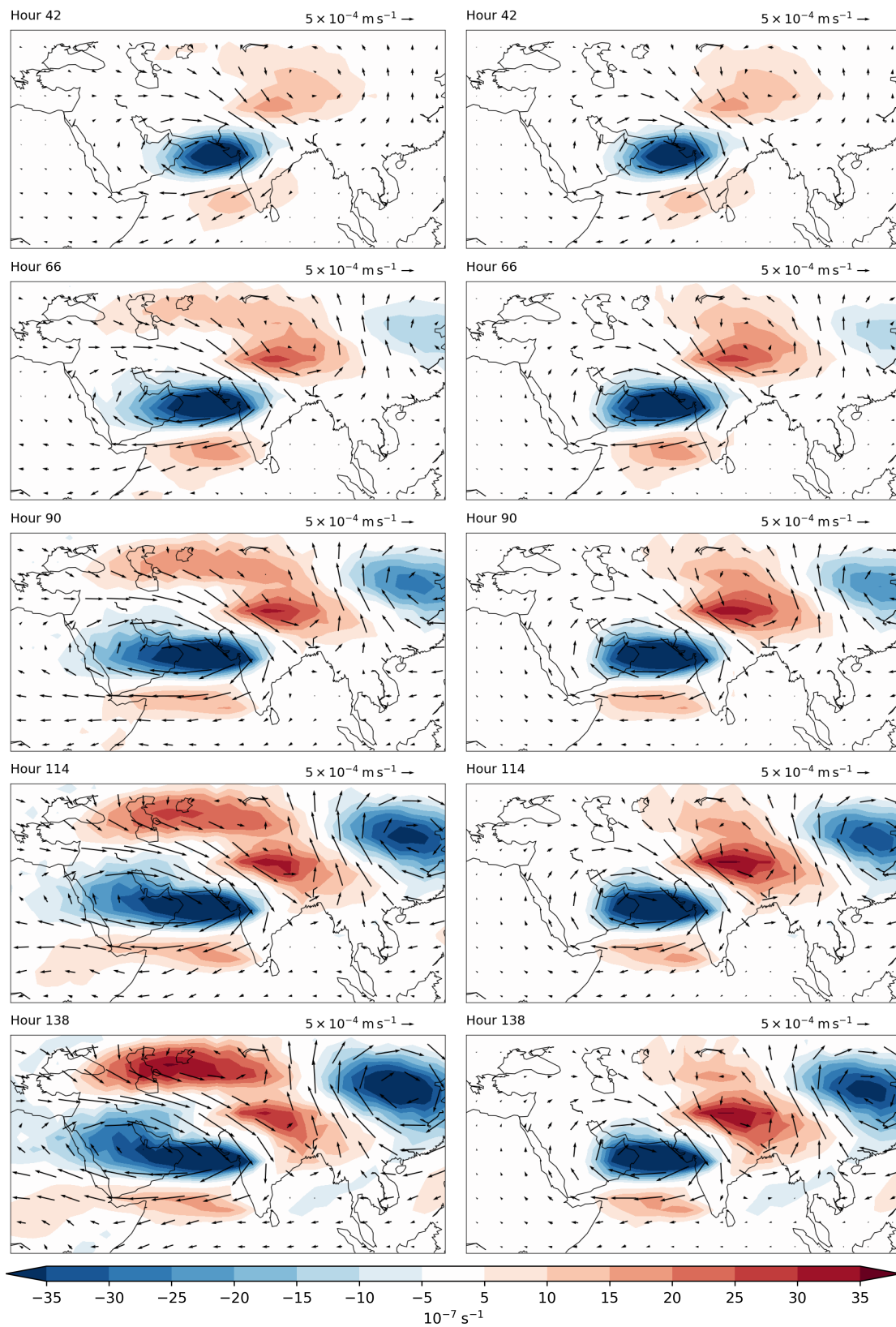


**Figure 6.20:** Left-hand column: Vorticity (coloured contours) and wind (barbs) anomalies in BT\_ISMN at hour 42, 66, 90, 114 and 138. Right-hand column: Same as the left-hand column, but for BT\_EUR\_DAMP.

the Mediterranean to the central Atlantic.

However, the differences over Europe are the opposite of what would be expected for the CGT, with cyclonic anomalies over most of northern Europe in the positive heating experiment. These appear to result from a westward- and northwestward-propagating signal from the ISM forcing region. These cyclonic anomalies develop before the eastward-propagating Rossby waves have travelled around the hemisphere, and are almost fully developed within 15 days of the application of the forcing.

Although the signal over Europe as a result of the forcing in the ISM region does not appear to arise as a result of a CGT-like response to the heating, the circulation is still affected as a result of the heating. Examination of the occurrence of blocking in the two thermal forcing experiments found that the negative heating experiment has on average around 20% more blocked days over northwest Europe than the positive heating experiment.

However, there is a reasonable amount of interannual variability in the difference in the number of blocked days in the two heating experiments, with some years with very small differences between them. In years when there is a large difference in the total number of blocked days in the two experiments, the North Pacific jet stream is located further north. This implies that there may be some influence on Europe via the eastward-propagating response. If the RWS associated with the ISM heating is in a different location relative to the jet stream in the two experiments in these years, then Rossby waves may be more easily able to propagate away from this region and influence the downstream circulation, resulting in a larger difference in the occurrence of blocking in the two experiments.

Further experiments in the barotropic model, in which a RWS forcing calculated using the difference in divergence between the thermal forcing experiments and the control was applied over India, showed a response consistent with that seen in the thermal forcing experiments, with similar eastward- and westward-propagating signals. In particular, the European response develops in a very similar way, through the northwestward propagation of waves from the forcing region, resulting in anticyclonic streamfunction anomalies over southern Europe and weaker cyclonic anomalies over northern Europe.

Contrary to the barotropic model experiments in Chapter 5, changing the basic state when forcing the barotropic model over India does result in different wave propagation characteristics. Until Day 12, experiments using ERA-Interim and ECMWF model basic states have similar solutions. However, after this point they begin to diverge. By Day 28, the streamfunction anomalies associated with the two experiments significantly differ over the North Pacific, North America and also over the North Atlantic and northwest Europe. The anomalies over Europe are larger when using the ERA-Interim basic state, with a greater westward extent of the anomalies associated with the monsoon-desert mechanism.

Following Shaman and Tziperman (2007) and O'Reilly et al. (2018), further barotropic model experiments were carried out in which sponge layers were added at certain longitudes in order to damp vorticity anomalies and prevent the zonal propagation of Rossby waves through the layer. When a sponge layer was added at 60°W, the 40–50 day average vorticity anomalies throughout the midlatitudes are extremely similar to the equivalent experiment with no damping. In particular, the response over Europe is very similar, which further indicates that the anomalies seen over Europe develop as a result of westward-propagating Rossby waves, rather than an eastward-moving wave train from the forcing region.

Stephan et al. (2019) hypothesised that the SRP wave train relies on a positive feedback loop between ascent over India and descent over the Mediterranean. In order to further investigate this mechanism, and its importance in the propagation of the Rossby wave train across the Pacific to North America, another experiment was carried out in which the damping was applied at 30°E. In this experiment, the vorticity anomalies have a weaker magnitude by Day 40–50 when compared to the equivalent experiment without damping. When examining the response near the forcing region in closer detail, it was found that in the damped experiment there is a much greater southerly component to the anomalous wind over the Middle East. This acts to advect low vorticity air to higher latitudes and suppresses the positive vorticity anomaly that develops near the Caspian Sea in the undamped experiment, which is important in the subsequent downstream reinforcement of the wave train. This agrees with the hypothesis of Stephan et al. (2019) and suggests that the westward-propagating Rossby wave response to forcing in the ISM region is crucial in the downstream strengthening of the SRP/Tokyo–Chicago Express wave train.

## Chapter 7:

# Discussion and conclusions

## 7.1 Overview

Variations in summer climate extremes in Europe can have far-reaching socio-economic impacts. Recent summer drought and flooding events have highlighted the vulnerability of society to summer seasonal climate extremes. The potential benefits of more accurate long-range forecasts for the European summer are clear. Advance warning of an increased likelihood of flood or drought several weeks or months in advance would allow governments and businesses to make the necessary preparations to mitigate against potential impacts.

This thesis has aimed to investigate the relationship between European summer seasonal forecast skill and the representation of the circumglobal teleconnection (CGT) in a seasonal forecast model. Possible causes of errors in the representation of the CGT in the European Centre for Medium-Range Weather Forecasts (ECMWF) seasonal forecast model have been investigated; relaxation experiments were performed to further analyse these model errors and improve knowledge of the CGT mechanism; and barotropic model and thermal forcing experiments in the ECMWF model have been performed to explore the relationship between Indian summer monsoon (ISM) precipitation (heating) and variability of the summer circulation over Europe. This analysis has been performed with the intention of answering the following questions, as posed in Chapter 1:

1. How well is the CGT represented in a state-of-the-art seasonal forecast model?

2. What is the role of the Indian summer monsoon in driving the CGT?
3. How does the Indian summer monsoon influence circulation variability over Europe?

A discussion and the main conclusions of the analysis performed in this thesis is presented in Section 7.2, to address the questions posed above, with an overall summary given in Section 7.3. Possible directions for future work are discussed in Section 7.4.

## **7.2 Discussion and conclusions**

### **7.2.1 How well is the circumglobal teleconnection represented in a state-of-the-art seasonal forecast model?**

In order to diagnose the role of the CGT in influencing European summer seasonal forecast skill, it first had to be determined how well the model represents this teleconnection mechanism. To do this, work in Chapter 4 used seasonal hindcasts using Cycle 41r1 of the ECMWF seasonal forecast model to examine the skill of the model during the summer, and the model performance at representing the CGT. It was found that the model generally has a weaker than observed CGT wave train, with a median northern hemisphere pattern correlation for the wave train of 0.60 when compared to ERA-Interim. Associated with this, the correlations between the D&W Index (a region proposed by Ding and Wang (2005, 2007) as linking ISM precipitation and the CGT) and other centres of action of the CGT are too weak in August, when the observed wave train is strongest, with the exception of the D&W vs. east Asia (EASIA) region correlations which are well captured. However, beyond EASIA the model wave train becomes weaker. The relationship between the EASIA and North Pacific (NPAC) region, which also forms part of a teleconnection known as the “Tokyo–Chicago Express” (Wang et al., 2001; Lau et al., 2004) and which have an observed correlation of 0.71, have a weaker than observed relationship in the model, although the majority of members do have a significant correlation between these two regions.

A number of potential sources for the weak representation of the CGT in the model were investigated in Chapter 4. Given the hypothesis of Ding and Wang (2007) that the

D&W region plays an important role in the maintenance of the CGT, the skill of the model in this region was investigated. It was shown in Chapter 4 that the model has very little correlation skill for 200 hPa geopotential height in this region in July and August, and it was also found that the variance of the D&W Index is lower than observed in these months. A possible reason for this lower model variance is a weak representation of the link between ISM precipitation and the D&W Index. In observations there is a significant correlation between these indices in all months, and while this relationship is well captured in June, the correlations in July and August are much weaker. This in turn may be related to lower than observed variance of ISM precipitation in the model, and therefore the poor variance of the D&W Index in July and August may be linked to poor representation of the variance of ISM precipitation in the model.

Another possible source of errors in the CGT was found to be the Rossby wave source (RWS), which describes the forcing of Rossby waves by the divergent flow at 200 hPa. It was found that the centre of positive RWS located near the D&W region in the model is slightly stronger than in ERA-Interim. However, it is displaced northeastwards relative to ERA-Interim, meaning that the model RWS in the D&W region is much weaker than in observations. The displacement of the model RWS was shown to be related to a northward displacement of the jet stream over this region by several degrees latitude. Analysis of the divergence and precipitation showed that the difference in RWS magnitude between the model and ERA-Interim can be attributed to differences in the convergence associated with the area of positive RWS. This convergence is also greater in magnitude in the model, and this magnitude difference may be related to greater model divergence over the Bay of Bengal and the Arabian Sea, which in turn is associated with increased amounts of model precipitation in these regions when compared to observations.

A northward displacement of the jet stream in the model was also found across much of the northern hemisphere. In June, July and August the model jet stream is located several degrees too far north across most of Eurasia and the North Pacific. Rossby waves propagate along the jet stream, which acts as a waveguide, so these biases, which are located along the CGT pathway, are likely to have an impact on the propagation characteristics of Rossby waves associated with the CGT in the model. The combination of the errors in RWS along with the bias in the jet stream location may be important in the weak representation of the CGT in the model.

## **7.2.2 What is the role of the Indian summer monsoon in driving the circumglobal teleconnection?**

Ding and Wang (2005) hypothesised that the ISM plays an important role in the forcing or maintenance of the CGT, either by exciting Rossby waves which then propagate downstream and influence the midlatitude circulation, or through the interaction of a Rossby wave train which propagates from Europe to west-central Asia, before being reinforced by precipitation associated with the ISM. Subsequently, Ding and Wang (2007) suggested that the second mechanism is likely to be the more dominant of the two and that Rossby waves which propagate from Europe can initially trigger precipitation in the north ISM region, and also that this convection then re-energises the downstream propagation of the wave train. Other studies have also identified the possible role of the ISM in exciting eastward propagating Rossby waves. Wang et al. (2001) and Wu and Wang (2002) both found that ISM precipitation modulates the west-central Asia anomalous anticyclone, and that this is also responsible for the formation of an anomalous anticyclone over east Asia.

To examine the role of the ISM in forcing or maintaining the CGT, and also to investigate the above hypothesis of Ding and Wang (2007), three relaxation experiments were carried out, results of which are presented in Chapter 5. In these, the circulation was relaxed towards ERA-Interim in specific regions of interest. In Chapter 4 it was shown that there is weak model variability in the D&W region and a weak relationship between the D&W Index and the ISM. To examine whether the weak representation of the CGT in the model occurs as a result of weak forcing from the D&W region, the first experiment relaxed the circulation near this region. Analysis showed that the representation of the CGT in this experiment is poorer than in the control, and 200 hPa geopotential height skill is not much improved outside Asia, with the skill over Europe largely unchanged. This may suggest that the CGT is not being forced from west-central Asia, and also that the skill over Europe is not reliant on errors in the D&W region. However, the northward jet biases seen in the control experiment are still present in much of the northern hemisphere, which means that there are still likely to be errors in Rossby wave propagation. Also, as a consequence of the relaxation, the variance in the D&W region will have been increased. If the model teleconnection pathway is incorrect, then this may mean that a stronger version of the incorrect response is being forced, which could explain the reduced CGT pattern correlation in this experiment. The link between ISM precipitation and the D&W Index

is very poorly represented in this experiment, with an overall reduction in the strength of the correlation compared to the control. This could also be a factor in the reduced CGT pattern correlation as the wave train may not be being reinforced correctly.

The second experiment relaxed a region over northwest Europe. This experiment was performed to investigate the Ding and Wang (2007) hypothesis that the midlatitude wave train originates over northwest Europe and subsequently propagates to west-central Asia. Also, an area of reduced skill in the control appears over northwest Europe in June, before the development of areas of reduced skill over Asia in July and August, so this experiment was also designed to reveal if the errors over west-central Asia arise as a result of errors propagating from northwest Europe. Results from this experiment show that a greater area of the northern hemisphere shows improvements in geopotential height skill compared to the west-central Asia relaxation. The CGT pattern correlations in this experiment are also improved slightly compared to the control. These results strongly suggest that northwest Europe has a much more influential role in the forcing of the CGT than west-central Asia. While the link between ISM precipitation and the D&W Index is improved with respect to the control and is the closest to observations of all the relaxation experiments, it is still weaker than observed and the majority of members have a correlation that is not significant. This suggests that precipitation over northern India is a response to forcing from northwest Europe via the CGT wave train. This in turn suggests that the ISM has a limited role in the initial forcing of the CGT, but could still play an important role in the subsequent downstream propagation of the Rossby wave train.

The third experiment involved relaxing a larger region which encompassed most of the ISM region. As the relationship between ISM precipitation and the D&W Index is too weak in both previous relaxation experiments and in the control, and given the modest skill for the model representation of the ISM, this experiment was designed to investigate the impact of correcting the monsoon circulation on extratropical skill and on the representation of the CGT. It was found that the extratropical skill is not particularly dependent on errors in the ISM circulation. In particular, the skill over Europe in June and July is largely unaffected, although some improvements were seen in August. The CGT pattern correlations were also very similar to the control, with a slight reduction in the median value. This suggests that the ISM is not the main driver of the CGT or that errors in the ISM are not responsible for the weak representation of the CGT in the ECMWF model.

However, the jet biases that were also present in previous experiments still remain, which could limit any improvements in the representation of the CGT. As with the other relaxation experiments, the correlation between ISM precipitation and the D&W Index is too weak, despite the monsoon circulation being corrected. This may limit the skill of the model at representing the CGT, as the monsoon precipitation will not be reinforcing the wave train correctly.

Results from barotropic model experiments shown in Chapter 5 suggested that differences in the strength of the forcing in the D&W region affects the strength of the response, whereas differences in the basic state do not vastly alter the phase or wavenumber of the response when forced from this region. Two thermal forcing experiments were carried out in the ECMWF model to further investigate the role of the ISM in driving the CGT and in influencing the extratropical circulation. Results from these experiments indicated that heating in the ISM region does drive an extratropical response. In particular, the response in east Asia, the North Pacific and North America is broadly consistent with a CGT-like response, with anticyclonic anomalies in these regions in the positive thermal forcing experiment. There is also a strong monsoon-desert mechanism response, with positive anomalies extending across North Africa and the Mediterranean. However, the response over northern Europe is not similar to the CGT, with cyclonic anomalies across much of the region associated with a signal that develops to the northwest of the forcing region. This suggests that, while the ISM does excite a CGT-like response in much of the northern hemisphere, the circulation over Europe is primarily not forced by the ISM via the CGT. However, there is some evidence that the circulation over Europe can be affected via eastward-propagating waves, and this is explained in Section 7.2.3.

Further experiments carried out in the barotropic model in which RWS forcings, calculated using the difference in divergence between the positive and negative heating experiments and the control, were applied over India showed a response which is consistent with the thermal forcing experiments. In these experiments, the response between Asia and North America is similar to the CGT, but the European response is related to a northwestward-propagating signal from the forcing region rather than an extension of the CGT wave train from North America. Unlike the previous barotropic model experiments, varying the basic state in the divergence forcing experiments does affect the wave propagation characteristics. Relating to research question 1 posed in Chapter 1, contrary to results from Chapter 5, this suggests that errors in the model basic state, such as the

northward jet bias, may be important in the model representation of the CGT.

Barotropic model experiments in which a sponge layer was applied at specific longitudes provide additional evidence that the response over Europe in the thermal forcing experiments results largely from westward-propagating Rossby waves from the ISM region. When a damping was applied at 60°W, the vorticity anomalies compared to the equivalent experiment without damping were almost identical, both in the European response, and in the eastward propagation of the wave train across the North Pacific to North America. When the damping was moved to 30°E, this wave train (the Silk Road Pattern (SRP)/Tokyo–Chicago Express) was weakened. Analysis of the wind anomalies near the forcing region showed that in this damped experiment there was a much larger southerly component to the wind anomalies to the west of the forcing region, which causes the advection of low vorticity air northwards. This in turn prevents the development of the positive vorticity anomalies near the Caspian Sea which occur in the undamped experiment, and which propagate along the Asian jet and reinforce the downstream wave train. This agrees with the results of Stephan et al. (2019), who showed that there is a positive feedback between ascent over India and descent over the Mediterranean, which drives the SRP. The analysis presented here also suggests that the westward-propagating Rossby wave response associated with ISM heating is crucial in the downstream reinforcement of the SRP/Tokyo–Chicago Express wave train.

Overall, it seems that the ISM can drive the extratropical northern hemisphere circulation through a CGT-like mechanism, with the exception of Europe, which is influenced more by northwestward propagating signals associated with the monsoon-desert mechanism. While the relaxation experiments suggested that northwest Europe is a more important region for the excitation of the CGT, the thermal forcing and barotropic model experiments suggested that the ISM does influence the circulation over east Asia, the North Pacific and North America via the CGT mechanism. It also affects the circulation over Europe but largely through a different mechanism - here, the response is related more to a monsoon-desert type mechanism than the CGT.

### **7.2.3 How does the Indian summer monsoon influence circulation variability over Europe?**

As described earlier, analysis of thermal forcing experiments carried out in the ECMWF model, along with barotropic model results, suggested that the circulation over Europe is not affected as part of a CGT wave train that is forced by the ISM. However, the European circulation is influenced by heating associated with the ISM in other ways. This appears to be primarily through a northwestward-moving signal from the forcing region, as part of a Rodwell and Hoskins (1996) monsoon-desert mechanism response. Both the thermal forcing and barotropic model experiments show that ISM heating is associated with a strong anticyclonic anomaly which extends across the Mediterranean and North Africa, which is consistent with the results of Rodwell and Hoskins (1996). To the north of this, over much of northern Europe, are anomalies of the opposite sign. Analysis of the heating experiments showed that these anomalies develop soon after the heating is applied, and that the European response is almost fully developed by Day 10. These anomalies also appear before the eastward-travelling Rossby waves have propagated around the hemisphere, indicating that they are not associated with this Rossby wave train. This result is further backed up by results from a damped barotropic model experiment, in which the European response when the damping is applied at 60°W is very similar to that of the undamped experiment.

One of the limitations of the thermal forcing experiments is that they were only run with five ensemble members. Analysis of the 25 member control experiment, in which correlations between centres of action of the CGT were calculated for five member subsamples, showed some variability in the strength of the model correlations when comparing different samples. However, results from the barotropic model suggest that the response seen in the thermal forcing experiments is robust and is not likely to be greatly affected by increasing the number of ensemble members.

Results from an ISM relaxation experiment are presented in Chapter 5. In this experiment, the skill over Europe in June and July remains largely unchanged compared to the control. In August, however, there are some improvements over northwest Europe, the UK and parts of the Mediterranean, suggesting that there may be a link between the ISM and Europe. Given that other results suggest limited impact of the ISM via eastward-propagating Rossby waves, this improvement in skill is more likely to be related

to the northwestward-moving signal seen in experiments in Chapter 6. Indeed, some of the largest improvements in skill are seen in the regions associated with the monsoon-desert mechanism.

One measure of the impact of heating associated with the ISM is through analysis of the total number of blocked days in both the positive and negative heating experiments. It is shown in Chapter 6 that there is a larger number of blocked days in northwest Europe in the negative heating experiment than the positive heating experiment. On average, across the 34 year period, there is around 20% more blocked days in the negative heating experiment, suggesting that the response over Europe to additional monsoon heating is a reduction in the frequency of blocking. This could be related to the northwestward-propagating signal, which results in the development of cyclonic anomalies over northern Europe in the positive heating experiment. However, there are also differences in the basic state in years with the greatest difference in total blocked days between the two heating experiments, whereby the North Pacific jet is located further north. This will affect the Rossby wave propagation characteristics for waves propagating away from east Asia, and suggests that there may be an influence of the eastward-propagating waves on the circulation over Europe. A combination of these factors may be responsible for the response seen over Europe to additional monsoon heating.

Overall, while the ISM does not appear to influence the circulation over Europe in the manner that would be expected as a result of the CGT, it can cause changes to the circulation in other ways. In particular, cyclonic anomalies over northern Europe develop associated with the northwestward propagating signal from the ISM region when ISM heating is increased, and vice versa. Possibly associated with this mechanism, along with the possible influence of eastward-propagating waves, there is a decrease in the occurrence of blocking in response to additional heating. Whether this mechanism is also present in observations, and whether it could be used as a source of skill for European summer seasonal forecasts, is unclear and requires further investigation.

### **7.3 Summary**

This thesis investigated the relationship between the CGT, the ISM and European summer seasonal forecast skill. The ECMWF model has a weak representation of the

CGT, although evidence in Chapter 5 suggests that this is not likely to be related to errors in the representation of the ISM. However, the relationship between ISM precipitation and the D&W region is not well represented, so it may be that ISM precipitation is not responding correctly to forcing from Europe as a result of model errors in this region, and this may subsequently affect the reinforcement of the CGT wave train by ISM precipitation, as hypothesised by Ding and Wang (2007). This is supported by analysis in Chapter 5, where relaxing the circulation over Europe resulted in the largest improvement in the correlation between ISM precipitation and the D&W Index.

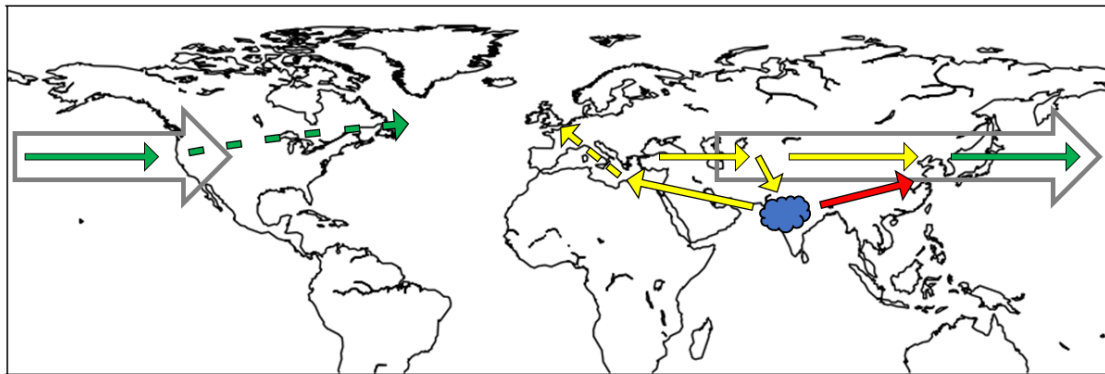


**Figure 7.1:** Schematic to show the possible mechanisms linking the ISM and the extratropical northern hemisphere circulation (adapted from Stephan et al., 2019). Precipitation associated with the ISM over northern India (blue cloud) leads to anomalous descent over the Mediterranean region via the monsoon-desert mechanism. This then induces a response downstream which subsequently reinforces the monsoon precipitation in a positive feedback loop (the Silk Road Pattern (SRP), yellow arrows). The ISM precipitation also excites an eastward-propagating response (red arrow) which leads to an anomalous anticyclone over east Asia, and this is then subsequently reinforced by the downstream propagation of waves from west-central Asia associated with the SRP. This reinforcement of the wave train as a result of the westward component of the response to ISM precipitation via the Mediterranean is crucial in the subsequent downstream propagation of the waves across the North Pacific (the Tokyo–Chicago Express, green arrows) along the Asian jet stream (large grey arrow). The circulation over northwest Europe may be influenced by a combination of the response to the monsoon-desert mechanism (dashed yellow arrow) and perturbations to the jet caused by the eastward-propagating Rossby waves (dashed green arrow) although the relative influence of each of these mechanisms is unclear.

While it appears that the CGT is not primarily driven by the ISM, evidence in Chapter 6 suggests that the ISM does play an important role in influencing the circulation in much of the northern hemisphere. When adding a thermal forcing in the ISM region, the response over east Asia, the North Pacific and North America appears similar to the CGT. This suggests that the ISM does play a role in forcing a CGT-like pattern in these regions via an eastward-propagating Rossby wave response. The response over Europe,

however, does not appear to be related to this mechanism, and anomalies in this region are of the opposite sign to those over east Asia, the North Pacific and North America. The European response seems to be dominated by a westward-propagating signal, possibly associated with the Rodwell and Hoskins (1996) monsoon-desert mechanism. However, there is some evidence that the circulation over Europe can be influenced by eastward-propagating Rossby waves from the ISM. In response to additional monsoon heating, the frequency of blocking over northwest Europe is reduced. This may be related to a combination of the westward-moving response to additional heating, where cyclonic anomalies develop over Europe, and differences in the position of the North Pacific jet, such that perturbations of the jet associated with monsoon heating have a downstream effect on the frequency of blocking over Europe. The proposed mechanisms linking ISM precipitation and the extratropical circulation are summarised in the schematic in Figure 7.1.

Barotropic model results in Chapter 6 show good agreement with the ECMWF thermal forcing experiments, with both the eastward- and westward-propagating responses appearing similar. It was also found that the westward-propagating response is important in the subsequent downstream reinforcement of the wave train between Asia and North America, which is likely to be associated with the positive feedback mechanism proposed by Stephan et al. (2019). When the westward Rossby wave response was damped, the wave train between Asia and North America was weakened. The role of the competing eastward- and westward-propagating mechanisms in determining the circulation variability over Europe is not straightforward and requires further investigation.

## **7.4 Future work**

In this section, potential avenues of future work are discussed in terms of three unanswered research questions relating to the work presented in this thesis.

### **7.4.1 What is the source of the weak representation of the circumglobal teleconnection in the model?**

A number of potential causes of the weak representation of the CGT in the model were investigated throughout this thesis. However, the processes that explain the weak model CGT remain largely unknown. From the analysis in Chapters 5 and 6 it seems unlikely that they arise from errors associated with the ISM, as the CGT does not appear to be primarily forced by the ISM, although the ISM does appear to have an important role in forcing the circulation in many regions associated with the CGT. It is also possible that the CGT could be forced from other tropical regions. Several studies have found evidence of Rossby wave propagation towards Europe from forcing in the central (O'Reilly et al., 2018) and western (A. Ossó, personal communication; Li et al., 2014) Pacific. It is therefore possible that errors in the CGT could arise if there are errors in the forcing from these regions. This could be addressed through further relaxation or thermal forcing experiments in the ECMWF model, focussing on the western and central Pacific as possible forcing regions.

In this thesis, the initial hypothesis was that the CGT is an important driver of European summer weather, and that it is forced by the ISM. Through the course of the research presented here, it appears more likely that the ISM is not forcing the CGT, particularly when it comes to the European response. However, it does appear that the ISM could influence the circulation in Europe in other ways, which is the subject of the next unanswered research question. It also seems very likely that the ISM can affect the circulation in much of the northern hemisphere through the excitation of eastward-propagating Rossby waves. An alternative approach would therefore be to start from the ISM, rather than the CGT, and conduct a study into the sensitivity of the northern hemisphere summer circulation to variations in ISM heating. The work in Chapter 6 only utilised two thermal forcing experiments, so further work could involve conducting more heating experiments, with varying levels of heating, to further examine the linearity of the extratropical response to variations in ISM heating, as well as varying the location of the heating within the ISM region. The analysis here focussed on the mean response, which is the predictable part of the signal on seasonal timescales. A further avenue for future research could therefore be to investigate how the ISM influences the likelihood of different circulation regimes occurring over Europe, in a similar manner to the analysis of Cassou (2008).

### **7.4.2 Is the signal between the Indian summer monsoon and northwest Europe seen in the model also present in observations, and if so can it be used as a source of predictability for the European summer?**

From analysis of the thermal forcing and barotropic model experiments presented in Chapter 6, in which a large forcing was applied over India, it appears that the application of additional heating in the ISM region does affect the circulation over Europe, although this does not appear to be the result of what would be expected from the CGT mechanism; rather, the European anomalies associated with additional ISM heating seem to be related more to the Rodwell and Hoskins (1996) monsoon-desert mechanism, via a westward- or northwestward-moving signal. It is not clear whether this mechanism to northwest Europe is also present in observations, and this will likely require analysis of daily observations to determine. The monsoon-desert mechanism and its influence on the Mediterranean climate has been explored in many studies, and it is unclear if the model signal over northwest Europe is as a direct consequence of this mechanism. If it is observed in the real world, then it could provide a source of predictive skill for the European summer. The heating that was applied in the thermal forcing experiments was very large compared to natural variability of the ISM, therefore the actual observed signal may be much weaker.

### **7.4.3 How do other seasonal forecast models perform at representing the circumglobal teleconnection?**

This study has been limited to the analysis of one seasonal forecast model: the ECMWF IFS. This has provided some valuable insights into the performance of this model at representing the CGT, and also provided further understanding of the CGT mechanism. However, there would be obvious benefits to examining how other models perform at representing the CGT, and also what, if any, similarities there are between the ECMWF model and other models. The work in Chapter 6 suggested that errors in the basic state, particularly jet stream biases, may cause variations in the propagation characteristics of Rossby waves associated with tropical diabatic heating. Therefore, through examining other seasonal forecast models, which have differing levels of biases, the overall impact of the ECMWF model jet biases on the representation of the CGT may be made clearer.

Analysis of several other seasonal forecast models would also help improve knowledge of several aspects of the CGT, as well as the potential influence of the ISM on the circulation in Europe. As posed earlier, the source of the weak representation of the CGT in the model is still unknown. By performing an intercomparison of the ability of a few other seasonal forecast models to represent the CGT, potential sources of the weak representation, such as forcing or wave propagation errors, could be ruled out. Another option would be to investigate the performance of the new ECMWF seasonal forecast system, SEAS5 (Johnson et al., 2019) at representing the CGT. In SEAS5, the extratropical jet stream bias is actually slightly more pronounced than in System 4. If, as hypothesised, jet stream biases are an important factor in the CGT representation, then it may be expected that the SEAS5 CGT is poorer than in the model version analysed here, taking into account other differences in background state and forcing between the two model versions.

# References

- Adler, R. F., G. J. Huffman, A. Chang, R. Ferraro, P.-P. Xie, J. Janowiak, B. Rudolf, U. Schneider, S. Curtis, D. Bolvin, A. Gruber, J. Susskind, P. Arkin, and E. Nelkin, 2003: The Version-2 Global Precipitation Climatology Project (GPCP) Monthly Precipitation Analysis (1979–Present). *J. Hydrometeor.*, **4**, 1147–1167, doi:10.1175/1525-7541(2003)004<1147:TVGPCP>2.0.CO;2.
- Allan, R., D. Chambers, W. Drosowsky, H. Hendon, M. Latif, N. Nicholls, I. Smith, R. Stone, and Y. Tourre, 2001: Is there an Indian Ocean dipole and is it independent of the El Niño–Southern Oscillation? *CLIVAR exchanges*, **21**, 18–22.
- Annamalai, H., R. Murtugudde, J. Potemra, S.-P. Xie, P. Liu, and B. Wang, 2003: Coupled dynamics over the Indian Ocean: Spring initiation of the zonal mode. *Deep Sea Res., Part II*, **50**, 2305–2330.
- Annamalai, H. and J. Slingo, 2001: Active/break cycles: diagnosis of the intraseasonal variability of the Asian summer monsoon. *Clim. Dyn.*, **18**, 85–102.
- Ashok, K., Z. Guan, N. Saji, and T. Yamagata, 2004: Individual and combined influences of ENSO and the Indian Ocean dipole on the Indian summer monsoon. *J. Climate*, **17**, 3141–3155.
- Ashok, K., Z. Guan, and T. Yamagata, 2001: Impact of the Indian Ocean Dipole on the Relationship between the Indian Monsoon Rainfall and ENSO. *Geophys. Res. Lett.*, **28**, 4499–4502.
- 2003: A look at the relationship between the ENSO and the Indian Ocean dipole. *J. Meteor. Soc. Japan.*, **81**, 41–56.
- Ashok, K. and N. Saji, 2007: On the impacts of ENSO and Indian Ocean dipole events on sub-regional Indian summer monsoon rainfall. *Nat. Hazards*, **42**, 273–285.
- Balmaseda, M. A., K. Mogensen, and A. T. Weaver, 2013: Evaluation of the ECMWF ocean reanalysis system ORAS4. *Quart. J. Roy. Meteor. Soc.*, **139**, 1132–1161.
- Bauer, P. and E. Andersson, 2011: New model cycle 37r2. *ECMWF Newsletter 128*, 10–11.
- Beverly, J. D., S. J. Woolnough, L. H. Baker, S. J. Johnson, and A. Weisheimer, 2019: The northern hemisphere circumglobal teleconnection in a seasonal forecast model and its relationship to European summer forecast skill. *Clim. Dyn.*, **52**, 3759–3771, doi:10.1007/s00382-018-4371-4.
- Bjerknes, J., 1969: Atmospheric teleconnections from the equatorial Pacific. *Mon. Wea. Rev.*, **97**, 163–172.
- Black, E., M. Blackburn, G. Harrison, B. Hoskins, and J. Methven, 2004: Factors contributing to the summer 2003 European heatwave. *Weather*, **59**, 217–223.
- Blackburn, M., J. Methven, N. Roberts, et al., 2008: Large-scale Context for the UK Floods in Summer 2007. *Weather*, **63**, 280.

- Branstator, G., 2002: Circumglobal teleconnections, the jet stream waveguide, and the North Atlantic Oscillation. *J. Climate*, **15**, 1893–1910.
- Brönnimann, S., 2007: Impact of El Niño–southern oscillation on European climate. *Rev. Geophys.*, **45**.
- Cassou, C., 2008: Intraseasonal interaction between the Madden–Julian oscillation and the North Atlantic Oscillation. *Nature*, **455**, 523.
- Cassou, C. and L. Terray, 2001: Dual influence of Atlantic and Pacific SST anomalies on the North Atlantic/Europe winter climate. *Geophys. Res. Lett.*, **28**, 3195–3198.
- Cassou, C., L. Terray, and A. S. Phillips, 2005: Tropical Atlantic influence on European heat waves. *J. Climate*, **18**, 2805–2811.
- Charney, J. and J. Shukla, 1981: Predictability of monsoons. *Monsoon dynamics*, Sir James Lighthill and R. P. Pearce, Eds., Cambridge University Press, 99–109.
- Charney, J. G., 1947: The dynamics of long waves in a baroclinic westerly current. *J. Meteorol.*, **4**, 136–162.
- Chen, G. and R. Huang, 2012: Excitation mechanisms of the teleconnection patterns affecting the July precipitation in Northwest China. *J. Climate*, **25**, 7834–7851.
- Cherchi, A., H. Annamalai, S. Masina, and A. Navarra, 2014: South Asian summer monsoon and the eastern Mediterranean climate: The monsoon–desert mechanism in CMIP5 simulations. *J. Climate*, **27**, 6877–6903.
- Chou, C., 2003: Land–sea heating contrast in an idealized Asian summer monsoon. *Clim. Dyn.*, **21**, 11–25.
- Colman, A., 1997: Prediction of summer central England temperature from preceding North Atlantic winter sea surface temperature. *Int. J. Climatol.*, **17**, 1285–1300.
- Colman, A. and M. Davey, 1999: Prediction of summer temperature, rainfall and pressure in Europe from preceding winter North Atlantic Ocean temperature. *Int. J. Climatol.*, **19**, 513–536.
- Dee, D. P., S. M. Uppala, a. J. Simmons, P. Berrisford, P. Poli, S. Kobayashi, U. Andrae, M. a. Balsameda, G. Balsamo, P. Bauer, P. Bechtold, a. C. M. Beljaars, L. van de Berg, J. Bidlot, N. Bormann, C. Delsol, R. Dragani, M. Fuentes, a. J. Geer, L. Haimberger, S. B. Healy, H. Hersbach, E. V. Hólm, L. Isaksen, P. Kållberg, M. Köhler, M. Matricardi, a. P. McNally, B. M. Monge-Sanz, J. J. Morcrette, B. K. Park, C. Peubey, P. de Rosnay, C. Tavolato, J. N. Thépaut, and F. Vitart, 2011: The ERA-Interim Reanalysis: Configuration and Performance of the Data Assimilation System. *Quart. J. Roy. Meteor. Soc.*, **137**, 553–597, doi:10.1002/qj.828.
- Della-Marta, P. M., J. Luterbacher, H. von Weissenfluh, E. Xoplaki, M. Brunet, and H. Wanner, 2007: Summer heat waves over western Europe 1880–2003, their relationship to large-scale forcings and predictability. *Clim. Dyn.*, **29**, 251–275.
- Ding, Q. and B. Wang, 2005: Circumglobal Teleconnection in the Northern Hemisphere Summer. *J. Climate*, **18**, 3483–3505, doi:10.1175/JCLI3473.1.
- 2007: Intraseasonal Teleconnection Between the Summer Eurasian Wave Train and the Indian Monsoon. *J. Climate*, **20**, 3751–3767.

- Ding, Q., B. Wang, J. M. Wallace, and G. Branstator, 2011: Tropical-extratropical Teleconnections in Boreal Summer: Observed Interannual Variability. *J. Climate*, **24**, 1878–1896, doi:10.1175/2011JCLI3621.1.
- Donald, A., H. Meinke, B. Power, A. d. H. Maia, M. C. Wheeler, N. White, R. C. Stone, and J. Ribbe, 2006: Near-global impact of the Madden-Julian Oscillation on rainfall. *Geophys. Res. Lett.*, **33**.
- Dong, B., R. Sutton, and T. Woollings, 2013a: The extreme European summer 2012. *Bull. Amer. Meteor. Soc.*, **94**, s28–s32.
- Dong, B., R. T. Sutton, T. Woollings, and K. Hodges, 2013b: Variability of the North Atlantic summer storm track: mechanisms and impacts on European climate. *Environ. Res. Lett.*, **8**, 034037.
- Douville, H., S. Bielli, C. Cassou, M. Déqué, N. M. Hall, S. Tyteca, and A. Voldoire, 2011: Tropical influence on boreal summer mid-latitude stationary waves. *Clim. Dyn.*, **37**, 1783–1798.
- Dunstone, N., D. Smith, A. Scaife, L. Hermanson, R. Eade, N. Robinson, M. Andrews, and J. Knight, 2016: Skilful predictions of the winter North Atlantic Oscillation one year ahead. *Nat. Geosci.*, **9**, 809–814.
- Dunstone, N., D. Smith, A. Scaife, L. Hermanson, D. Fereday, C. O’Reilly, A. Stirling, R. Eade, M. Gordon, C. MacLachlan, et al., 2018: Skilful seasonal predictions of Summer European rainfall. *Geophys. Res. Lett.*, **45**, 3246–3254.
- Eady, E. T., 1949: Long waves and cyclone waves. *Tellus*, **1**, 33–52.
- ECMWF, 2015: Cycle 41r1 summary of changes. <https://www.ecmwf.int/en/forecasts/documentation-and-support/changes-ecmwf-model/cy41r1-summary-changes>, accessed: 2019-07-07.
- Enomoto, T., B. J. Hoskins, and Y. Matsuda, 2003: The formation mechanism of the Bonin high in August. *Quart. J. Roy. Meteor. Soc.*, **129**, 157–178.
- Ferranti, L., T. Palmer, F. Molteni, and E. Klinker, 1990: Tropical-extratropical interaction associated with the 30–60 day oscillation and its impact on medium and extended range prediction. *J. Atmos. Sci.*, **47**, 2177–2199.
- Folland, C. K., J. Knight, H. W. Linderholm, D. Fereday, S. Ineson, and J. W. Hurrell, 2009: The Summer North Atlantic Oscillation: Past, Present, and Future. *J. Climate*, **22**, 1082–1103.
- García-Herrera, R., J. Díaz, R. M. Trigo, J. Luterbacher, and E. M. Fischer, 2010: A review of the European summer heat wave of 2003. *Crit. Rev. Env. Sci. Tech.*, **40**, 267–306.
- Ghosh, R., W. A. Müller, J. Baehr, and J. Bader, 2017: Impact of observed North Atlantic multidecadal variations to European summer climate: A linear baroclinic response to surface heating. *Clim. Dyn.*, **48**, 3547–3563.
- Gill, A., 1980: Some simple solutions for heat-induced tropical circulation. *Quart. J. Roy. Meteor. Soc.*, **106**, 447–462.
- Gouirand, I. and V. Moron, 2003: Variability of the impact of El Niño–southern oscillation on sea-level pressure anomalies over the North Atlantic in January to March (1874–1996). *Int. J. Climatol.*, **23**, 1549–1566.

- Ha, K.-J., J.-E. Chu, J.-Y. Lee, B. Wang, S. N. Hameed, and M. Watanabe, 2012: What caused the cool summer over northern Central Asia, East Asia and central North America during 2009? *Environ. Res. Lett.*, **7**, 044015.
- Haiden, T., J. Bidlot, L. Ferranti, P. Bauer, M. Dahoui, M. Janousek, F. Prates, F. Vitart, and D. Richardson, 2015: Evaluation of ECMWF forecasts, including 2014–2015 upgrades. *European Centre for Medium-Range Weather Forecasts*.
- Hall, N. M., H. Douville, and L. Li, 2013: Extratropical summertime response to tropical interannual variability in an idealized GCM. *J. Climate*, **26**, 7060–7079.
- Hong, X. and R. Lu, 2016: The meridional displacement of the summer Asian jet, Silk Road Pattern, and tropical SST anomalies. *J. Climate*, **29**, 3753–3766.
- Hoskins, B., H. H. Hsu, I. N. James, M. Masatani, P. D. Sardeshmukh, and G. H. White, 1989: Diagnostics of the global atmospheric circulation based on ECMWF analyses 1979–1989. *WCRP-27, World Meteorological Organization*.
- Hoskins, B. J. and T. Ambrizzi, 1993: Rossby wave propagation on a realistic longitudinally varying flow. *J. Atmos. Sci.*, **50**, 1661–1671.
- Hoskins, B. J. and D. J. Karoly, 1981: The steady linear response of a spherical atmosphere to thermal and orographic forcing. *J. Atmos. Sci.*, **38**, 1179–1196.
- Hoskins, B. J. and P. D. Sardeshmukh, 1987: A Diagnostic Study of the Dynamics of the Northern Hemisphere Winter of 1985–86. *Quart. J. Roy. Meteor. Soc.*, **113**, 759–778.
- Houze Jr, R., K. Rasmussen, S. Medina, S. Brodzik, and U. Romatschke, 2011: Anomalous atmospheric events leading to the summer 2010 floods in Pakistan. *Bull. Amer. Meteor. Soc.*, **92**, 291–298.
- Hsu, H.-H., C.-H. Weng, and C.-H. Wu, 2004: Contrasting Characteristics between the Northward and Eastward Propagation of the Intraseasonal Oscillation during the Boreal Summer. *J. Climate*, **17**, 727–743.
- Hughes, T. and S. Gambrill, 2012: Summer floods in the UK: Comparing 2012 and 2007. *Tech. rep., AIR Worldwide, London, UK*.
- Hurrell, J. W., Y. Kushnir, G. Ottersen, and M. Visbeck, 2003: An overview of the North Atlantic Oscillation. *The North Atlantic Oscillation: Climatic Significance and Environmental Impact, Geophys. Monogr.*, **134**, 1–35.
- James, I. N., 1995: Introduction to circulating atmospheres. *Cambridge University Press*.
- Johnson, S. J., T. N. Stockdale, L. Ferranti, M. A. Balmaseda, F. Molteni, L. Magnusson, S. Tietsche, D. Decremer, A. Weisheimer, G. Balsamo, S. P. E. Keeley, K. Mogensen, H. Zuo, and B. M. Monge-Sanz, 2019: SEAS5: the new ECMWF seasonal forecast system. *Geosci. Model Dev.*, **12**, 1087–1117.
- Johnson, S. J., A. Turner, S. Woolnough, G. Martin, and C. MacLachlan, 2016: An Assessment of Indian Monsoon Seasonal Forecasts and Mechanisms Underlying Monsoon Interannual Variability in the Met Office GloSea5-GC2 System. *Clim. Dyn.*, 1–19.
- Jones, C., D. E. Waliser, K. Lau, and W. Stern, 2004: Global occurrences of extreme precipitation and the Madden–Julian oscillation: Observations and predictability. *J. Climate*, **17**, 4575–4589.

- Joseph, P. and J. Srinivasan, 1999: Rossby Waves in May and the Indian Summer Monsoon Rainfall. *Tellus A*, **51**, 854–864, doi:10.1034/j.1600-0870.1999.00021.
- Ju, J. and J. Slingo, 1995: The Asian Summer Monsoon and ENSO. *Quart. J. Roy. Meteor. Soc.*, **121**, 1133–1168.
- Jung, T., M. Miller, and T. Palmer, 2010a: Diagnosing the origin of extended-range forecast errors. *Mon. Wea. Rev.*, **138**, 2434–2446.
- Jung, T., T. Palmer, M. Rodwell, and S. Serrar, 2008: Diagnosing forecast error using relaxation experiments. *ECMWF Newsletter 116*, 24–34.
- 2010b: Understanding the anomalously cold European winter of 2005/06 using relaxation experiments. *Mon. Wea. Rev.*, **138**, 3157–3174.
- Kalnay, E., M. Kanamitsu, R. Kistler, W. Collins, D. Deaven, L. Gandin, M. Iredell, S. Saha, G. White, J. Woollen, et al., 1996: The NCEP/NCAR 40-year reanalysis project. *Bull. Amer. Meteor. Soc.*, **77**, 437–472.
- Kim, H.-M., P. J. Webster, J. A. Curry, and V. E. Toma, 2012: Asian summer monsoon prediction in ECMWF System 4 and NCEP CFSv2 retrospective seasonal forecasts. *Clim. Dyn.*, **39**, 2975–2991.
- Kim, K.-Y., J. Kim, K.-O. Boo, S. Shim, and Y. Kim, 2019: Intercomparison of precipitation datasets for summer precipitation characteristics over East Asia. *Clim. Dyn.*, **52**, 3005–3022.
- Klinker, E., 1990: Investigation of systematic errors by relaxation experiments. *Quart. J. Roy. Meteor. Soc.*, **116**, 573–594.
- Kosaka, Y., J. Chowdary, S.-P. Xie, Y.-M. Min, and J.-Y. Lee, 2012: Limitations of seasonal predictability for summer climate over East Asia and the Northwestern Pacific. *J. Climate*, **25**, 7574–7589.
- Kripalani, R. H. and A. Kulkarni, 1997: Rainfall variability over South-east Asia—connections with Indian monsoon and ENSO extremes: new perspectives. *Int. J. Climatol.*, **17**, 1155–1168.
- 2001: Monsoon rainfall variations and teleconnections over South and East Asia. *Int. J. Climatol.*, **21**, 603–616.
- Kumar, K. K., B. Rajagopalan, M. Hoerling, G. Bates, and M. Cane, 2006: Unraveling the Mystery of Indian Monsoon Failure During El Niño. *Science*, **314**, 115–119.
- Lau, K.-M. and H. Weng, 2002: Recurrent teleconnection patterns linking summertime precipitation variability over East Asia and North America. *J. Meteor. Soc. Japan.*, **80**, 1309–1324.
- Lau, W. K. and K.-M. Kim, 2012: The 2010 Pakistan flood and Russian heat wave: Teleconnection of hydrometeorological extremes. *J. Hydrometeor.*, **13**, 392–403.
- Lau, W. K.-M., K.-M. Kim, and J.-Y. Lee, 2004: Interannual variability, global teleconnection, and potential predictability associated with the Asian summer monsoon. *East Asian Monsoon*, C.P. Chang, Ed., World Scientific, 153–176.
- Lee, J.-Y., B. Wang, Q. Ding, K.-J. Ha, J.-B. Ahn, A. Kumar, B. Stern, and O. Alves, 2011: How predictable is the northern hemisphere summer upper-tropospheric circulation? *Clim. Dyn.*, **37**, 1189–1203.

- Li, C., X. Jia, J. Ling, W. Zhou, and C. Zhang, 2009: Sensitivity of MJO simulations to diabatic heating profiles. *Clim. Dyn.*, **32**, 167–187.
- Li, R. C., W. Zhou, and T. Li, 2014: Influences of the Pacific–Japan teleconnection pattern on synoptic-scale variability in the western North Pacific. *J. Climate*, **27**, 140–154.
- Liu, F. and B. Wang, 2013: Mechanisms of global teleconnections associated with the Asian summer monsoon: An intermediate model analysis. *J. Climate*, **26**, 1791–1806.
- Lorenz, D. J. and D. L. Hartmann, 2006: The effect of the MJO on the North American monsoon. *J. Climate*, **19**, 333–343.
- Lu, R.-Y., J.-H. Oh, and B.-J. Kim, 2002: A teleconnection pattern in upper-level meridional wind over the North African and Eurasian continent in summer. *Tellus A*, **54**, 44–55.
- Luterbacher, J., D. Dietrich, E. Xoplaki, M. Grosjean, and H. Wanner, 2004: European seasonal and annual temperature variability, trends, and extremes since 1500. *Science*, **303**, 1499–1503.
- Madden, R. A. and P. R. Julian, 1971: Detection of a 40–50 Day Oscillation in the Zonal Wind in the Tropical Pacific. *J. Atmos. Sci.*, **28**, 702–708.
- 1972: Description of global-scale circulation cells in the tropics with a 40–50 day period. *J. Atmos. Sci.*, **29**, 1109–1123.
- Mariotti, A., N. Zeng, and K.-M. Lau, 2002: Euro-Mediterranean rainfall and ENSO—a seasonally varying relationship. *Geophys. Res. Lett.*, **29**, 59–1.
- Met Office, 2018: Was summer 2018 the hottest on record? <https://www.metoffice.gov.uk/about-us/press-office/news/weather-and-climate/2018/end-of-summer-stats>, accessed: 2019-07-08.
- Mishra, N., C. Prodhomme, and V. Guemas, 2019: Multi-model skill assessment of seasonal temperature and precipitation forecasts over Europe. *Clim. Dyn.*, **52**, 4207–4225.
- Molteni, F., T. Stockdale, M. Balsameda, G. Balsamo, R. Buizza, L. Ferranti, L. Magnusson, K. Mogensen, T. Palmer, and F. Vitart, 2011: The new ECMWF seasonal forecast system (System 4). *European Centre for Medium-Range Weather Forecasts*.
- Muñoz-Díaz, D. and F. Rodrigo, 2005: Influence of the El Niño-Southern Oscillation on the probability of dry and wet seasons in Spain. *Clim. Res.*, **30**, 1–12.
- Nitta, T., 1987: Convective activities in the tropical western Pacific and their impact on the Northern Hemisphere summer circulation. *J. Meteor. Soc. Japan.*, **65**, 373–390.
- O’Reilly, C. H., T. Woollings, L. Zanna, and A. Weisheimer, 2018: The impact of tropical precipitation on summertime Euro-Atlantic circulation via a circumglobal wave-train. *J. Climate*.
- Osborn, T. J., 2011: Winter 2009/2010 temperatures and a record-breaking North Atlantic Oscillation index. *Weather*, **66**, 19–21.
- Ossó, A., R. Sutton, L. Shaffrey, and B. Dong, 2018: Observational evidence of European summer weather patterns predictable from spring. *Proc. Natl. Acad. Sci. USA*, **115**, 59–63.
- Philander, S. G. H., 1983: El Nino southern oscillation phenomena. *Nature*, **302**, 295.

- Pitt, M., 2008: The Pitt Review: Learning lessons from the 2007 floods. *Cabinet Office Independent Review*.
- Pozo-Vázquez, D., M. Esteban-Parra, F. Rodrigo, and Y. Castro-Diez, 2001: The association between ENSO and winter atmospheric circulation and temperature in the North Atlantic region. *J. Climate*, **14**, 3408–3420.
- Rajeevan, M., C. Unnikrishnan, and B. Preethi, 2012: Evaluation of the ENSEMBLES multi-model seasonal forecasts of Indian summer monsoon variability. *Clim. Dyn.*, **38**, 2257–2274.
- Rex, D. F., 1950: Blocking action in the middle troposphere and its effect upon regional climate. *Tellus*, **2**, 275–301.
- Richardson, D. and P. Bauer, 2015: New model cycle launched in May. *ECMWF Newsletter 144*, 4–5.
- Robine, J.-M., S. L. K. Cheung, S. Le Roy, H. Van Oyen, C. Griffiths, J.-P. Michel, and F. R. Herrmann, 2008: Death toll exceeded 70,000 in Europe during the summer of 2003. *C. R. Biol.*, **331**, 171–178.
- Rodwell, M. J. and B. J. Hoskins, 1996: Monsoons and the Dynamics of Deserts. *Quart. J. Roy. Meteor. Soc.*, **122**, 1385–1404, doi:10.1002/qj.49712253408.
- 2001: Subtropical anticyclones and summer monsoons. *J. Climate*, **14**, 3192–3211.
- Ropelewski, C. F. and M. S. Halpert, 1987: Global and Regional Scale Precipitation Patterns Associated with the El Niño/Southern Oscillation. *Mon. Wea. Rev.*, **115**, 1606–1626.
- Rossby, C.-G., 1939: Relation between variations in the intensity of the zonal circulation of the atmosphere and the displacements of the semi-permanent centers of action. *J. Meteor. Res.*, **2**, 38–55.
- Sardeshmukh, P. D. and B. J. Hoskins, 1988: The Generation of Global Rotational Flow by Steady Idealized Tropical Divergence. *J. Atmos. Sci.*, **45**, 1228–1251.
- Scaife, A. A., D. Copesey, C. Gordon, C. Harris, T. Hinton, S. Keeley, A. O’Neill, M. Roberts, and K. Williams, 2011: Improved Atlantic winter blocking in a climate model. *Geophys. Res. Lett.*, **38**.
- Schaller, N., J. Sillmann, J. Anstey, E. Fischer, C. Grams, and S. Russo, 2018: Influence of blocking on Northern European and Western Russian heatwaves in large climate model ensembles. *Environ. Res. Lett.*, **13**, 054015.
- Scherrer, S. C., M. Croci-Maspoli, C. Schwierz, and C. Appenzeller, 2006: Two-dimensional indices of atmospheric blocking and their statistical relationship with winter climate patterns in the Euro-Atlantic region. *Int. J. Climatol.*, **26**, 233–249.
- Schubert, S., H. Wang, and M. Suarez, 2011: Warm season subseasonal variability and climate extremes in the Northern Hemisphere: The role of stationary Rossby waves. *J. Climate*, **24**, 4773–4792.
- Schumacher, C., R. A. Houze Jr, and I. Kraucunas, 2004: The tropical dynamical response to latent heating estimates derived from the TRMM precipitation radar. *J. Atmos. Sci.*, **61**, 1341–1358.

- Shaman, J., 2014: The seasonal effects of ENSO on atmospheric conditions associated with European precipitation: Model simulations of seasonal teleconnections. *J. Climate*, **27**, 1010–1028.
- Shaman, J. and E. Tziperman, 2007: Summertime ENSO–North African–Asian Jet teleconnection and implications for the Indian monsoons. *Geophys. Res. Lett.*, **34**.
- Shimizu, M. H. and I. F. de Albuquerque Cavalcanti, 2011: Variability patterns of Rossby wave source. *Clim. Dyn.*, **37**, 441–454.
- Shukla, J. and D. A. Paolino, 1983: The Southern Oscillation and Long-Range Forecasting of the Summer Monsoon Rainfall over India. *Mon. Wea. Rev.*, **111**, 1830–1837.
- Simmons, A. J. and B. J. Hoskins, 1978: The life cycles of some nonlinear baroclinic waves. *J. Atmos. Sci.*, **35**, 414–432.
- Sousa, P. M., R. M. Trigo, D. Barriopedro, P. M. Soares, and J. A. Santos, 2018: European temperature responses to blocking and ridge regional patterns. *Clim. Dyn.*, **50**, 457–477.
- Sperber, K., H. Annamalai, I.-S. Kang, A. Kitoh, A. Moise, A. Turner, B. Wang, and T. Zhou, 2013: The Asian summer monsoon: an intercomparison of CMIP5 vs. CMIP3 simulations of the late 20th century. *Clim. Dyn.*, **41**, 2711–2744.
- Stephan, C. C., N. P. Klingaman, and A. G. Turner, 2019: A mechanism for the recently increased interdecadal variability of the Silk Road Pattern. *J. Climate*, **32**, 717–736.
- Sterl, A., 2004: On the (In)Homogeneity of Reanalysis Products. *J. Climate*, **17**, 3866–3873.
- Stockdale, T. N., F. Molteni, and L. Ferranti, 2015: Atmospheric initial conditions and the predictability of the Arctic Oscillation. *Geophys. Res. Lett.*, **42**, 1173–1179.
- Sun, Q., C. Miao, Q. Duan, H. Ashouri, S. Sorooshian, and K.-L. Hsu, 2018: A review of global precipitation data sets: data sources, estimation, and intercomparisons. *Rev. Geophys.*, **56**, 79–107.
- Sutton, R. T. and D. L. Hodson, 2005: Atlantic Ocean forcing of North American and European summer climate. *Science*, **309**, 115–118.
- Taylor, K. E., R. J. Stouffer, and G. A. Meehl, 2012: An overview of CMIP5 and the experiment design. *Bull. Amer. Meteor. Soc.*, **93**, 485–498.
- Tibaldi, S. and F. Molteni, 1990: On the operational predictability of blocking. *Tellus A*, **42**, 343–365.
- Trenberth, K. E., 1997: The Definition of El Niño. *Bull. Amer. Meteor. Soc.*, **78**, 2771–2778.
- Trenberth, K. E., T. Koike, and K. Onogi, 2008: Progress and prospects for reanalysis for weather and climate. *Eos, Trans. Amer. Geophys. Union*, **89**, 234–235.
- Tyrlis, E. and B. Hoskins, 2008: Aspects of a Northern Hemisphere atmospheric blocking climatology. *J. Atmos. Sci.*, **65**, 1638–1652.
- Tyrlis, E., J. Lelieveld, and B. Steil, 2013: The summer circulation over the eastern Mediterranean and the Middle East: influence of the South Asian monsoon. *Clim. Dyn.*, **40**, 1103–1123.

- van Loon, H. and R. A. Madden, 1981: The Southern Oscillation. Part I: Global associations with pressure and temperature in northern winter. *Mon. Wea. Rev.*, **109**, 1150–1162.
- Walker, G. T., 1923: Correlation in seasonal variation of weather VIII: A preliminary study of world weather. *Mem. Indian Meteor. Dep.*, **24**, 75–131.
- 1924a: Correlation in seasonal variation of weather IX: A further study of world weather. *Mem. Indian Meteor. Dep.*, **24**, 225–232.
- 1924b: Correlations in seasonal variations of weather, XI. A further study of world weather. *Mem. Indian Meteor. Dep.*, **24**, 275–332.
- Walker, G. T. and E. Bliss, 1932: World weather V. *Mem. Roy. Meteor. Soc.*, **4**, 53–84.
- Wang, B., R. Wu, and K. Lau, 2001: Interannual variability of the Asian summer monsoon: Contrasts between the Indian and the western North Pacific–East Asian monsoons. *J. Climate*, **14**, 4073–4090.
- Wang, H., B. Wang, F. Huang, Q. Ding, and J.-Y. Lee, 2012: Interdecadal change of the boreal summer circumglobal teleconnection (1958–2010). *Geophys. Res. Lett.*, **39**.
- Wang, L., P. Xu, W. Chen, and Y. Liu, 2017: Interdecadal variations of the Silk Road pattern. *J. Climate*, **30**, 9915–9932.
- Watson, P. A., A. Weisheimer, J. R. Knight, and T. Palmer, 2016: The role of the tropical West Pacific in the extreme Northern Hemisphere winter of 2013/2014. *J. Geophys. Res. Atmos.*, **121**, 1698–1714.
- Wei, W., R. Zhang, M. Wen, X. Rong, and T. Li, 2014: Impact of Indian summer monsoon on the South Asian High and its influence on summer rainfall over China. *Clim. Dyn.*, **43**, 1257–1269.
- Weisheimer, A., F. Doblas-Reyes, T. Palmer, A. Alessandri, A. Arribas, M. Déqué, N. Keenlyside, M. MacVean, A. Navarra, and P. Rogel, 2009: ENSEMBLES: A new multi-model ensemble for seasonal-to-annual predictions—Skill and progress beyond DEMETER in forecasting tropical Pacific SSTs. *Geophys. Res. Lett.*, **36**.
- Weisheimer, A., N. Schaller, C. O’Reilly, D. A. MacLeod, and T. Palmer, 2017: Atmospheric seasonal forecasts of the twentieth century: multi-decadal variability in predictive skill of the winter North Atlantic Oscillation (NAO) and their potential value for extreme event attribution. *Quart. J. Roy. Meteor. Soc.*
- Willmott, C. J. and K. Matsuura, 2001: Terrestrial air temperature and precipitation: Monthly and annual time series (1950–1999) version 1.02. *Center for Climatic Research, University of Delaware, Newark*.
- Woollings, T., 2010: Dynamical influences on European climate: an uncertain future. *Phil. Trans. R. Soc. A*, **368**, 3733–3756.
- Woollings, T., A. Hannachi, B. Hoskins, and A. Turner, 2010: A regime view of the North Atlantic Oscillation and its response to anthropogenic forcing. *J. Climate*, **23**, 1291–1307.
- Wu, B., T. Zhou, and T. Li, 2016: Impacts of the Pacific–Japan and circumglobal teleconnection patterns on the interdecadal variability of the East Asian summer monsoon. *J. Climate*, **29**, 3253–3271.

- Wu, R. and B. Wang, 2002: A contrast of the East Asian summer monsoon–ENSO relationship between 1962–77 and 1978–93. *J. Climate*, **15**, 3266–3279.
- Xie, S.-P., K. Hu, J. Hafner, H. Tokinaga, Y. Du, G. Huang, and T. Sampe, 2009: Indian Ocean capacitor effect on Indo–western Pacific climate during the summer following El Niño. *J. Climate*, **22**, 730–747.
- Yasui, S. and M. Watanabe, 2010: Forcing processes of the summertime circumglobal teleconnection pattern in a dry AGCM. *J. Climate*, **23**, 2093–2114.
- Yunyun, L. and D. Yihui, 2008: Analysis and numerical simulations of the teleconnection between Indian summer monsoon and precipitation in North China. *J. Meteor. Res.*, **22**, 489–501.
- Zebiak, S. E., 1993: Air–sea interaction in the equatorial Atlantic region. *J. Climate*, **6**, 1567–1586.
- Zhang, R., A. Sumi, and M. Kimoto, 1999: A diagnostic study of the impact of El Niño on the precipitation in China. *Adv. Atmos. Sci.*, **16**, 229–241.
- Zhang, W., Y. Wang, F.-F. Jin, M. F. Stuecker, and A. G. Turner, 2015: Impact of different El Niño types on the El Niño/IOD relationship. *Geophys. Res. Lett.*, **42**, 8570–8576.

